NASA CR-134536
LMSC/D465537

FINAL REPORT

WALL MOUNTED HEAT EXCHANGER CHARACTERIZATION

By

B. R. BULLARD

LOCKHEED MISSILES & SPACE COMPANY, INC.

Prepared for

NATIONAL AERONAUTICS AND SPACE ADMINISTRATION

NASA Lewis Research Center
Contract NAS 3-16769

1. Report No.	2. Government Accession No.	3. Recipient's Catalog No.
NASA CR-134536		

4. Title and Subtitle	5. Report Date
Final Report Wall Mounted Heat Exchanger Characterization	January 1975
	6. Performing Organization Code
7. Author(s)	8. Performing Organization Report No.
B. R. Bullard	LMSC
	10. Work Unit No.
9. Performing Organization Name and Address	
Lockheed Missiles & Space Co., Inc. Sunnyvale, California 94088	11. Contract or Grant No. NAS3-16769
	13. Type of Report and Period Covered
12. Sponsoring Agency Name and Address	Contractor Report
National Aeronautics and Space Administration Washington, D. C. 20546	14. Sponsoring Agency Code

15. Supplementary Notes

Project Manager, D. E. Sokolowski, Chemical Propulsion Division
NASA Lewis Research Center, Cleveland, Ohio

16. Abstract

Analytical models are presented for describing the heat and mass transfer and the energy distribution in the contents of a cryogenic propellant tank, under varying gravity levels. These models are used to analytically evaluate the effectiveness of a wall heat exchanger as a means of controlling the pressure in the tank during flight and during fill operations. Pressure and temperature histories are presented for tanks varying in size from 4 to 22.5 feet in diameter and gravity levels from 0-1. Results from the subscale test program, utilizing both non-cryogenic and cryogenic fluid, designed to evaluate a tank wall heat exchanger are described and compared with the analytical models. Both the model and test results indicate that a passive tank wall heat exchanger can effectively control tank pressure. However, the weight of such a system is considerably higher than that of an active mixer system.

17. Key Words (Suggested by Author(s))	18. Distribution Statement
Cryogenics Tank Pressure Control Thermal Conditioning Systems Thermodynamic Vent Systems	Unclassified – unlimited

19. Security Classif. (of this report)	20. Security Classif. (of this page)	21. No. of Pages	22. Price*
Unclassified	Unclassified		

* For sale by the National Technical Information Service, Springfield, Virginia 22151

FOREWORD

The Lockheed Missiles and Space Company (LMSC) is submitting this report in fulfillment of the requirements of contract NAS 3-16769. The program was conducted by the Space Systems Division of LMSC, under the management of the NASA Project Manager, Mr. D. E. Sokolowski, NASA Lewis Research Center.

CONTENTS

ILLUSTRATIONS

Section 1

SUMMARY

A thermodynamic vent system is one wherein vent fluid is extracted from a tank, expanded through a Joule-Thompson valve to produce a temperature drop, and then passed through a heat exchanger to cool the remaining fluid in the tank. The program described in this report was designed to evaluate a passive system for which the heat exchanger is formed by wrapping tubing over the tank wall. No active mixing is used to stir the tank contents. Therefore, conduction and/or free convection will control the energy distribution within the tank and the rate at which the tank pressure can be controlled by cooling at the tank wall. This suggests that the system efficiency, which is based on the ability to control pressure while minimizing total mass loss, may be gravity dependent.

The objectives of this program were to: (1) develop analytical models which describe the mass and energy distribution inside cryogenic tanks and relate these to the pressure control characteristics (primary variables were gravity level, heat flux, and tank size), (2) develop design models for the wall mounted system, (3) devise and implement a one-g test program to simulate the low-g conditions and provide data to supplement the analytical models, and (4) evaluate the validity of the models.

The program was divided into the following five technical tasks:

- Task I – Characterization of Cryogenic Tank Pressure Histories
- Task II – Experimental Evaluation of the Heat Transfer Model
- Task III – Design and Fabrication of System for Experimental Evaluation of Design Model
- Task IV – Test Evaluation of Design Model System
- Task V – Correlation of Analytical and Experimental Data

Two models were developed in Task I; one for the case of pure conduction (zero-g) and one for the case where heat transfer was convection dominated. Further, the zero-g case requires that a model be developed for each tank shape (i.e., sphere, cylinder with L/D = 2, 3, 4, etc.). An R-C network is generated for each configuration and ullage volume with the liquid-vapor interface assumed to be spherical. Phase change occurs anywhere in the liquid if the local temperature is above the instantaneous saturation temperature. The R-C nodal network is put into a thermal analyzer program along with criteria for phase change. The program computes the mass and energy balances and corresponding pressure and temperature histories for a given heat exchanger resistance (wall-to-tube). This model indicates that the tank wall heat exchanger will control tank pressure, even under zero-g conditions.

With an active mixer system the tank contents are maintained in a funiform condition with mechanical mixing. Thus, there is no subcooling in the bottom of tank which results in excess loss of vented propellant. With the tank wall heat exchanger colder fluid collects in the bottom during the cooling cycle giving rise to nonuniform conditions; this results in some subcooling and a concommitant excess vented propellant. However, even in zero-g this becomes a relatively insignificant penalty when the vehicle has been through 5 or 6 vent cycles.

Section 2

INTRODUCTION

So effective have become the thermal protection systems for cryogenic space propulsion vehicles that nonvented storage of liquid cryogens is now a practical consideration for Earth-orbital and planetary orbit injection missions. Even so, in all propellant tankage systems a pressure relief system is mandatory for safety and system operational considerations. For example, venting may be desired for reduction of tank pressure after an engine firing. In this way, lower tank operating pressures and tank weights may be used and still provide the required net positive suction pressure to the engine, when successive firings are demanded by the mission profile.

Normally, a gas-vent relief valve might be considered for venting the cryogen tank. In space flight, however, long periods of near zero-gravity coast of the spacecraft occur. Space flight experience has shown that in zero-gravity the location and movement of the liquid propellant in the tank is uncertain. Thus, under such conditions, pressure relief of the tank through an ordinary relief valve is unreliable and possibly very inefficient because of the likely ingestion of large amounts of liquid cryogen that would be vented directly overboard. Actual mission failures have occurred because of excessive propellant loss and consumption of attitude control propellants to correct for large variations and unbalances in vehicle motions that were induced by the vent system.

One concept for providing effective control without the above mentioned problems is a thermodynamic vent system. During operation of this system, vent fluid is withdrawn from the tank and expanded through a Joule-Thompson valve to produce a refrigerated vapor. This cold fluid is then passed through a heat exchanger that is in contact with the tank propellants, where it absorbs enough energy to vaporize the liquid in the wet vapor. The vented propellant is then vented overboard as a saturated or superheated vapor just as though it had been extracted directly from the ullage. The thermodynamic process is illustrated on figure 2-1.

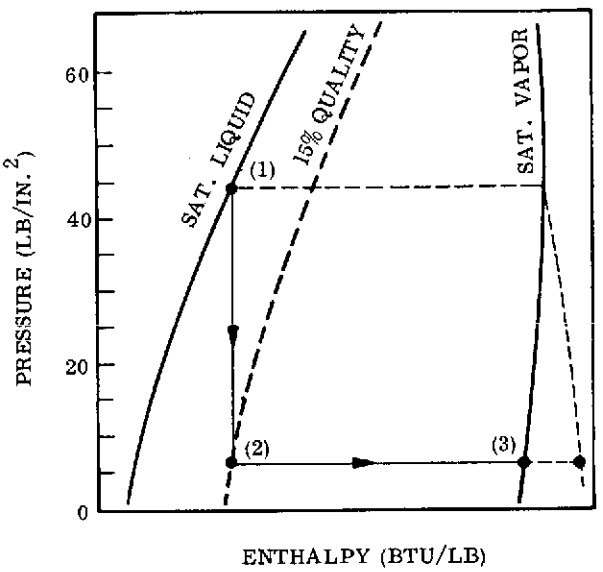

Fig. 2-1 Thermodynamic Process

The NASA-LeRC recognized the potential of this type of system some time ago and awarded contracts to LMSC (NAS 3-7942, 3-12033) which resulted in the design, development and experimental demonstration of an active system that used a compact heat exchanger.

In this previous work, design data and analysis techniques were developed which related both the thermal and hydrodynamic (mixing) characteristics of the vent system to the pressure response in the tank. It was shown that when the mixer jet velocity exceeded a critical valve necessary to give complete circulation, the tank pressure could be predicted with mixed model theory and pressure response was limited by the thermal capacity of the heat exchanger. The analytical models were confirmed with approximately 1500 hours of testing in 41.5 inch and 109 inch diameter tanks. The results of this previous work on the active system are presented in Ref. 1-3. A similar program is described in Ref. 4.

The basic objective of this program was to provide techniques and data for the passive tank wall heat exchanger concept that would parallel that previously obtained for the

active system. The program is both analytical and experimental in nature and is designed to measure the effectiveness of the tank wall heat exchanger system as a low gravity tank pressure control device. Specific objectives which served to accomplish the foregoing broad objective were as follows:

1. Develop analytical models which describe the energy distribution inside cryogenic tanks and which relate these to the pressure control characteristics.
2. Develop design models for the wall mounted heat exchanger.
3. Devise and implement a one-g test program for simulating low-g convection and provide data to supplement the analytical models.
4. Correlate the experimental results with the analytical models.

Performance curves have been generated for a wide range of tank sizes, g-level, heat flux, etc., and are contained herein. However, the theoretical developments, evaluation criteria, and test techniques can be used for any specific application, such as a cryogenic space tug. They are also valid for non-cryogenic fluids. Details of the program are described in the following sections of the report.

Section 3
CHARACTERIZATION OF CRYOGENIC TANK PRESSURES

When no active mixing is used to stir the contents, conduction and/or free convection will control the energy distribution within a space vehicle cryogen tank. The extent to which one mode will limit the pressure control process depends upon the heat flux and g-level. This is illustrated on Fig. 3-1a as a thermal resistance dependency. If the g-level is sufficiently high to induce free convection it takes time to establish a boundary layer. During this transient period, the thermal resistance could be expected to vary in a manner depicted in Fig. 3-1b. An analysis was performed to estimate the time required to develop the boundary layer. However, the approach in this program was to determine the pressure response using conduction models, and convection model with fully established flow. If the convection model results in vent periods of the same order, or shorter, than the predicted time for developing the boundary layer, then the more conservative conduction model would be used for the heat exchanger design.

The basic configurations and operational parameters for this study are listed in Table 3-1. However, this wide matrix can more easily be assimilated reducing it to physically meaningful dimensionless parameters, such as the Bond number (Bo) and Raleigh number (Ra). These dimensionless parameters indicate the importance of liquid orientation, free convection, conduction, etc. and thus the type of analytical models that are needed.

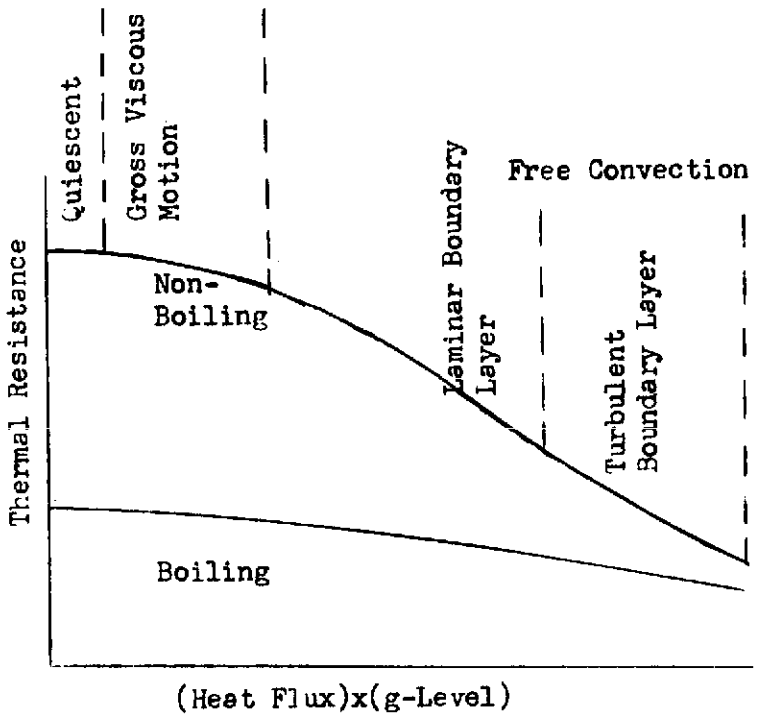

(a) Heat Transfer Domains

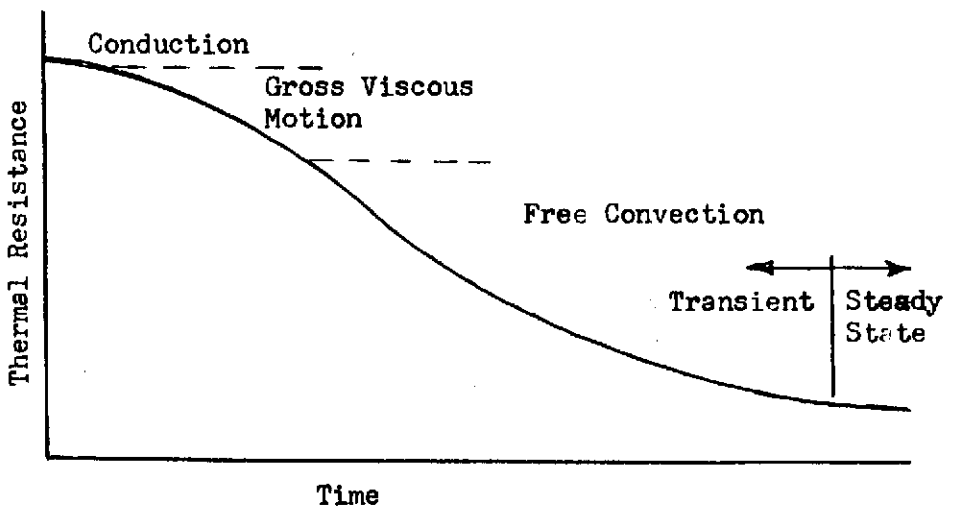

(b) Thermal Resistance Related to Time

Fig. 3-1 Pictorial Illustration of Heat Transfer Domains and Thermal Resistance

Table 3-1

TANK CONFIGURATIONS

Configuration	Diameter m (feet)	Tank No.	Ullage Ratio	Acceleration g/g_o	Heat Flux, w/m^2 ($Btu/Hr-Ft^2$)
Sphere	1.22, 2.44, 12.2 (4), (8), (40)	1, 2, 3	0.05, 0.50, 0.90	0, 10^{-6}, 1	0.31, 1.56, 3.14 (0.1), (0.5), (1.0)
Cylinder	0.90 L/D = 2 (2.95)	4	0.05, 0.50, 0.90	0, 10^{-6}, 1	0.31, 1.56, 3.14
	1.80 L/D = 2 (5.9)	5	0.05, 0.50, 0.90	0, 10^{-6}, 1	0.31, 1.56, 3.14
	1.37 L/D = 4 (4.5)	7	0.05, 0.50, 0.90	0, 10^{-6}, 1	0.31, 1.56, 3.14
	3.66 L/D = 4 (12.0)	8	0.05, 0.50, 0.90	0, 10^{-6}, 1	0.31, 1.56, 3.14
	8.84 L/D = 2 (29.0)	6	0.05, 0.50, 0.90	0, 10^{-6}, 1	0.31, 1.56, 3.14
	6.86 L/D = 4 (22.5)	9	0.05, 0.50, 0.90	0, 10^{-6}, 1	0.31, 1.56, 3.14

The liquid-ullage interface configuration can be inferred from the Bond number which can be computed from the following relationship:

$$Bo = \alpha D^2 \frac{\rho g_o}{4\sigma g_c}$$

where: $\alpha = g/g_o$, ρ = liquid density, σ = surface tension

g_o = standard gravitational acceleration

g_c = universal gravitational constant

This Equation is graphed as Figs. 3-2 and 3-3 for hydrogen and oxygen, respectively. Also shown are the points from Table 3-1, identified by tank number, and g level (except where g = Bo = 0). As indicated on the figures, at 10^{-6} g's, the four largest tanks will have interface configurations somewhere between spherical and flat (i.e., $1 \leq Bo \leq 10^2$). The other tanks and g-levels can be treated with either a flat or spherical interface model.

The heat transfer domains to be modeled can be characterized by a modified Raleigh number defined by:

$$Ra^* = g_o X^4 q_w \left(\frac{\beta \rho^2 C}{\mu k^2}\right)$$

This Equation is graphed on Figs. 3-4 and 3-5 for LH_2 and LO_2, respectively, which also show the computed points from the Table 3-1 matrix for $\alpha = 1$, and 10^{-6}. A non-dimensional heat flux, $q_w^* = q_w / 1.0$ has been used for convenience in plotting Figs. 3-4 and 3-5. The characteristic length used in the computation was approximated from the tank length (L) and ullage ratio (V_u^*) as $X = L (1 - V_u^*)$.

The study points plotted on Figs. 3-4 and 3-5 can be compared with the types of convection indicated for various values of the Raleigh number ($\overset{*}{Ra}$), as shown along the right hand edge of these graphs. The study points lie within rather narrow bands along each of the acceleration levels considered, $\alpha = 0$, 10^{-6} and 1, since a limited range of q_w^* was considered, $0.1 \leq q_w \leq 1.0$. For the one gravity study points, $10^{-1} \leq \alpha q^* \leq 1$, the flow regime should vary from transition flow between laminar and turbulent boundary layers for the smallest scale tanks up to fully established turbulent convection for all larger scale tanks. Even the smallest scale tanks with one gravity acceleration and a ground hold heat rate would all experience turbulent free convection boundary layers.

The study points for $\alpha = 10^{-6}$ acceleration level and $0.1 \leq q_w{}^* \leq 1.0$ wall heat flux, range from gross viscous motion for the smallest dimensions X to a turbulent free convection boundary layer for large scale X dimensions. Notice that the first five sets of study points, designated by tank numbers 1, 4, 2, 5 and 7, at the smallest X lengths, all apply to low Bond numbers, $B_o < 1.0$, and low fill levels, $(1 - V_u{}^*) = 0.1$. The liquid configuration in these tanks will result in longer values of X than those estimated in this study, so that the values of Ra^* might be one or two orders of magnitude higher than shown for these points. Hence, all of the $\alpha = 10^{-6}$ acceleration level study points would be in the laminar and turbulent boundary layer regimes. Based upon the Figs. 3-4 and 3-5 study points, therefore, gross viscous motion was not modeled.

For zero gravity, ($\alpha = 0$), the modified Raleigh number $Ra^* = 0$. Hence, one third of the total study points, are in the pure conduction heat transfer domain. Although this acceleration level could never be practically obtained, its heat transfer model represents a limiting solution of the tank pressurization time.

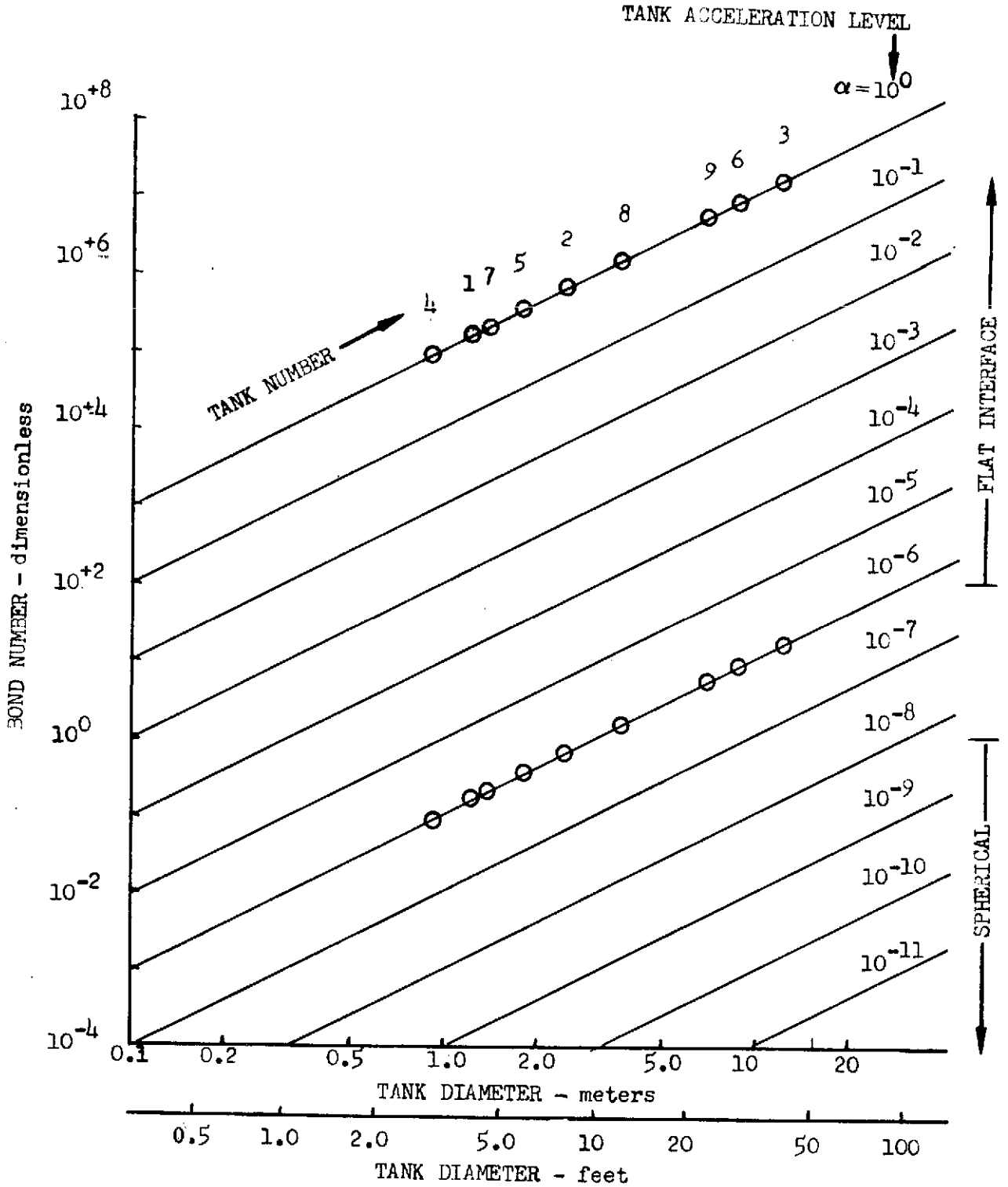

Fig. 3-2 Bond Number as a Function of Acceleration and Tank Size for LH_2

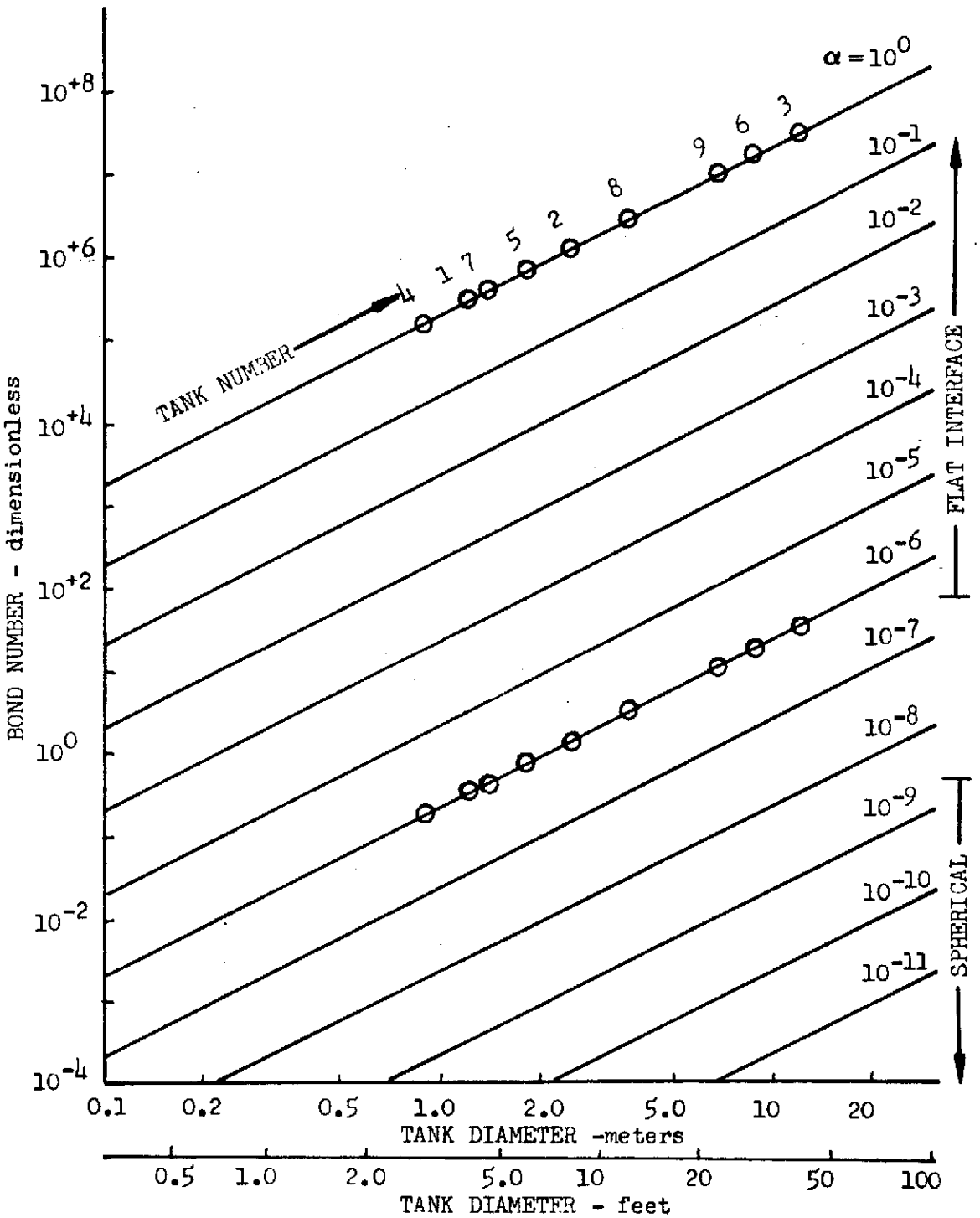

Fig. 3-3 Bond Number as a Function of Acceleration and Tank Size for LO_2

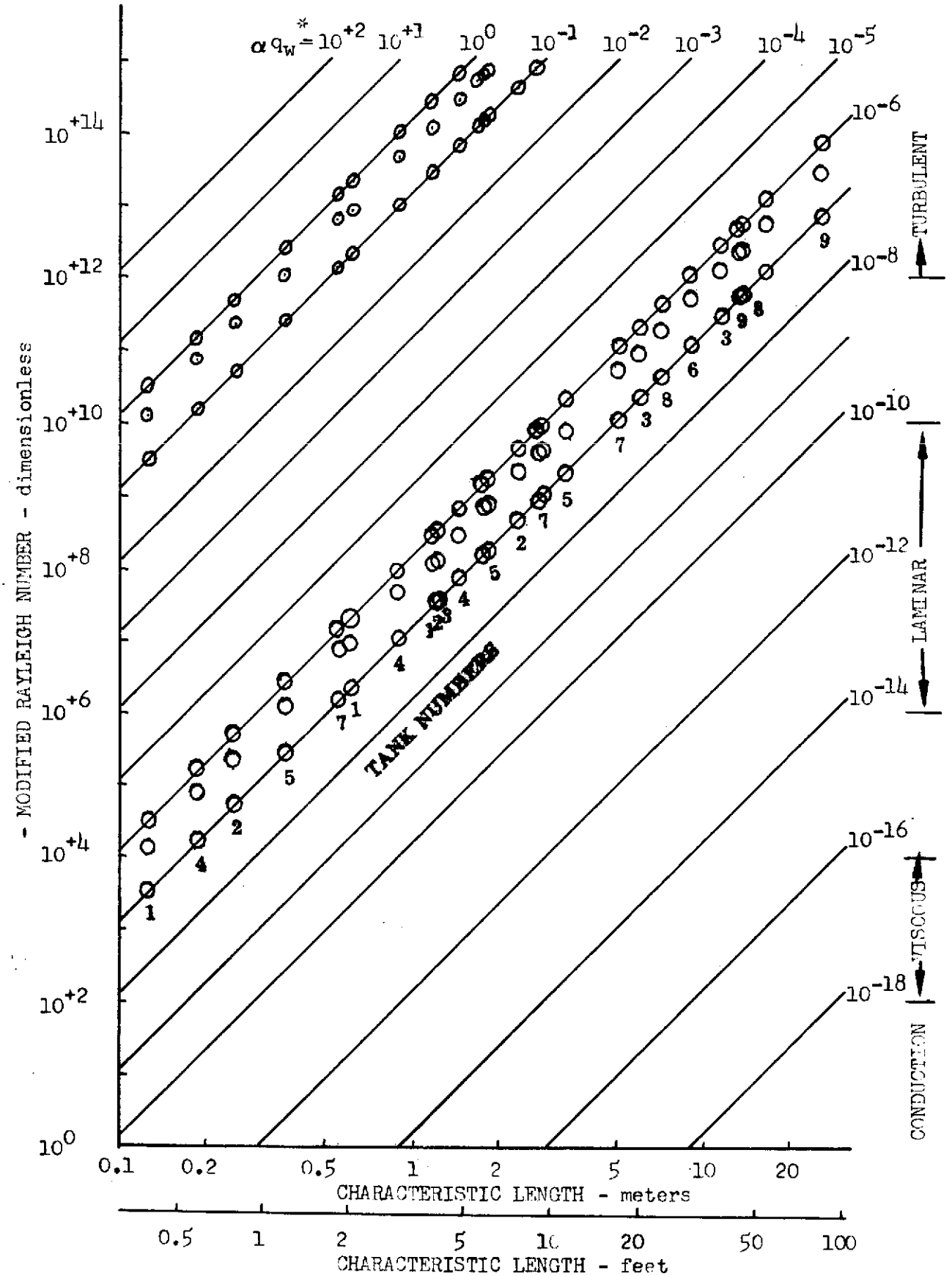

Fig. 3-4 Raleigh Number as a function of Length and Acceleration for LH_2

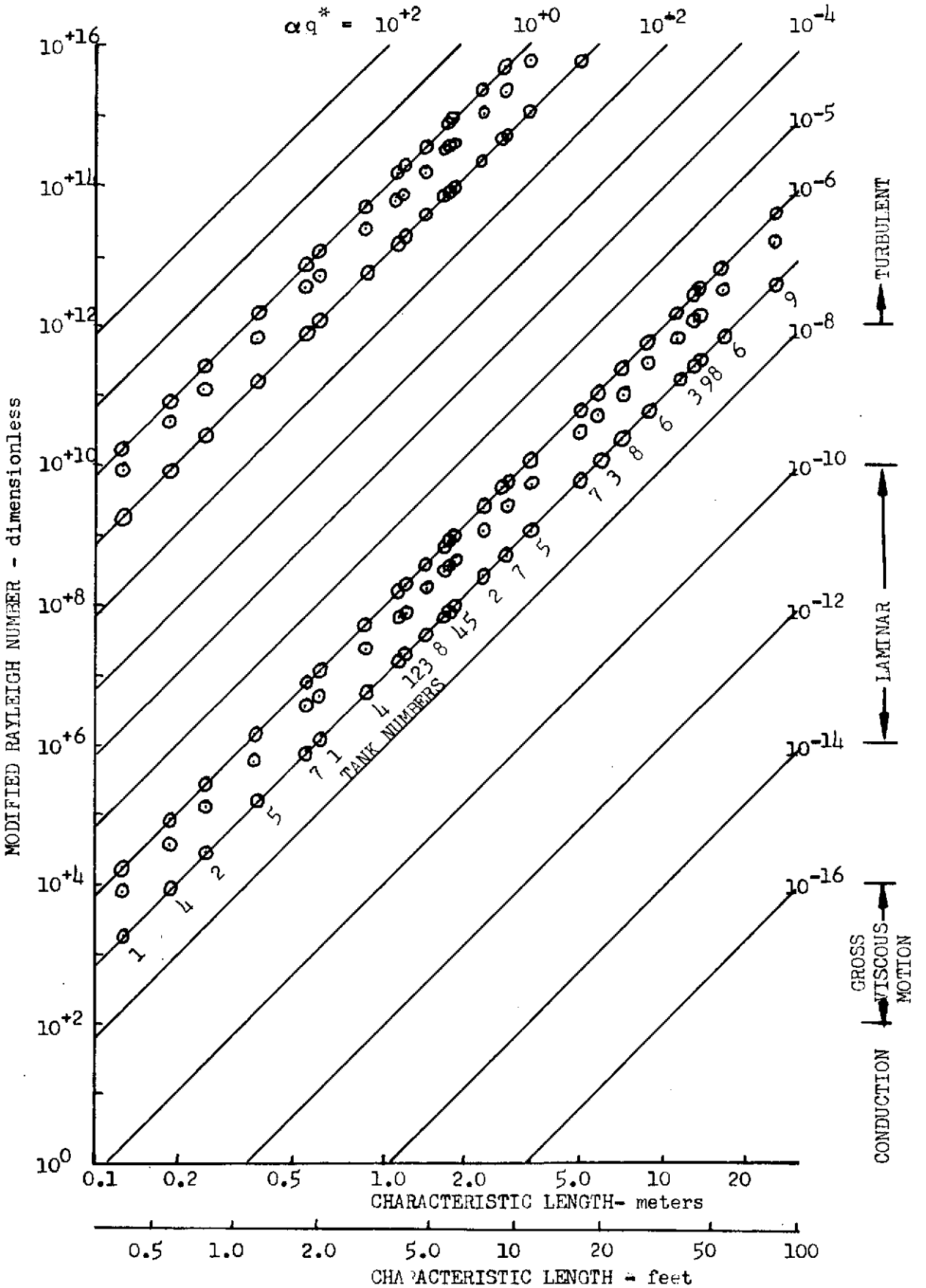

Fig. 3-5 Raleigh Number as a Function of Length and Acceleration for LO_2

3.1 TRANSIENT BOUNDARY LAYER ANALYSIS

One of the important considerations involved in selecting a heat transfer model for low-g conditions is the amount of time required to establish a natural convection boundary layer. Expressions have been developed by Schwartz and Adelberg (Ref. 5) for such time constants for the case of uniform wall temperature and by Siegal (Ref. 6) for a laminar boundary layer with uniform heat flux. An analysis has been conducted to derive the time constant for the turbulent boundary layer with uniform heat flux. The system used in the analysis is illustrated in Fig. 3-6.

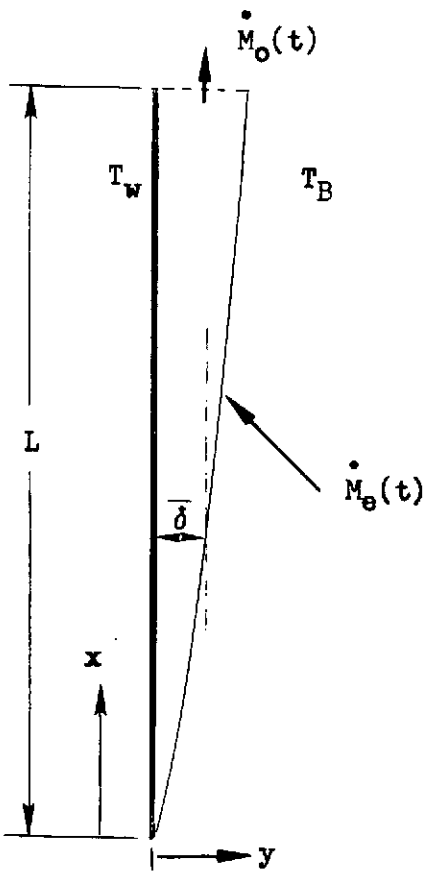

Fig. 3-6 Model for Boundary Layer Analysis During Transient

Vliet (Ref. 7) gives the following expressions for boundary layer thickness and for a fictitious velocity which characterizes a fully developed, turbulent boundary layer with uniform heat flux.

$$U_1 = 13.15\ \nu \left(\frac{\beta}{\rho C_p \nu^3}\right)^{5/14} \left(\eta q_{w,t}\right)^{5-14} x^{3/7}$$

$$\delta_s = 0.40 \left(\frac{\rho C_p \nu^3}{\beta}\right)^{1/14} \left(\frac{1}{\eta q_{w,t}}\right)^{1/14} x^{5/17}$$

Using the velocity profile from Ref. 8, the steady state velocity at any distance y from the wall, in the X direction is given by:

$$U_s/U_1 = \left(y/\delta\right)^{1/7} \left(1 - y/\delta\right)^4$$

The average velocity in the boundary layer is obtained by integrating over the thickness of the boundary layer. Therefore,

$$\overline{U}_s = 1/\delta_s \int_o^{\delta_s} U_s\, dy = 0.147\ U_1$$

By substitution, we get:

$$\overline{U}_s = 1.93\ \nu \left(\frac{\beta}{\rho C_p \nu^3}\right)^{5/14} \left(\eta q_{w,t}\right)^{5/14} x^{3/7}$$

Adelberg (Ref. 5) used a Taylor series to describe the thickness ratio between the transient and fully developed boundary layer, i.e.,

$$\frac{\delta_{(x,t)}}{\delta_s} = 2\left(\frac{t}{t_s}\right) - \left(\frac{t}{t_s}\right)^2 \quad \left(0 \leq t \leq t_s\right)$$

where: $\delta_{(x,t)}$ = thickness at location x, and time

t = time

t_s = time required to reach steady state

The equations for δ_s and $\overline{U}_s$ can be combined to give:

$$\overline{U}_s = C\left(\delta_s\right)^{3/5}$$

Assuming the expression for $\overline{U}_s$, to hold at any time, we can get by integration:

$$\overline{U}_{x,t} = \overline{U}_s \left[2\left(\frac{t}{t_s}\right) - \left(\frac{t}{t_s}\right)^2\right]^{3/5}$$

Conservation of mass in a control volume of unit width gives:

$$\int_o^{t_s} \left(\dot{M}_e - \dot{M}_o\right) dt = \int_o^{t_s} \dot{M}_{STORED}\, dt = \rho \overline{\delta}_s L$$

where: $\dot{M}_o = \rho \overline{U}_{(x,t)}\, \delta_{(x,\,t)}$ o 1

$$\dot{M}_e = \dot{M}_s + \left(\dot{M}_{ei} - \dot{M}_s\right) e^{-t/t_r} \qquad \text{(Ref. 1)}$$

and t_r is a reference time constant which must be significantly less than t_s.

Substituting the thickness ratio into the expression for $\bar{U}_{x,t}$, we get:

$$\int_0^{t_s} \dot{M}_o \, dt = \int^{t_s} \dot{M}_s \left[2\left(t/t_s\right) - \left(t/t_s\right)^2 \right]^{8/5} \quad dt = 0.57 \; \dot{M}_s t_s$$

Combining the two preceding equations, gives:

$$\lim_{t_s/t_r \to \alpha} \left[\int_0^{t_s} \left(\dot{M}_e - \dot{M}_o \right) dt \right] = 0.43 \; \dot{M}_s \, t_s = \rho \delta_s \, L \; . \; 1$$

At steady state conditions the mass flow rate $\dot{M}_s$ is proportional to the average velocity and the boundary layer thickness at any location x. Evaluating at $x = L$, we have

$$\dot{M}_s = \rho \bar{U}_{S,L} \, \delta_{S,L}$$

Combining the preceding two expressions, gives:

$$0.43 \, \rho \; \bar{U}_{S,L} \, \delta_{S,L} t_s = \rho \bar{\delta}_s \, L$$

$$\bar{\delta}_s \doteq \frac{1}{L} \int_0^L \delta_s \, dx = 7/12 \; \delta_{s,L}$$

These equations combine to give an expression for t_s in terms of the fully developed average exit velocity and the boundary layer run length.

$$t_s = 1.37 \left(L/\bar{U}_{s,L} \right)$$

The bracketed quantity is the time it would take a particle of fluid moving at the fully developed velocity $U_{s,L}$ to traverse the length of the boundary layer. During the transient, this time is effectively increased by 37 percent.

$$t_s = \frac{0.71}{\nu} \left(\frac{\rho C_p \nu^3}{\beta}\right)^{5/14} \frac{L^{4/7}}{\left(\eta q_{w,t}\right)^{5/14}}$$

Figures 3-7 and 3-8 show the calculated transient for hydrogen and oxygen, respectively. Also shown is Siegal's solution for laminar boundary layers. Siegal's solution gives:

$$t_s = 4.33\,(1.68 + p_r)^{2/5} \left(\frac{\eta g_o \beta q_{w,t}}{R\nu^2}\right)^{-2/5} \frac{P_r^{2/5} X^{2/5}}{\alpha}$$

The resulting transient times can be compared to the vent cycle period as determined with a pure conduction model and with a steady state, free convection model to gain insight into the controlling mechanism. It can be seen on Figs. 3-7 and 3-8 that for the large tanks, the time constants are on the order of 10-20 hours.

3.2 ZERO-GRAVITY MODEL DESCRIPTION

The zero-gravity model of the propellant tanks and thier contents is based upon conduction heat transfer between the tank, ullage, and liquid nodes, with vaporization or condensation changes of phase of the propellant. The liquid was considered to have a fixed zero-gravity orientation in the tank, and the liquid volume was divided into nodes. These liquid noses and the tanks wall nodes were then programmed into THERM, which computes the heat transfer in the tank system.

Once a nodal structure has been generated for a given geometry (L/D) any tank diameter can be run by inputing the appropriate scaling factors, and any fluid can be used by inputing the appropriate fluid properties.

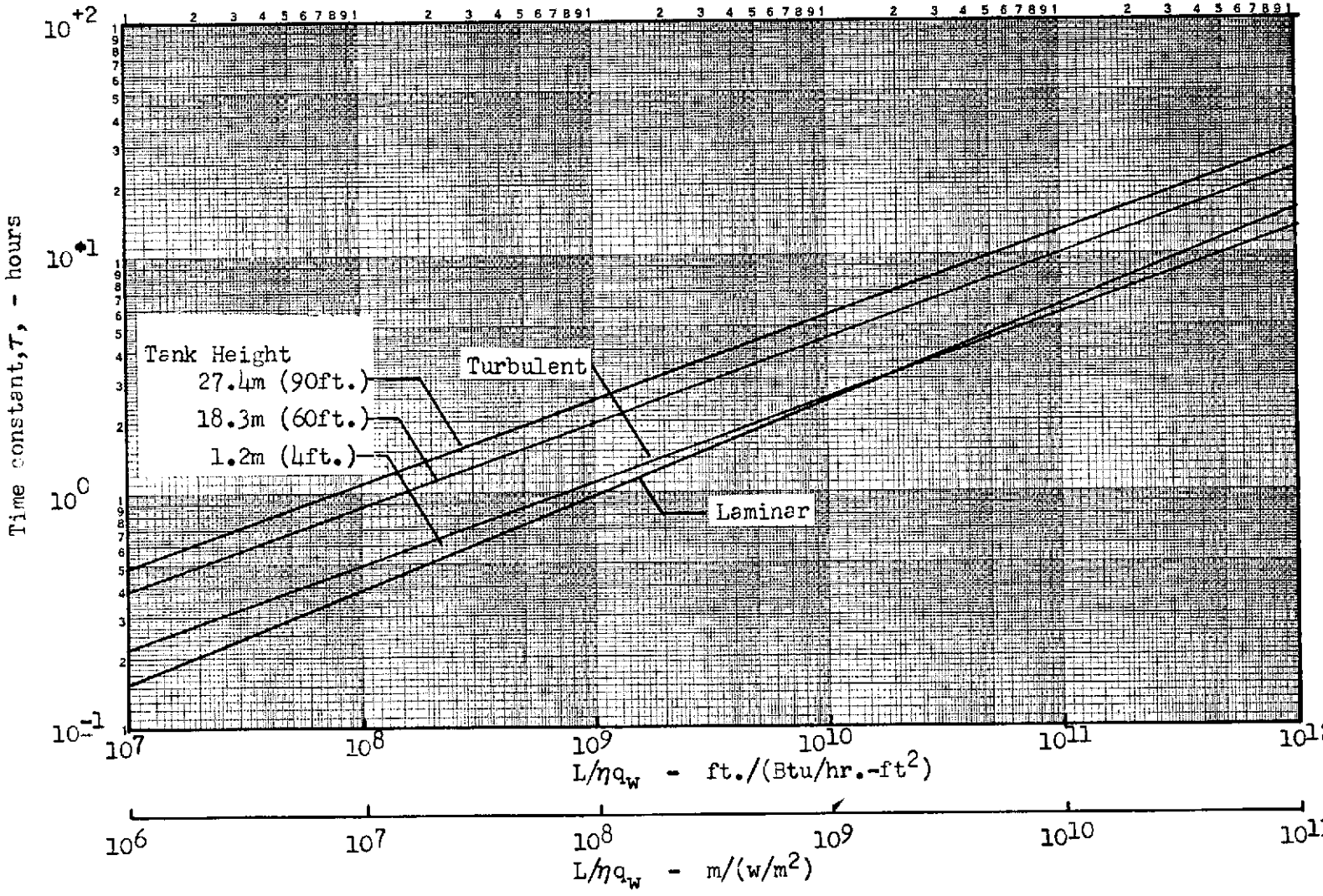

Fig. 3-7 Transient Periods for Development of Boundary Layers in Liquid Hydrogen (q_w = constant)

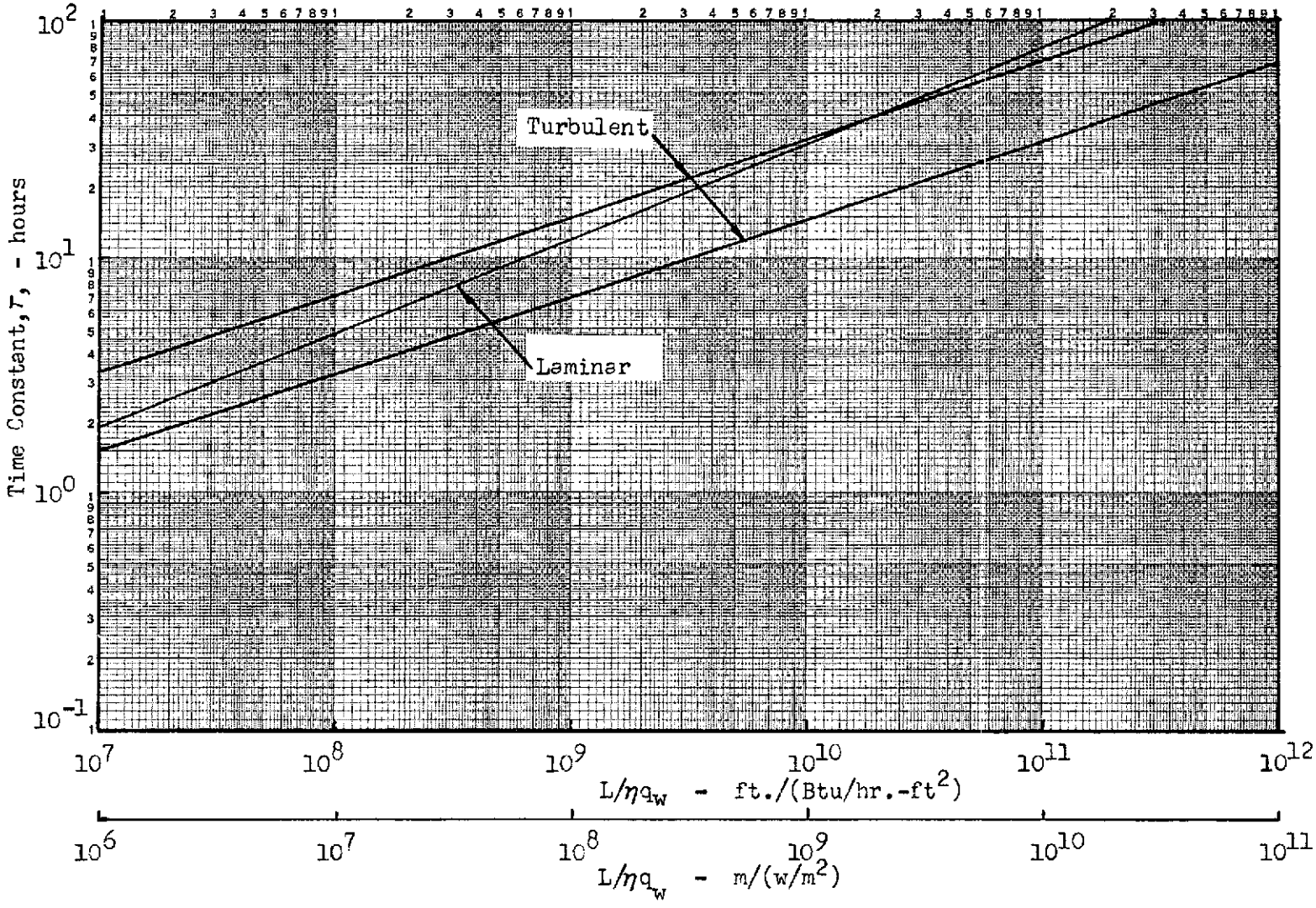

Fig. 3-8 Transient Periods for Development of Boundary Layers in Liquid Oxygen (q_w = constant)

Liquid/ullage coupling model was programmed in subroutine external to THERM, and at each THERM time step, new values of ullage volume, ullage vapor mass, ullage temperature, and tanks saturation temperature and pressure are computed based upon the THERM mode temperatures and heat rates.

3.2.1 ULLAGE Subroutine

This subroutine is used to solve a matrix of four simultaneous equations which relate energy and mass balances of the liquid and vapor in the propellant tank.

Primary effort in this model was spent in simulating the evaporation and condensation effects that would occur in zero-gravity conditions. Besides evaporation or condensation that would always occur on the normal liquid/vapor interface; vaporization and subsequent condensation is allowed on the liquid covered tank nodes or in the bulk liquid nodes, while condensation and subsequent evaporation is allowed on the normally dry tank wall nodes opposite the ullage space. Liquid or vapor respectively formed by condensation or evaporation is always assumed to remain at the same location where it was formed, and the mass of such liquid or vapor was continually summed at each tanks wall node and bulk liquid node. The opposite and subsequent change of phase is then limited by the mass formed originally, and if this mass was exhausted, the corresponding node is then returned to its normal thermal capacity status in THERM. In this way, the zero-gravity boiling and condensation effects are handled by the combination of the THERM model and the liquid/ullage coupling model, for each of the THERM nodes.

A basic block diagram of the zero-gravity computer model is shown in Fig. 3-9, with the interactions of THERM and the liquid/ullage coupling model solution subroutine, ULLAGE

An energy balance in the liquid gives:

$$\lambda \Delta M + C_{sB} \Delta T_s = \Delta Q_{su} + \Delta Q_{ST} + \Delta Q_{sB}$$

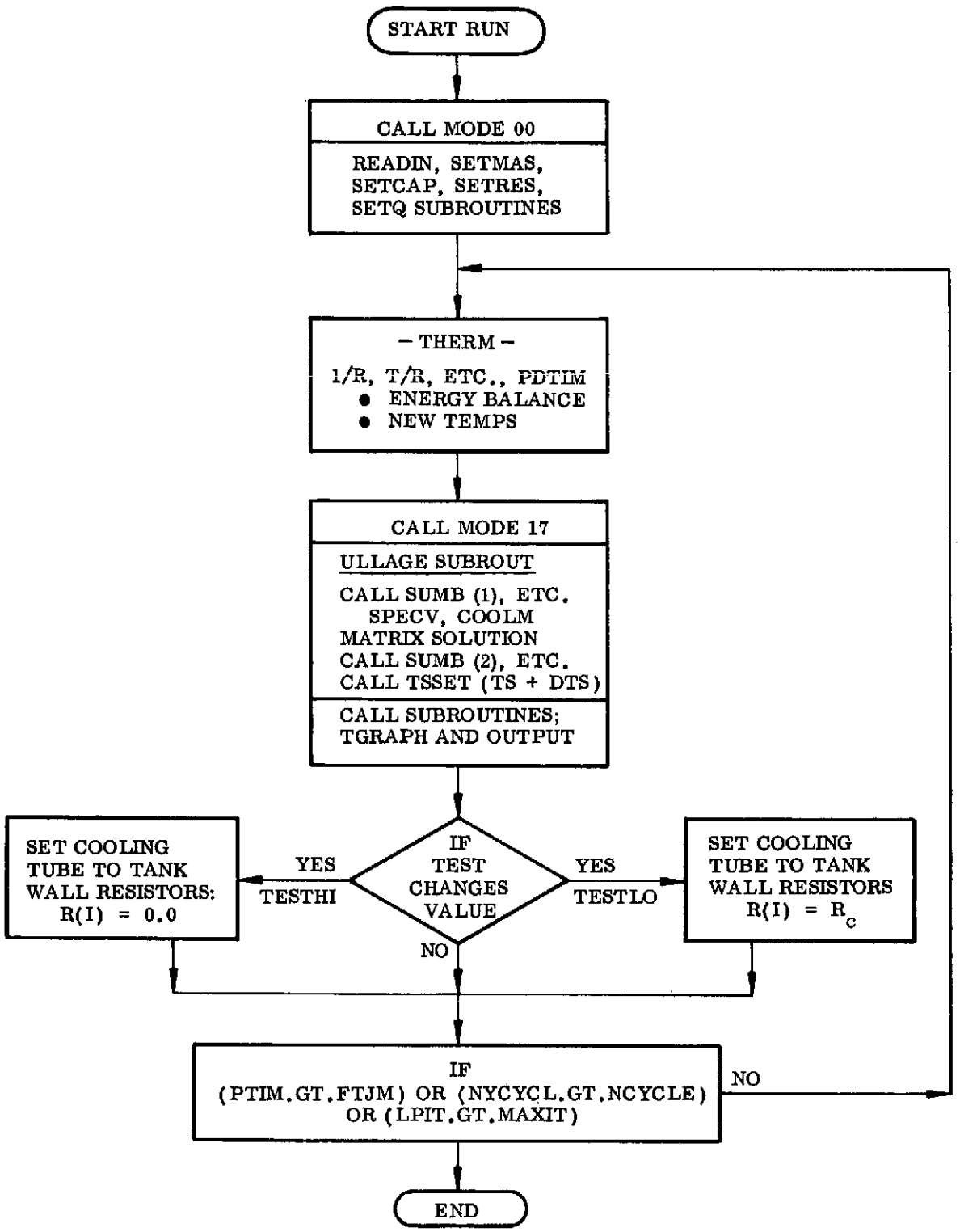

Fig. 3-9 Block Diagram for the Zero-Gravity Computer Models

where the three terms on the right represent respectively, the energy transfer at the liquid-vapor interface, at the wall, and in the bulk liquid, as determined by THERM.

The bulk capacity, $C_{SB} = \sum_i \left[C_{Li}\right]_{T_L = T_S}$

From an energy balance on the total ullage volume V_u, we get:

$$(C_v T - C_p T_s)\,\Delta M + C_v M\,\Delta T + P_s\,\Delta V_u = \Delta Q_u$$

It is assumed that the vapor behaves as a perfect gas over the limited pressures of interest. Thus the equation of state is used to relate tank pressure and vapor mass. The expanded form gives the following expression.

$$ZRT\,\Delta M + ZRM\,\Delta T - V_u K_S\,\Delta T_S - P_S\,\Delta V_u = 0$$

K_S in the above equation is the slope of the saturation line, i.e., $K_S = \frac{dP_S}{dT_S}$.

The ullage volume is related to the liquid volume and the constant total volume, such that $V_u = V_T - V_L$. When this is expanded in finite difference form, we have:

$$-v_L\,\Delta M + \Delta V_u = v_L\,\Delta M_{CL} - \Delta M_L\,\Delta v_L$$

The four equations given above form a B matrix. The computer solves the matrix for the changes in total vapor mass, M, ullage temperature, T, saturation temperature, T_s, and pressure, P_s.

3.3 FREE CONVECTION MODEL DESCRIPTION

Figure 3-10 is a block diagram illustrating the interaction between the four subroutines within the free convection program. The problem is divided into a heating and cool-down phase. Transition between the two is set by the maximum and minimum pressures specified for tank pressure control.

The basic approach is to determine the interface configuration and associated liquid height at the wall, for a given g level, tank size and ullage volume. This is then used to determine a psuedo-geometry for a flat bottomed, cylindrical tank that will yield the same modified Grashof (Gr*) number, liquid volume, and wall heat rates as the actual tank. This geometry conversion is accomplished in a GEOM subrountine. This geometry is then used in the STRAT subroutine to compute the pressure rise during the heating portion and in the COOLIT subroutine during the cooling phase. The ULLAGE subroutine is the same as that in the conduction model.

3.3.1 GEOM Subroutine

For any tank with hemispherical ends the volume is given by:

$$V_T = {}^{\pi}/_{12}\, D^3 \left[3\ ({}^{L}/_{D}) - 1\right]$$

The ullage and liquid volumes are:

$$V_u = V_T \left({}^{V_u}/_{V_T}\right)$$

$$V_L = V_T \left(1 - {}^{V_u}/_{V_T}\right)$$

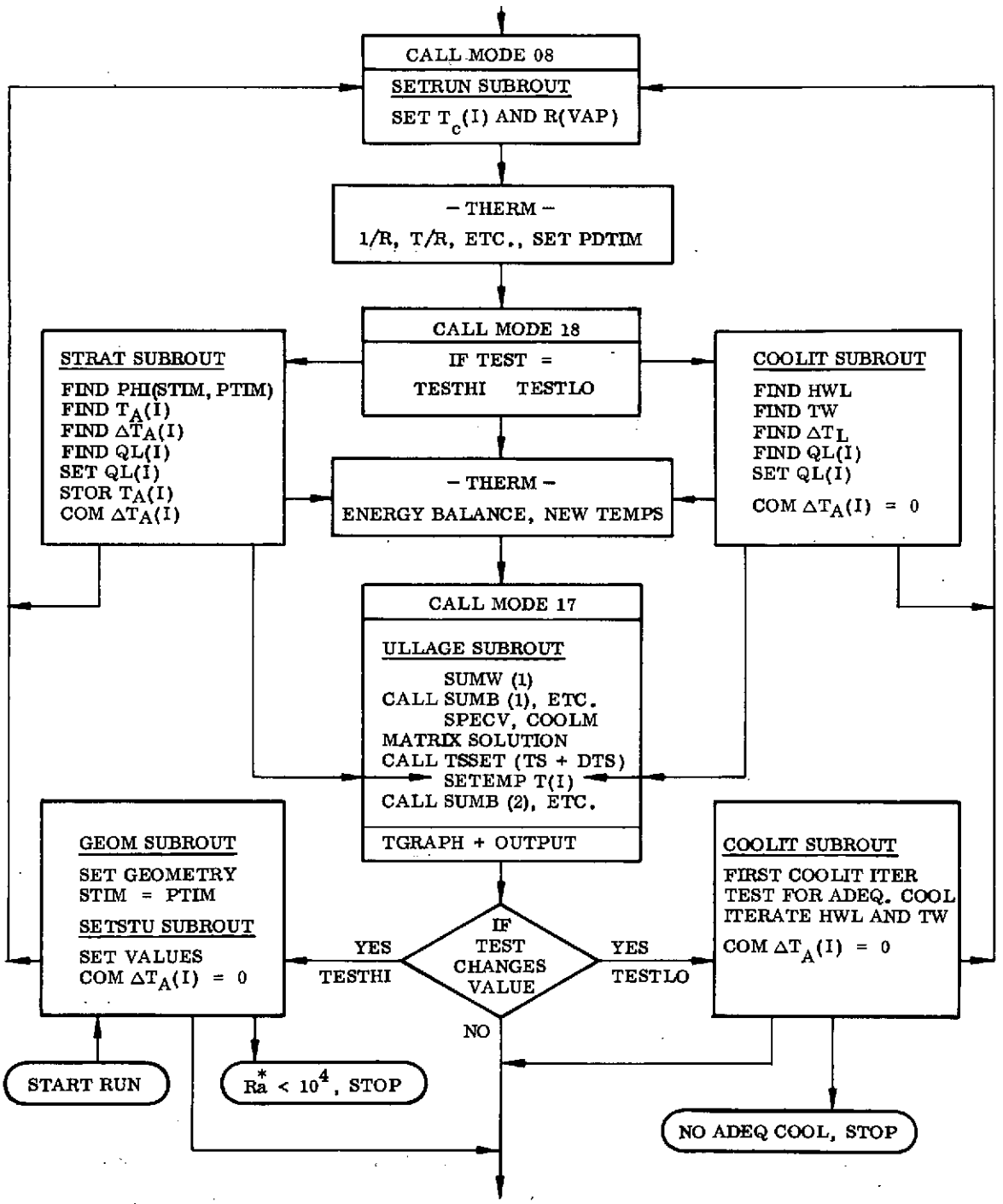

Fig. 3-10 Block Diagram for the Free Convection Computer Program

The volume and height relationship of a spherical segment is,

$$h = R + 2R \cos \left[\psi/3 + 2/3\,\pi k\right] \quad , \text{for } k = 0, 1, 2$$

where

$$R = D/2$$

$$\psi = \cos^{-1}\left[+ \sqrt{1 - \frac{3}{\pi}\frac{V_S}{R^3} + \frac{9}{4\pi^2}\frac{V_S^2}{R^6}}\right]$$

The correct height h of the spherical segment is the one of the three values in the range $0 < h_k < R$.

The liquid elevation Z of the flat interface is found in the following manner for any tank fill level.

If

$$V_L < 2/3\ \pi R^3, \text{ then } Z = h$$

If

$$2/3\,\pi R^3 < V_L < 2/3\,\pi R^3 \left[3\ (L/D) - 2\right] \text{ then } Z = R + 2/3\ R \left[3\ (L/D) - 2\right]$$

If

$$V_L > 2/3\,\pi R^3 \left[3\ (L/D) - 2\right] \text{ then set } V_S = V_u \text{ in the spherical segment solution}$$

$$Z = L - h$$

The interface shape due to low bond number accelerations must also be defined. This is accomplished with the ellipsoidal shape approximation of Satterlee (Ref. 9) from which the rise, at the wall, above the flat interface is found. For the propellants LH_2

and LO_2, the contact angle $\theta \approx 0^o$, and this yields a very simple ellipsoidal approximation of the interface shape.

$$Bo = \frac{g\rho R^2}{\sigma}$$

For $\theta = 0^o$ in a cylindrical section, then $\alpha = 1.0$ and $\cos\ \theta = 1.0$, and Ref. 9 gives the following expressions:

$$Bo = \frac{\alpha^4 \left(\frac{\cos\ \theta}{\beta}\right)^3 + \left(\frac{\cos\ \theta}{\beta}\right) - \frac{2}{\alpha^2}}{\left[1 - \sqrt{1 - (1/\alpha)^2}\right]}$$

$$Bo = \left(\frac{1}{\beta}\right)^3 + \left(\frac{1}{\beta}\right) - 2 \quad \text{Now, letting } \xi = 1/\beta$$

$$\xi^3 + \xi - (B\sigma + 2) = 0, \quad \text{which has the form}$$

$$\xi^3 + a\xi + b = 0, \quad \text{where } a = 1 \text{ and } b = -(B\sigma + 2)$$

$$\left(\frac{b^2}{4} + \frac{a^3}{27}\right) = + \frac{(Bo + 2)^2}{4} + \frac{1}{27} > 0$$

Since the bracketed quantity > 0, there is only one real root to the ξ cubic equation.

$$\xi = A + B = \sqrt[3]{-\frac{b}{2} + \sqrt{\frac{b^2}{4} + \frac{a^3}{27}}} + \sqrt[3]{-\frac{b}{2} - \sqrt{\frac{b^2}{4} - \frac{a^3}{27}}}$$

$$\xi = \sqrt[3]{\frac{(Bo + 2)}{2} + \sqrt{\frac{(Bo + 2)^2}{4} + \frac{1}{27}}} \sqrt[3]{\frac{(Bo + 2)}{2} - \sqrt{\frac{(Bo + 2)^2}{4} + \frac{1}{27}}}$$

$\beta = \frac{1}{\xi}$, where β = semi-minor axis of the ellipse.

Additional length ΔZ along the wall above the flat interface is:

$$\frac{\Delta Z}{R} = 2/3\,\beta \text{ , or } \Delta Z = 2/3\,\beta\, R$$

In cylindrical section or the bottom hemisphere this would also be increased elevation. However, in the upper hemisphere, the following relation for ΔZ is used where $h < R$:

$$\Delta Z = 2/3\ \beta\, h$$

This always insures some dry tank wall at the ullage, which would effectively be present with thin liquid layers.

The liquid/vapor interface area is based upon the computed β value and the area of the flat liquid/vapor interface A_F . In the cylindrical section, the flat surface radius, R_F is:

$$R_F = D/2$$

In the hemispherical ends, the radius of the flat interface R_F is

$$R_F = \sqrt{R^2 - (R - h)^2} = \sqrt{2\,Rh - h^2}$$

The flat interface area A_F is then:

$$A_F = \pi R_F^{\,2}$$

The actual interface area A is:

$$A = (1+\beta)A_F$$

The tank wall areas for bottom heating A_B, side wall heating A_W and dry tank wall ullage A_u can now be defined. If θ_B is the angle from the tank centerline at which the boundary layer starts, then this height h_B above the tank bottom is:

$$h_B = R(1 - \cos \theta_B)$$

The three areas of the tank wall are then:

$$A_B = \pi D h_B \qquad A_L = A_B + A_W$$

$$A_u = \pi D\left[L - (Z+\Delta Z)\right] = \pi D\left[D\left(\frac{L}{D}\right) - (Z+\Delta Z)\right]$$

$$A_W = \pi D\left[(Z+\Delta Z)\right] - h_B$$

$$A_T = \pi DL = A_B + A_W + A_u = \pi D\left[h_B + L - (Z+\Delta Z) + (Z+\Delta Z) - h_B\right] = \pi DL$$

The boundary layer run length x along the wall can now be computed, depending on the value of $(Z+\Delta Z)$.

If $(Z+\Delta Z) > R$ and $(Z+\Delta Z) < (L - R)$, then:

$$X = R\left(\pi/2 - \theta_B\right) + (Z+\Delta Z) - R$$

A different approach is required if the interface at the tank wall is located in either hemispherical end.

If $(Z+\Delta Z) < R$, then:

$$\theta_u = \cos^{-1}\left[1 - \frac{(Z+\Delta Z)}{R}\right]$$

$$X = R\,(\theta_u - \theta_B)$$

If $(Z+\Delta Z) > (L - R)$

$$\theta_u = \sin^{-1}\left[\frac{(Z+\Delta Z) - (L-R)}{R}\right] = \sin^{-1}\left[1 - \frac{L - (Z+\Delta Z)}{R}\right]$$

$$X = R\,(\pi/2 - \theta_B) + (L - D) + R\theta_u$$

The above relations complete the geometry considerations required for the actual tank.

3.3.2 STRAT Subroutine

The heating portion of the cycle, uses the Tellep and Harper Stratification Model I (Ref. 10). The actual tank is transformed to a cylindrical tank with a flat bottom, that will yield the same modified Grashof No., Gr*, same liquid volume, V_L, and same wall heat rates, q_w, and q_B as the actual tank. With a uniform wall heat rate of q''_w on the actual tank, the parameters to be held constant from the actual tank are:

$$Gr^* = \frac{g^* g_o \; q''_w \; X^4 \; \beta}{k\nu^2}$$

where:

$$\nu = \frac{\mu}{\rho}$$

V_L = liquid volume in the tank, which is kept current with time

$q_w = q''_w \, A_w$

$q_B = q''_w \, A_B$

For the pure cylindrical tank (subscript c), these parameters can be expressed as:

$$Gr^* = \frac{g^* g_o \beta q''_{w_c} \; X_c^{\,4}}{k\nu^2}$$

$$V_L = \pi/4 \; D_c^{\,2} \; X_c$$

$$q_w = q''_{w_c} \, A_{w_c} = q''_{w_c} \cdot \pi D_c \, X_c$$

$$q_B = q''_{B_c} \, A_{B_c} = q''_{B_c} \cdot \pi/4 \; D_c^{\,2}$$

The first three relationships above must be solved simultaneously for q''_{w_c}, D_c and X_c for the pure cylindrical tank model, and yields:

$$X_c = \left(\frac{k\nu^2 Gr^*}{g^* g_o \beta q_w}\right)^{1/3.5} \left(4\pi V_L\right)^{1/7.0}$$

$$D_c = \sqrt{\frac{4 V_L}{\pi X_c}} \qquad \text{and} \qquad R_c = \frac{D_c}{2}$$

$$q''_{w_c} = \frac{k\nu^2 Gr^*}{g^* g_o \beta X_c^4}$$

The bottom heat flux q''_{B_c} can be then fixed as:

$$q''_{B_c} = q''_w \frac{A_B}{A_{B_c}} = q''_w \frac{A_B}{\pi R_c^2} = q''_w \frac{4A_B}{\pi D_c^2}$$

The Model I stratification solutions of Tellep and Harper have both laminar and turbulent free convection mechanisms. However, it is assumed that transistion occurs at one value of the Rayleigh number, where

$$Ra^* = Gr^* Pr = \frac{g^* g_o \beta q''_{w_c} X_c^4}{k\nu^2} \cdot \frac{\mu C_p}{k}$$

for all liquid properties, then there would be a sharp discontinuity between the laminar and turbulent solutions at the transition Ra^* number. To get around this problem, transition is allowed to occur over a Rayleigh number range of $Ra^*_{MIN} = 10^{11} < Ra^* < Ra^*_{MAX} = 10^{13}$. For Ra^* values below this range, the pure laminar solution is used, whereas for values above this range, the pure turbulent solution is used. For solutions in this range, the parameter K is averaged in a weighted manner with respect to the Rayleigh number:

$$K_{ave} = \frac{\left(Ra^*_{MAX} - Ra^*\right) K_{LAM} + \left(Ra^* - Ra^*_{MIN}\right) K_{TURB}}{\left(Ra^*_{MAX} - Ra^*_{MIN}\right)}$$

In the Tellep and Harper Model I, the solution is divided into two regimes, depending of the mass startified layer Δ, has reached the bottom of the tank or not. The time parameter for these solutions is:

$$\phi = \nu t / X_c^2$$

The $\frac{\Delta 1}{X_c}$ solution before $\frac{\Delta 1}{X_c} = 1.0$ has the following solution:

$$\left(\frac{\Delta 1}{X_c}\right)_{LAM} = 1 - \left[1 - 0.630\left(\frac{X_c}{R_c}\right)\phi \frac{Gr^{*\,1/5}}{Pr^{0.388}}\right]^5$$

$$\left(\frac{\Delta 1}{X_c}\right)_{TURB} = 1 - \left[1 + 0.0924\left(\frac{X_c}{R_c}\right)\frac{\phi}{Pr^{2/3}}\left(\frac{Gr^*}{1 + 0.443\,Pr^{2/3}}\right)^{2/7}\right]^{-7}$$

The time ϕ_A required for the mass layer to reach bottom has been solved from the above equations:

$$\left(\phi_A\right)_{LAM} = 1.5873\,\frac{Pr^{0.388}}{\left(\frac{X_c}{R_c}\right) Gr^{*\,1/5}}$$

$$\left(\phi_A\right)_{TURB} = \frac{5.75\,Pr^{2/3}}{\left(\frac{X_c}{R_c}\right)}\left[\frac{1 + 0.443\,Pr^{2/3}}{Gr^*}\right]^{2/7}$$

For $\phi < \phi_A$,

$$\left(\frac{\Delta_1}{X_c}\right)_{LAM} = 1 - \left[1 - 0.630\left(\frac{X_c}{R_c}\right)\phi \frac{Gr^{*\,1/5}}{Pr^{0.388}}\right]^5$$

$$\left(\frac{\Delta_1}{X_c}\right)_{TURB} = 1 - \left[1 + 0.0924\left(\frac{X_c}{R_c}\right)\frac{\phi}{Pr^{2/3}}\left(\frac{Gr^*}{1 + 0.443\,Pr^{2/3}}\right)^{2/7}\right]^{-7}$$

With the appropriate value of $\left(\frac{\Delta_1}{X_c}\right)$, expressions for the three desired quantities T_S , Δ_2 and T_B follow. T_o is the initial liquid temperature at time $t = 0$.

$$\frac{(T_S - T_o)}{\left(\frac{q''_{w_c} X_c}{k}\right)} = \frac{2\left(\frac{X_c}{R_c}\right)\phi}{F\,Pr\left(\frac{\Delta 1}{X_c}\right)}$$

$$T_S - T_o = \frac{2\left(\frac{X_c}{R_c}\right)\phi}{F\,Pr\left(\frac{\Delta 1}{X_c}\right)} \cdot \left(\frac{q''_{w_c} X_c}{k}\right)$$

$$\frac{\Delta_2}{X_c} = 1/2 + \frac{\left[(1-F)\left(\frac{q''_{B_c} X_c}{k}\right) + 2\left(\frac{X_c}{R_c}\right)\frac{q''_{w_c} X_c}{k}\right]\phi}{2\,F\,Pr\,(T_S - T_o)}$$

$$- \left\{\left[1/2 + \frac{\left[(1-F)\left(\frac{q''_{B_c} X_c}{k}\right) + 2\,\frac{X_c}{R_c}\left(\frac{q''_{w_c} X_c}{k}\right)\right]\phi}{2\,F\,Pr\,(T_S - T_o)}\right]^2 - \frac{2\left(\frac{X_c}{R_c}\right)\left(\frac{q''_{w_c} X_c}{k}\right)\phi}{F\,Pr\,(T_S - T_o)}\right\}^{1/2}$$

$$\frac{(T_B - T_o)}{(q''_{B_c} X_c)} = \frac{\phi}{Pr\left[1 - \frac{\Delta_2}{X_c}\right]}$$

$$(T_B - T_o) = \frac{\phi}{Pr\left[1 - \frac{\Delta_2}{X_c}\right]} \cdot \frac{q''_{B_c} X_c}{k}$$

When the stratified layer reaches the bottom of the tank ($\phi > \phi_A$) any additional heat is asumed to be distributed uniformly, thus maintaining the shape of the temperature profile that occurs at time $\phi = \phi_A$.

Below the temperature stratified layer Δ_2, the liquid temperature is a uniform T_B. In the stratified layer, the temperature distribution will be:

$$\frac{T - T_B}{T_S - T_B} = f(y^*)$$

where $y^* = \frac{y}{\Delta_2}$, y is the depth below the liquid surface, and the equation applies $0 < y^* < 1$.

Using the Tellep and Harper expression for $f(y^*)$ yields:

$$\frac{T - T_B}{T_S - T_B} = (1 - y^*)^e \quad \text{where } e = \text{exponent.}$$

The exponent **e** is defined by fixing the value of the energy integral F, and using the relation:

$$F = \int_o^1 f(y^*)\, dy^* = \int_o^1 (1 - y^*)^e\, dy^* = \left.\frac{-(1 - y^*)^{e+1}}{e + 1}\right]_0^1$$

$$F = \frac{+ (1)^{e+1}}{e+1} = \frac{1}{e+1}$$

$$F(e+1) = 1$$

$$Fe = 1 - F$$

$$e = \frac{1 - F}{F}$$

This completes the model of temperature stratification due to tank wall heating in the equivalent cylindrical tank with no cooling present.

3.3.3 COOLIT Subroutine

During cooldown, cold liquid stratification will occur to the bottom of the tank, and bulk boiling will occur in the upper warm stratified layer. The bulk boiling near the top is treated by the liquid ullage coupling model. For a constant cooling tube temperature T_c and a decreasing mean liquid temperature, T_L, the mean wall cooling rate will decrease with time. Since the cooling model must always result in net cooling to the liquid, a test must be made to insure this effect. Based upon a unit area of liquid/tank wall surface area, where $h_{cw} = \frac{1}{R_{cw}}$ and $h_{LW} = f(Ra)$ for the free convection, then the requirement for net liquid cooling would be:

$$h_{cw} \left(T_{L\,min} - T_c \right) > q''_w$$

Where $T_{L\,min}$ = saturation temperature at minimum pressure.

An energy balance on a unit area of liquid tank wall surface area would be as follows, assuming T_L = mean liquid temp in the tank.

$$h_{cw} (T_W - T_c) = q''_w + h_{LW} (T_L - T_W), \quad \text{and}$$

$$(T_L - T_w) = \frac{h_{cw}(T_L - T_c) - q''_w}{(h_{cw} + h_{LW})}$$

The free convection heat transfer coefficient h_{LW} is based upon correlations for constant ΔT. The actual tank dimensions are used to compute Ra and the tank cooling:

$$Gr = \frac{g^* g_o X^3}{\nu^2}(T_L - T_w) = \text{regular Grashof number based upon } \Delta T.$$

$$Pr = \frac{C_L \mu}{k} = \text{liquid Prandtl number.}$$

$$Ra = Gr\ Pr = \text{regular Rayleigh number based on } \Delta T.$$

Based upon the Rayleigh number magnitude, the Nusselt number is calculated from the following:

$$Nu = \frac{h_{LW} X}{k} = 0.105\ Ra^{1/3} \quad \text{For } Ra > 10^9 \quad \text{(Turbulent)}$$

$$Nu = 0.59\ Ra^{1/4} \quad \text{For } 10^4 < R < 10^9 \quad \text{(Laminar)}$$

$$Nu = 5.90 \quad \text{For } Ra < 10^4 \quad \text{(Viscous and Conduction)}$$

The value of h_{LW} is updated for each computed time step based upon the initial value of $(T_L - T_w)$. Since the wall temperature is not known at the start of the cooling cycle, the following method is used to estimate it:

1. Set $h_{LW} = 0$ and estimate first value of $(T_L - T_w)$.
2. Use this $(T_L - T_w)$ to compute Ra, Nu, and h_{LW}.
3. Use this h_{LW} to compute next the value of $(T_L - T_w)$.

After this first cooling iteration, the current value of $(T_L - T_w)$ is used to predict a value of h_{LW} for the next time step.

The energy transferred from the total liquid mass is.

$$q_L = h_{LW} A_L (T_L - T_w)$$

This mean drop in temperature of the liquid T_L is found from q_L

$$C_L \frac{dT_L}{dt} = q_L, \quad \text{hence} \quad \frac{dT_L}{dt} = \frac{q_L}{C_L}$$

$$\Delta T_L = \left(\frac{dT_L}{dt}\right) \cdot (\Delta t), \quad \text{where} \Delta t = \text{compute time step.}$$

This ΔT_L is successively added to the liquid temperature distribution. During cooling, a deeper layer of liquid at the top will be at saturation temperature T_s, which will have the capacity C_{SB}. For the matrix solution in the liquid-ullage coupling subroutine, the average heat rate q_{SB} to this layer must be fixed from the overall cooling value q_L.

$$q_{SB} = \frac{C_{SB}}{C_L} \cdot q_L$$

The mean liquid temperature T_L is found during heating and cooling in the following manner. The temperatures of the upper liquid layers, the remaining stratified layer, and the bulk liquid at the tank bottom are averaged, with respect to capacity, to yield temperature T_L. A running average is kept for this quantity. During cooling the liquid withdrawn for the cooling tubes is assumed to come from the bottom of the tank at this mean bulk liquid temperature.

This program computes the liquid and tank geometry only once, at the minium pressure, during each cycle. As with the conduction model, the liquid capacity is also updated only at each restart of a pressure cycle.

3.4 ANALYTICAL PRESSURE HISTORIES

The previously described conduction and convection models have been used to generate pressure and temperature histories that span the range of tank sizes, orbital heat fluxes and gravity levels of interest. These are presented to illustrate the influence of the various parameters.

3.4.1 Conduction Results

Results are presented for the tanks with the largest and smallest capacity, and for both 5 percent and 90 percent ullages. Tanks sizes are, respectively: D = 6.86 M (22.5 ft) x L/D = 4, and D = 1.22 M (4 ft) x L/D = 1. The nodal structures are shown in Figs. 3-11 through 3-14.

Figures 3-15, a through f, show the resulting pressure and temperature histories in hydrogen for the large tank configuration shown on Fig. 3-11. Figures a through c are for a heating rate of 3.15 w/m^2 (1.0 $Btu/hr\text{-}ft^2$), and cooling resistances of .09, .35, .88 $\frac{m^2{}^oK}{w}$ (0.5, 2.0, and 5.0 $\frac{hr\text{-}ft^2{}^oR}{Btu}$.

Figures d through f are for similar resistances but the heating rate is 0.1 $Btu/hr\text{-}ft^2$. For all the runs, the operating pressure was (15-18 psi).

It can be seen from Fig. 3-15 a through c that the heat exchanger (R_{CW}) does affect the vent cycle period, and in fact, for the largest resistance (wide tube spacing) the cooling rates were insufficient to pull the pressure back to the starting pressure (i.e., could not control).

The liquid node temperatures are referenced to Fig. 3-11. They contain temperatures along a radius from the wall to the tank centerline and axially from the bottom to the liquid-ullage interface. They confirm that the changes are limited to the region near the tank wall. They also indicate that subcooling is more severe for the first cycle. This appears to be a consequence of the starting condition wherein all vapor is contained in the ullage. However, part of the initial ullage condenses and vapor is generated along

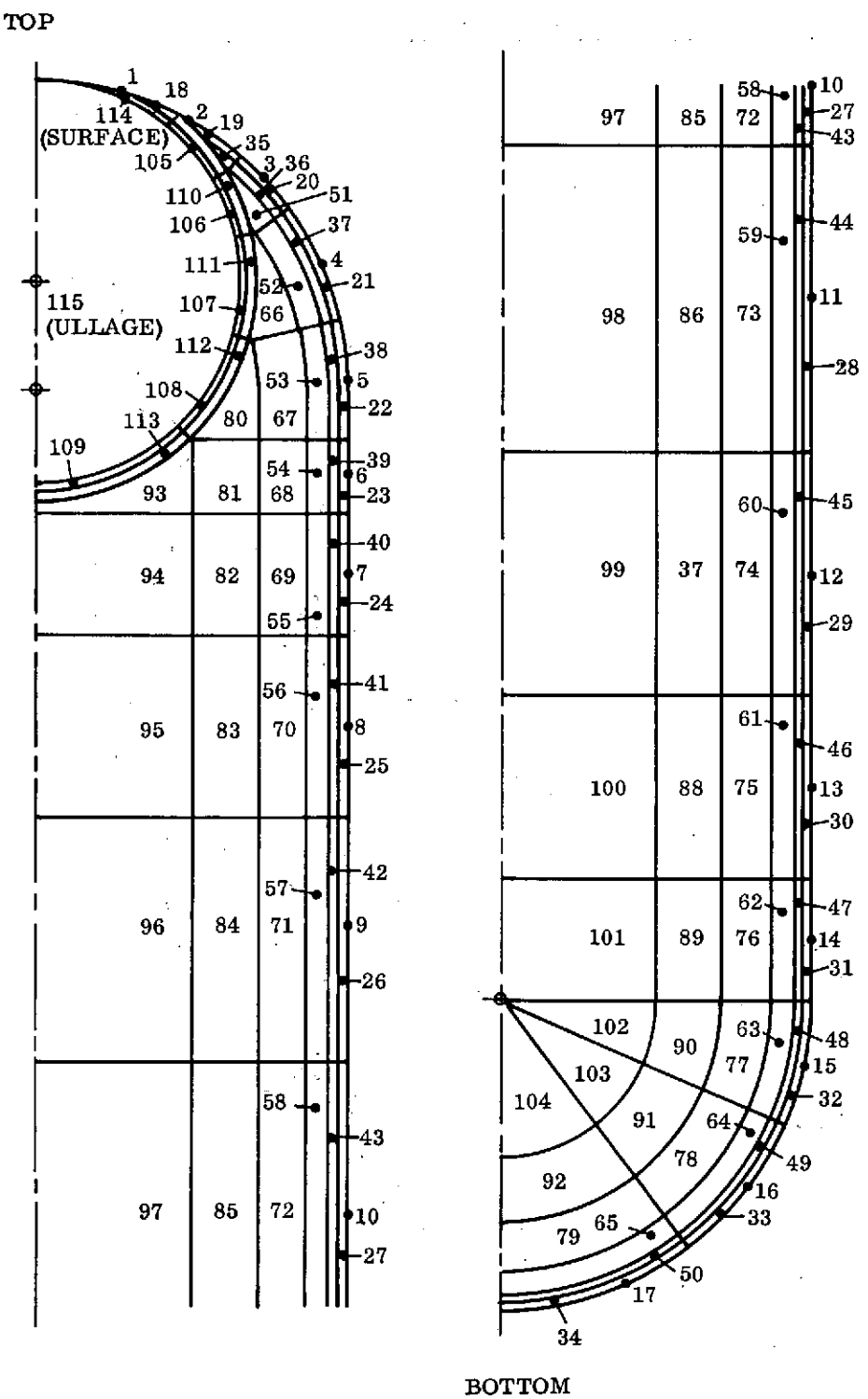

Fig. 3-11 Conduction Model for Cylindrical Tanks = L/D = 4; 5% Ullage

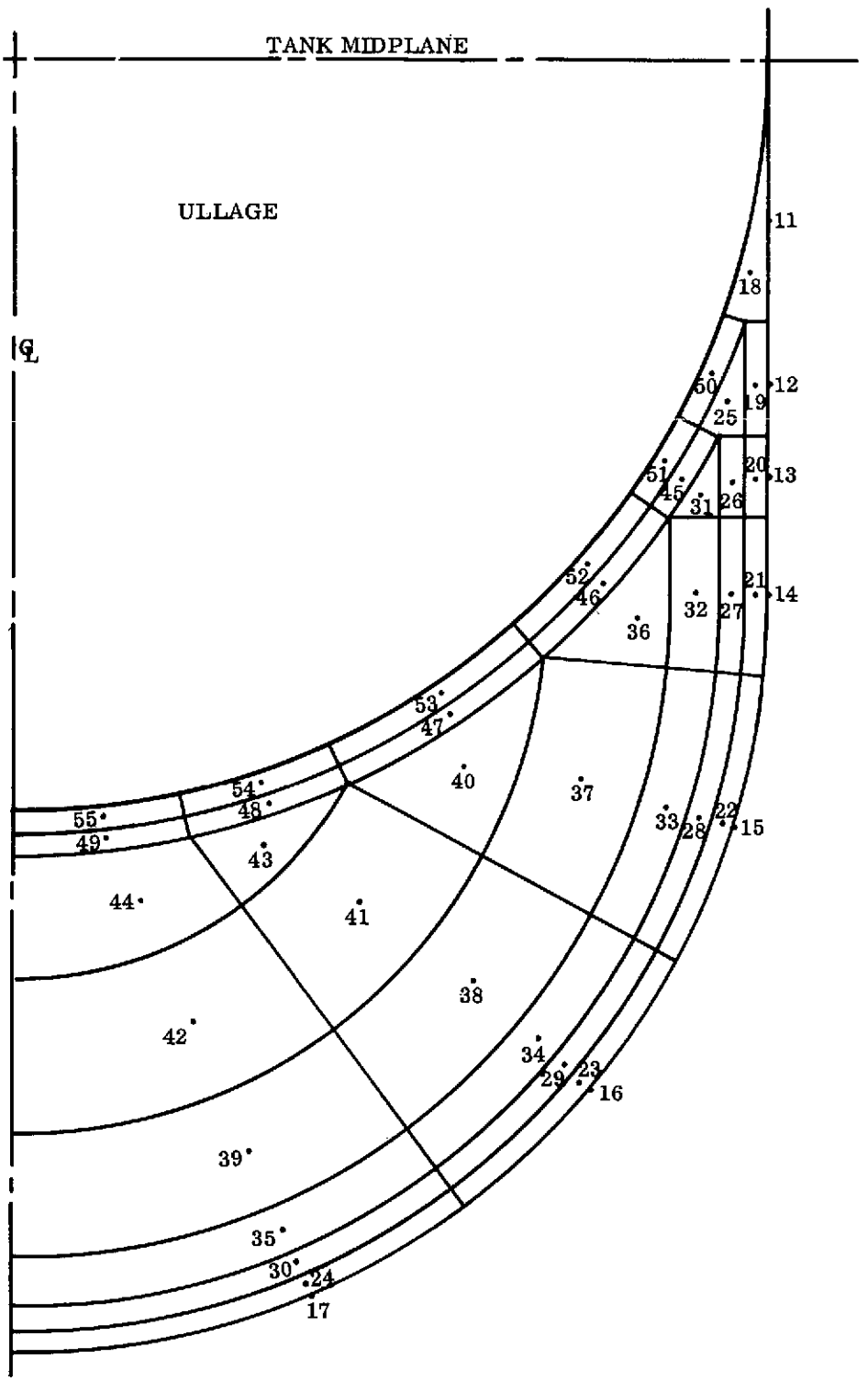

Fig. 3-12 Liquid Node Structure For Conduction Model With a Cylindrical Tank - L/D = 4; 90% Ullage

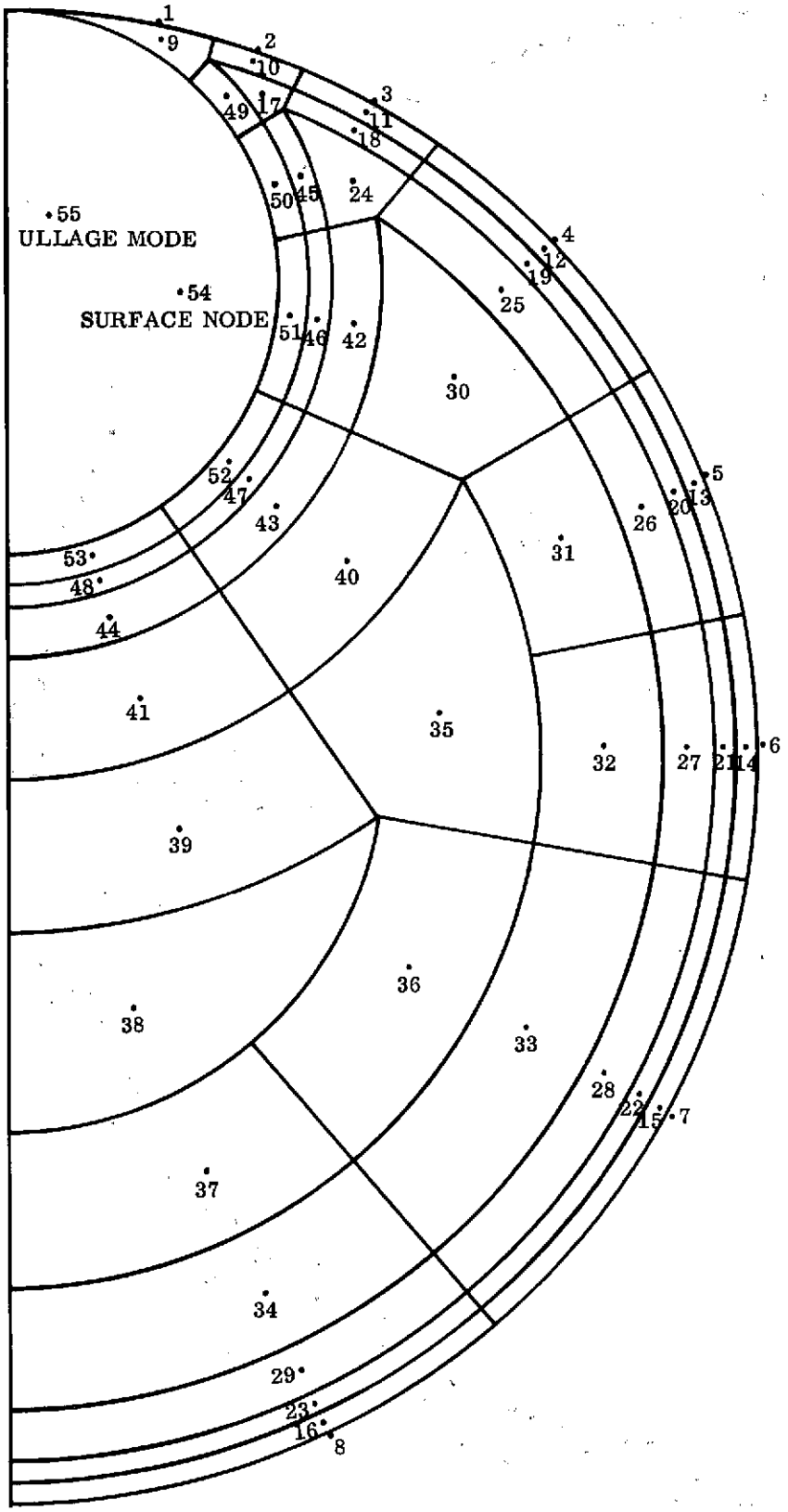

Fig. 3-13 Liquid Node Structure For Conduction Model With a Spherical Tank; 5% Ullage

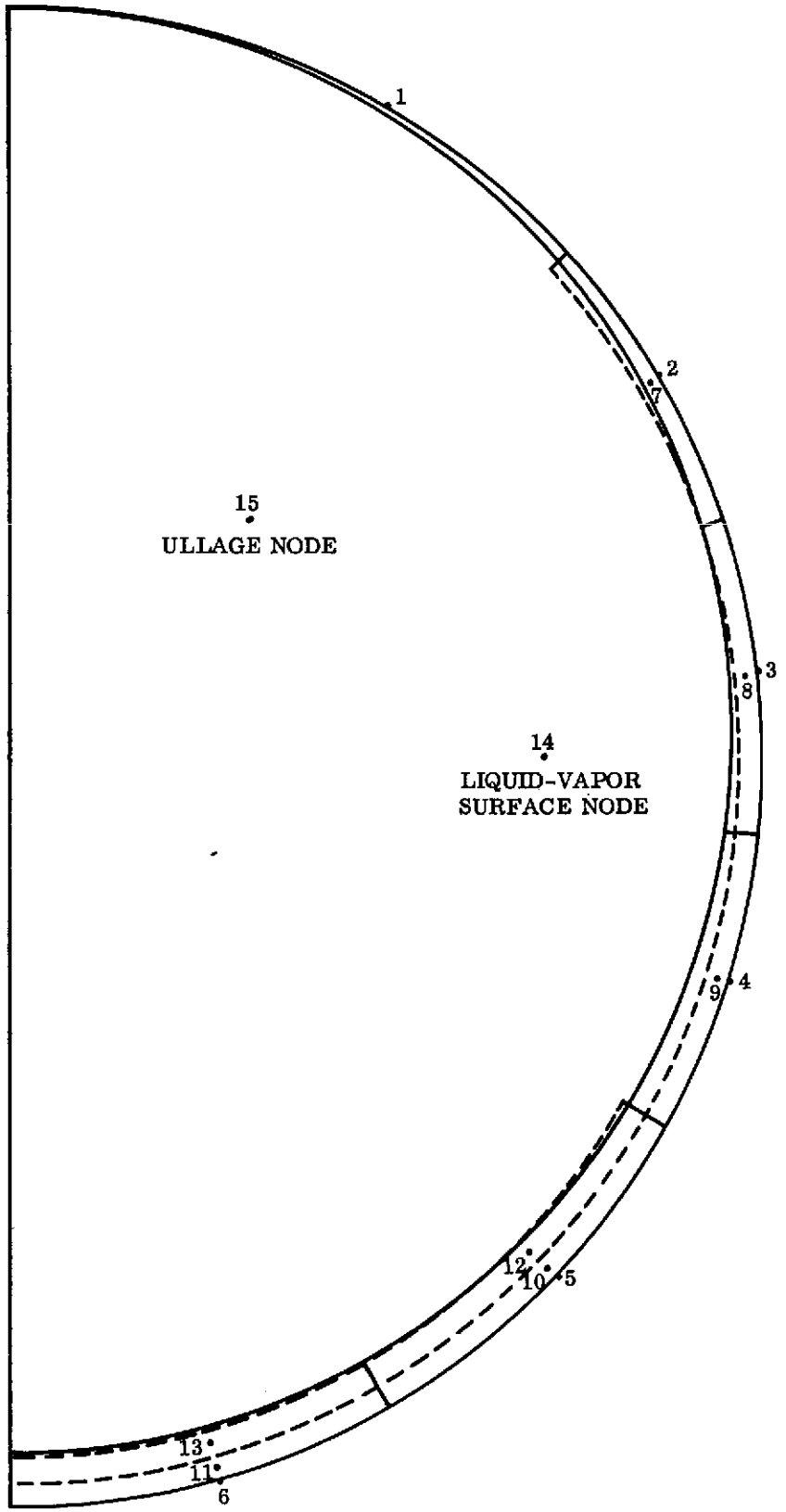

Fig. 3-14 Liquid Node Structure For Conduction Model With a Spherical Tank: 90% Ullage

the wall during the first cycle. Some subsurface vapor exists throughout the ensuing cycles. The subcooling is reflected on the pressure history curves as a lag in the start of a subsequent rise in pressure following cessation of cooling which occurs as soon as the pressure drops to minimum level. During this lag time the heat coming into the tank is going into warming up the subcooled field.

The results shown in Figs. 3-16 a and f are for the same tank with 90 percent ullage.

With 5 percent ullage, the vapor constitutes approximately 0.1 percent of the total thermal capacity whereas it represents 17 percent for the large ullage. The time period for a vent cycle is indicative of the extent to which energy is being distributed in the liquid. Uniform distribution would give much longer periods for the small ullage (large liquid capacitance). However, when the energy exchange is confined to a small portion of liquid, phase change and compression (or expansion) of the ullage results in rates of pressure change which are more nearly proportional to the ullage volume. In this situation larger vent cycle time occurs for the high ullage volume. The latter situation is found to be the case when the heat flux is 3.15 w/m^2 (1 Btu/ $Hr-Ft^2$), for which the vent periods were approximately an order of magnitude greater with 90 percent ullage than with 5 percent ullage. At the lower heat flux (0.1 Btu/ $Hr-Ft^2$), the vent cycle is only 20 percent longer for the large ullage. The implication of this is that non-uniform (stratification and subcooling is less severe at the high ullage volumes. This is substantiated by the temperature histories.

The temperature histories are shown in Figs. 3-17 and 3-18 for the small tank. The trends are what one might expect relative to the large tank results. The thermal oscillations penetrate further into the tank. In particular, notice that at the lower heat rate, (Figs. 3-17 d through f) even the center most liquid temperature (node 39) is affected. It continues to warm up for a few hours after the cooling is started until such time as the tank pressure drops to the point where boiling takes place (on Fig. 17f this occurs at 59 hours). During the cooldown, subcooling occurs in the three nodes nearest the wall (nodes 14, 23, and 27). There is also excess cooling of the ullage vapor which produced a pressure undershoot to 10^5 n/m^2 (14.6 psi). However, as with the large tank, the excess cooling was recouped by absorbing additional heat in the prolonged warmup portion of the next cycle.

For the purpose of comparison, a few selected cases are shown for oxygen on Figs. 3-19 through 3-22. For the small tank all liquid nodes have essentially the same temperature history, with 90 percent ullage, indicating a virtual absence of stratification.

The liquid oxygen runs display characteristics similar to those found with hydrogen. The most noticeable difference is that a higher resistance (wider spacing) heat exchanger design can be effectively used with oxygen. With hydrogen, a design resistance of $0.88 \frac{m^2 {}^oK}{w}$ (5 hr-ft^2 - ^oR/Btu) was so high that the heat removal rate was insufficient to effectively control the tank pressure. With oxygen, the total temperature difference between the bulk fluid temperature and that of the expanded fluid in the coolant tubes is $9R^o$ compared to $4.4R^o$ for hydrogen. This, coupled with the lower thermal diffusivity of oxygen indicates that the heat exchanger wall resistance can take on a higher value for oxygen than for hydrogen before it becomes the limiting factor in pressure control.

The hydrogen data indicated that an order of magnitude decrease in heat flux (from 3 to 0.3 w/m^2) increased the cycle time nearly two orders of magnitude for the 5 percent ullage. A similar effect was obtained with oxygen. The cycle time for liquid oxygen is approximately 6 to 10 times that for hydrogen with the full tank. The thermal capacity of LO_2, for a 3 psi control band, is 8.5 times that for hydrogen. With the high ullage, the cycle time is increased by a factor of 10 for a similar decrease in heat flux. This is consistent with the hydrogen runs.

The venting inefficiency at the end of a cooling period is represented by the amount of excess mass that was removed from the tank to produce the subcooled condition. This excess vented mass can be expressed as a percentage of that which would be vented up to that point in time for a completely mixed propellant; i.e.,

$$\eta = \frac{\Delta\omega_{VSC}}{\omega_{VO}} = \frac{\int_0^{M_T} C_{VL} \; T_L \; dm}{Q_T}$$

where

η = inefficiency factor

$\Delta\omega_{VSC}$ = Excess vented propellant

ω_{VO} = Vented propellant for mixed system

$\int_{o}^{M_T} C_{VL}\, Tdm$ = Amount of subcooling

Q_T = Total heat input that would produce ω_{VO}

Figures 3-23 and 3-24 show this inefficiency factor as a function of time. It decays exponentially, as one might expect, primarily due to linear increase in the denominator (Q_T). It is interesting to note that the effect of R_{CW} tends to converge as time progresses. This too, is because of the fact that subcooling becomes less important as the mission proceeds, and consequently, perturbations due to heat exchanger design become second order effects.

Figure 3-25 presents the same data correlated against vent cycle number. This tends to pull the data for the two heat rates together in spite of the fact that vent period and frequency differ by two orders of magnitude. This indicates that the performance is relatively independent of frequency, as long as the design is adequate to provide control (e.g., if $q = 1.0$ Btu/hr-ft^2, R_{CW} 5). Moreover, a space mission requiring this size tank, and these heat rates would likely be of long duration and require considerably more than 5 vent cycles which implies that a passive heat exchanger will not result in a significant weight penalty, even in the absence of convection. Also, it is important to note that the subcooling penalty is computed at the end of a cooling period and does, in fact, represent a penalty only if the mission were completed at that time. If the mission is not completed, the non-vent portion of the next cycle is prolonged by virtue of the increased thermal capacitance of the subcooled fluid. Thus, the weight penalty is a discontinuous function which is negated in the pressure rise portion of each pressure cycle. Inasmuch as these conduction-dominated cases represent the most severe

conditions for operation of a wall-mounted heat exchanger, there is no doubt that this concept can be effectively used in a thermodynamic vent system for hydrogen and oxygen propellant tanks that are to spend prolonged period in space. It is also applicable to non-cryogenic fluids, but the high vapor pressure cryogens present the most difficulty in storage and venting during low gravity space flight.

3.4.2 Convection Results

Figures 3-26 through 3-30 illustrate the type of results obtained with the convection model. These are for a tank that is 22.5 feet in diamter and 90 feet tall. Figures 3-26 through 3-28 indicate the relative effect of the thermal resistance in the tank wall (R_{cw}) between cooling tube attachment points.

A large resistance indicates wider spacing between tubes, fewer tubes, and thus lower heat exchanger weight. As expected, a larger resistance, required a longer time to pull the pressure down. Also, it can be seen that temperatures within the body of the liquid tend to decrease throughout the mission, and this subcooling is reduced with increasing values of R_{cw}.

Figures 3-29 and 3-30, in conjunction with Fig. 3-27 illustrate that the increased stratification associated with higher g-levels tends to shorten the pressure cycle as well as the amount of liquid subcooling. The average cooling flux is shown on Fig. 3-31, as a function of g-level for a design having a resistance value of $R_{cw} = 0.17 \frac{m^2 {}^oK}{w}$ $(2 \frac{ft^2 - {}^oR}{Btu})$.

Also shown is the cooling flux determined with the zero-g conduction model for the same tank and heat exchanger. The indication is that the latter model is appropriate below 10^{-6} standard gravities.

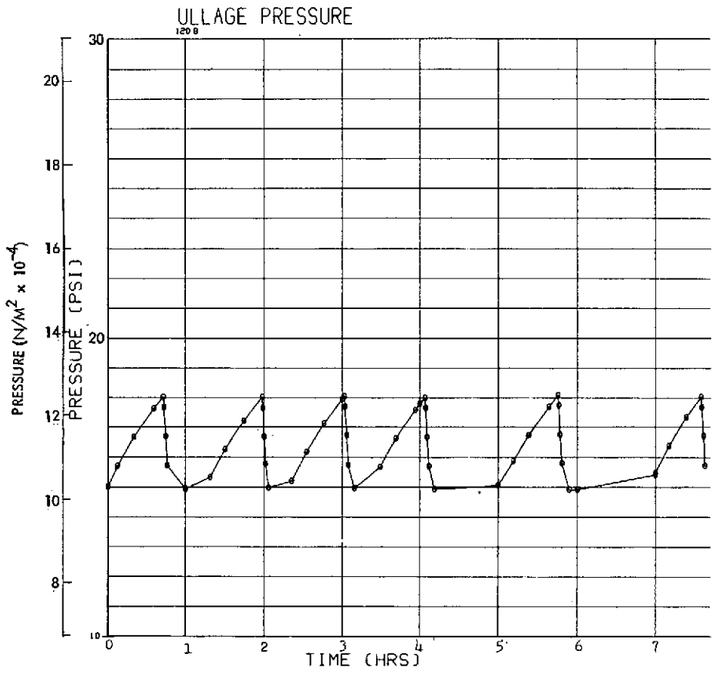

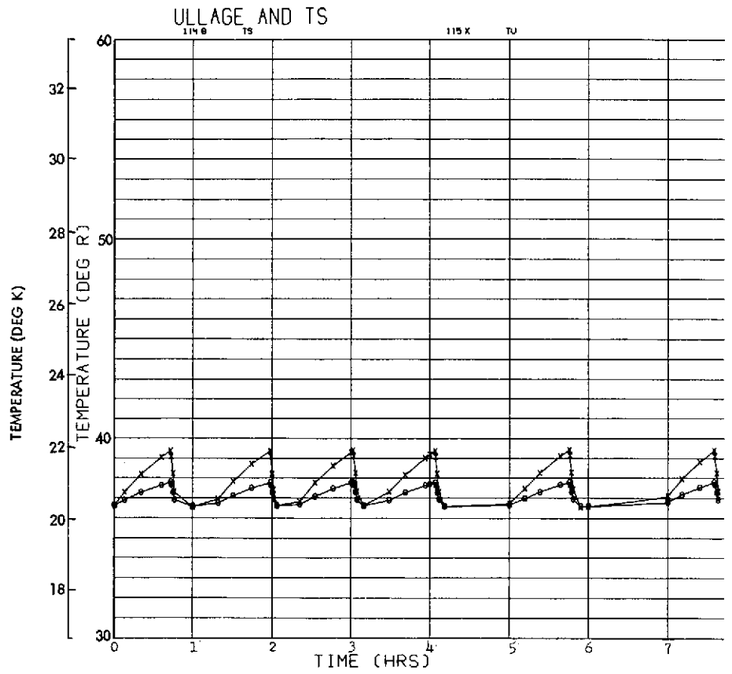

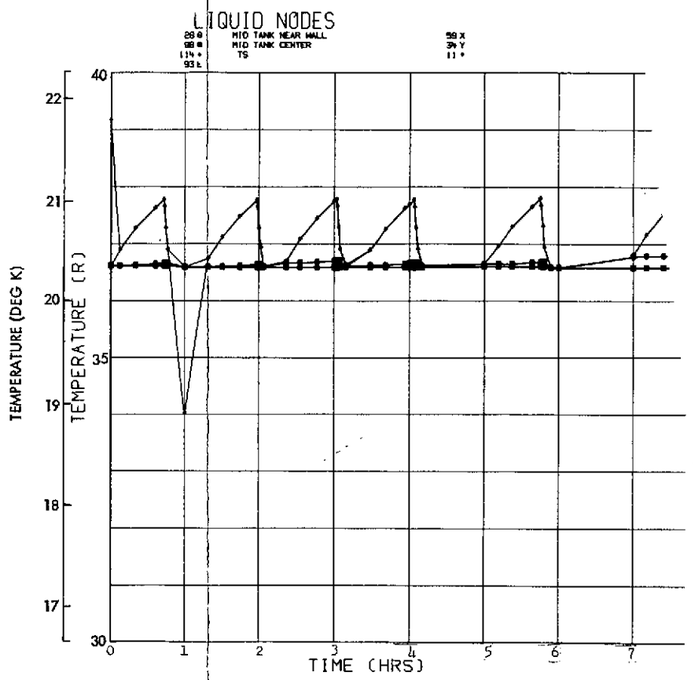

Fig. 3-15(a) $Q = 3.1\ w/m^2$ (1 Btu/Hr-Ft^2),
$R_{cw} = 0.088 \frac{m^2\text{-}^oK}{w} \left(0.5 \frac{Ft^2\text{-Hr-}^oR}{Btu}\right)$

Fig. 3-15 Pressure and Temperature Characteristics in LH_2 – Conduction Model, Tank Dia = 6.86m (22.5 Ft), L/D = 4, Ullage Volume = 5%

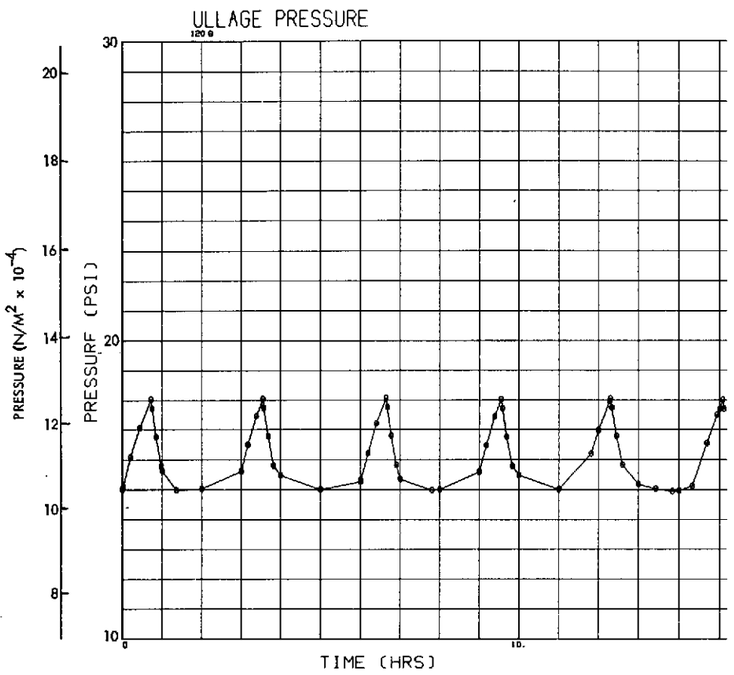

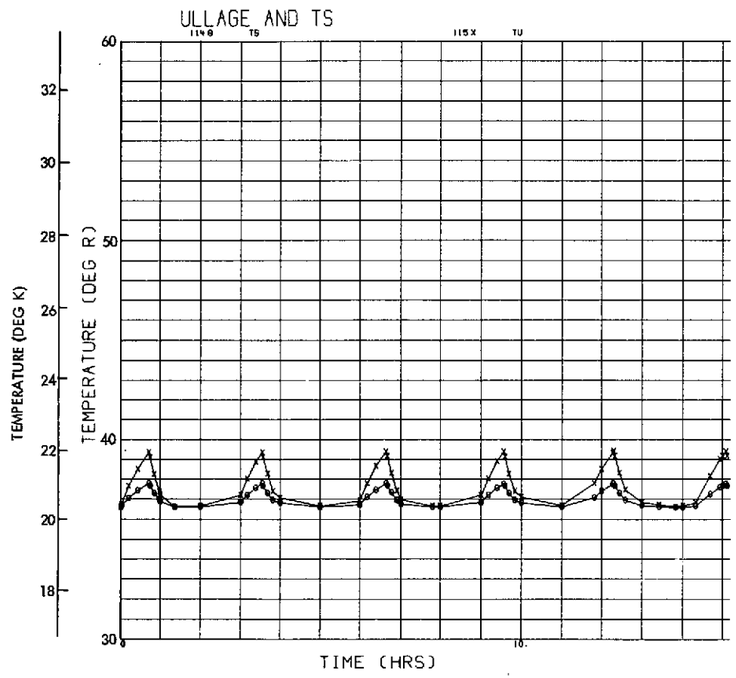

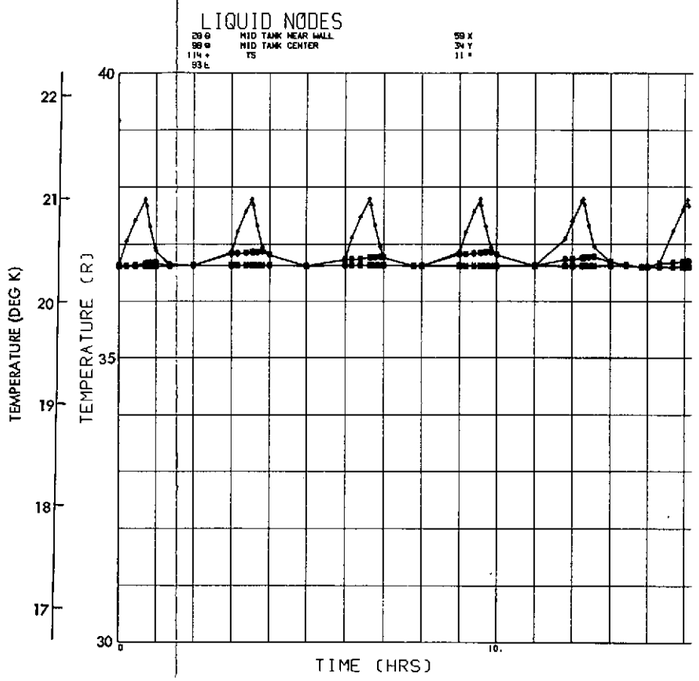

Fig. 3-15(b) $Q = 3.1\,w/m^2$,

$$R_{cw} = 0.35\ \frac{m^2\text{-}^oK}{w}\left(2\ \frac{Hr\text{-}Ft^2\text{-}^oR}{Btu}\right)$$

Fig. 3-15 Pressure and Temperature Characteristics in LH_2 – Conduction Model, Tank Dia = 6.86m (22.5 Ft), L/D = 4, Ullage Volume = 5%

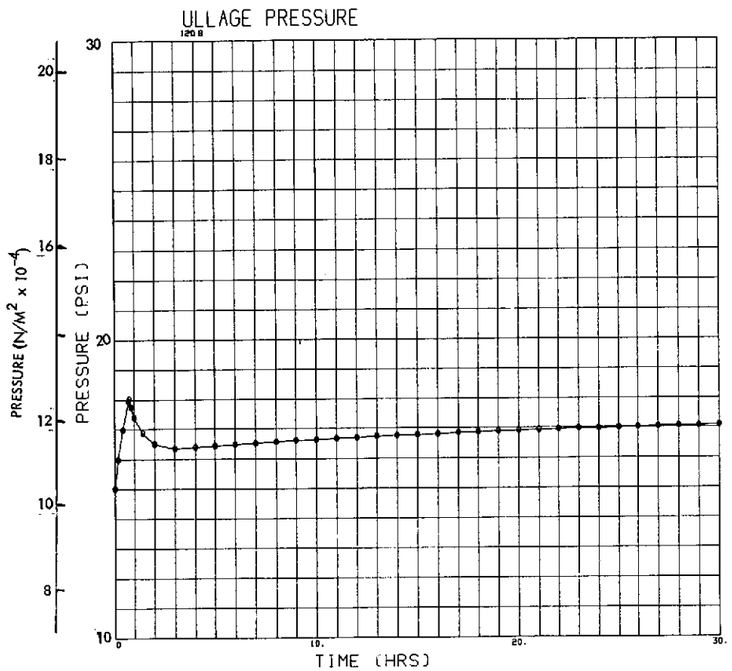

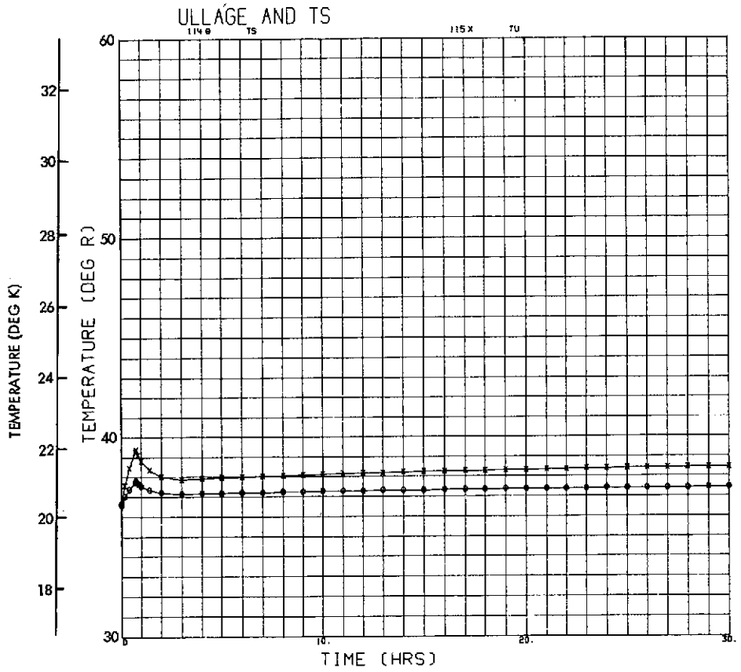

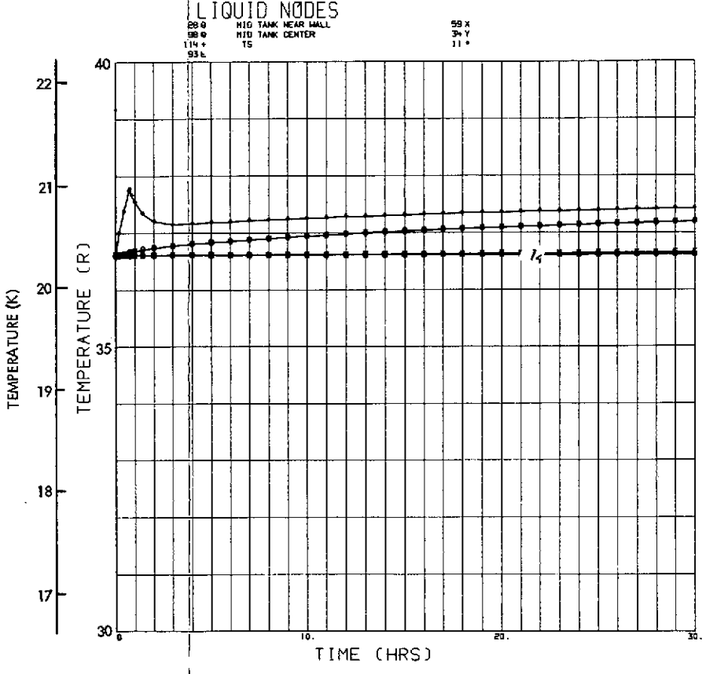

Fig. 3-15(c) $Q = 3.1\ w/m^2$,

$R_{cw} = 0.88\ \frac{m^2\text{-}^oK}{w}\left(5\ \frac{Hr\text{-}Ft^2\text{-}^oR}{Btu}\right)$

Fig. 3-15 Pressure and Temperature Characteristics in LH_2 – Conduction Model, Tank Dia = 6.86m (22.5 Ft), L/D = 4, Ullage Volume = 5%

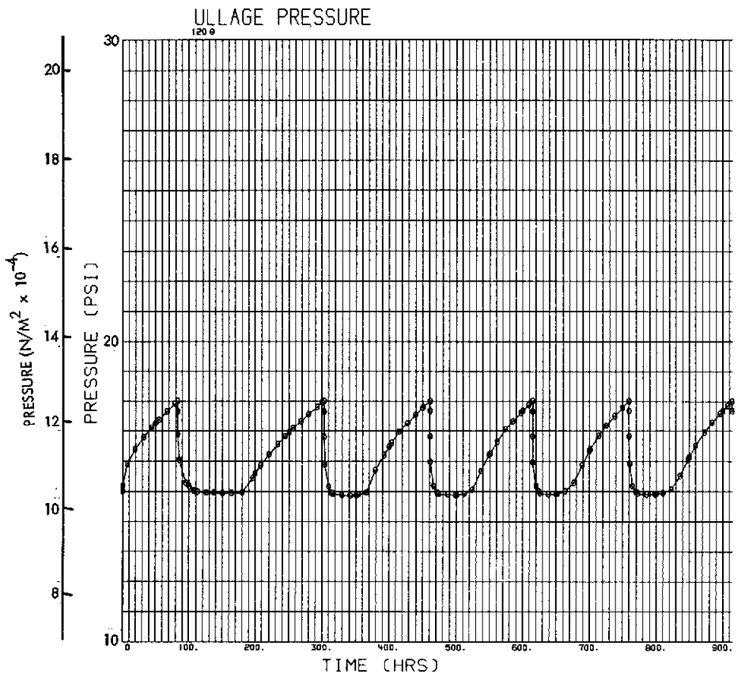

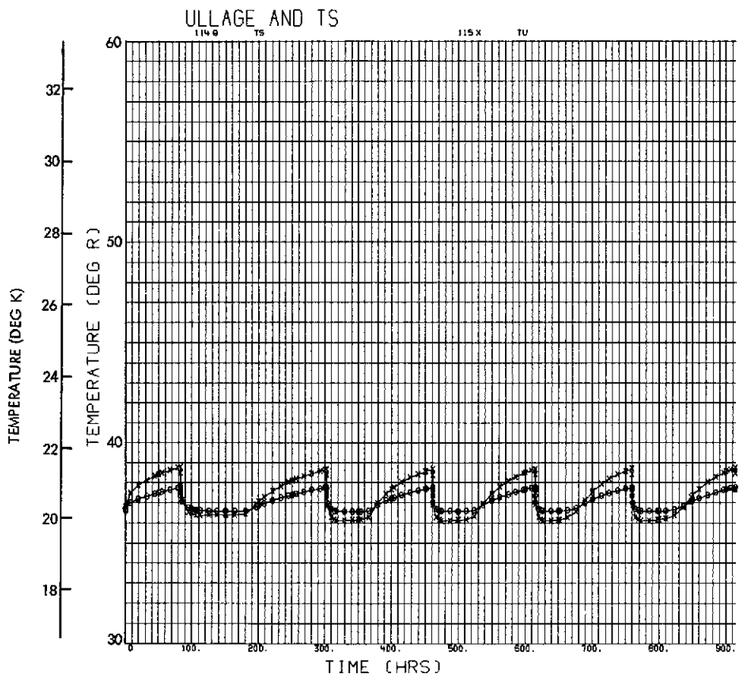

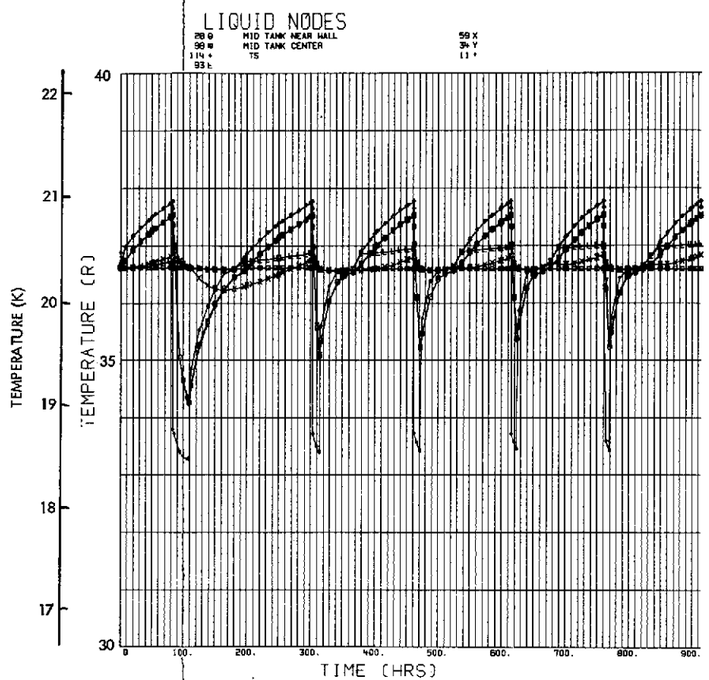

Fig. 3-15(d) $Q = 0.31\ w/m^2 \left(0.1\ \frac{Btu}{Hr\text{-}Ft^2}\right)$,

$R_{cw} = 0.088\ \frac{m^2\text{-}^oK}{w}$

Fig. 3-15 Pressure and Temperature Characteristics in LH_2 – Conduction Model, Tank Dia = 6.86m (22.5 Ft), L/D = 4, Ullage Volume = 5%

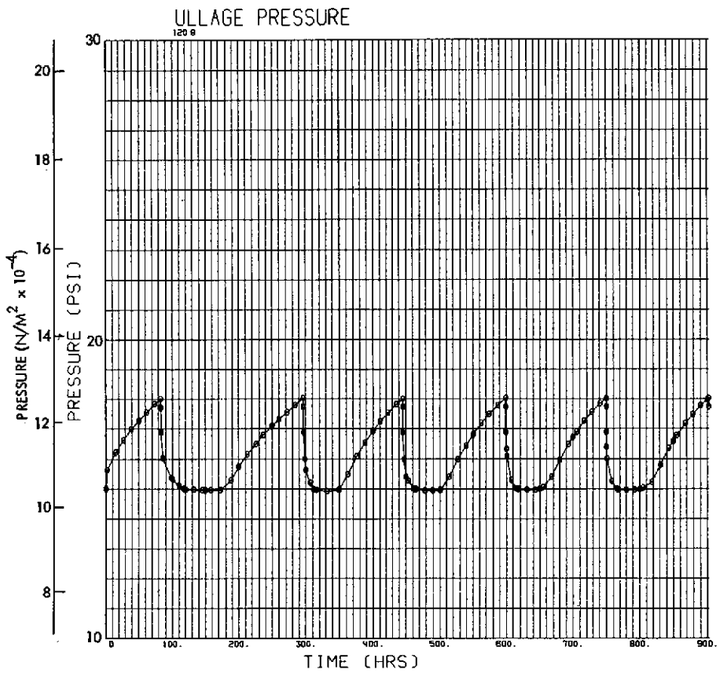

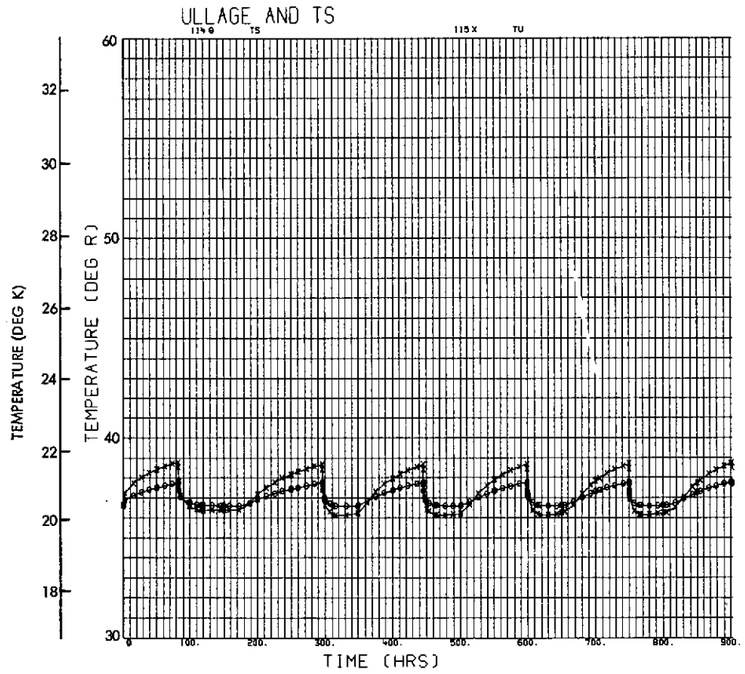

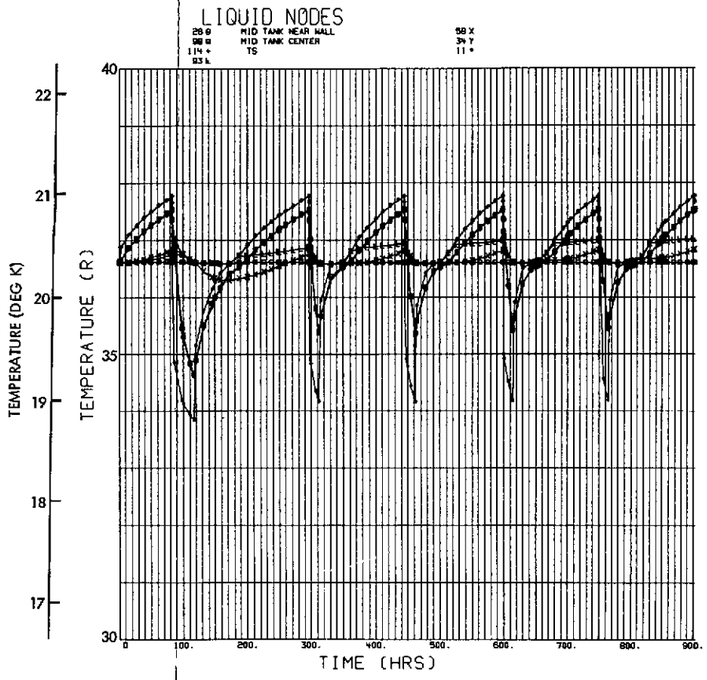

Fig. 3-15(e) $Q = 0.31\ w/m^2$,

$R_{cw} = 0.35\ \frac{m^2\text{-}^oK}{w}$

Fig. 3-15 Pressure and Temperature Characteristics in LH_2 – Conduction Model, Tank Dia = 6.86m (22.5 Ft), L/D = 4, Ullage Volume = 5%

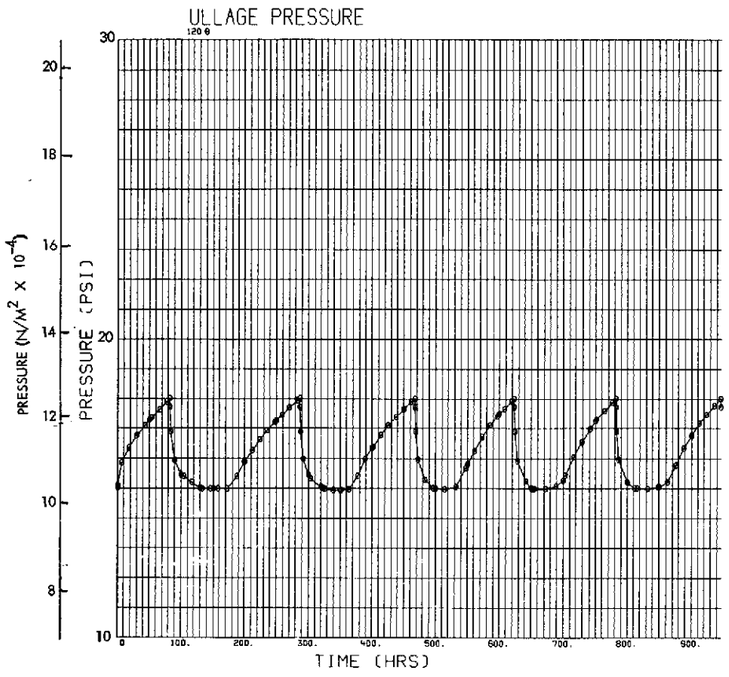

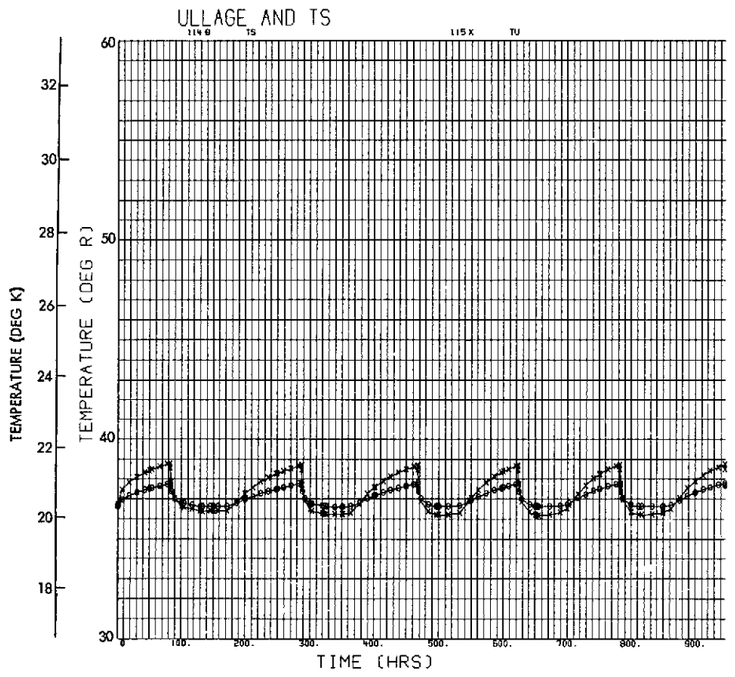

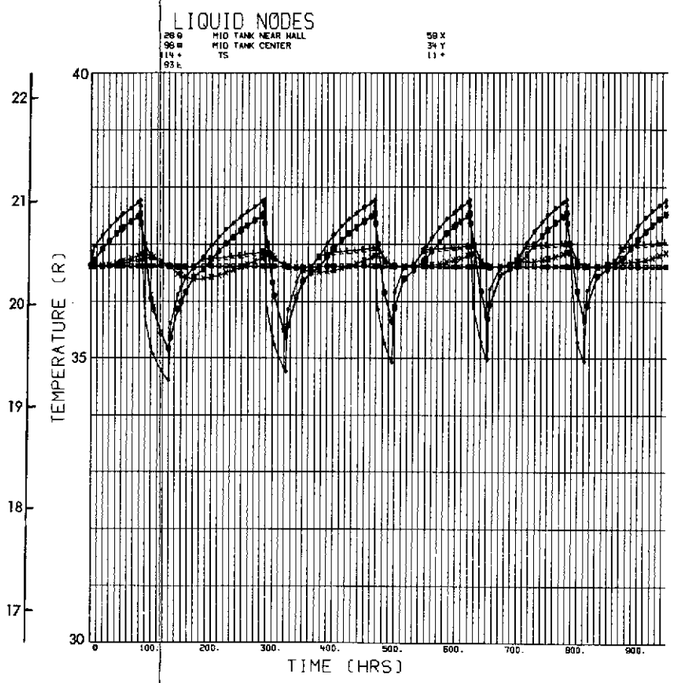

Fig. 3-15(f) $Q = 0.31\ w/m^2$,

$R_{cw} = 0.88\ \frac{m^2\text{-}^oK}{w}$

Fig. 3-15 Pressure and Temperature Characteristics in LH_2 – Conduction Model, Tank Dia = 6.86m (22.5 Ft), L/D = 4, Ullage Volume = 5%

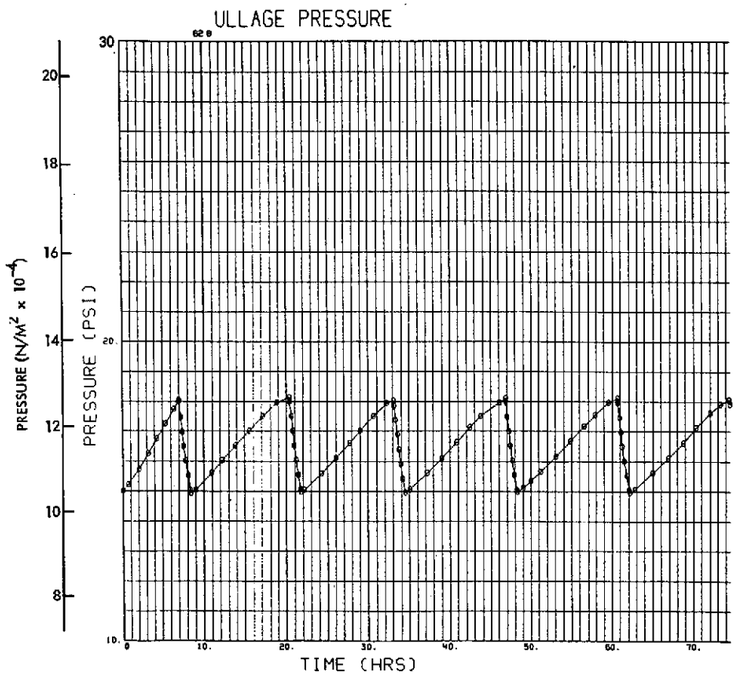

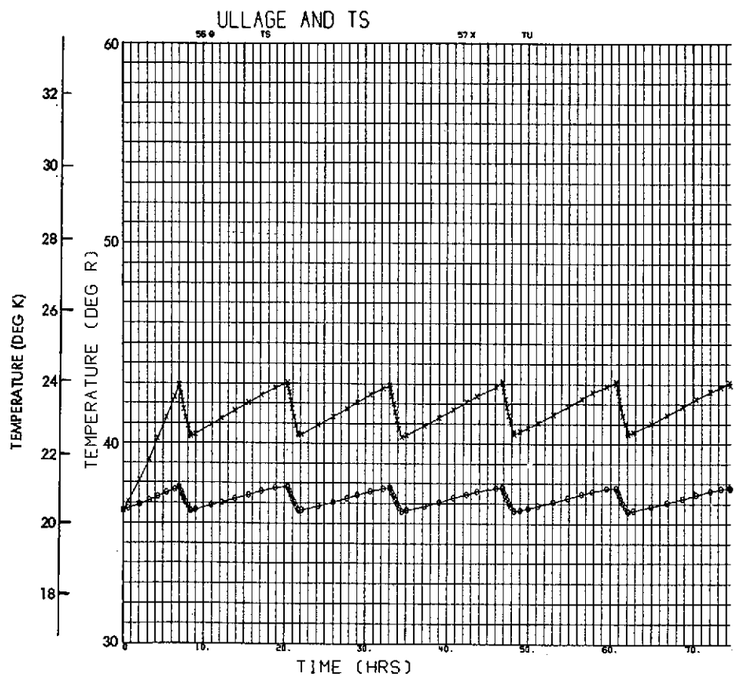

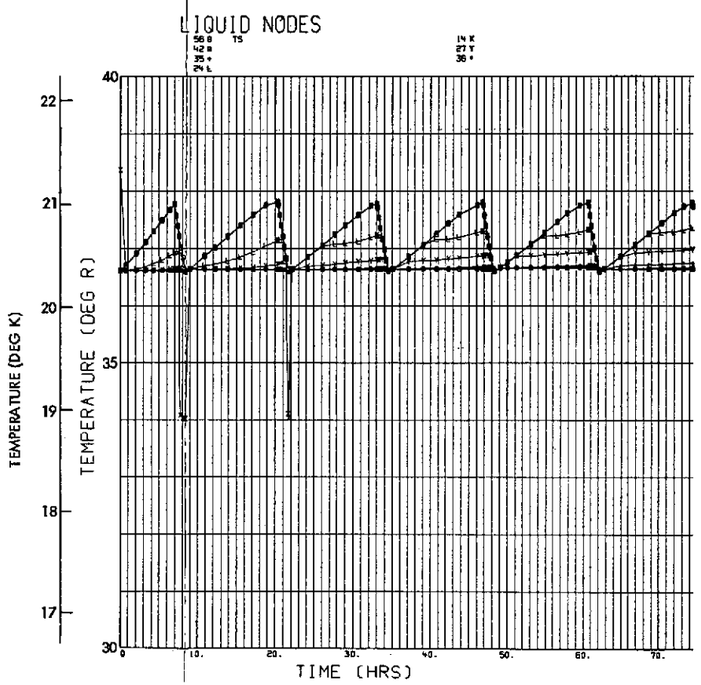

Fig. 3-16(a) $Q = 3.1\ w/m^2 \left(1 \frac{Btu}{Hr\text{-}Ft^2}\right)$,

$R_{cw} = 0.088 \frac{m^2\text{-}^oK}{w} \left(0.5 \frac{Hr\text{-}Ft^2\text{-}^oR}{Btu}\right)$

Fig. 3-16 Pressure and Temperature Characteristics in LH_2 – Conduction Model – Tank Dia = 6.86m (22.5 Ft), L/D = 4, Ullage Volume = 90%

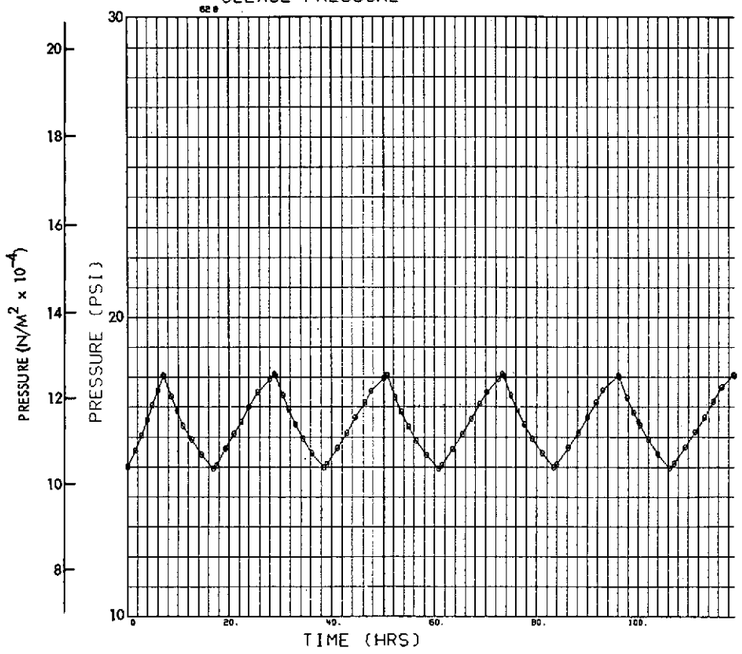

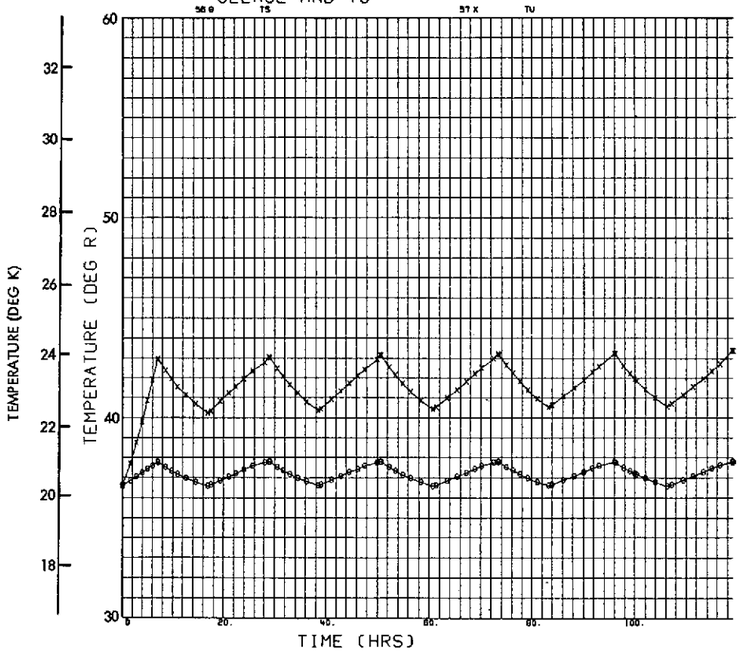

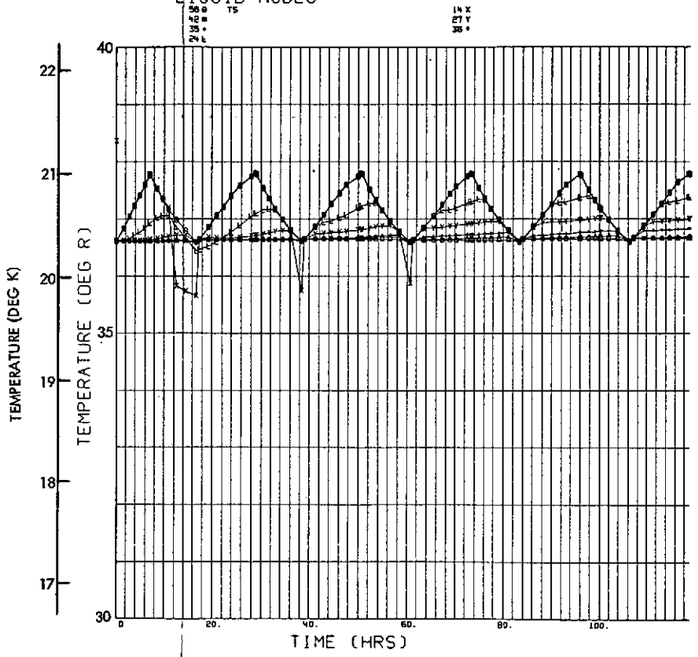

Fig. 3-16(b) $Q = 3.1\ w/m^2$,

$R_{cw} = 0.35\ \frac{m^2\text{-}^oK}{w}$

Fig. 3-16 Pressure and Temperature Characteristics in LH_2 – Conduction Model – Tank Dia = 6.86m (22.5 Ft), L/D = 4, Ullage Volume = 90%

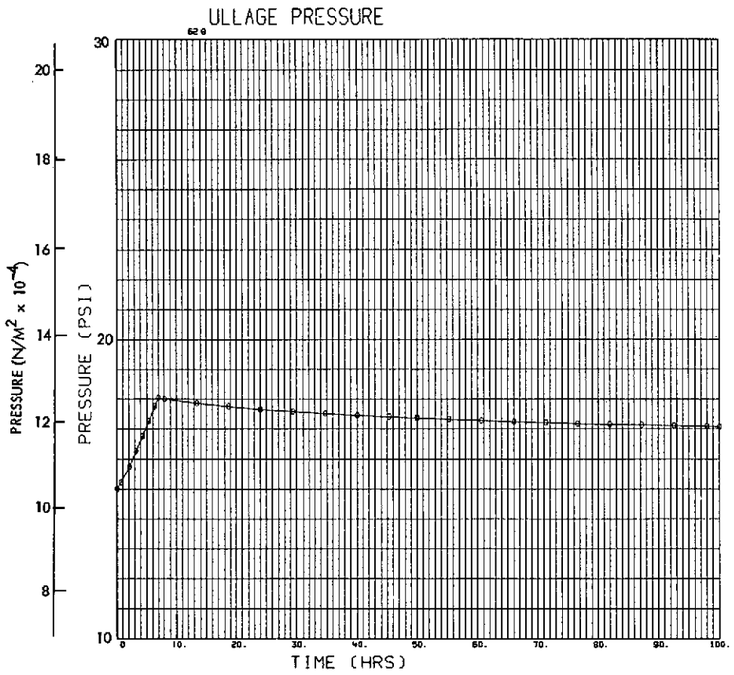

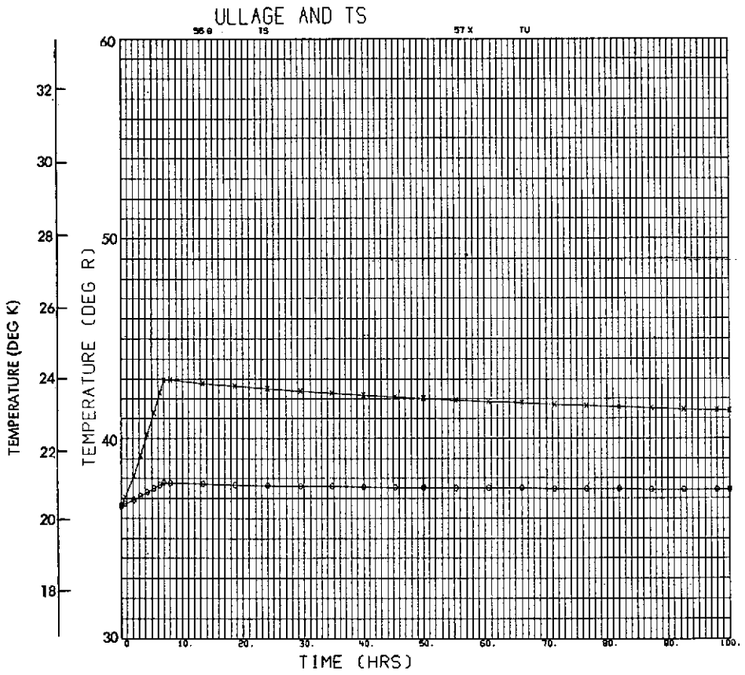

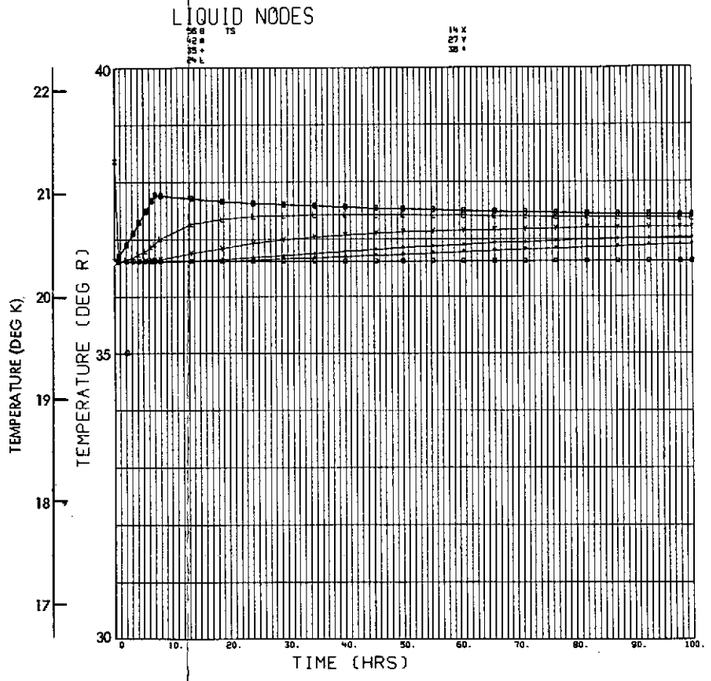

Fig. 3-16(c) $Q = 3.1\ w/m^2$,

$R_{cw} = 0.88\ \frac{m^2\text{-}^oK}{w}$

Fig. 3-16 Pressure and Temperature Characteristics in LH_2 – Conduction Model – Tank Dia = 6.86m (22.5 Ft), L/D = 4, Ullage Volume = 90%

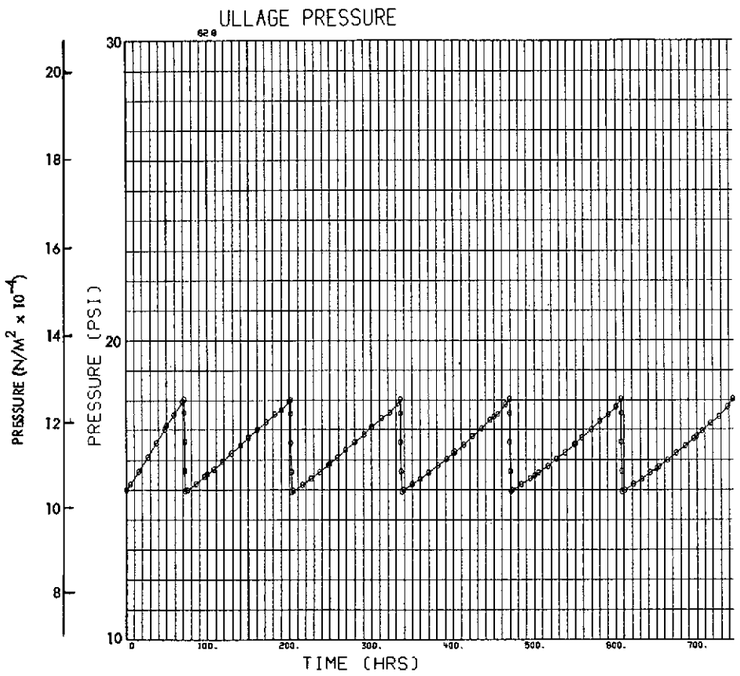

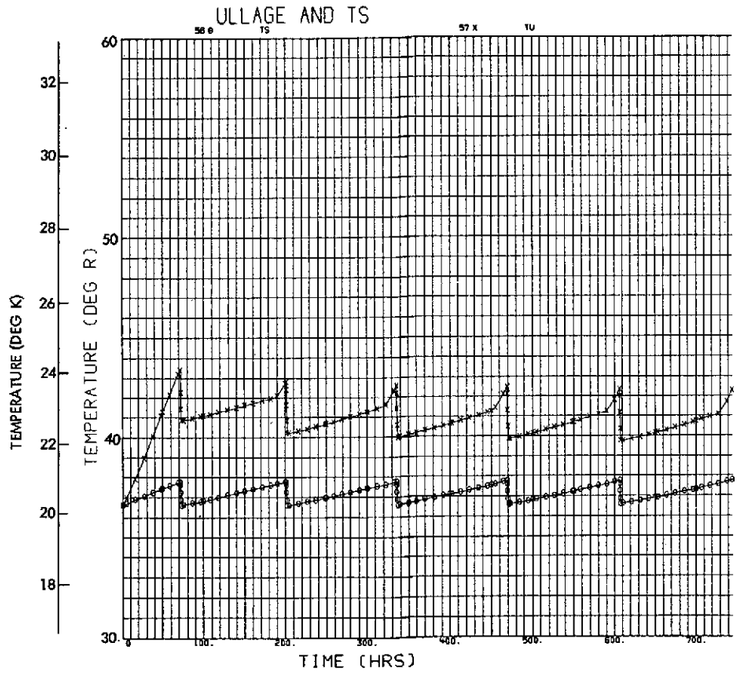

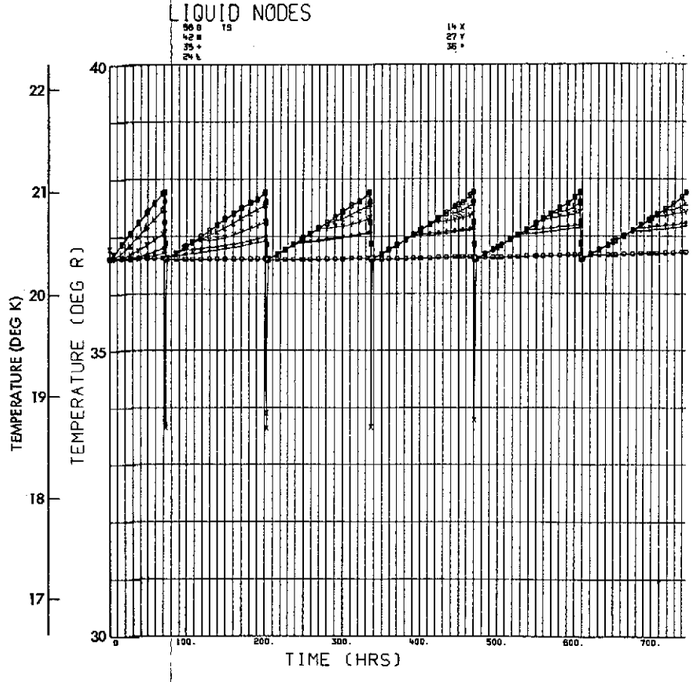

Fig. 3-16(d) $Q = 0.31\ w/m^2$,
$R_{cw} = 0.088\ \frac{m^2\text{-}^oK}{w}$

Fig. 3-16 Pressure and Temperature Characteristics in LH_2 – Conduction Model – Tank Dia = 6.86m (22.5 Ft), L/D = 4, Ullage Volume = 90%

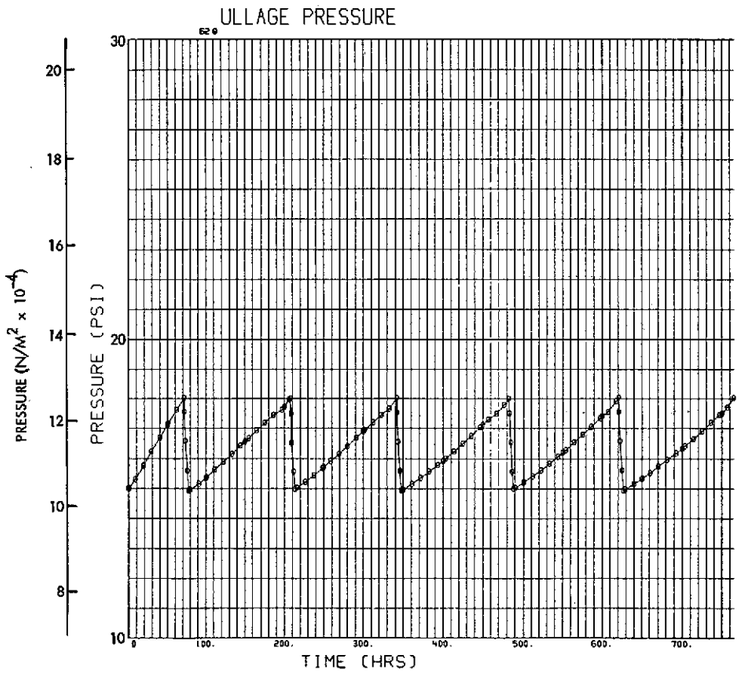

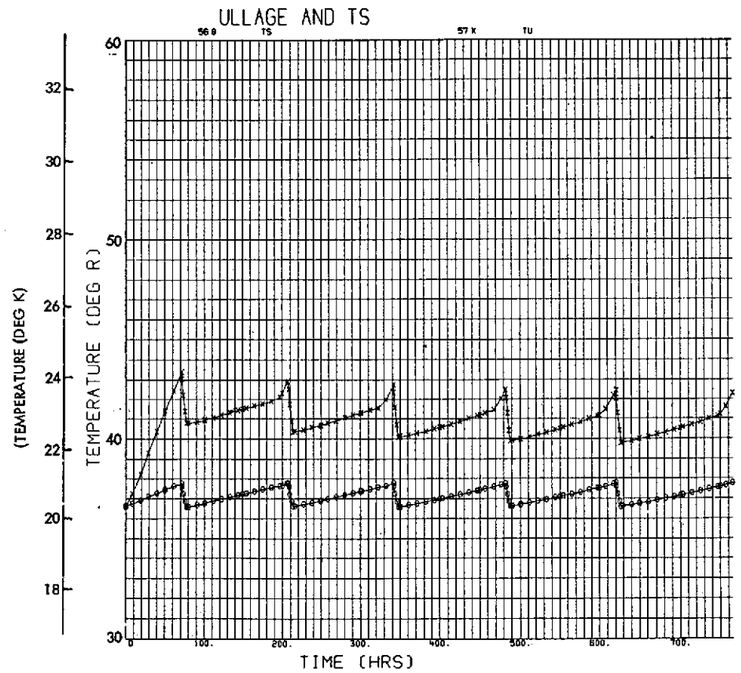

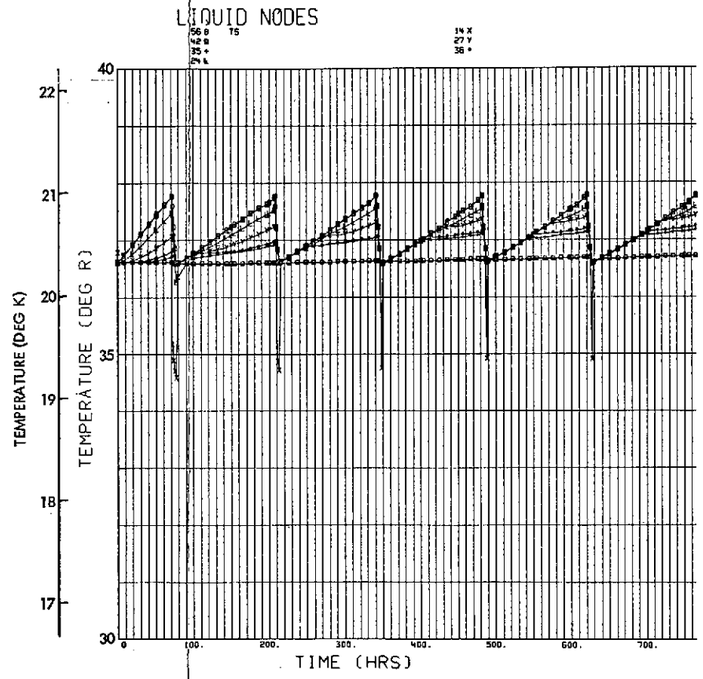

Fig. 3-16(e) $Q = 0.31\ w/m^2$,
$R_{cw} = 0.35\ \frac{m^2 - {}^oK}{w}$

Fig. 3-16 Pressure and Temperature Characteristics in LH_2 – Conduction Model – Tank Dia = 6.86m (22.5 Ft), L/D = 4, Ullage Volume = 90%

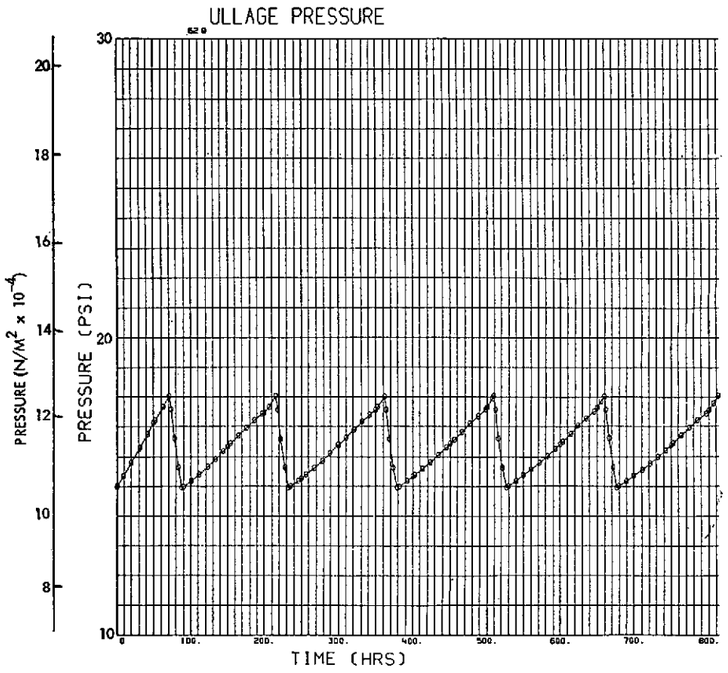

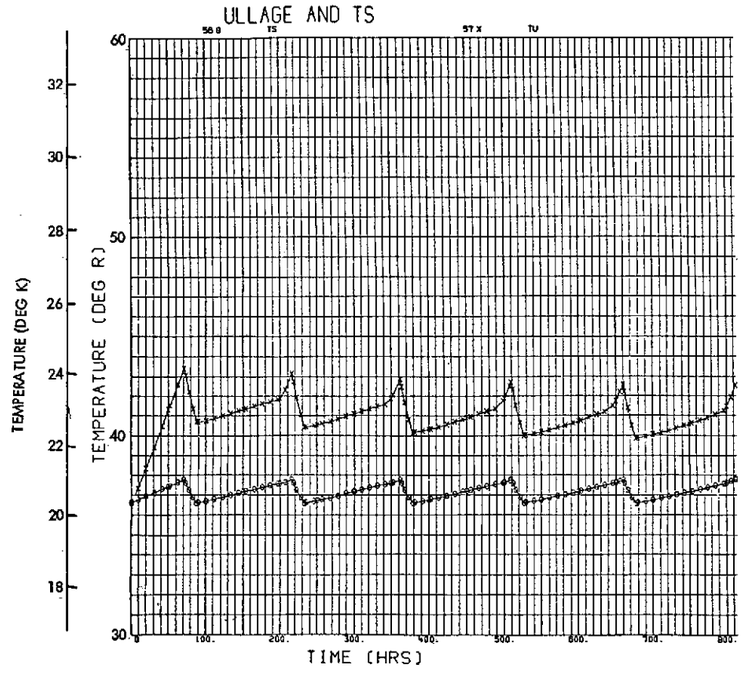

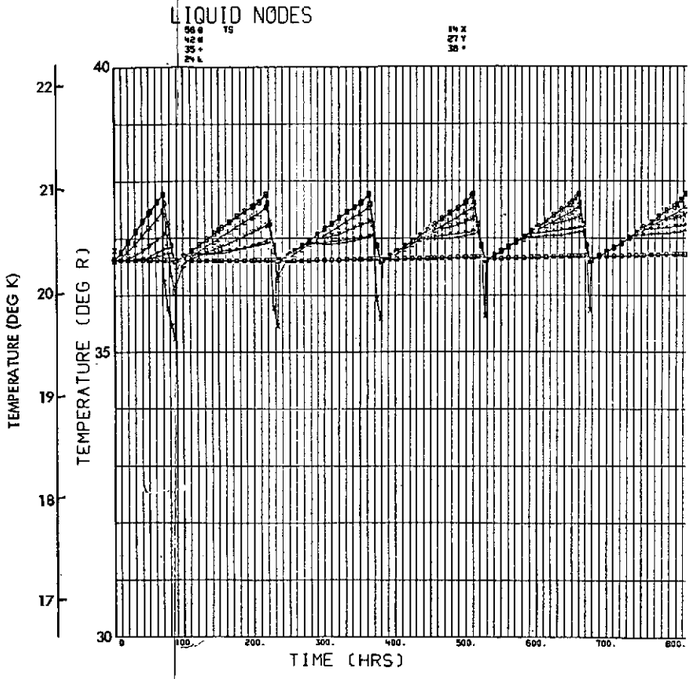

Fig. 3-16(f) $Q = 0.31\ w/m^2$,
$R_{cw} = 0.88\ \frac{m^2\text{-}^oK}{w}$

Fig. 3-16 Pressure and Temperature Characteristics in LH_2 – Conduction Model – Tank Dia = 6.86m (22.5 Ft), L/D = 4, Ullage Volume = 90%

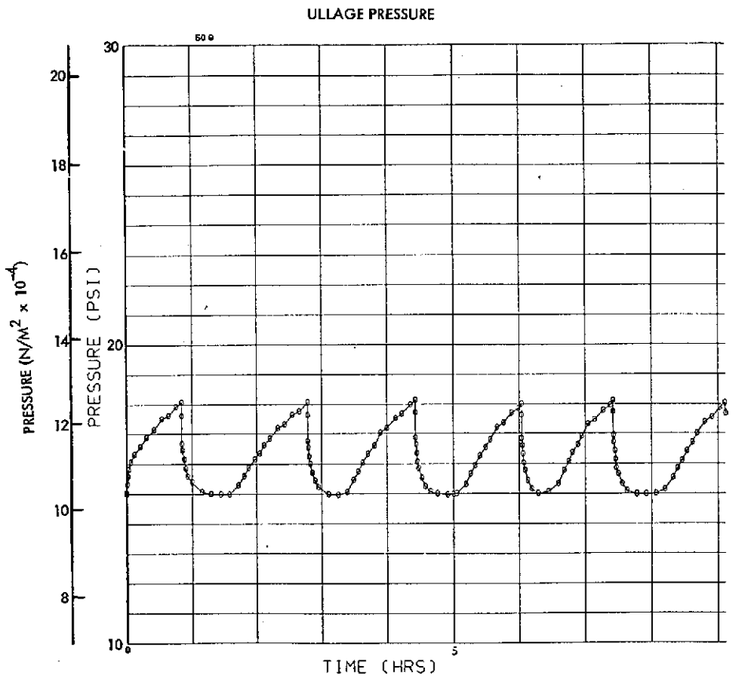

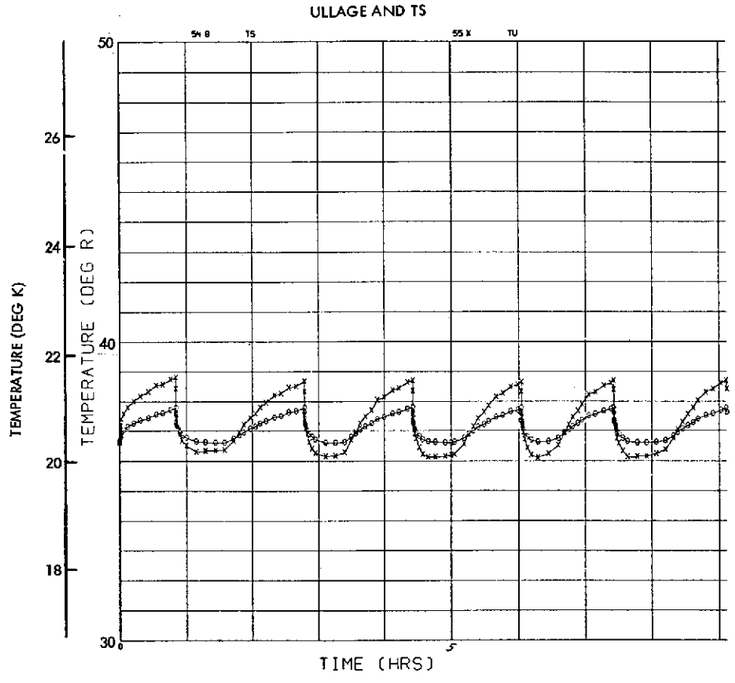

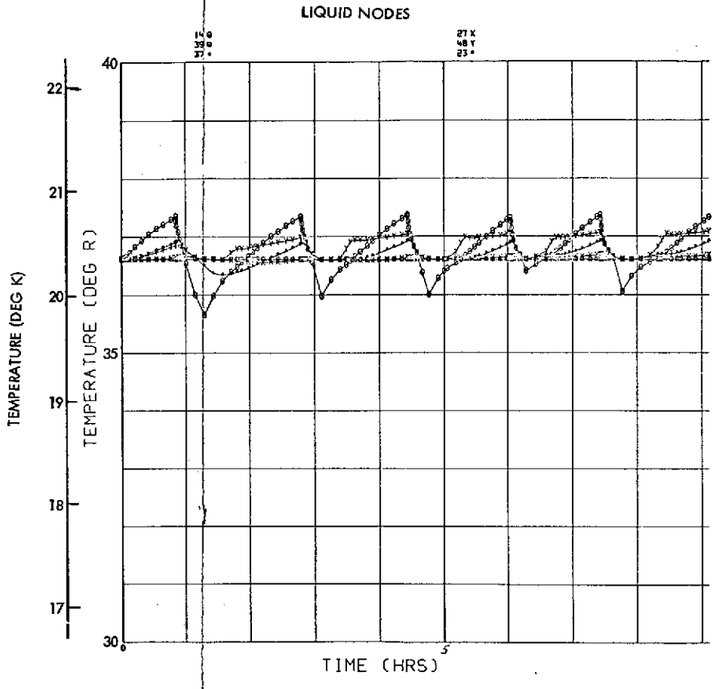

Fig. 3-17(a) $Q = 3.1\ w/m^2 \left(1 \frac{Btu}{Hr\text{-}Ft^2}\right)$,

$R_{cw} = 0.088 \frac{m^2\text{-}^oK}{w} \left(0.5 \frac{Hr\text{-}Ft^2\text{-}^oR}{Btu}\right)$

Fig. 3-17 Pressure and Temperature Characteristics in LH_2 – Conduction Model, Tank Dia = 1.2m (4 Ft), L/D = 1, Ullage Volume = 5%

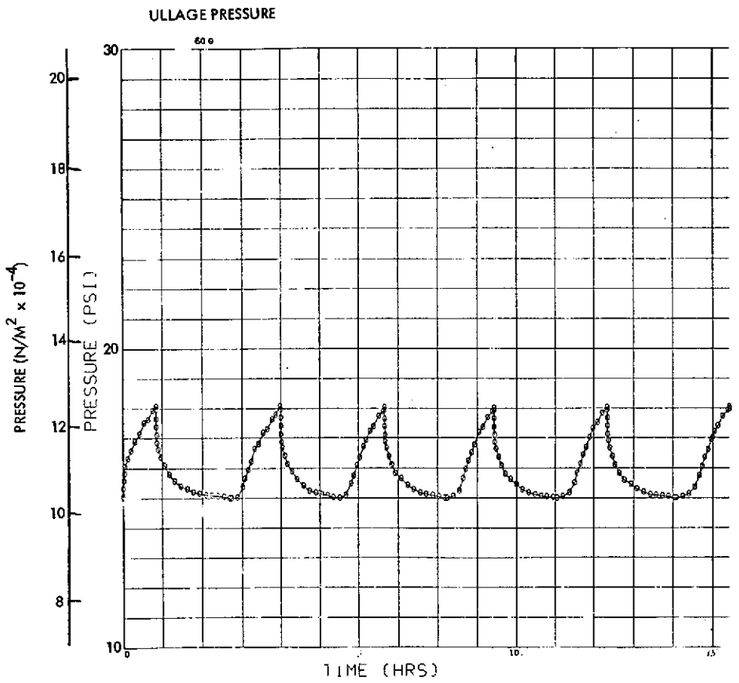

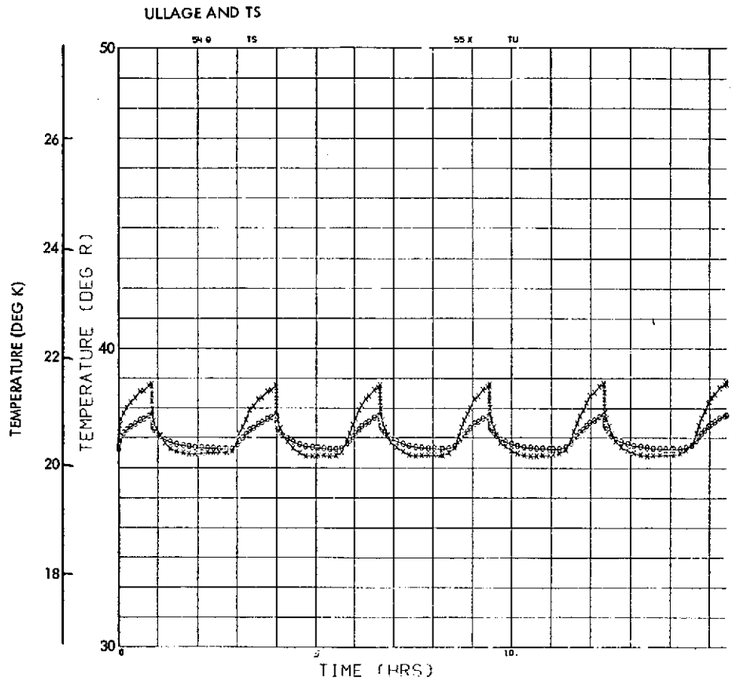

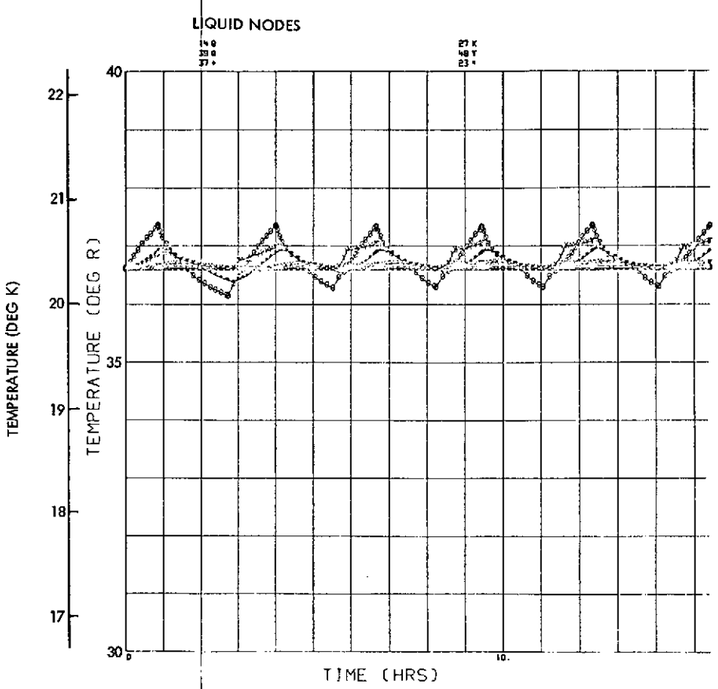

Fig. 3-17(b) $Q = 3.1\ w/m^2$,

$$R_{cw} = 0.35\ \frac{m^2\text{-}^oK}{w}\left(2\ \frac{Hr\text{-}Ft^2\text{-}^oR}{Btu}\right)$$

Fig. 3-17 Pressure and Temperature Characteristics in LH_2 – Conduction Model, Tank Dia = 1.2m (4 Ft), L/D = 1, Ullage Volume = 5%

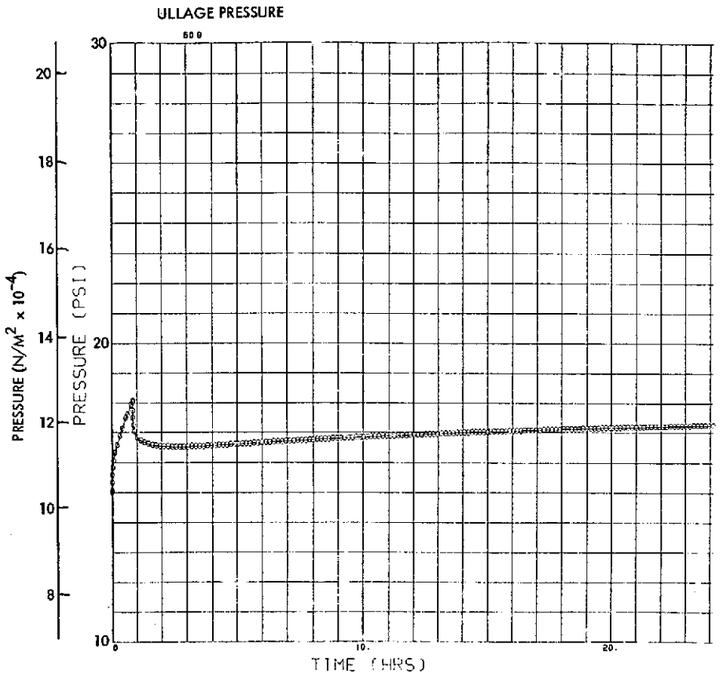

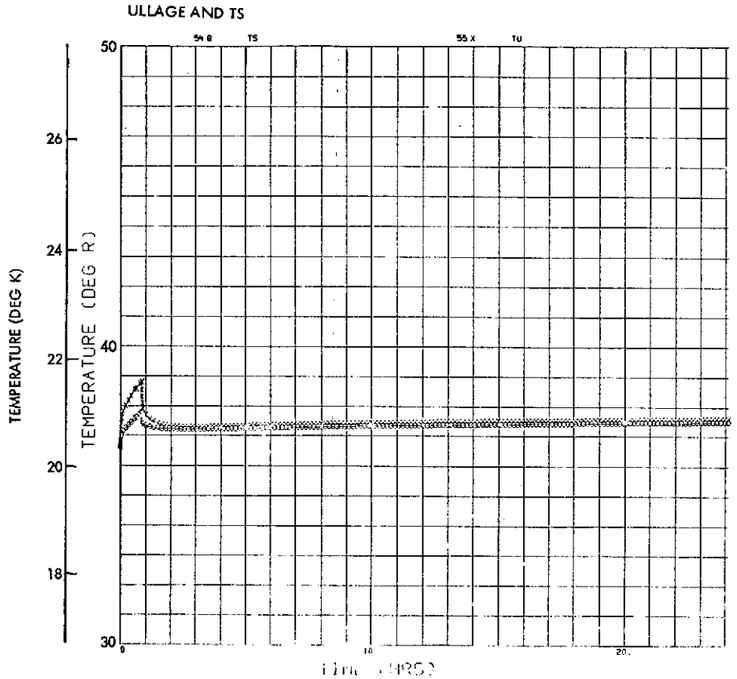

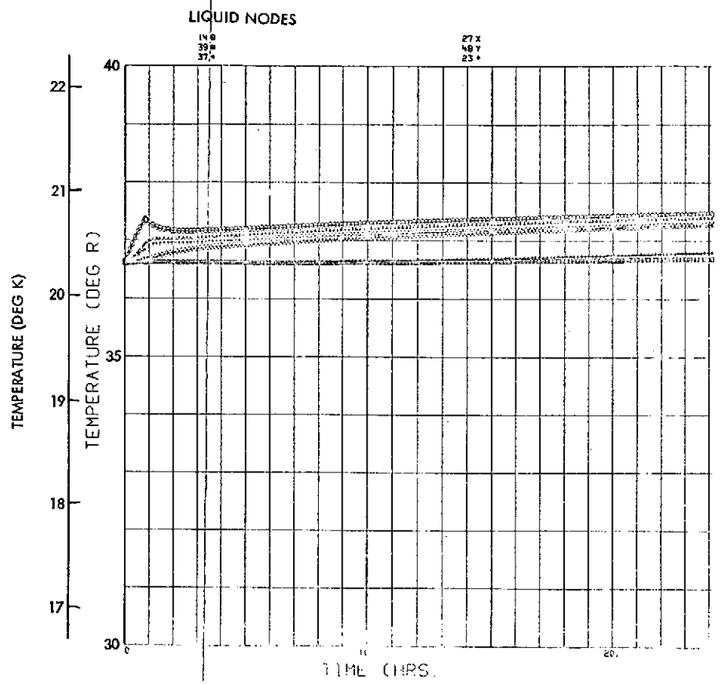

Fig. 3-17(c) $Q = 3.1\ w/m^2$,
$R_{cw} = 0.88 \frac{m^2\text{-}^oK}{w} \left(5 \frac{Hr\text{-}Ft^2\text{-}^oR}{Btu}\right)$

Fig. 3-17 Pressure and Temperature Characteristics in LH_2 – Conduction Model, Tank Dia = 1.2m (4 Ft), L/D = 1, Ullage Volume = 5%

FOLDOUT FRAME 1

PRECEDING PAGE BLANK NOT FILMED

FOLDOUT FRAME 2

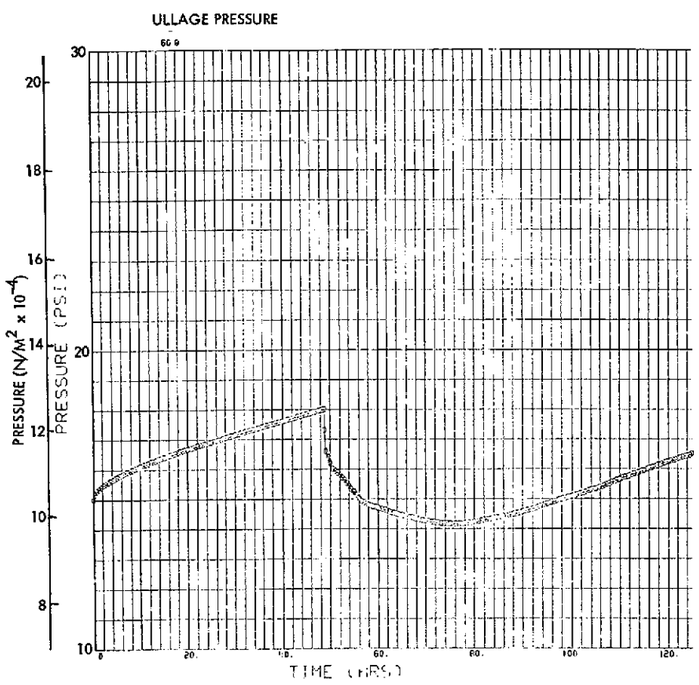

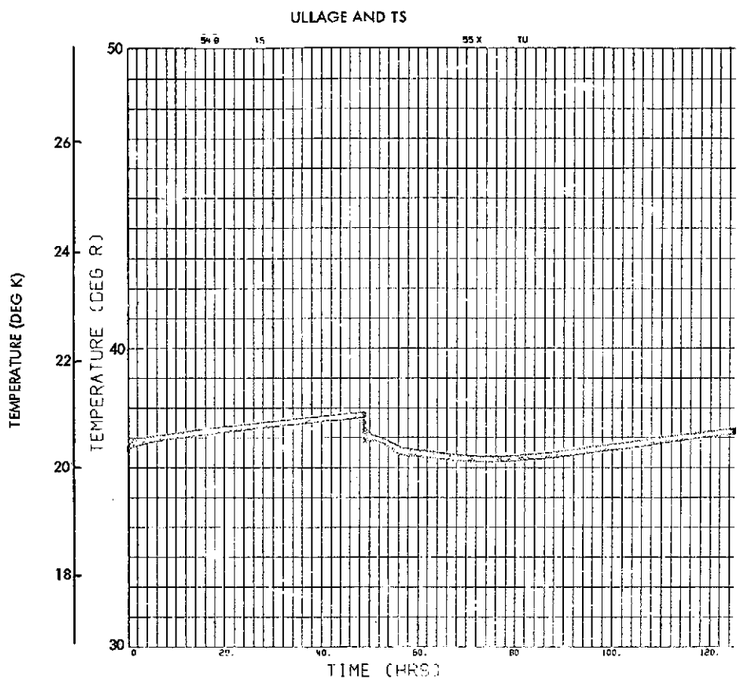

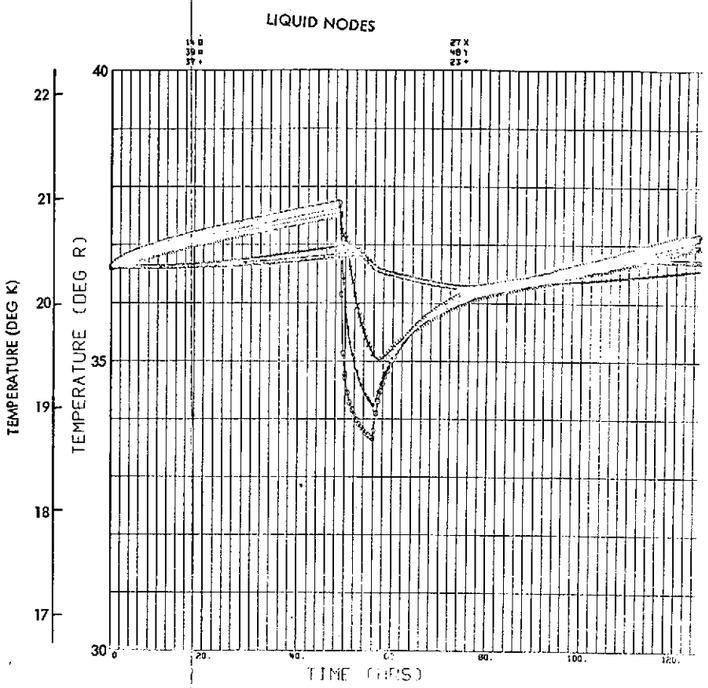

Fig. 3-17(d) $Q = 0.31\ w/m^2 \left(0.1 \frac{Btu}{Hr\text{-}Ft^2}\right)$,

$R_{cw} = 0.088 \frac{m^2\text{-}^oK}{w}$

Fig. 3-17 Pressure and Temperature Characteristics in LH_2 – Conduction Model, Tank Dia = 1.2m (4 Ft), L/D = 1, Ullage Volume = 5%

FOLDOUT FRAME 1

PRECEDING PAGE BLANK NOT FILMED

FOLDOUT FRAME 2

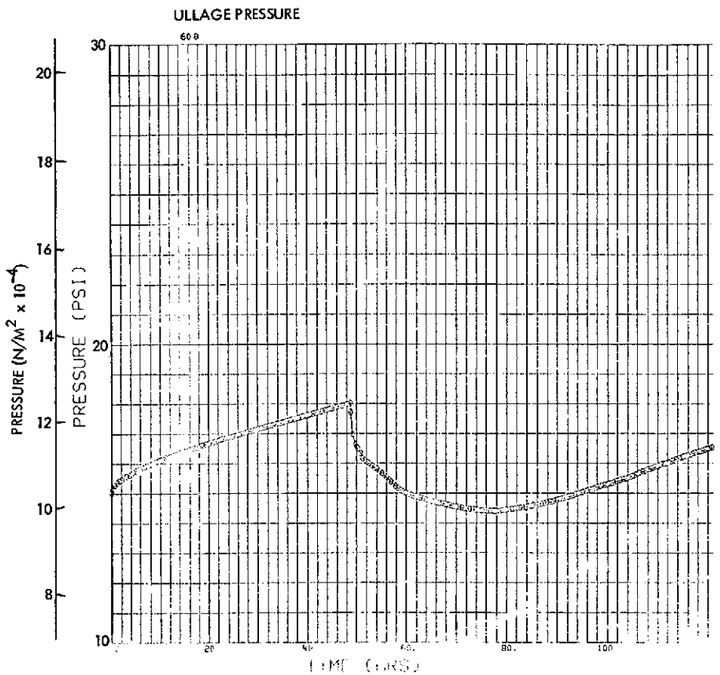

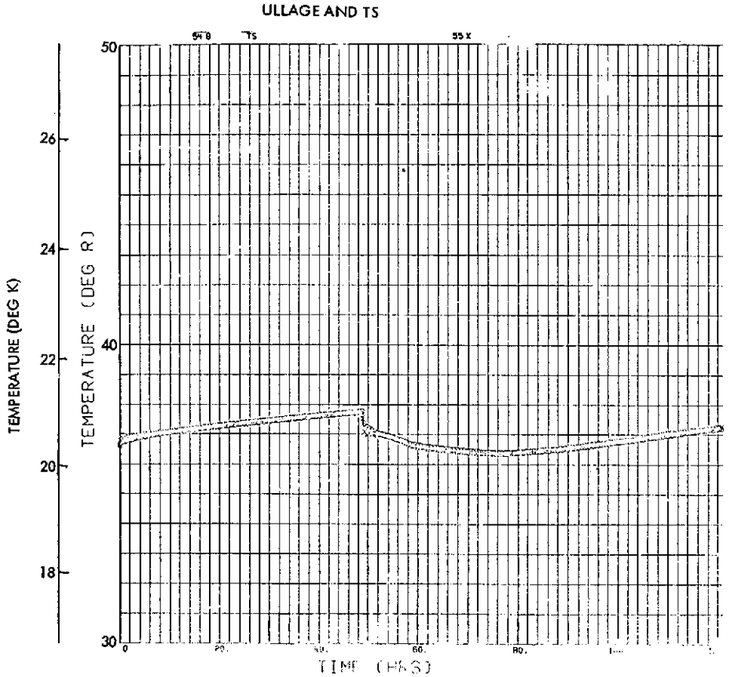

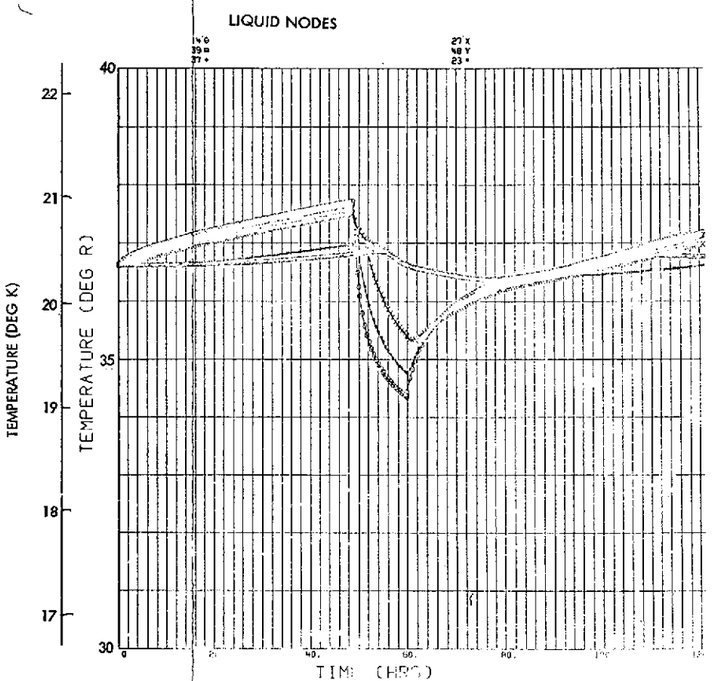

Fig. 3-17(e) $Q = 0.31\ w/m^2$,
$R_{cw} = 0.35\ \frac{m^2 - {}^oK}{w}$

Fig. 3-17 Pressure and Temperature Characteristics in LH_2 – Conduction Model, Tank Dia = 1.2m (4 Ft), L/D = 1, Ullage Volume = 5%

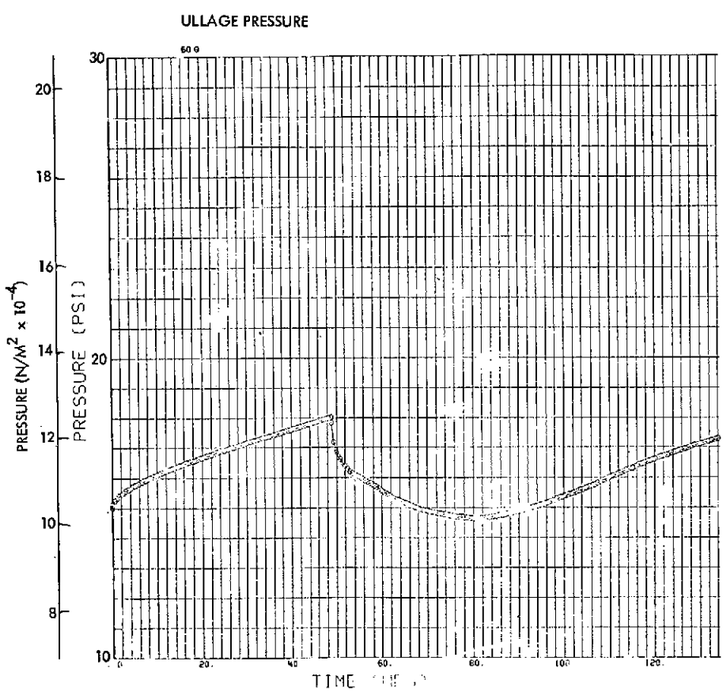

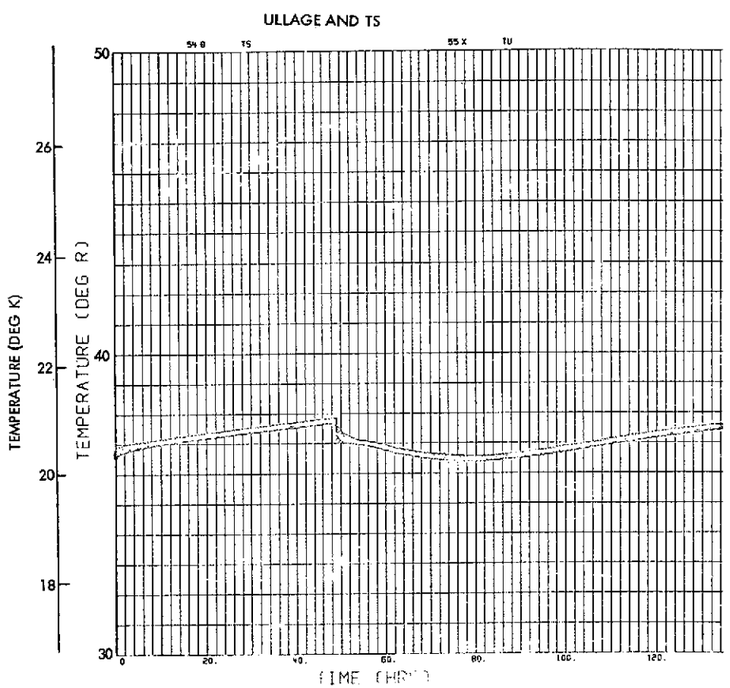

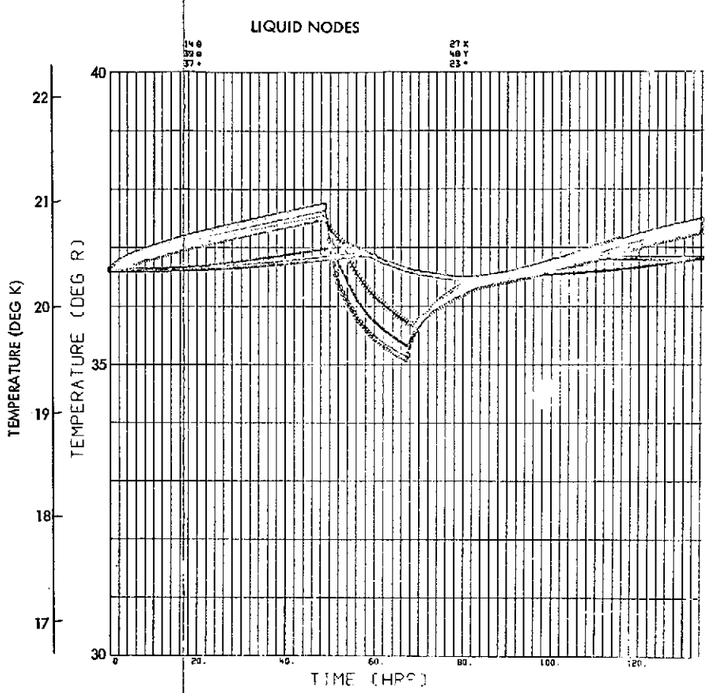

Fig. 3-17(f) $Q = 0.31\ w/m^2$,

$$R_{cw} = 0.88\ \frac{m^2\text{-}^oK}{w}$$

Fig. 3-17 Pressure and Temperature Characteristics in LH_2 – Conduction Model, Tank Dia = 1.2m (4 Ft), L/D = 1, Ullage Volume = 5%

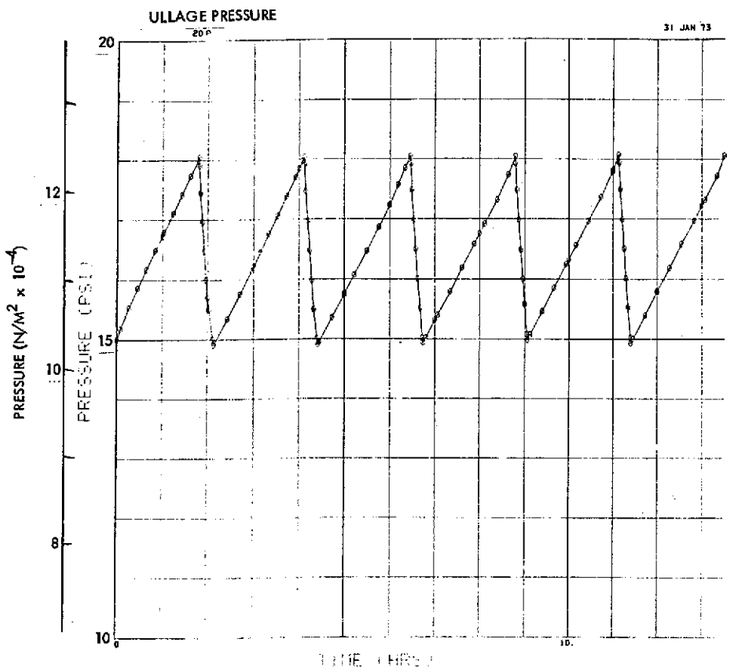

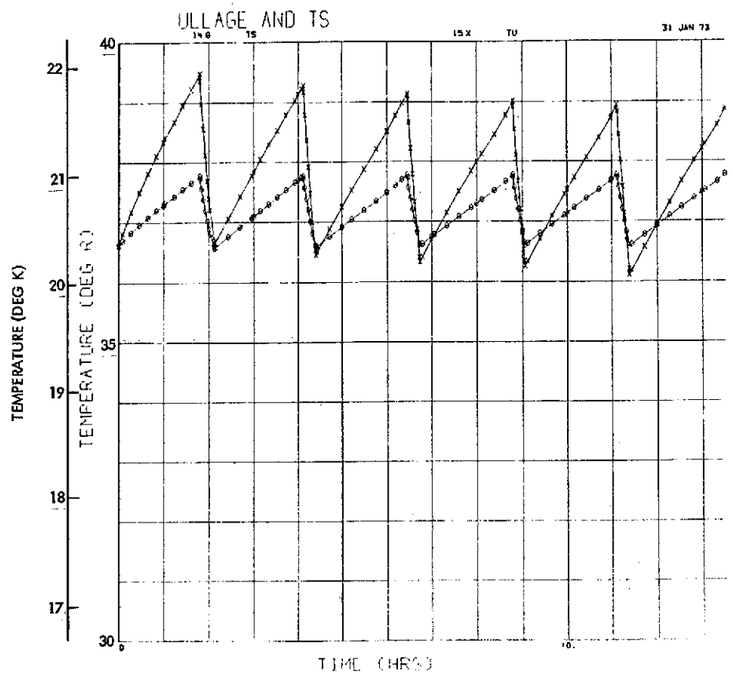

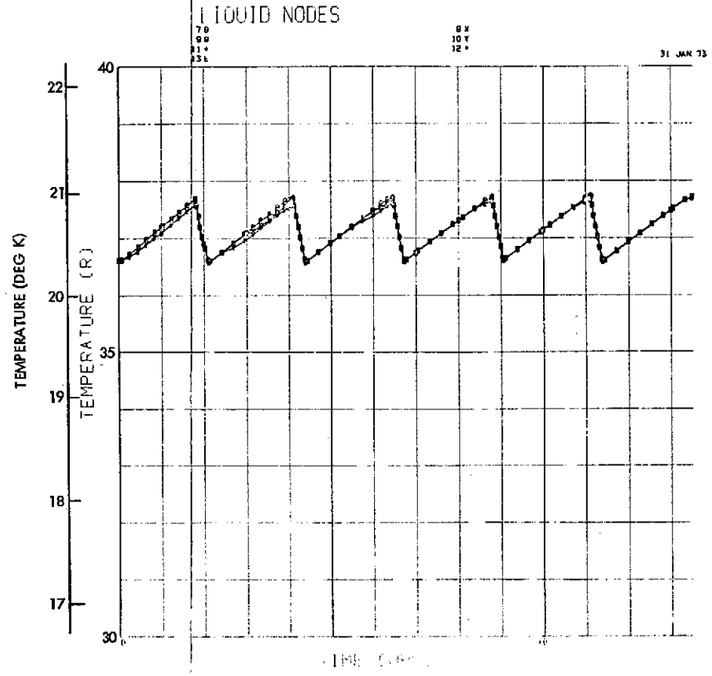

Fig. 3-18 (a) $Q = 3.1\ w/m^2 \left(\frac{1\ Btu}{Hr\text{-}Ft^2}\right)$

$R_{cw} = 0.088\ \frac{m^2\text{-}^oK}{w} \left(\frac{0.5\ Hr\text{-}Ft^2\text{-}^oR}{Btu}\right)$

Fig. 3-18 Pressure and Temperature Characteristics in LH_2 – Conduction Model, Tank Dia. = 1.2 m (4 Ft), L/D = 1, Ullage Volume = 90%

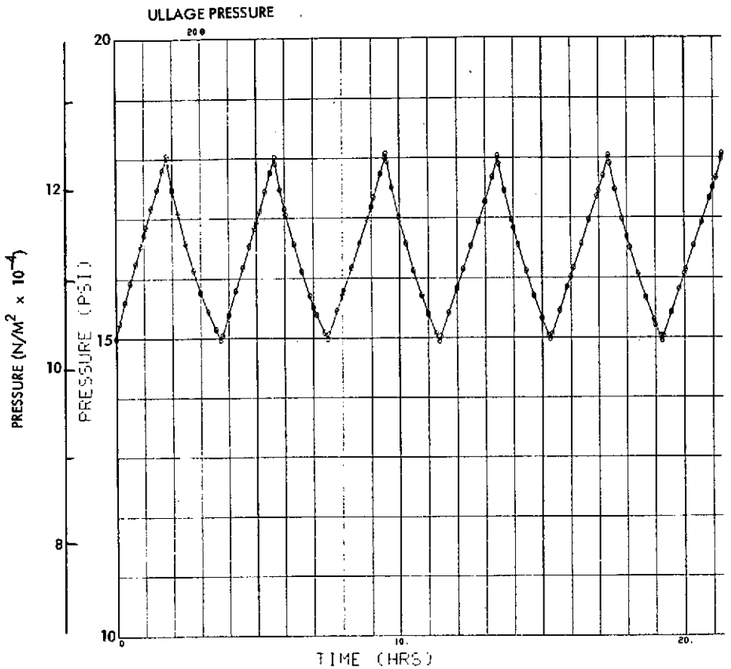

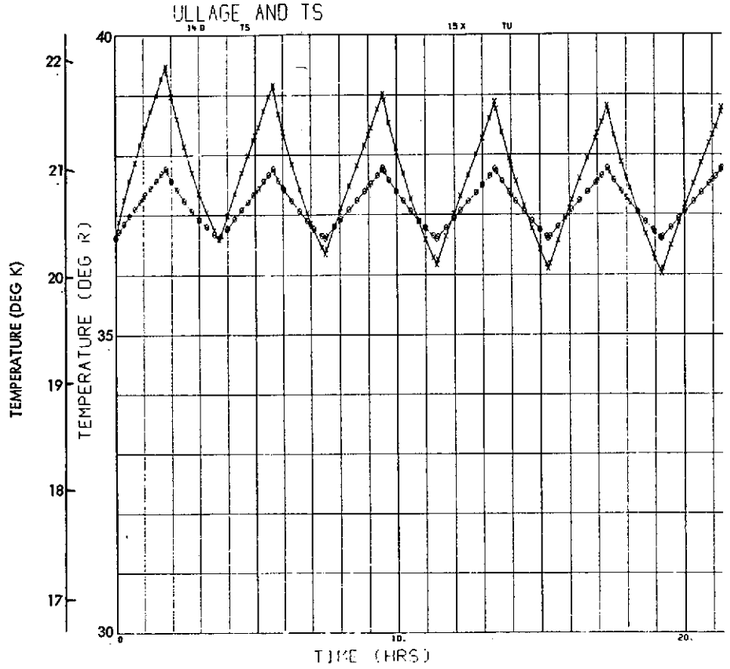

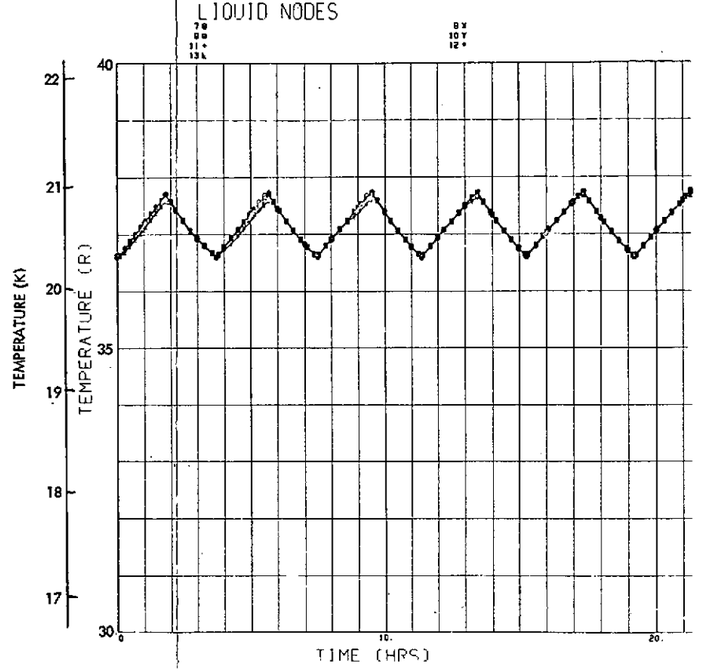

Fig. 3-18(b) $Q = 3.1\ w/m^2$, $R_{cw} = 0.35\ \frac{m^2\text{-}^oK}{w}\ \left(\frac{2\ Hr\text{-}Ft^2}{Btu}\right)$

Fig. 3-18 Pressure and Temperature Characteristics in LH_2 – Conduction Model, Tank Dia. = 1.2 m (4 Ft), L/D = 1, Ullage Volume = 90%

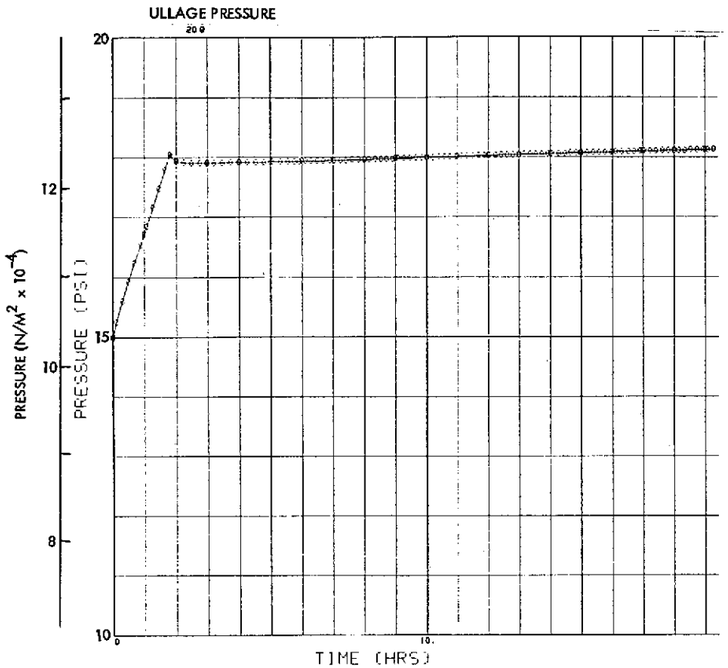

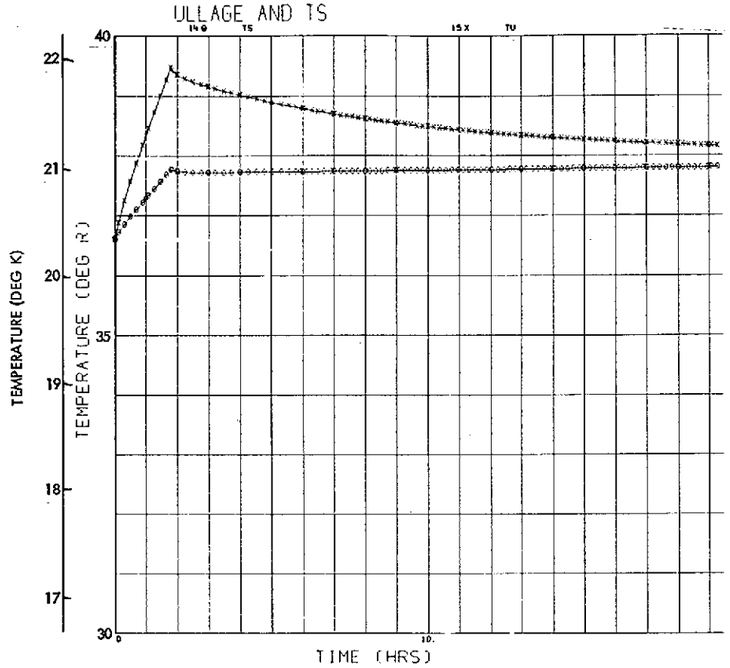

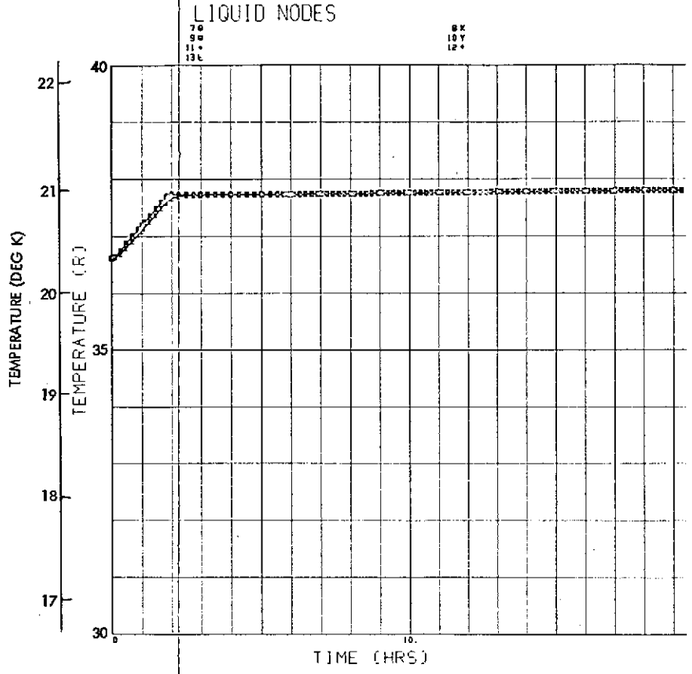

Fig. 3-18(c) Q = 3.1 w/m^2, R_{cw} = 0.88 $\frac{m^2\text{-}^oK}{w}$ $\left(\frac{5\ Hr\text{-}Ft^2\text{-}^oR}{Btu}\right)$

Fig. 3-18 Pressure and Temperature Characteristics in LH_2 – Conduction Model, Tank Dia. = 1.2 m (4 Ft), L/D = 1, Ullage Volume = 90%

C-2

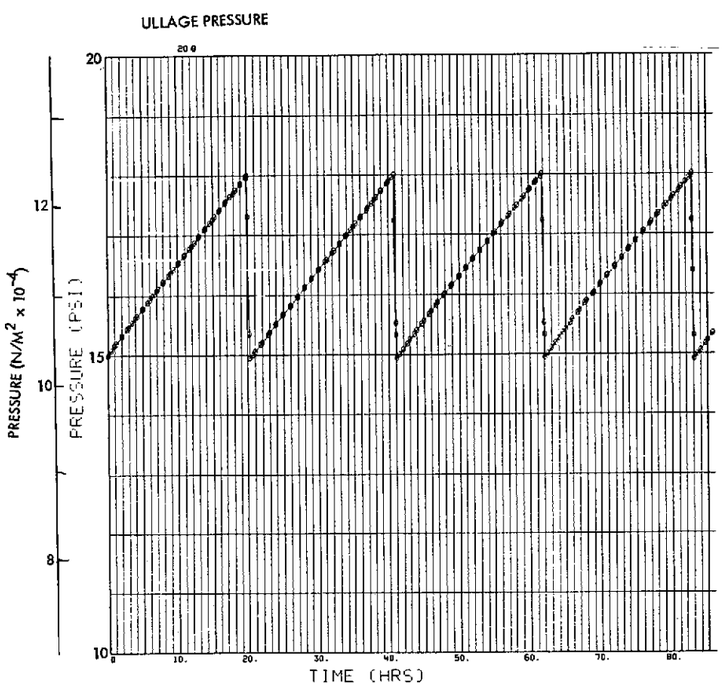

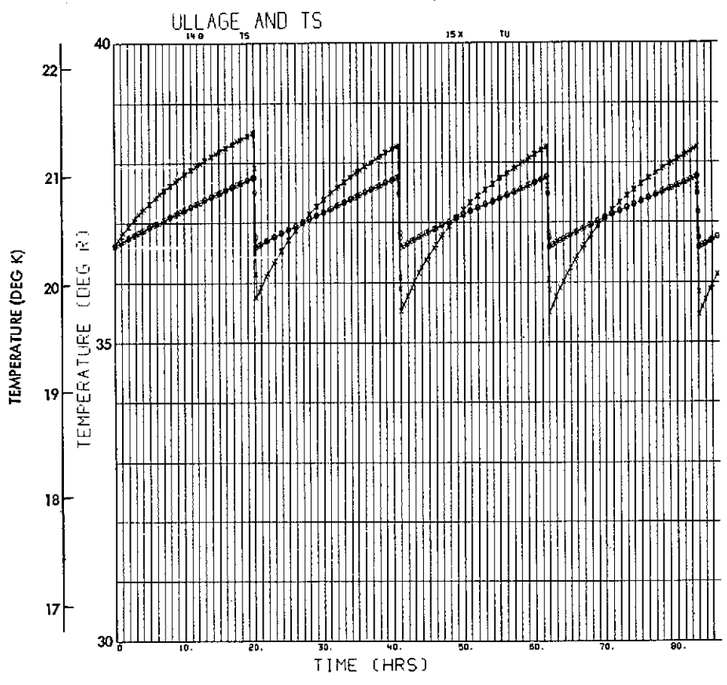

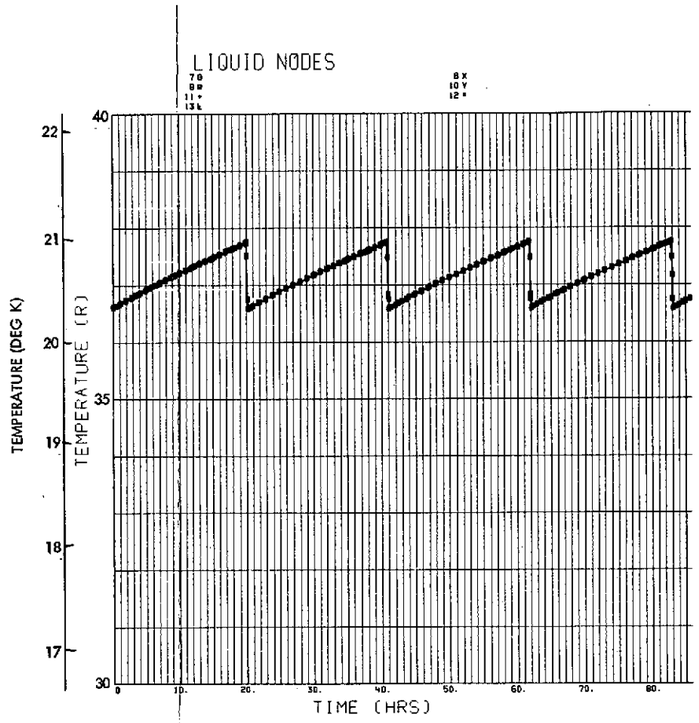

Fig. 3-18 (d) $Q = 0.31\ w/m^2 \left(0.1 \frac{Btu}{Hr\text{-}Ft^2}\right)$

$$R_{cw} = 0.088 \frac{m^2\text{-}^oK}{w}$$

Fig. 3-18 Pressure and Temperature Characteristics in LH_2 – Conduction Model, Tank Dia. = 1.2 m (4 Ft), L/D = 1, Ullage Volume = 90%

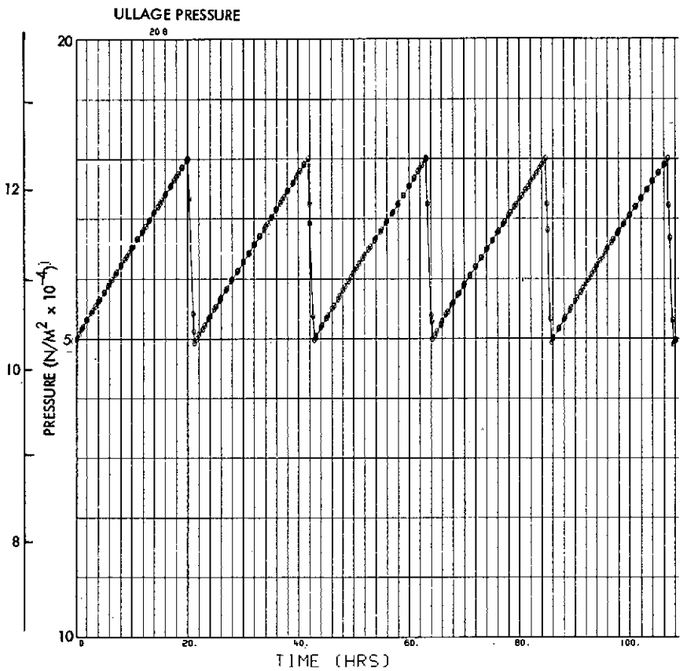

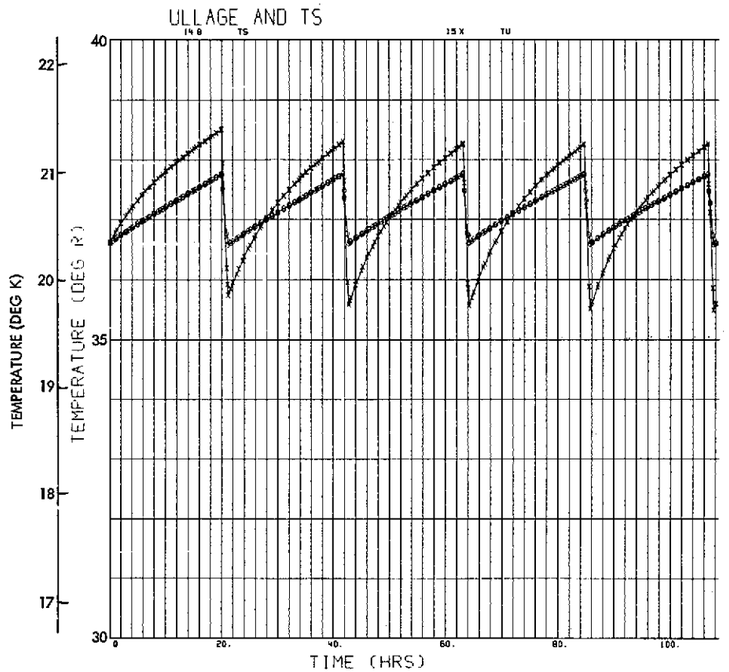

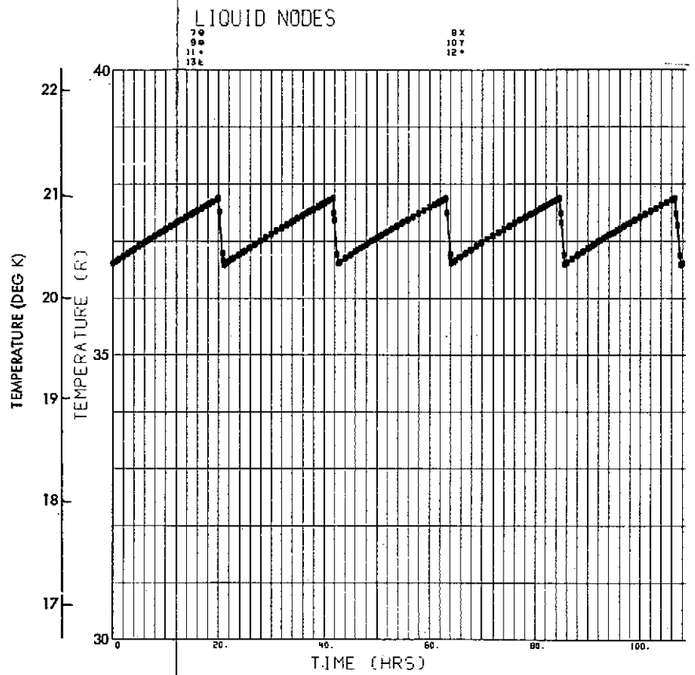

Fig. 3-18(e) $Q = 0.31\ w/m^2$, $R_{cw} = 0.35\ \frac{m^2\text{-}^oK}{w}$

Fig. 3-18 Pressure and Temperature Characteristics in LH_2 – Conduction Model, Tank Dia. = 1.2 m (4 Ft), L/D = 1, Ullage Volume = 90%

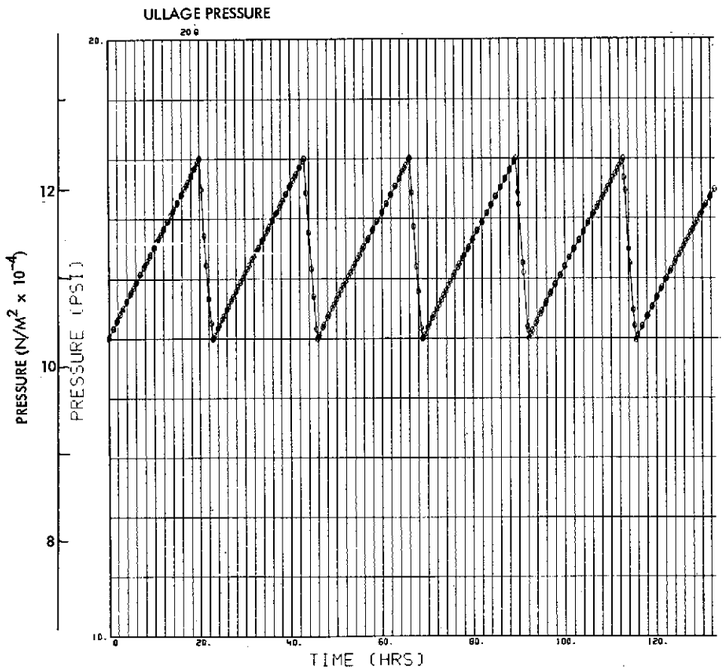

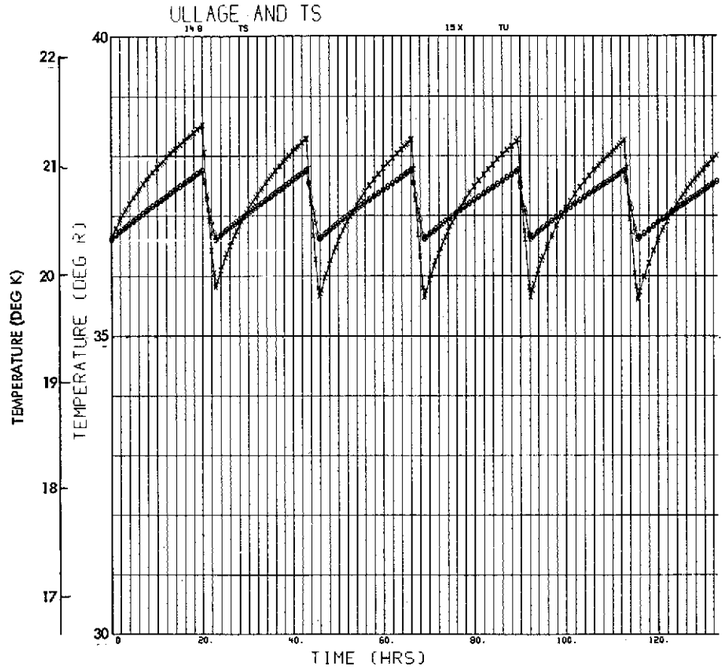

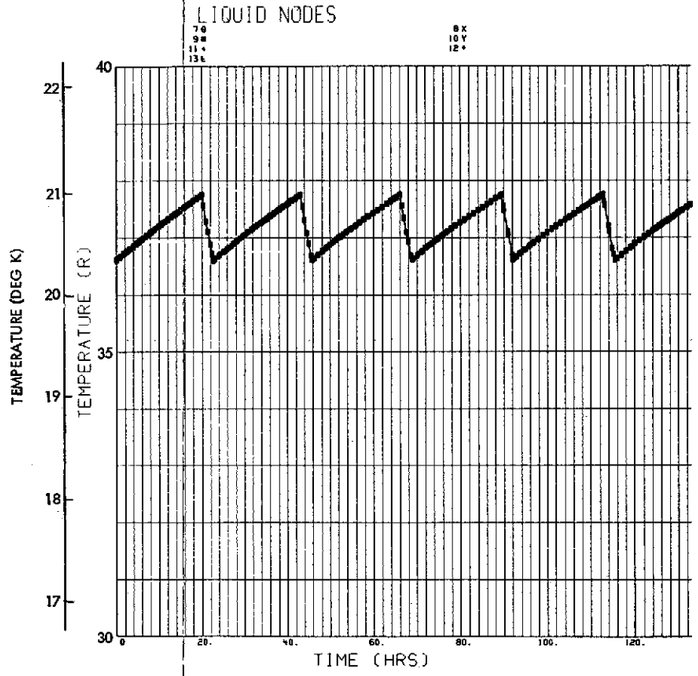

Fig. 3-18(f) $Q = 0.31\ w/m^2$, $R_{cw} = 0.88\ \frac{m^2 - {}^oK}{w}$

Fig. 3-18 Pressure and Temperature Characteristics in LH_2 – Conduction Model, Tank Dia. = 1.2 m (4 Ft), L/D = 1, Ullage Volume = 90%

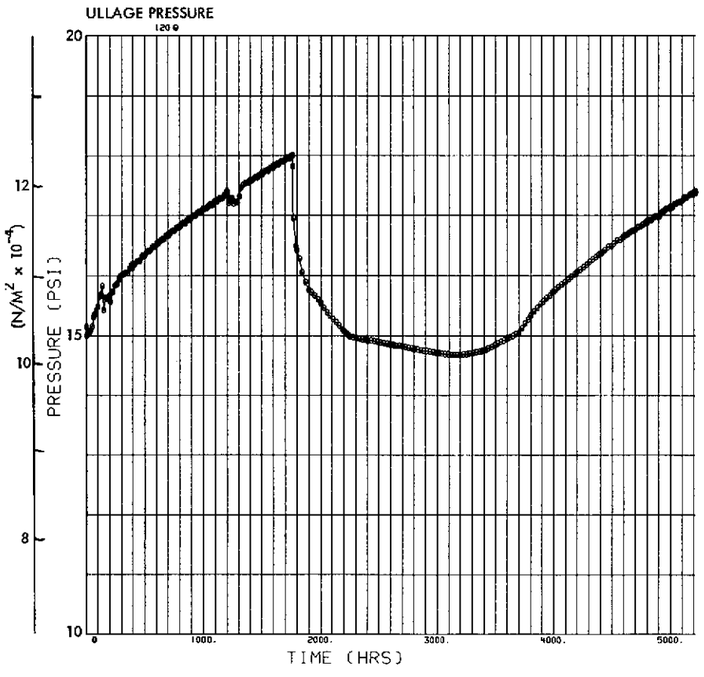

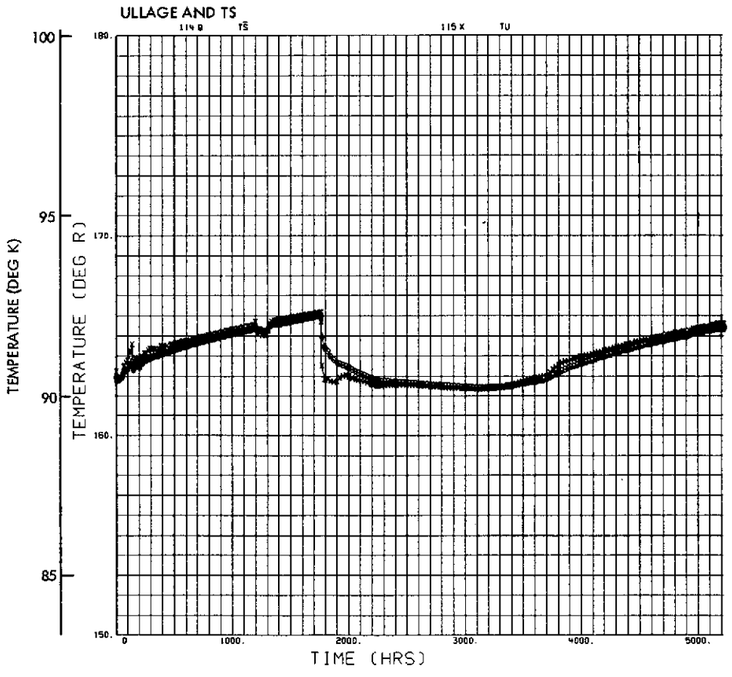

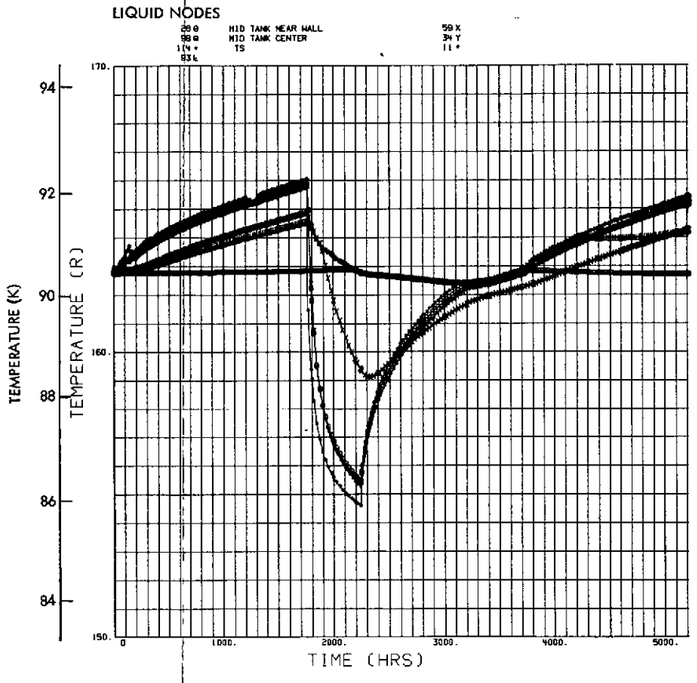

Fig. 3-19 Pressure and Temperature Characteristics in LO_2 – Conduction Model, Tank Dia = 6.9m (22.5 Ft); L/D = 4.0; Ullage Volume = 5%; Heat Flux = 0.31 w/m^2 (0.1 Btu/hr-ft^2) R_{cw} = 0.88 m^2-°K/w (5 ft^2-hr/Btu)

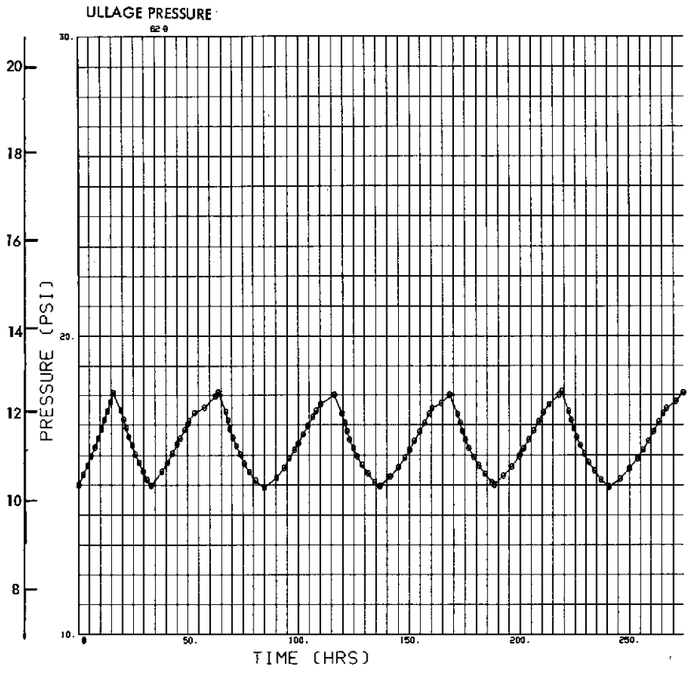

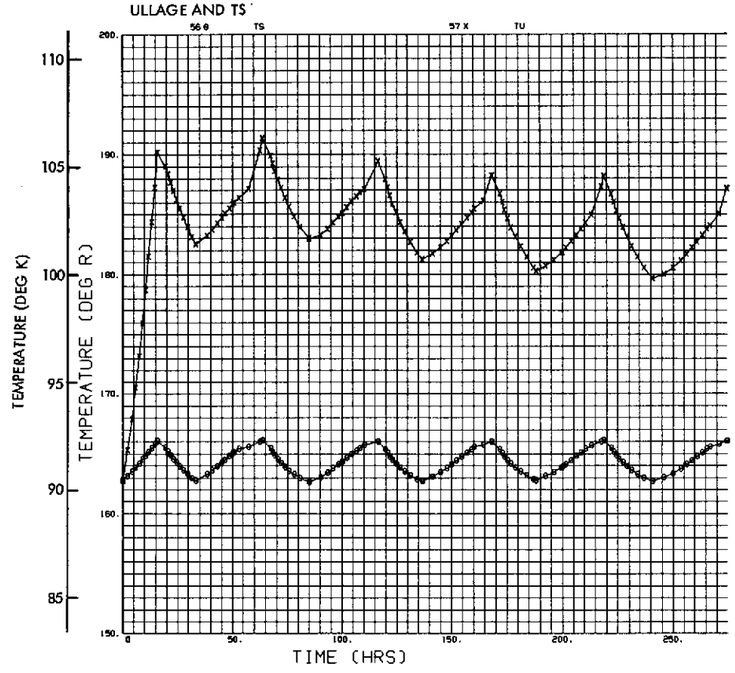

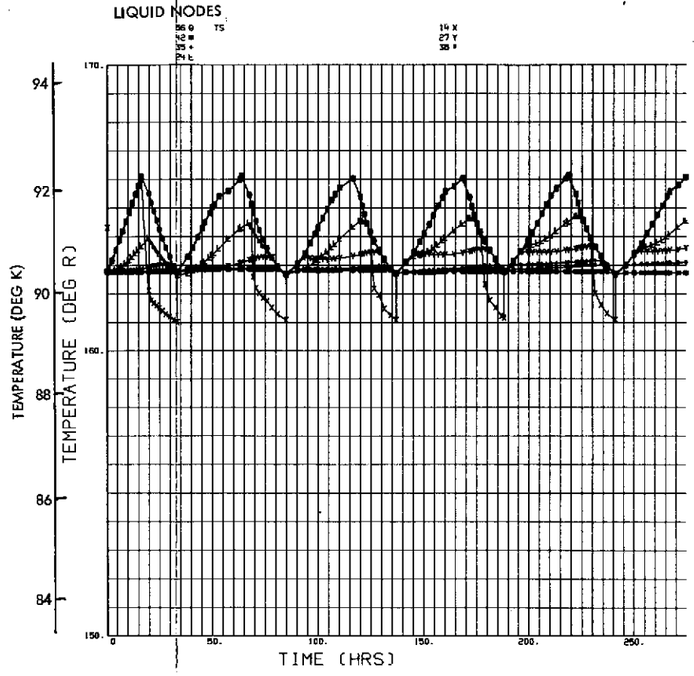

Fig. 3-20 Pressure and Temperature Characteristics in LO_2 – Conduction Model; Tank Dia = 6.9m; Ullage Volume = 90%; L/D = 4.0; Heat Flux = 3.1 w/m^2; R_{cw} = 0.88 m^2-$^oK/w$

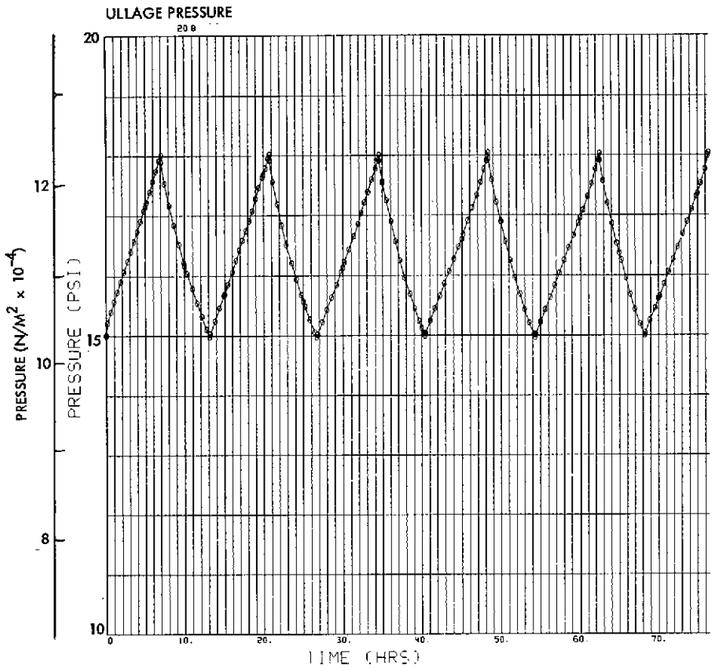

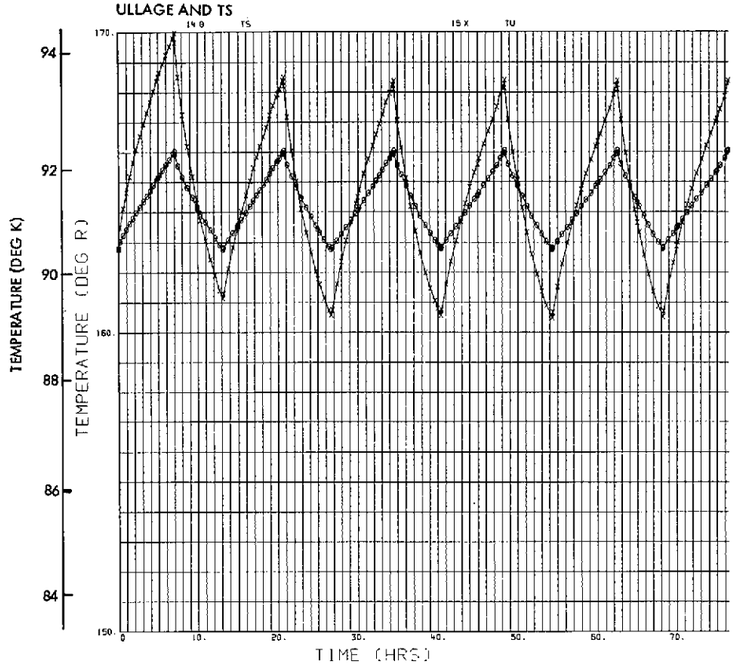

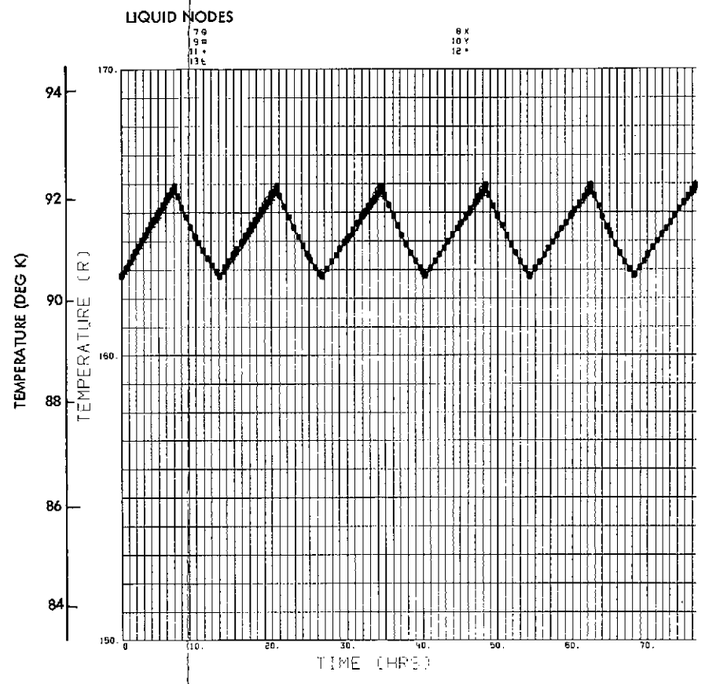

Fig. 3-21 Pressure and Temperature Characteristics in LO_2 – Conduction Model; Tank Dia = 1.2m (4 ft); L/D = 1.0; Ullage Volume = 90%; Heat Flux = 3.1 w/m^2 (1 Btu/hr-ft^2) R_{cw} = 0.88 m^2-°K/w (5 ft^2-°K/Btu)

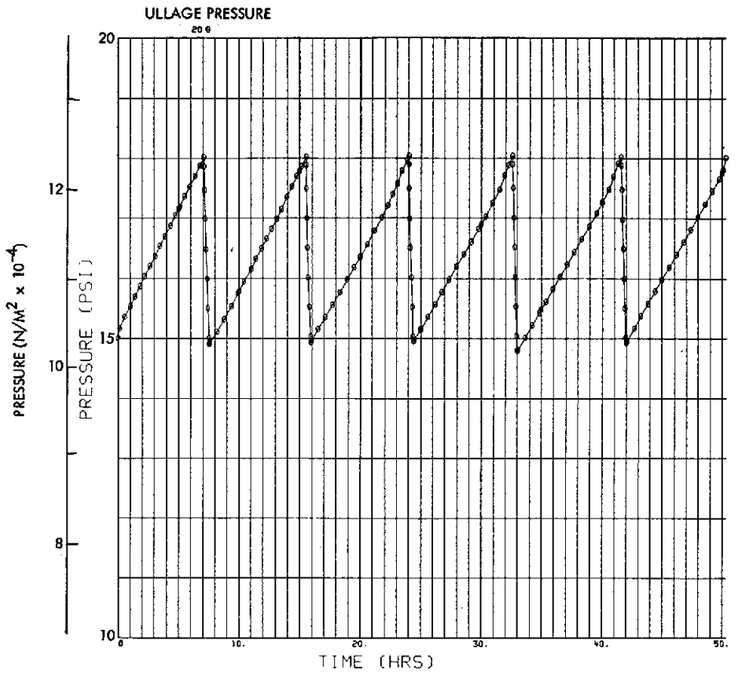

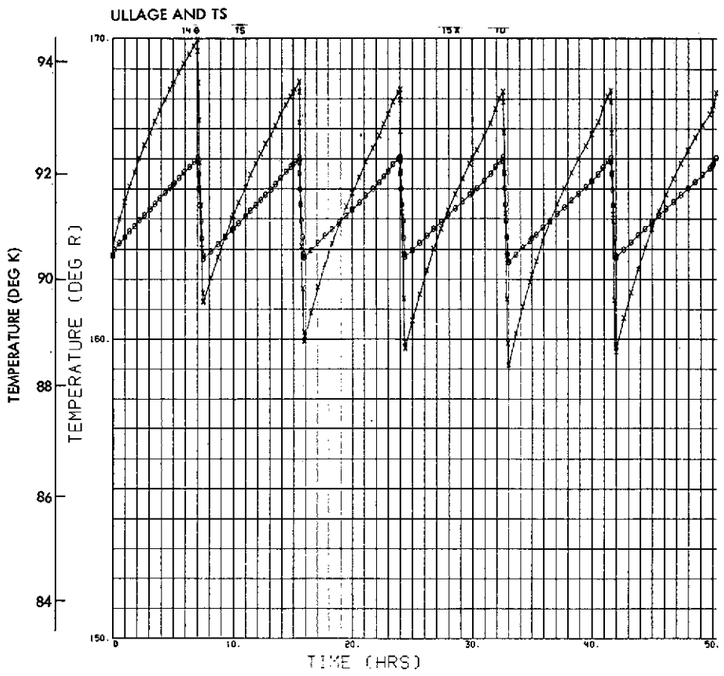

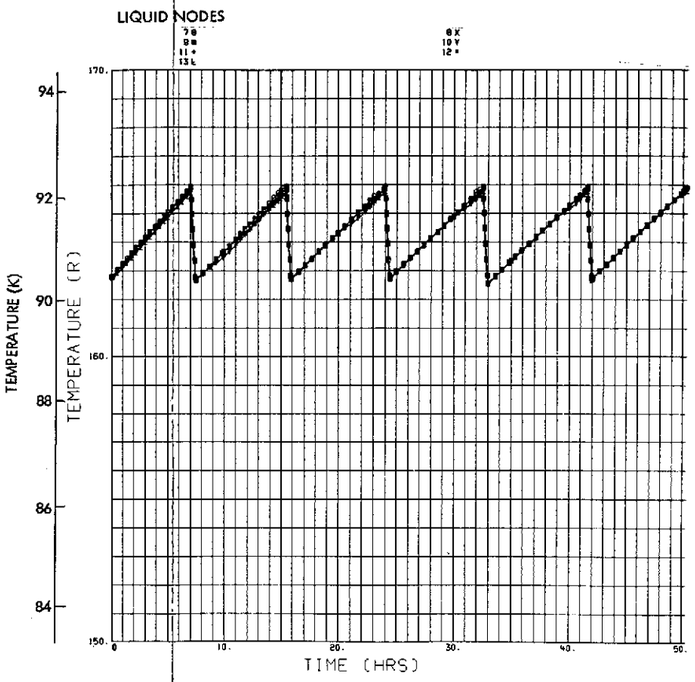

Fig. 3-22 Pressure and Temperature Characteristics in LO_2 – Conduction Model, Spherical Tank Dia = 1.2m (4 Ft), Ullage Volume = 90%, Q = 3.1 w/m^2 (1 Btu/Hr-Ft^2), R_{cw} = $0.088 \frac{m^2\text{-}^oK}{w}\left(0.5 \frac{Hr\text{-}Ft^2\text{-}^oR}{Btu}\right)$

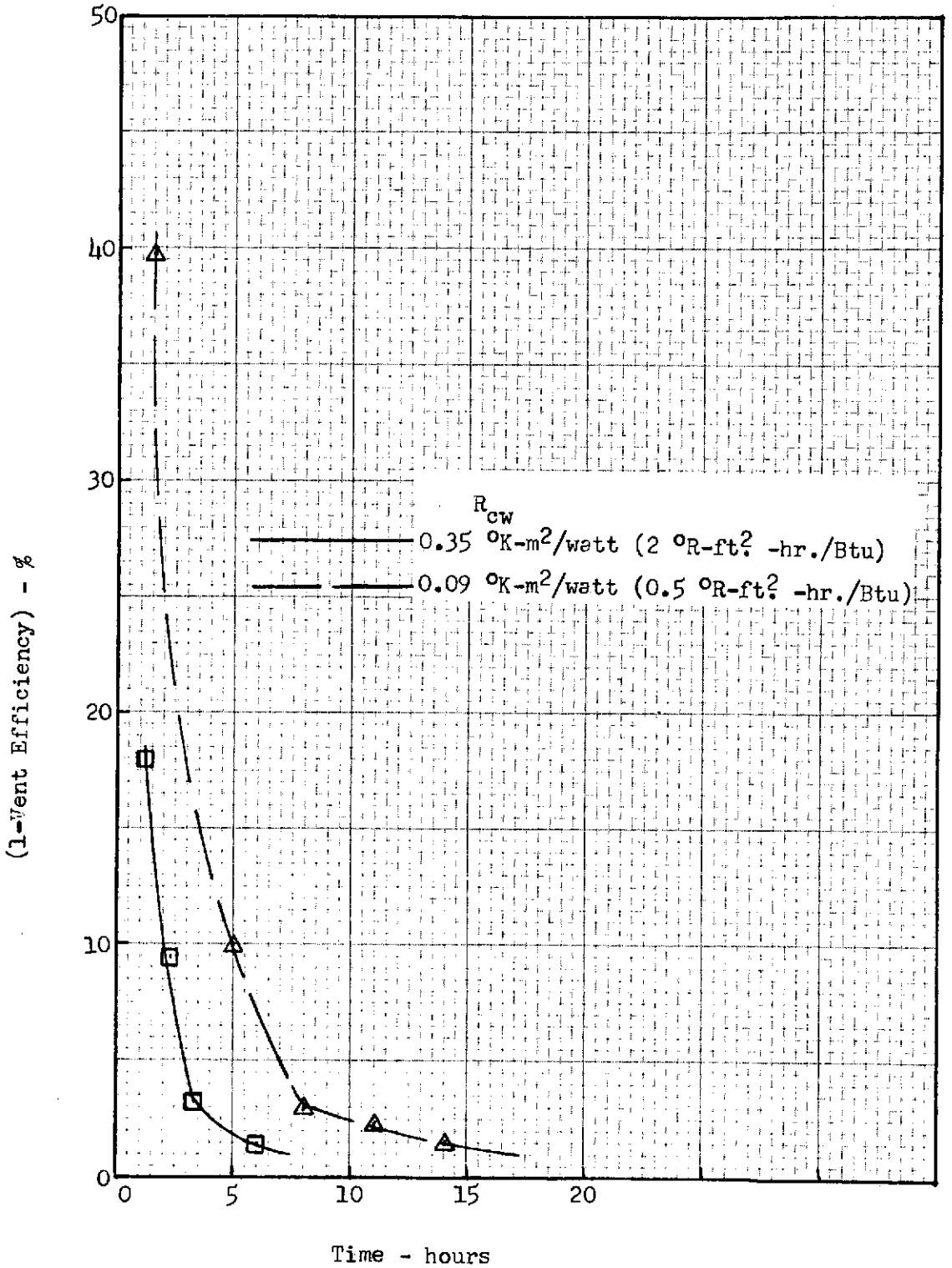

Figure 3-23 Vent Inefficiency vs. Time - Heat Flux = 3.1 w/m^2 (1 Btu/hr.-ft^2)

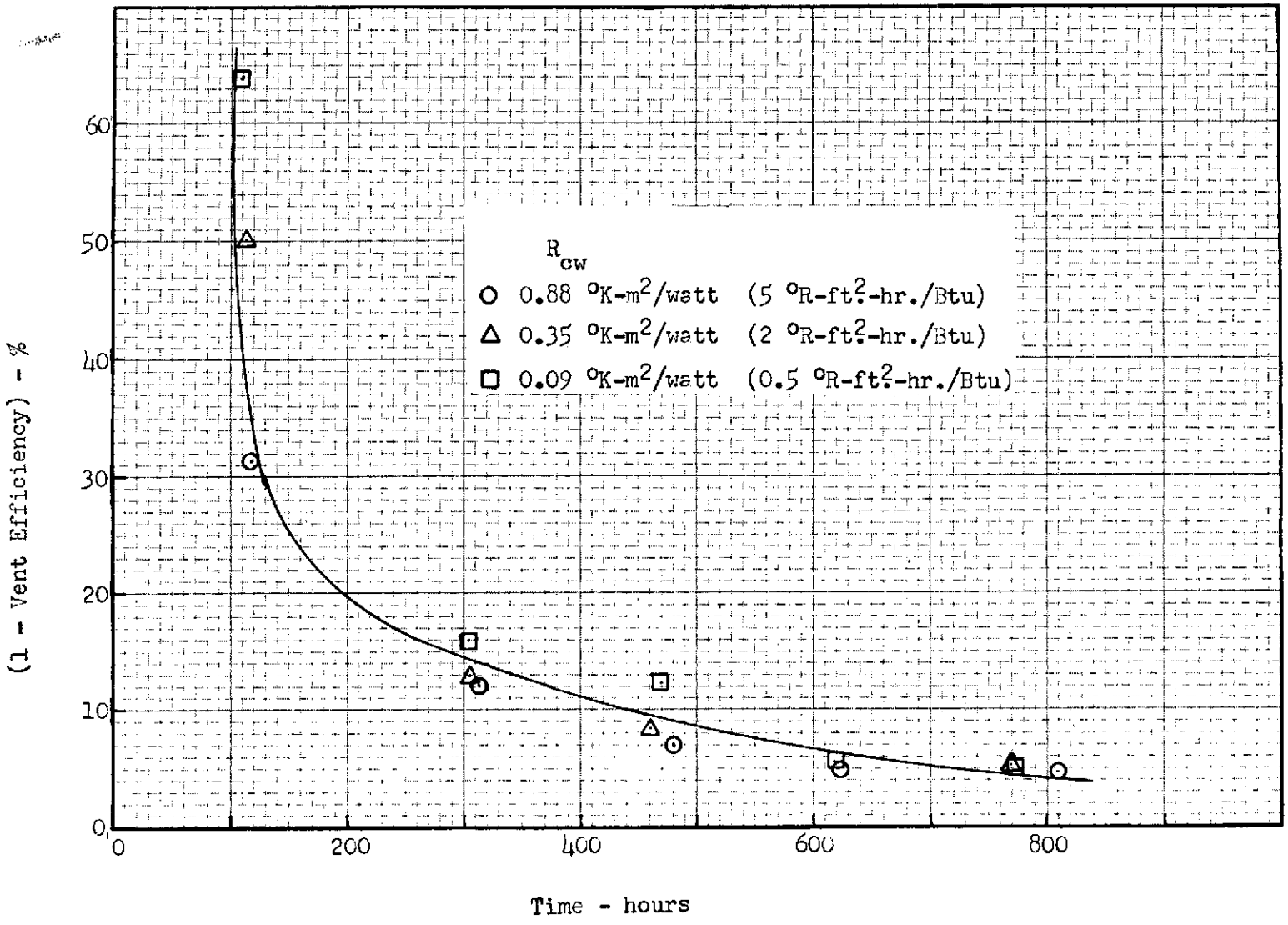

Figure 3-24 Vent Inefficiency vs. Time - Heat Flux = 0.31 w/m^2 (0.1 Btu/hr.-ft^2)

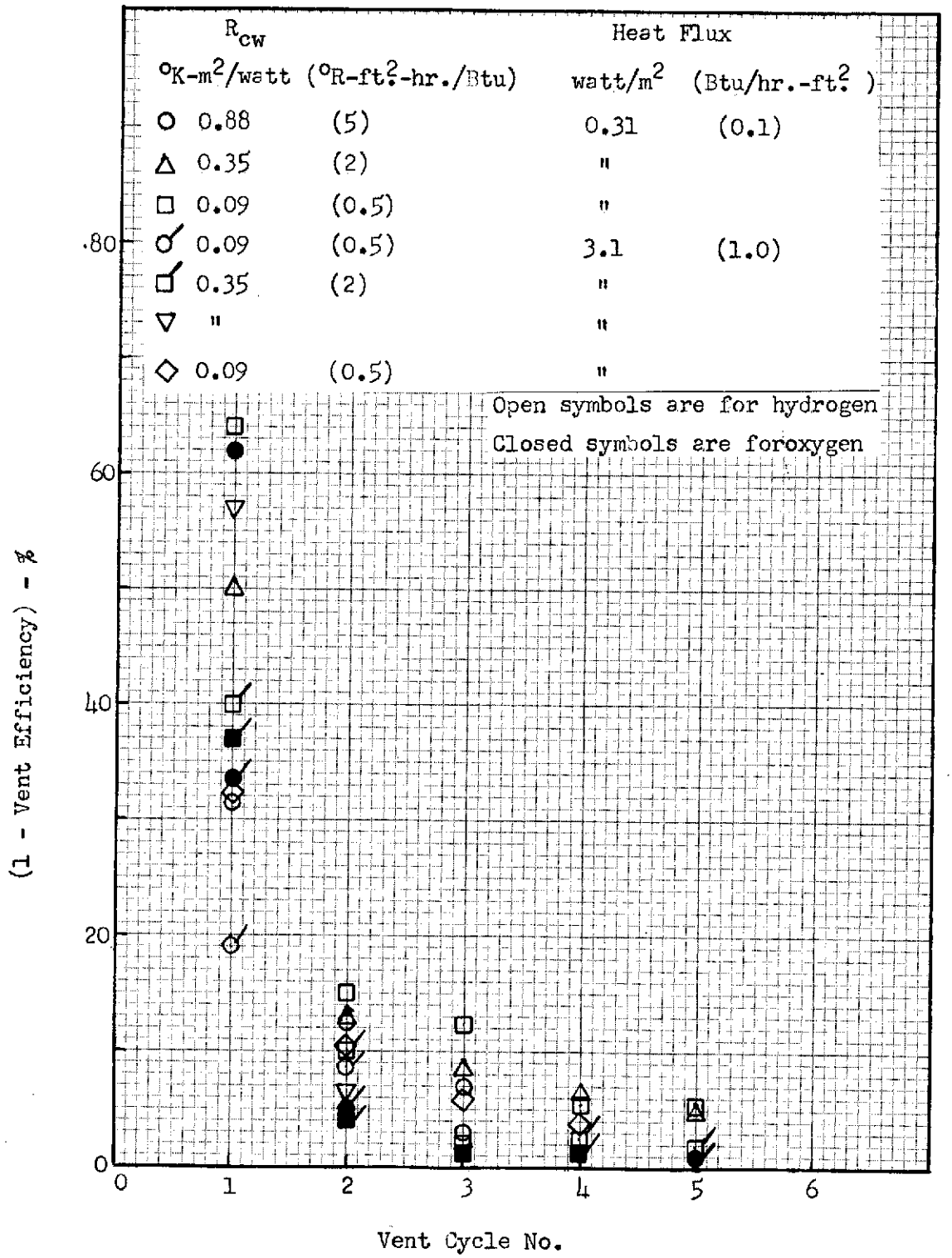

Figure 3-25 Vent Inefficiency vs. Vent Cycle Number

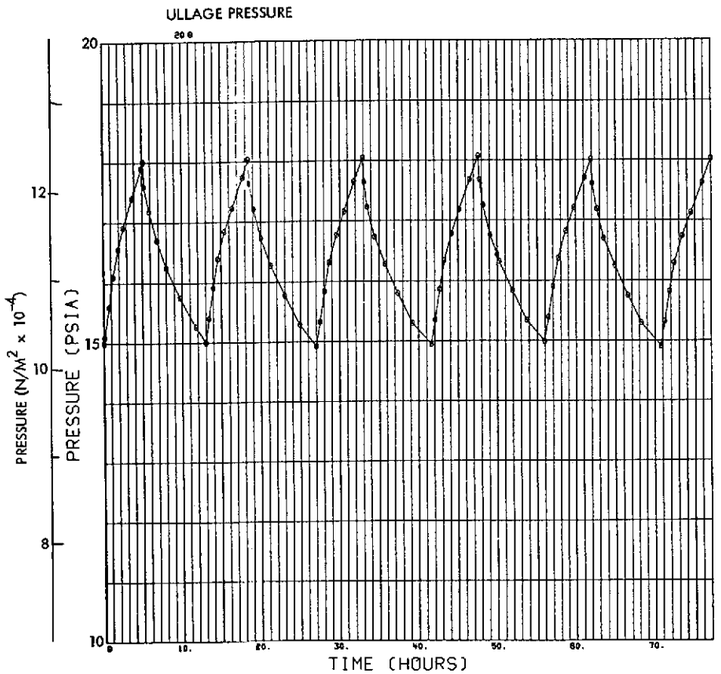

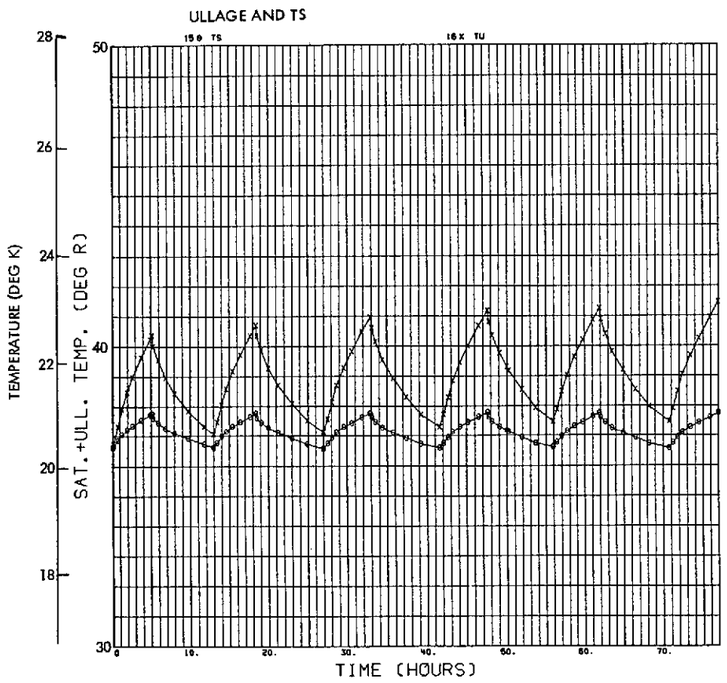

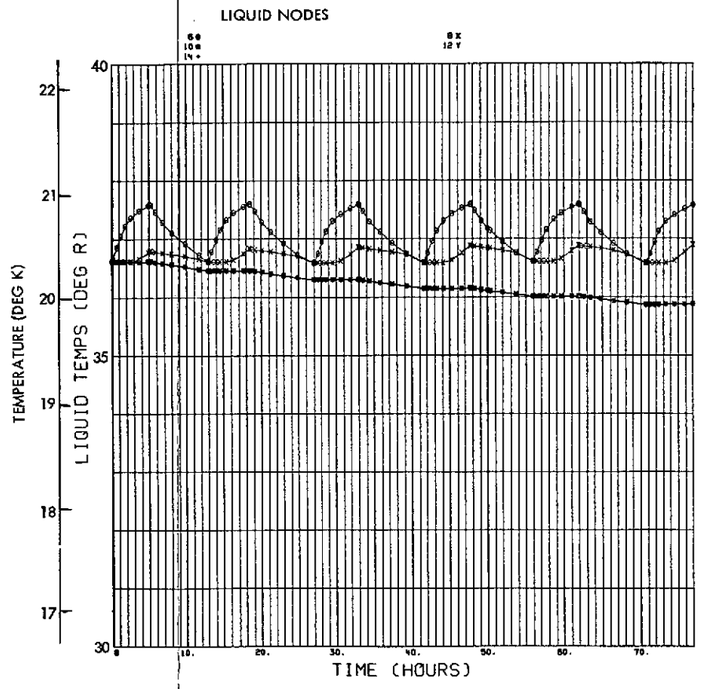

Fig. 3-26 Pressure and Temperature Characteristics in LH_2 at 10^{-6} g's – Convection Model, Tank Dia. = 6.86 m (22.5 Ft), L/D = 4, Ullage Volume = 5%, Q = 3.1 w/m^2 (1 Btu/Hr-Ft^2) $R_{cw} = 0.088 \frac{m^2\text{-}^oK}{w} \left(\frac{0.5\ Hr\text{-}Ft^2\text{-}^oR}{Btu}\right)$

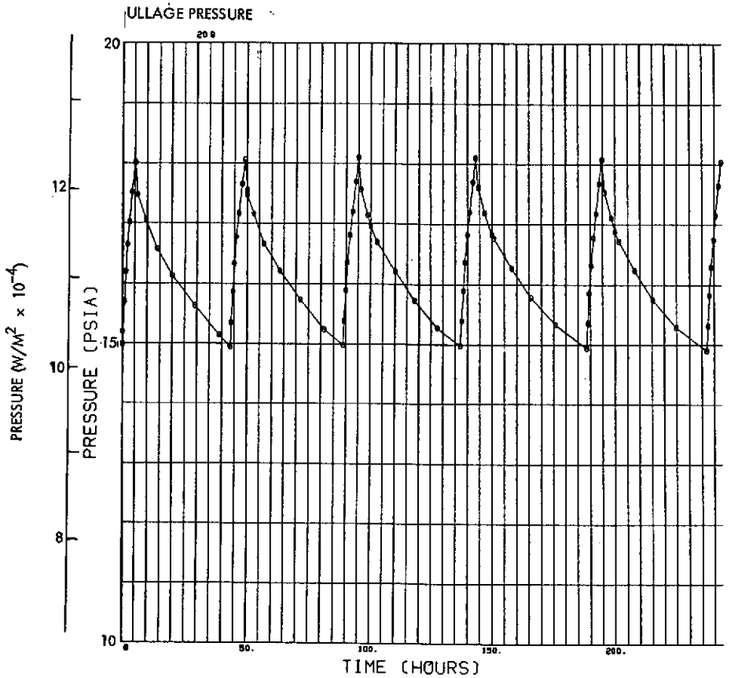

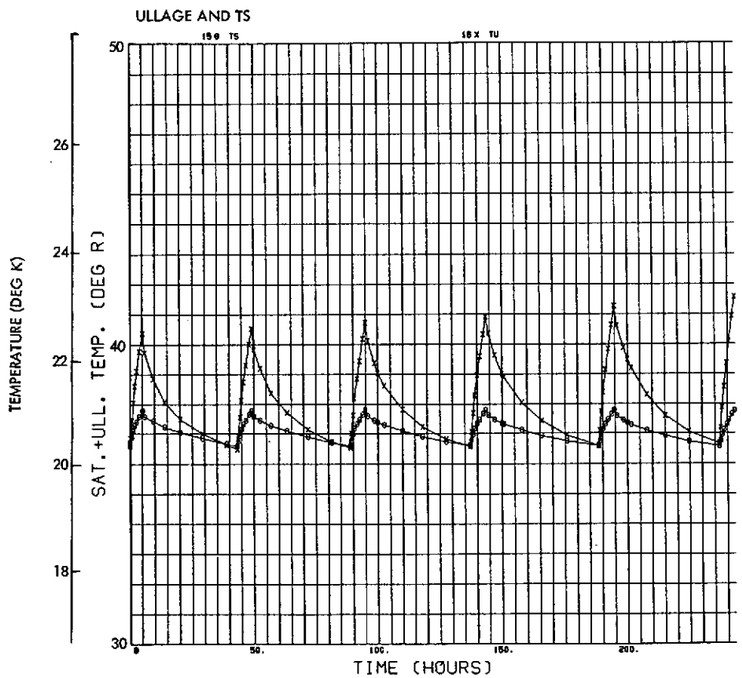

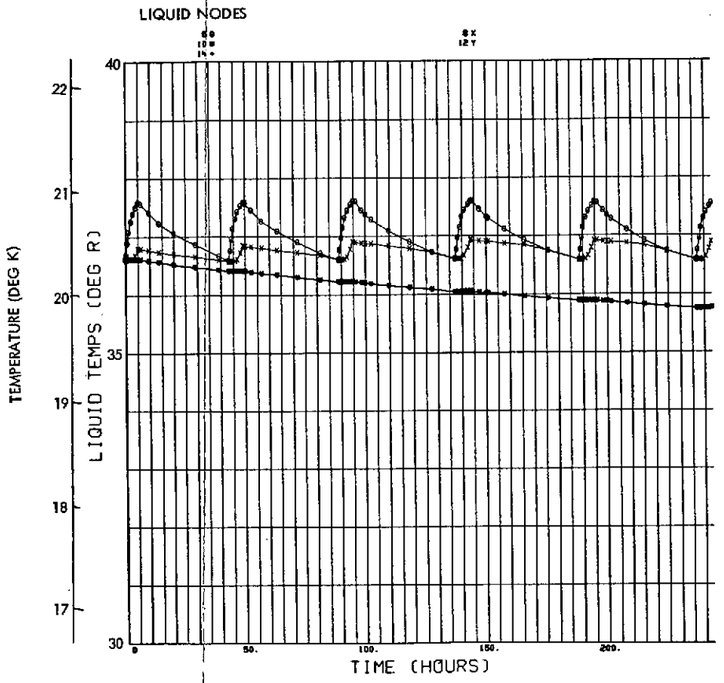

Fig. 3-27 Pressure and Temperature Characteristics in LH_2 at 10^{-6} g's – Convection Model, Tank Dia. = 6.86 m (22.5 Ft), L/D = 4, Ullage Volume = 5%, Q = 3.1 w/m^2 (1 Btu/Hr-Ft^2), R_{cw} = 0.35 $\frac{m^2\text{-}^oK}{w}$ $\left(2\ \frac{Hr\text{-}Ft^2\text{-}^oR}{Btu}\right)$

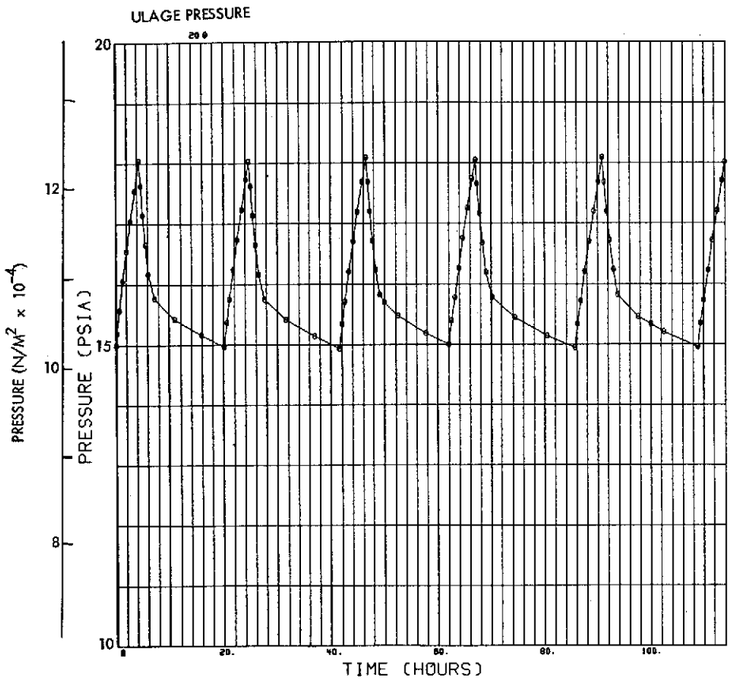

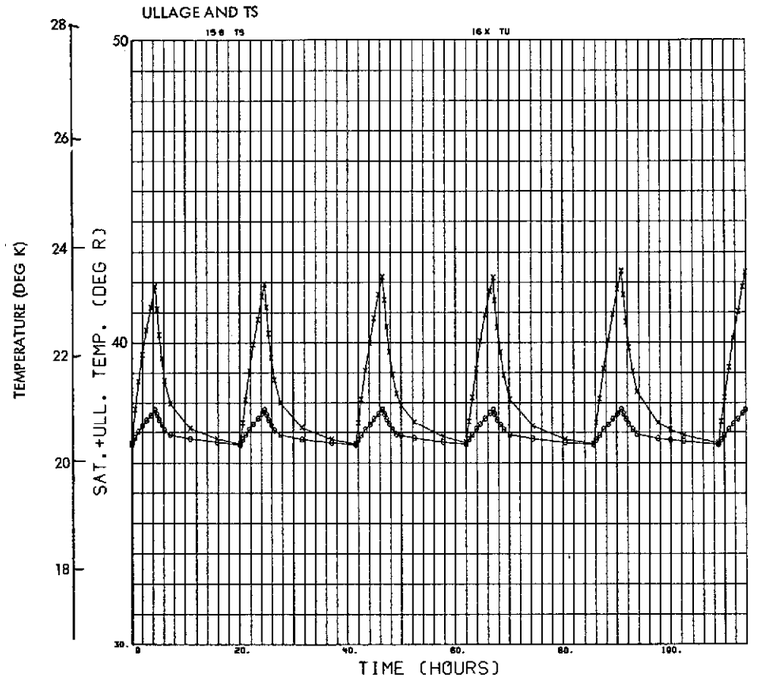

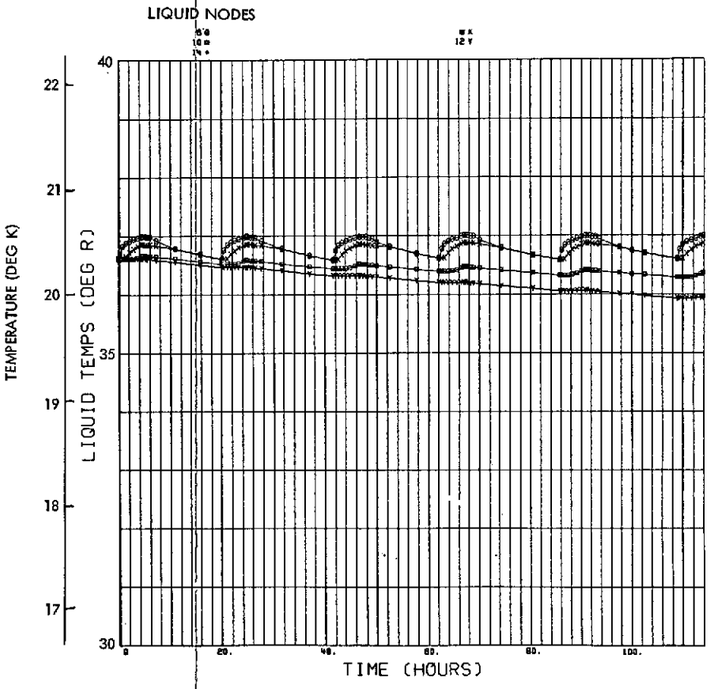

Fig. 3-28 Pressure and Temperature Characteristics in LH_2 at 10^{-4} g's – Convection Model, Tank Dia. = 6.86 m (22.5 Ft), L/D = 4, Ullage Volume = 5%, Q = 3.1 w/m^2 $1\left(\frac{1\ Btu}{Hr\text{-}Ft^2\text{-}^oR}\right)$ R_{cw} = 0.35 $\frac{m^2\text{-}^oK}{w}$ $2\left(\frac{Hr\text{-}Ft^2\text{-}^oR}{Btu}\right)$

FOLDOUT FRAME 1

FOLDOUT FRAME 2

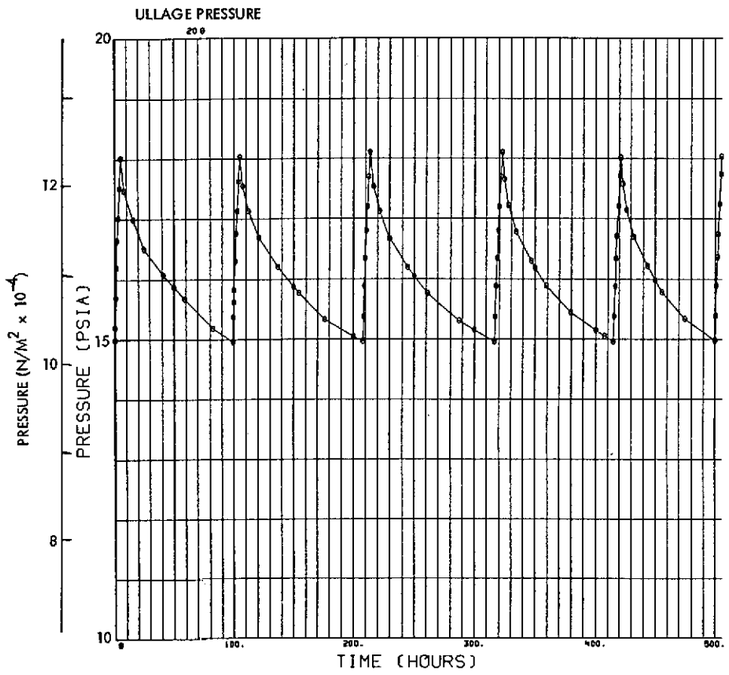

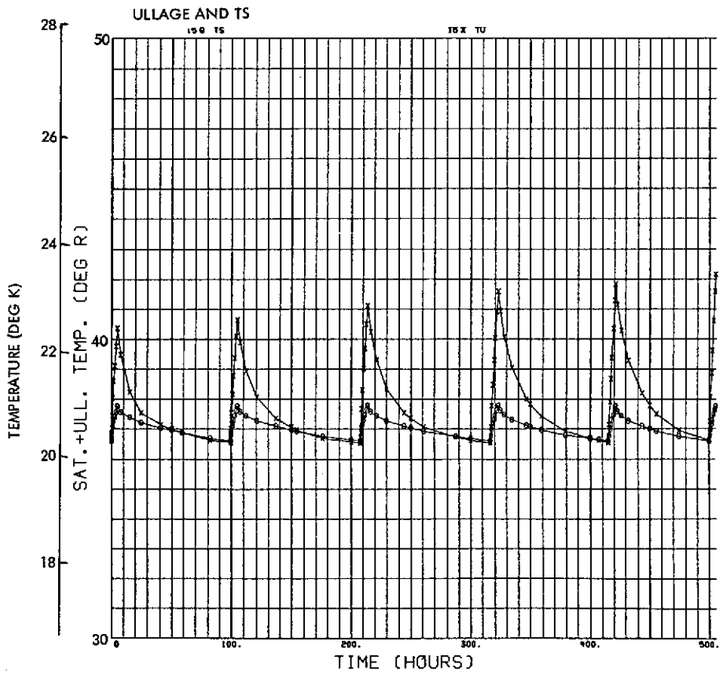

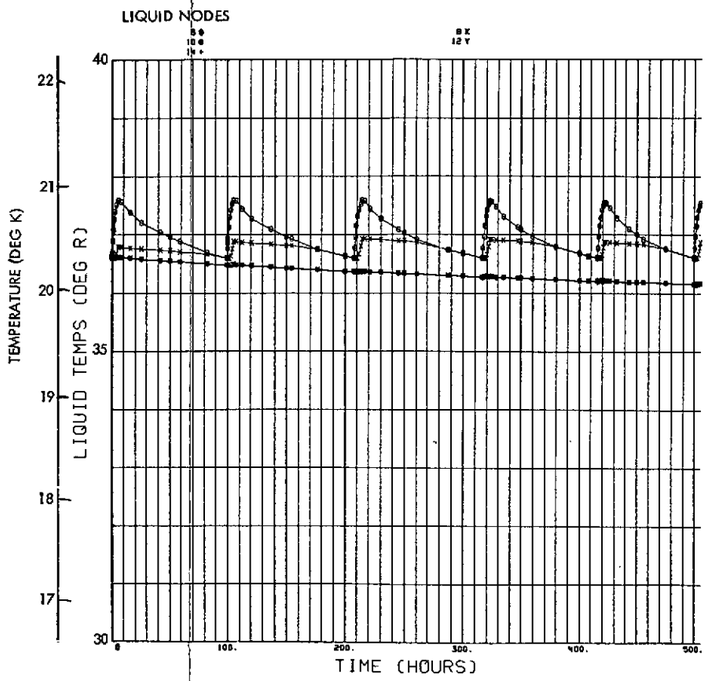

Fig. 3-29 Pressure and Temperature Characteristics in LH_2 at 10^{-6} g's, – Convection Model, Tank Dia. = 6.86 m (22.5 Ft), L/D = 4, Ullage Volume = 5%, Q = 3.1 w/m^2 (1 Btu/Hr-Ft^2), $R_{cw} = 0.53 \frac{m^2\text{-}^oK}{w}, \quad 3\left(\frac{Hr\text{-}Ft^2\text{-}^oR}{Btu}\right)$

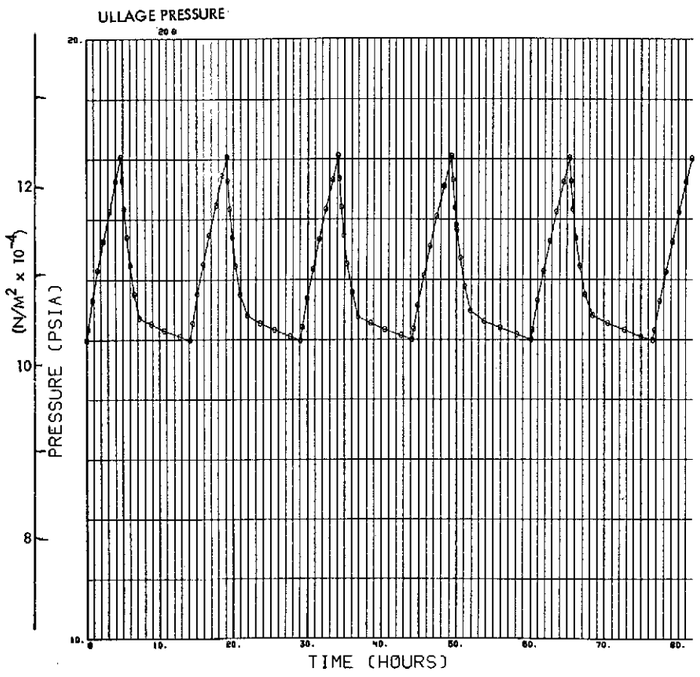

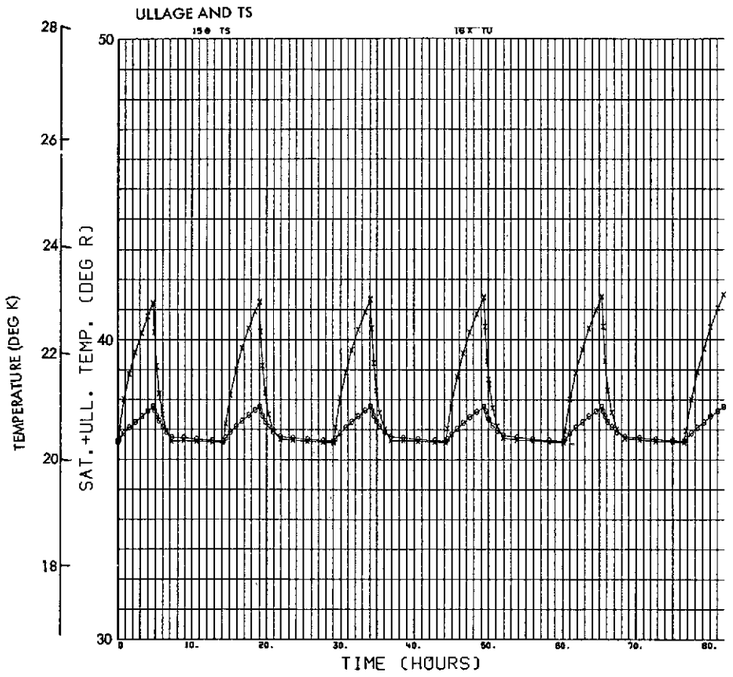

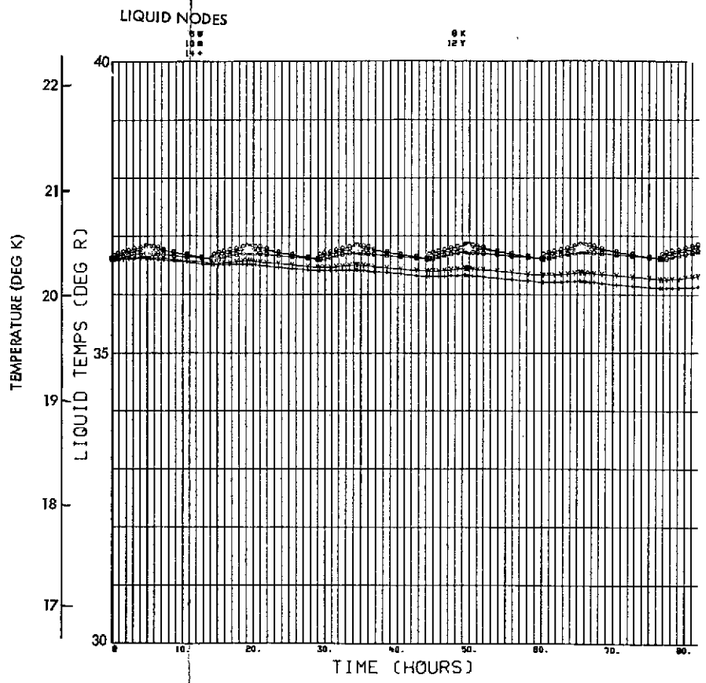

Fig. 3-30 Pressure and Temperature Characteristics in LH_2 at 10^{-2} g's – Convection Model, Tank Dia. = 6.86 m (22.5 Ft), L/D = 4, Ullage Volume = 5%, Q = 3.1 w/m^2 $\left(\frac{1\ Btu}{Hr\text{-}Ft^2}\right)$, $R_{cw} = 0.35\ \frac{m^2\text{-}^oK}{w}\ \left(2\ \frac{Hr\text{-}Ft^2\text{-}^oR}{Btu}\right)$

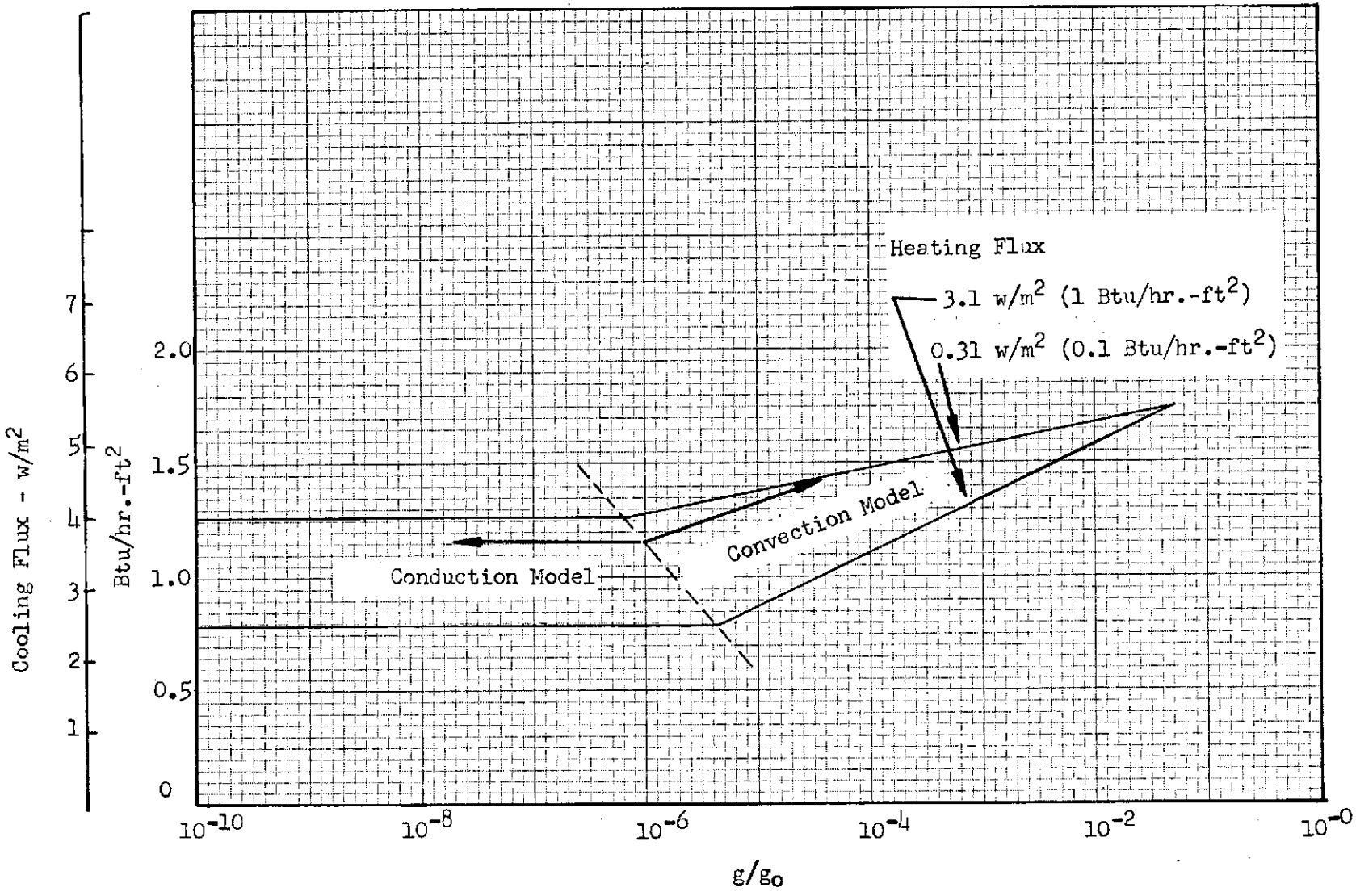

Figure 3-31 Effect of Gravity on Cooling Rate For a Fixed Heat Exchanger Resistance (Tank Size = 22.5 x 90 Ft., R_{cw} = 2.0)

3.5 HEAT EXCHANGER DESIGN MODEL

The conduction and convection models are basically performance analysis tools that describe the processes in the tank fluids for a given heat exchanger parameter (R_{cw}). R_{cw} is the thermal resistance between the tank wall and the vent fluid in the heat exchanger as illustrated on the sketch below.

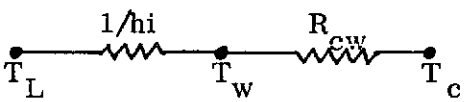

The heat exchanger geometry (tube spacing and diameter) must be derived from considerations of conduction in the tank wall and the pressure drop in the coolant tubes.

To be effective, any thermodynamic vent system must be designed to avoid excessive local heat transfer which might vaporize all of the refrigerant and inhibit effective cooling and depressurization of the ullage. With an active system, such as that developed in contracts NAS 3-7942 and NAS 3-12033, this is accomplished with use of a mixer in the propellant. For the tank wall exchanger the tubes will be attached to the tank wall at discreet points to provide uniform heat extraction over the tank surface. This divides the tank wall into a large number of fins. Heat is convected or conducted into the tank wall and then conducted radially to the attachment point. The heat to each attachment is given by:

$$Q_p = 2\pi kt \; (a\sqrt{\beta}) \frac{K_1(a\sqrt{\beta})}{K_0(a\sqrt{\beta})} \; (T_c - T_L)$$

The total heat rate is:

$$Q_T = NQ_P = (hA_s \eta) \; (T_c - T_L)$$

These equations are used to define an effectiveness which is:

$$\eta = \frac{N}{A_s} \frac{2\pi kt \; (a\sqrt{\beta}) \dfrac{K_1(a\sqrt{\beta})}{K_0(a\sqrt{\beta})}}{h} = \frac{N}{A_w} \; 2\pi \; \frac{K_1(a\sqrt{\beta})}{K_0(a\sqrt{\beta})} \Big/ (a\sqrt{\beta})$$

It can be shown that the Bessel function component of the above expression for the range of g levels and tank thicknesses of interest in this study is relatively constant at 0.5; i.e.,

$$\frac{K_1 (a\sqrt{\beta})}{K_0 (a\sqrt{B})} \Big/ (a\sqrt{\beta}) = 0.5 \text{ for } a\sqrt{\beta} < 0.7$$

If the attachment spacing, S , is small compared to the basic dimension of the tank wall, then one can approximate the tank surface area as NS^2 . Making this approximation the effectiveness for the externally mounted heat exchanger thus reduces to:

$$\eta_1 = (a/S)^2 \times \pi$$

For an internal heat exchanger heat will be transferred to the wall and also directly to the tubes. If it is assumed that there is no synergistic effects, and assuming that the tube dimension and tank attachment radius are the same, the effectiveness for an internal exchanger becomes:

$$\eta_2 = \eta_1 + 2\pi (a/S)$$

Figure 3-32 gives a graphical comparison of these two mounting arrangements. It indicates that on a theoretical basis, the internal mounting results in fewer tube attachments for a given effectiveness. Operationally, however, this concept is susceptible to failures if a leak develops. On Contract NAS 3-12033 leaks developed between the expansion unit and the heat exchanger which resulted in by passing the former and eliminating the temperature difference needed for the exchanger to operate. The tank pressure could not be controlled when that happened. In contrast, a leak in the external system will result in local degradation of the insulation system but will allow a mission to proceed at a reduced capability.

The difference between the internal and external effectiveness indicates that most of the heat is transferred directly to the tubes rather than to the tank wall. This tends to

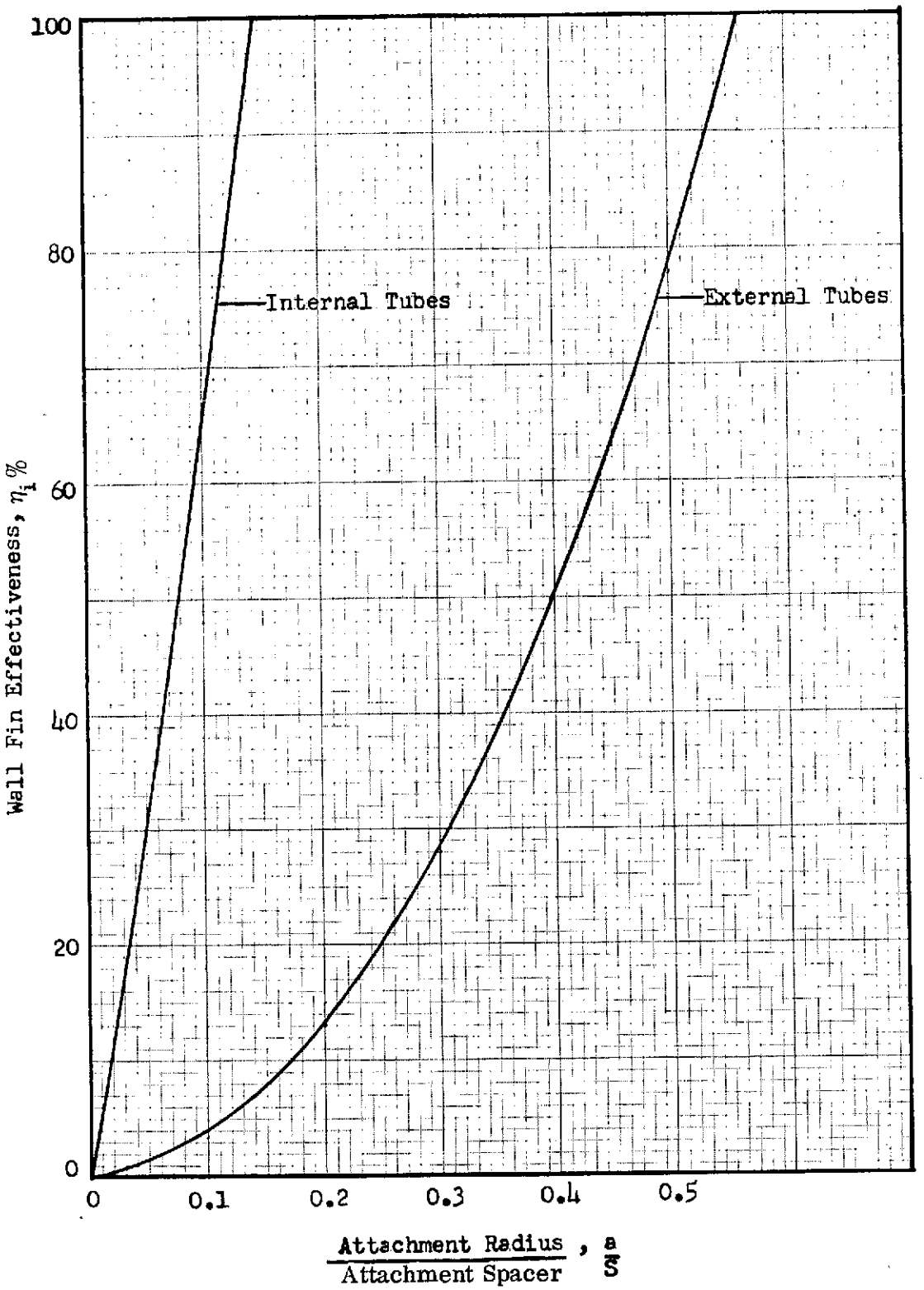

Figure 3-32 Effect of Tube Spacing on Tank Wall Fin Effectiveness

negate the purpose of the discreet point attachment concept for assuring uniform energy extraction.

Figure 3-32 provides a relationship between wall fin effectiveness and the geometry ratio (a/S) . The effectiveness is also related to the wall resistance R_{cw} by:

$$\eta = 1 - \frac{R_{cw}\, q_L}{(T_L - T_c)}$$

The average cooling flux, q_L , and temperatures were obtained from the computer results with the zero-gravity model, and the effectiveness computed with the above equation. Figure 3-33 shows the effectiveness obtained in this manner, using results for the 4 foot sphere and the large tank (22.5 x 90 feet). The indicated band represents scatter in the data from one pressure cycle to the other through the course of mission history. Figure 3-34 is a cross plot from Figures 3-32 and 3-33 to relate R_{cw} to the tube radius to spacing ratio.

It might be noted that the intercept ($0, R_{cw}$,) on Figure 3-33 corresponds to a heat flux conducted to the coolant that just equals the imposed heat flux from external environment. Therefore, any design resistance greater than the intercept value would result in a net heat into the propellant, even during the cooling portion of a pressure cycle. There would be a concomitant inability to control the tank pressure. This, indeed, was the case when the imposed heat flux was 1 Btu/hr-ft^2 and the value of R_{cw} was 5^{o}R-ft^2-hr/Btu for the hydrogen tanks.

R_{cw} is increased by increasing the spacing between attachments. Consequently, the number of tube coils and tube weight decrease with increasing R_{cw}, which indicates the desirability of operating near the intercept value and the attendant continuous venting mode.

In reality, continuous operation is impractical with a passive system because it does not provide any flexibility to accommodate changes in the environmental heating. For example, if a system is designed to maintain continuous, constant pressure with a

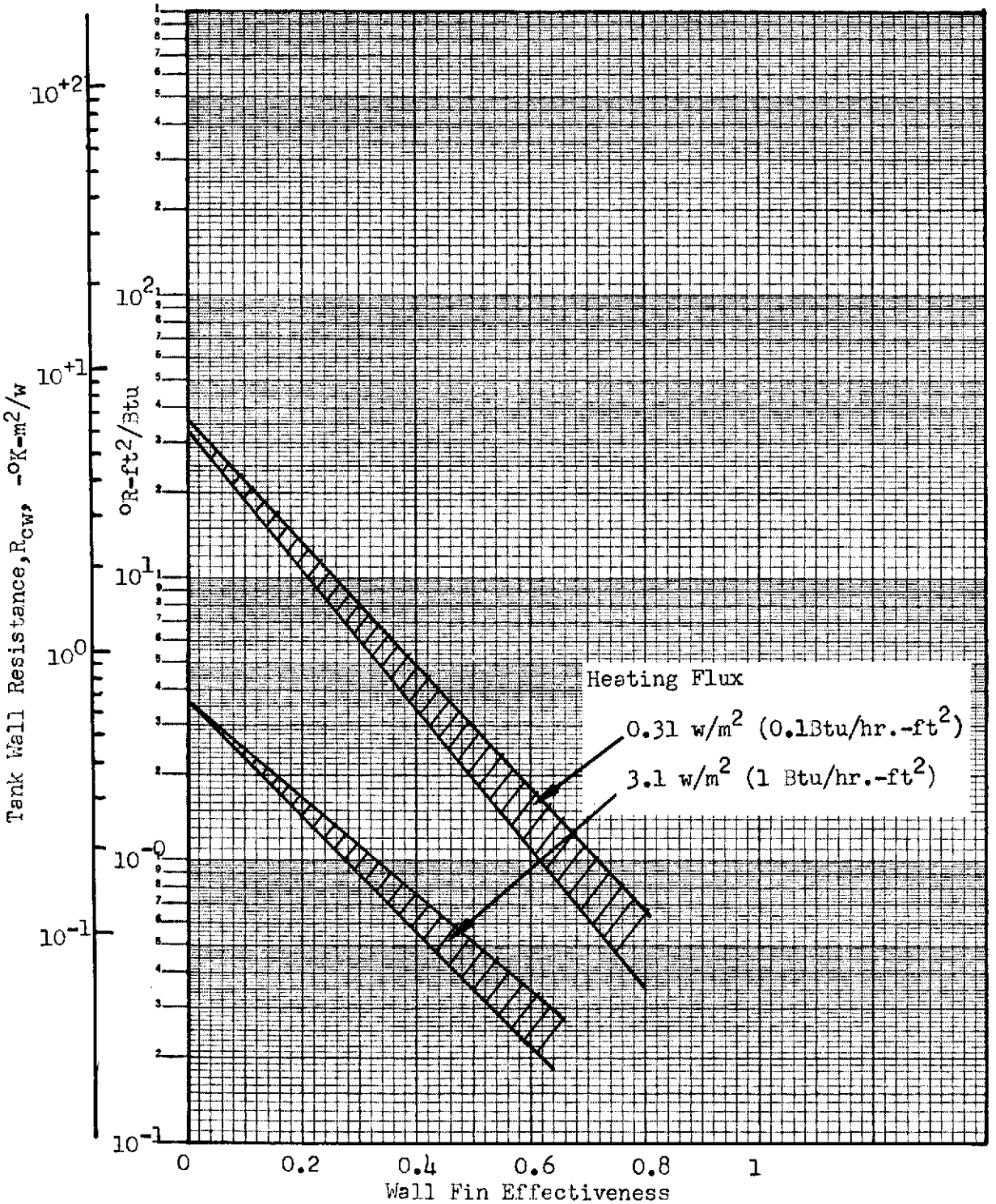

Figure 3-33 Correlation Between Heat Exchanger Design Resistance and Wall Fin Effectiveness

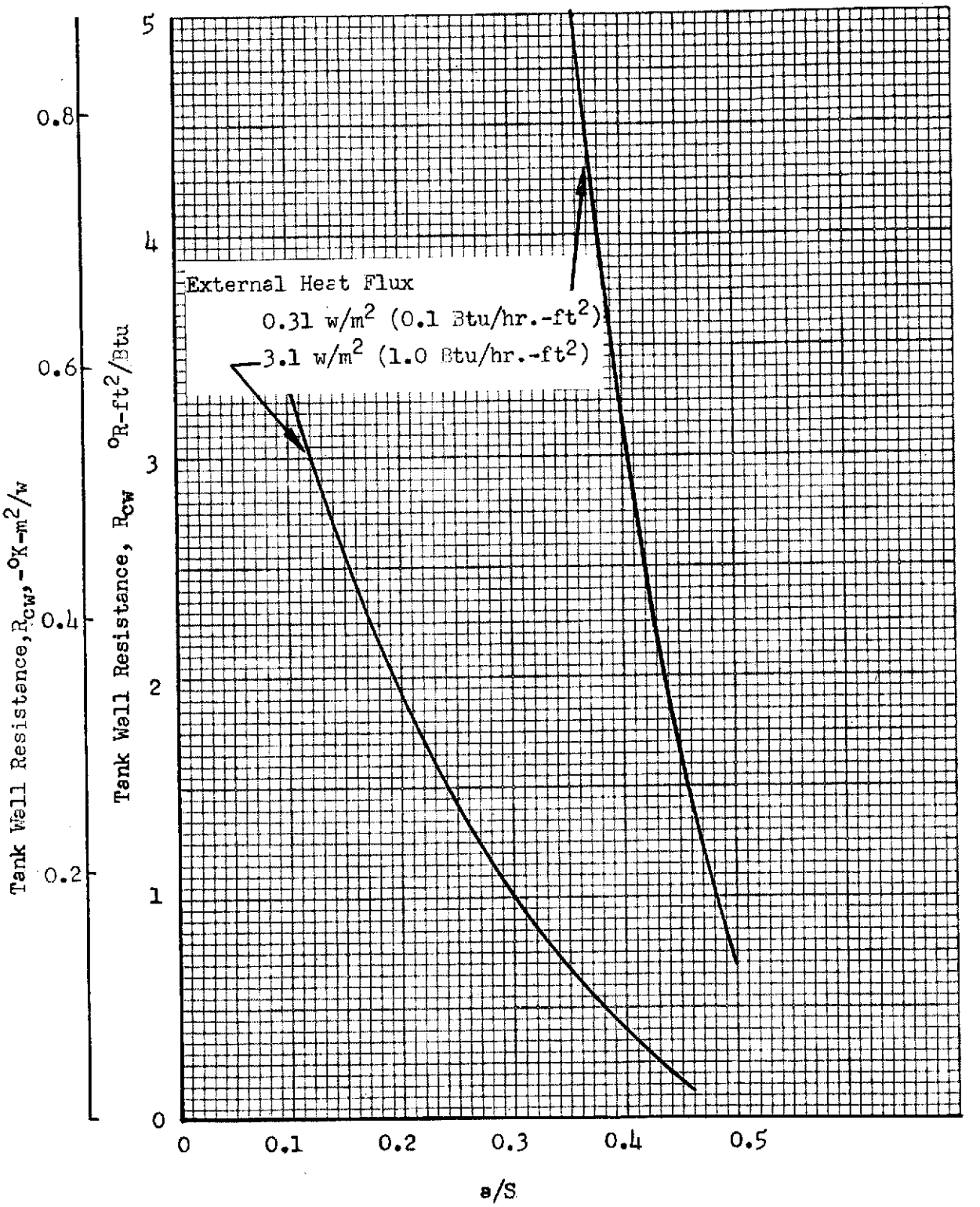

Figure 3-34 Effect of Attachment Radius to Spacing Ratio on Tank Wall Resistance – External Tubes

nominal heat flux, it will lose control if the actual heating during any portion of the mission is higher than the nominal value. Consequently, one will design for continuous operation at the highest potential heat flux and except intermittant operation at nominal anticipated values.

Another consideration in selecting a design is the practical limitation of other components in the thermodynamic vent system (i.e., expansion unit and flow control values). During the conduct of NAS 3-7942 it was estimated that design flow rates below 1 pound per hour were not realistic from the standpoint of automatic operation. To flow continuously at this rate corresponds to an effective heat rate of 190 Btu/hr. Thus, for an actual heating flux of 3.15 w/m^2 (1 Btu/hr-ft^2), continuous venting would be practical only for tanks having greater than 190 sq. feet of surface area. Conversely, continuous venting (effectively) of smaller tanks would be realistic only if the actual heating flux were greater than 3.15 w/m^2 . Figure 3-35 incorporates these considerations into a relationship between maximum R_{cw} and minimum tank surface area for which continuous operation might be feasible. For a given tank, the value of R_{cw} max obtained from Fig. 3-35 can be compared to the intercept value on Fig. 3-33 at the appropriate heat flux.

The smaller of the two values of R_{cw} is the appropriate design value. For example, the surface area of the 1.2 meter (4 ft) sphere is 4.7 m^2 (50 sq. feet). From Fig. 3-35 R_c max is 0.17. If the maximum anticipated heat flux is 3.15, then Fig. 3-33 gives an intercept value of 0.6 . Thus, R_{cw} = 0.17 is appropriate design value and the system would operate intermittently for a heat flux of 3.15 w/m^2 (1 Btu/hr-ft^2) .

Figure 3-34 provides the correlation between R_{cw} and a/S . The ratio between tube weight and tank membrane weight can be expressed as:

$$\frac{W_t}{W_s} = \frac{\rho_t \times 2\pi a S t_t}{\rho_x \times S^2 t_s} = 2\pi \frac{t_t}{t_s} \quad (a/S)\left(\frac{\rho_t}{\rho_x}\right)$$

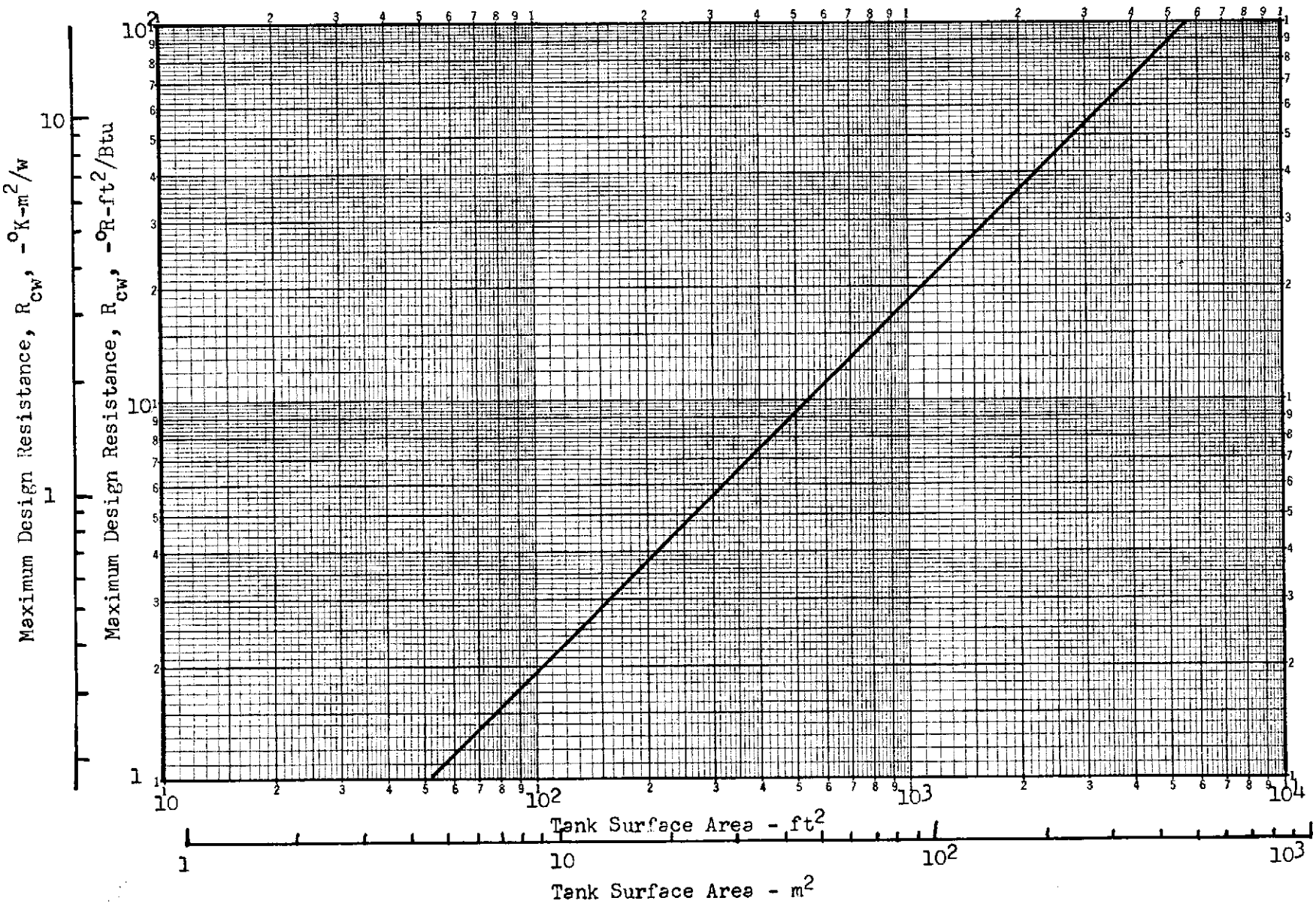

Figure 3-35 Relationship Between Minimum Tank Surface Area and Maximum R_{cw} For Continuous Operation

This weight ratio is shown in Fig. 3-36, for aluminum tubing on aluminum tanks. The magnitude of the heat exchanger tubing weight is given on Fig. 3-37 for specific tanks. The tube wall thickness used for Fig. 3-37 was 6 mils.

We must look to the pressure drop to actually size the tube. The pressure drop is comprised of three elements: That due to friction; due to gravity; and that due to acceleration when the fluid is being vaporized. The expression which describes the pressure drop from inlet to exit of the tube is derived in Appendix B. It is:

$$P_1 - P_2 = \int_0^L \left\{ \frac{\frac{f_1 G^2 v_1}{4 A g_c}\left[1 + X\left(\frac{v_g}{v_1} - 1\right)\right] + \frac{G^2 Ve}{g_c}\left(\frac{v_g}{v_1} - 1\right)\frac{dx}{d\ell} + \frac{g/g_c \sin\theta}{Ve\ 1 + X\ (v_g/v_1 - 1)}}{1 + X\ \frac{G^2}{g_c}\ \frac{dv_g}{dP}} \right\} d\ell$$

The solution can only be obtained by repeated iterations for specific mass fluxes and assumed geometries. However, the bracketed quantity in the denominator is the square of the Mach number in the vapor and must be less than 1 for a constant diameter tube to avoid choking. This fact can be used to estimate the absolute minimum tube size to be considered for a given tank. This would constitute a logical starting point for iteration on the complete solution in a very specific application.

Since the mass flux is the vent rate divided by the tube flow area, and the vent rate is determined by the thermal design parameters, one can derive the following expression for the tube radius.

$$\frac{a}{\sqrt{A_s}} = \left[\frac{(T_L - T_c)}{G\ \pi\ \lambda}\ \frac{(1 - \eta)}{R_{cw}}\right]^{1/2}$$

When G is large enough to choke at the exit, the tube radius is the minimum possible. The larger the pressure expansion between the tank and the heat exchanger inlet, the larger will be the temperature differential, but the smaller will be the possible pressure drop and mass flux. Assuming the expansion to 4 psi, which is the same as that

used for the active system in contract NAS 3-7942, one obtains the relationship between the normalized tube radius (normalized with tank surface area) and the tank wall design resistance that is shown on Fig. 3-38. For a given tank, the minimum tube spacing and radius can then be determined as shown on Figure 3-39.

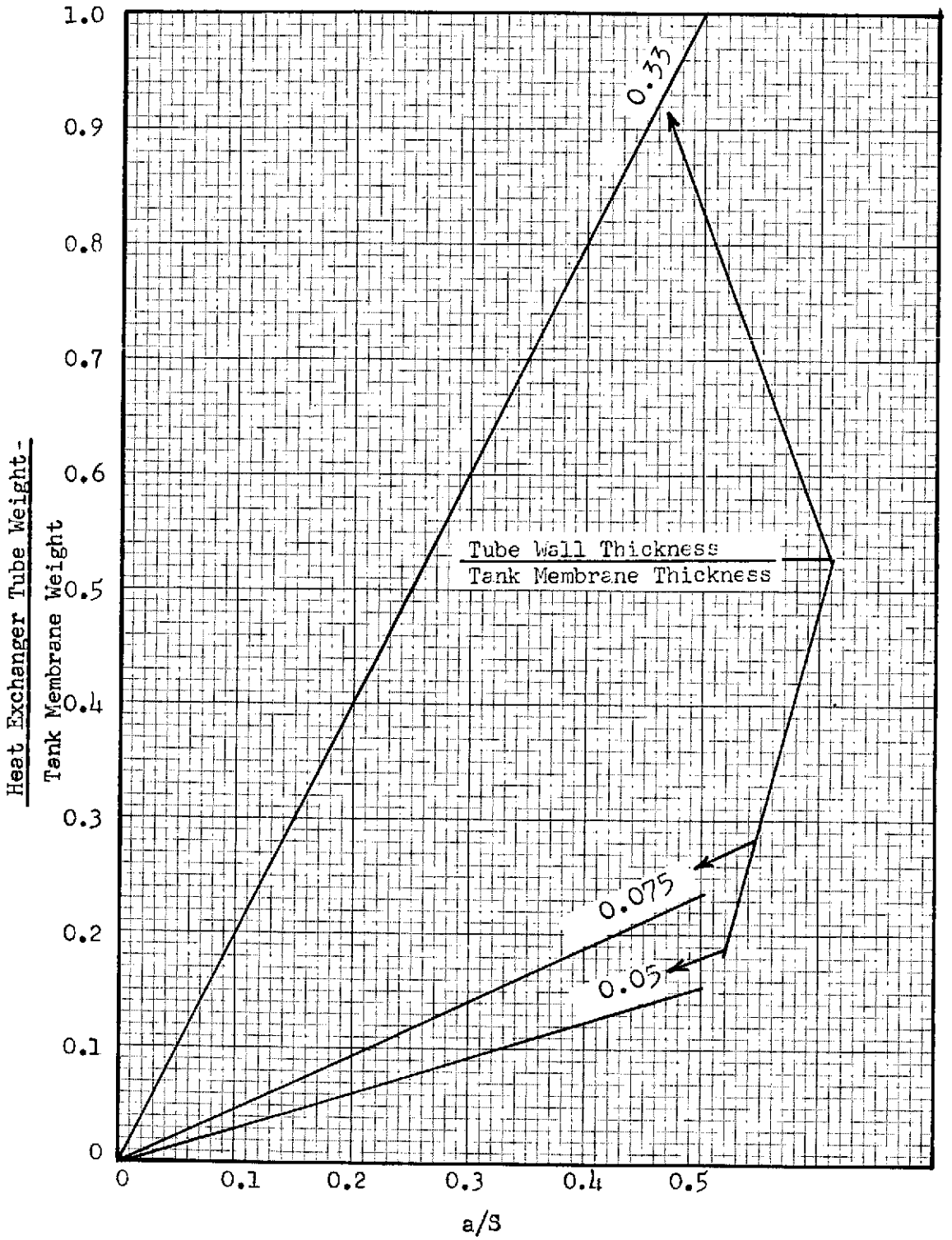

Figure 3-36 Heat Exchanger Weight as Percent of Tank Weight – Material: Aluminum

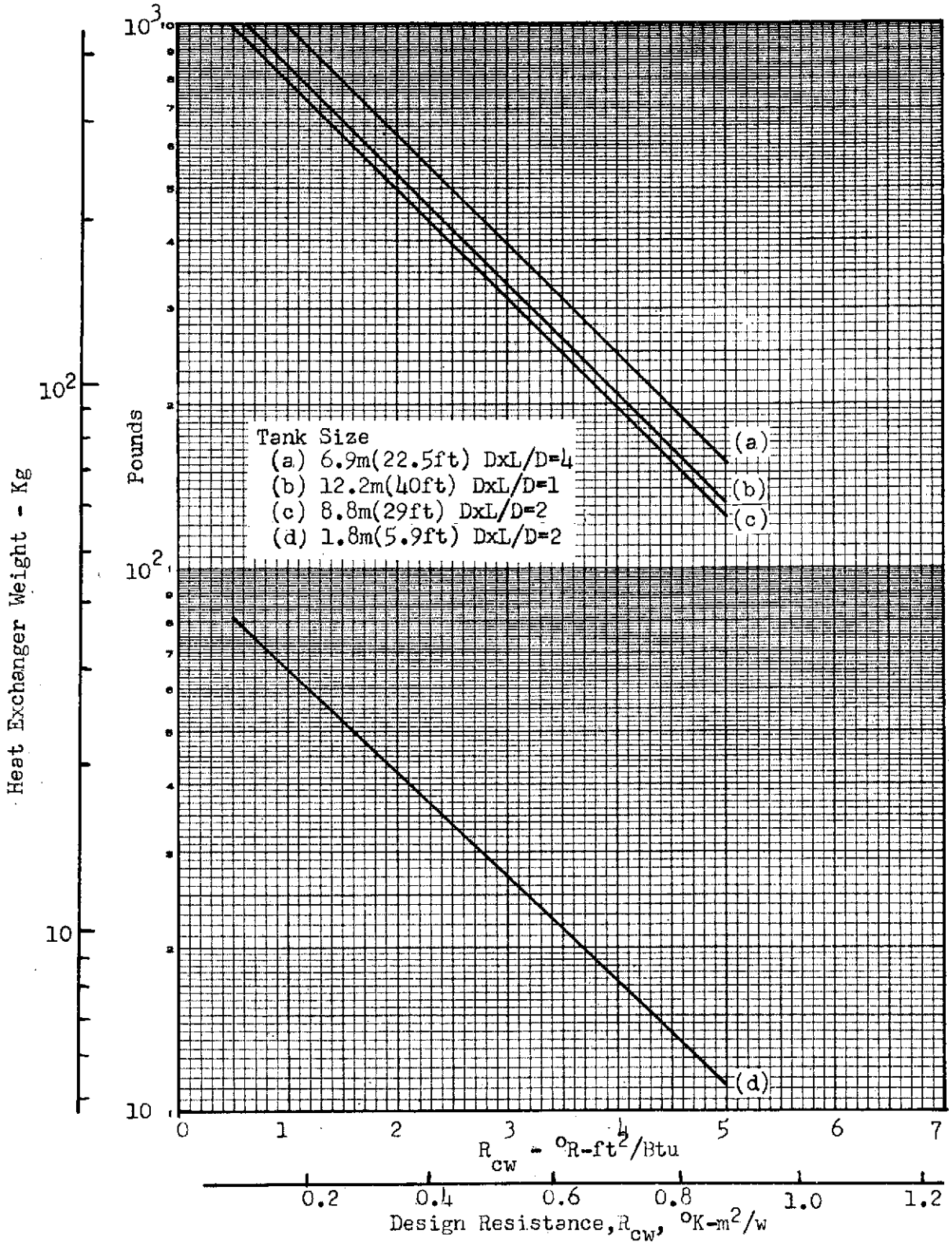

Figure 3-37 Heat Exchanger Tube Weight Variation With R_{cw}, Material: Aluminum, 6 mils

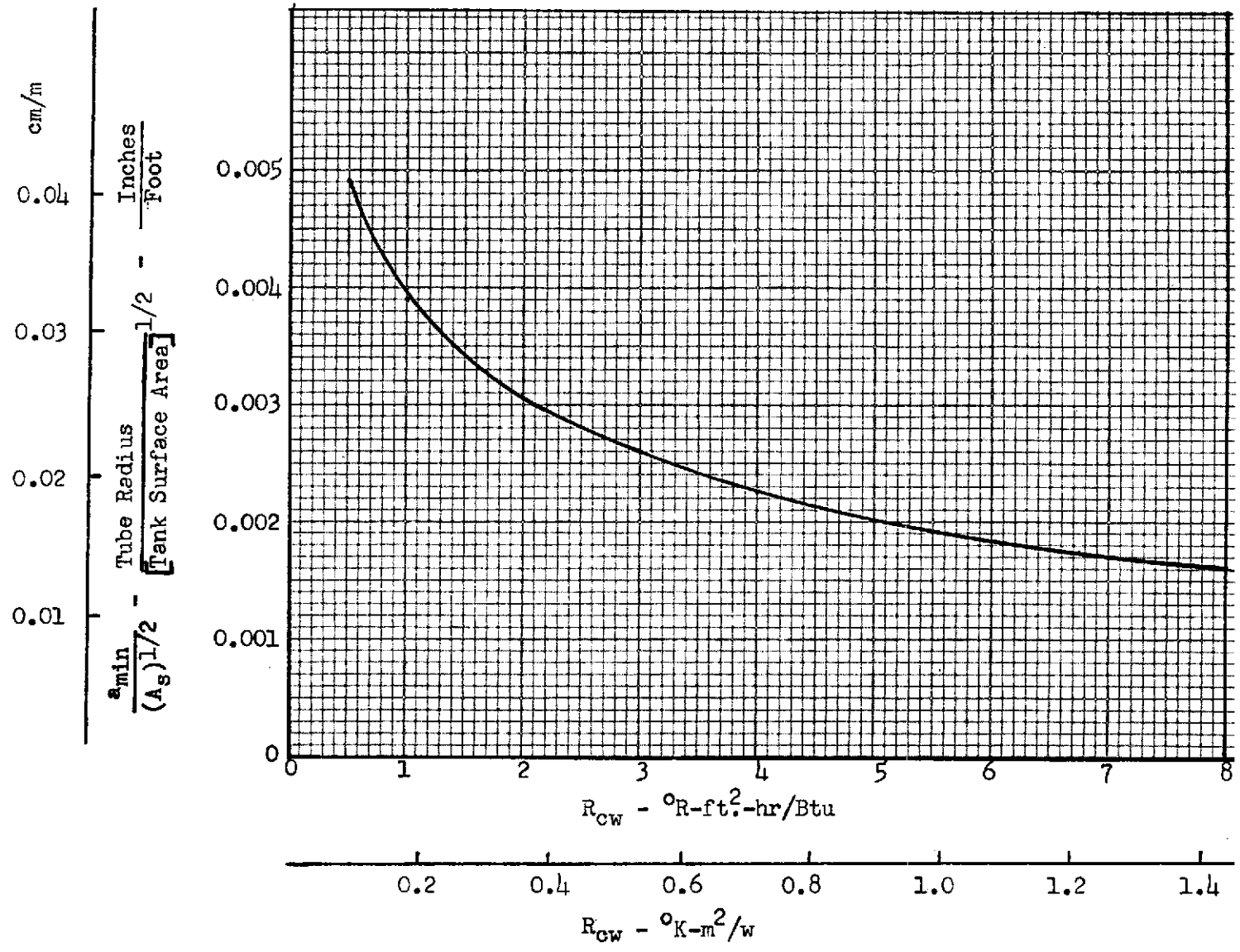

Figure 3-38 Normalized Heat Exchanger Tube Radius as a Function of Tank Wall Resistance

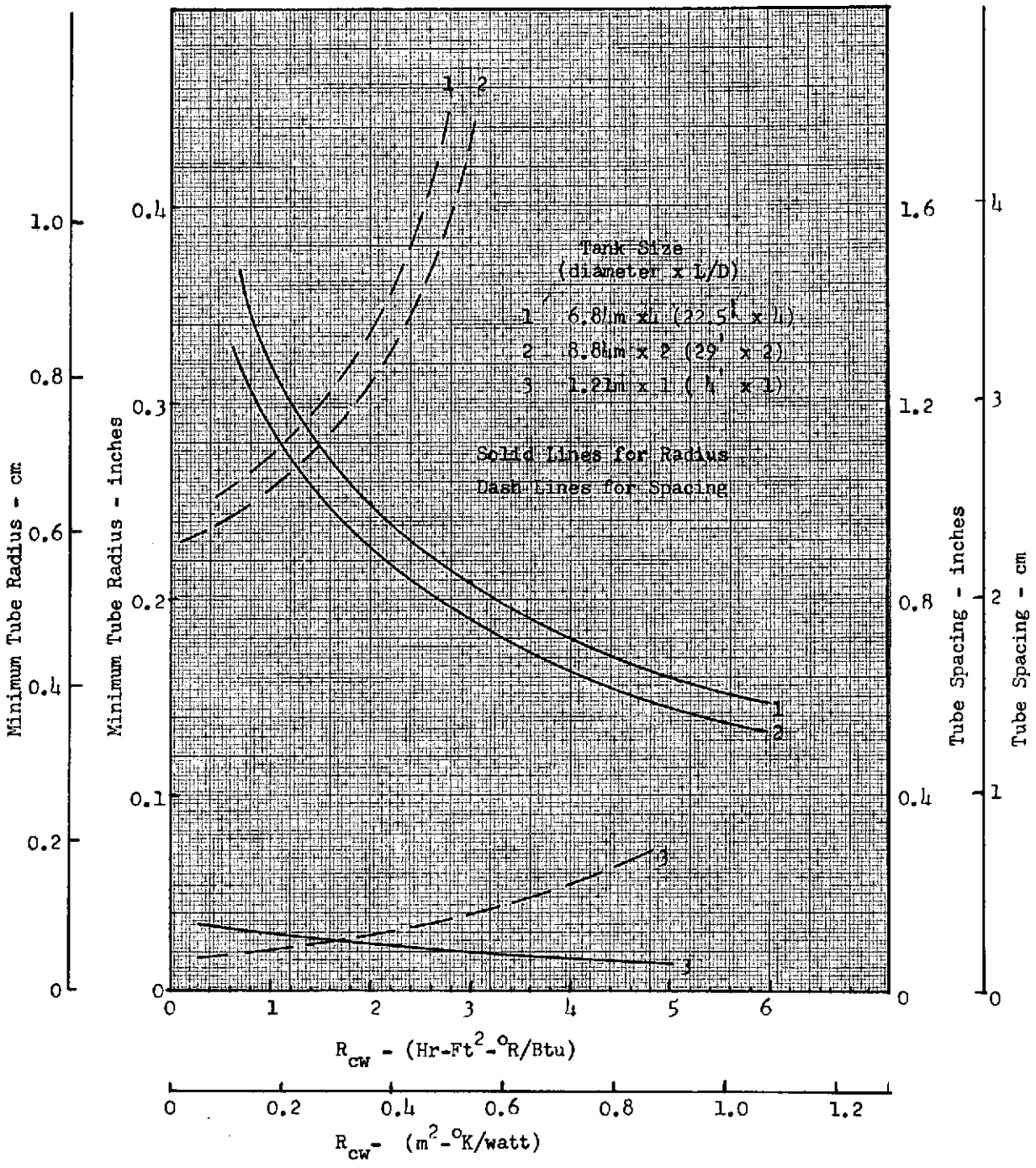

Fig. 3-39 Minimum Tube Radius and Spacing as a Function of Wall Resistance and Tank Size

Section 4

EXPERIMENTAL PROGRAM

This test program was designed to provide data needed to verify or modify the analytical models. Basically, this required determination of cooling rates, temperature distributions, and pressure responses with various input conditions selected to simulate a range of low gravity environments.

Testing was performed with three non-cryogenic and two cryogenic fluids to cover approximately a four decade range in Rayleigh number. Both a cylindrical and a spherical test apparatus were used and tests were conducted at various ullage volumes to determine the extent to which performance is effected by geometry. This section of the report contains a description of the test apparatus; instrumentation, conditions, procedures and results.

4.1 NON-CRYOGENIC TESTS

The three fluids used for these tests were: Freon-11; water; and 30 weight motor oil. The fluid properties give approximately 3 orders of magnitude variation in Rayleigh number. An attempt was made to extend the range by packing polyethelene spheres in the tanks. Several papers (e.g., Ref. 14) have shown that the onset of convection can be retarded by introducing a porous media, for which the effective Rayleigh number is defined as:

$$Ra_{eff} = Ra_o \left[\frac{\epsilon^3}{150\ (1-\epsilon)^2} \right] (d/L)^2$$

where:
- Ra_o is the basic fluid Rayleigh
- ϵ is media porosity (0.476 for packed spheres)
- d is diameter of packing spheres
- L is height of sphere packing

Both 3/4 and 1-1/2 inch diameter polyethelene spheres were used. Table 4-1 indicates the range of Rayleigh Nos. that were anticipated with these fluids, two tanks, and two porous media sizes.

Table 4-1

ESTIMATED RAYLEIGH NOS. FOR COOLING

Tank →	Cylinder			Sphere
Fluid →	Water	Oil	Freon	Freon
Media Size ↓				
None	$2x10^{10}$	$2x10^{8}$	$5x10^{11}$	$6x10^{11}$
3/4	$5x10^{4}$	$4x10^{2}$	$2x10^{6}$	$2x10^{6}$
1-1/2	$2x10^{5}$	$2x10^{3}$	$6x10^{6}$	$7x10^{6}$

Table 4-2 presents the matrix of test configurations that were included in these non-cryogenic tests.

Table 4-2

NON-CRYOGENIC TEST MATRIX

Tank →		Cylinder		Sphere
Fluid →	Water	Oil	Freon	Freon
Media Size ↓				
None	1,2,3	1,2,3	1,2,3,4	1,2,4
3/4		1,2,3	1,2	
1-1/2	1,2,3		1,2,3,4	1,2,4

(a) Numbers in the matrix columns refer to the following ullage configurations

1 5% ullage, Flat Interface
2 10% ullage, Flat Interface
3 10% ullage, Spherical Interface
4 50% ullage, Flat Interface

4.1.1 Non-Cryogenic Apparatus

The two test articles employed in these tests are shown in Fig. 4-1 and 4-2. The first is a right circular cylinder made from 12 inch stainless pipe. The wall thickness is 0.156 inches. The heat exchanger is made from 1/2 inch copper tubing. It consists of 7 coils attached to the tank with clips equally spaced at 3.5 inches. A nichrome wire heater is uniformly positioned between the heat exchanger coils to rapidly heat up the tank contents.

As illustrated in Fig. 4-1, the cylindrical apparatus had an 8 inch diameter aluminum sphere installed for part of the tests to simulate a submerged ullage bubble which was cooled indirectly by the heat exchanger. This sphere constituted 10 percent of the tank volume. The bubble had a neck made from 1/4 inch tubing which penetrated the flange cover in the top of the tank. This neck provided the physical support for the sphere and the fluid connection between it and the main tank. An isolation valve (IV01) was placed in the connecting line between the two tanks so that they could be filled with a common fill line and drained individually. For a spherical ullage simulation the tank was filled to the top. Drain valve DV01 was then opened, and when the sphere was empty, the isolation valve IV01 and DV01 were then closed to lockup the gas pocket. For flat ullage tests, the isolation valve was left open and the prescribed quantity of liquid was drained from the main tank through DV02.

The major element of the spherical test apparatus is a 22.5 inch diameter hydrogen tank that had been previously developed for an ID program. It was made from 2219 aluminum with a nominal membrane thickness of 0.019 inches. It had a 4 inch diameter opening with a mating, conoseal access cover. This prohibited the use of the 8 inch spherical ullage in this tank.

The heat exchanger consisted of 9 coils uniformly spaced, and attached to the tank at 3.4 inch intervals. This provided approximately the same thermal resistance as for the cylindrical apparatus.

Figure 4-3 is a schematic illustration of the test set-up for these non-cryogenic tests. The entire test apparatus was placed in an insulated box to minimize heating from the

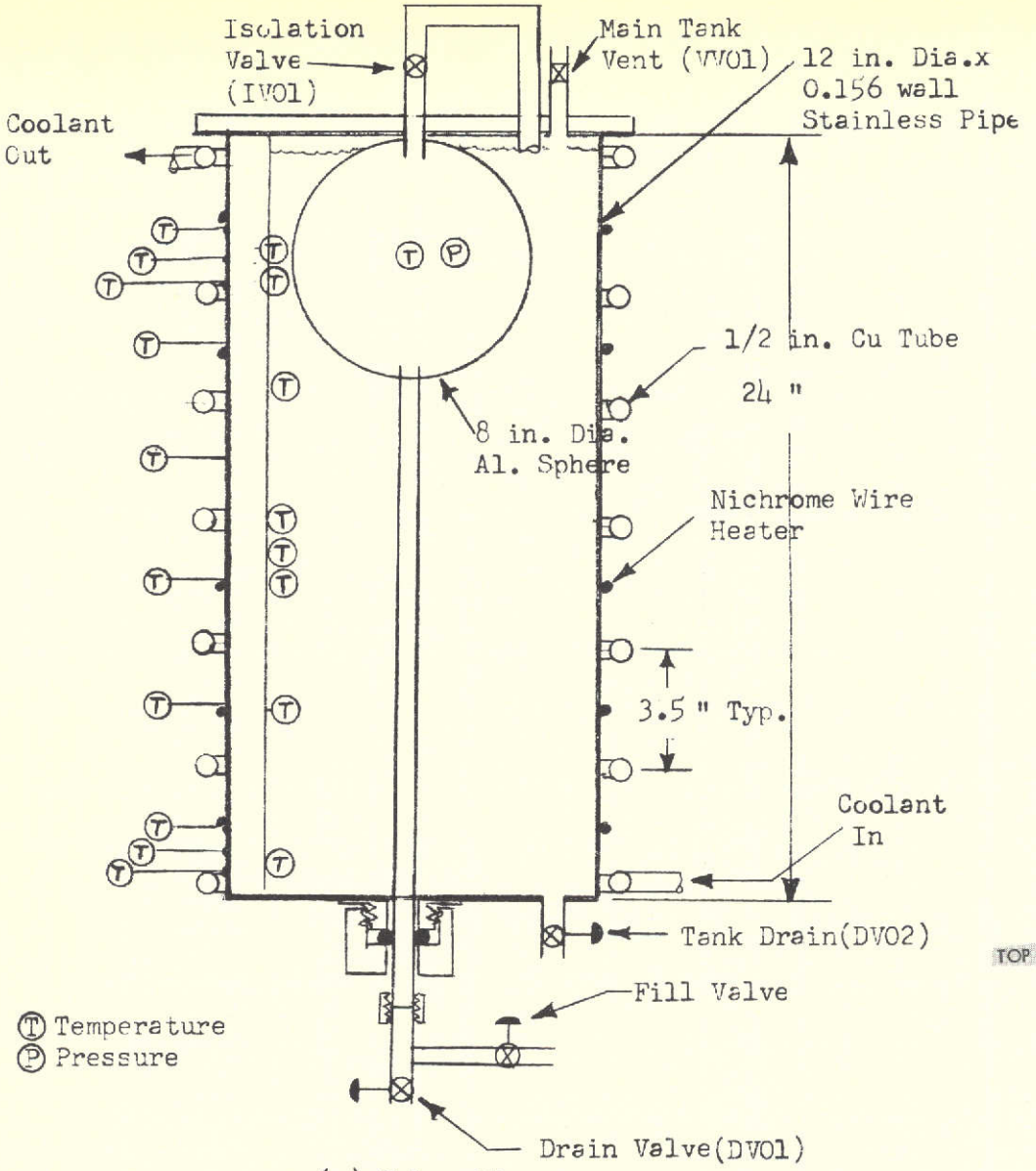

(a) Schematic

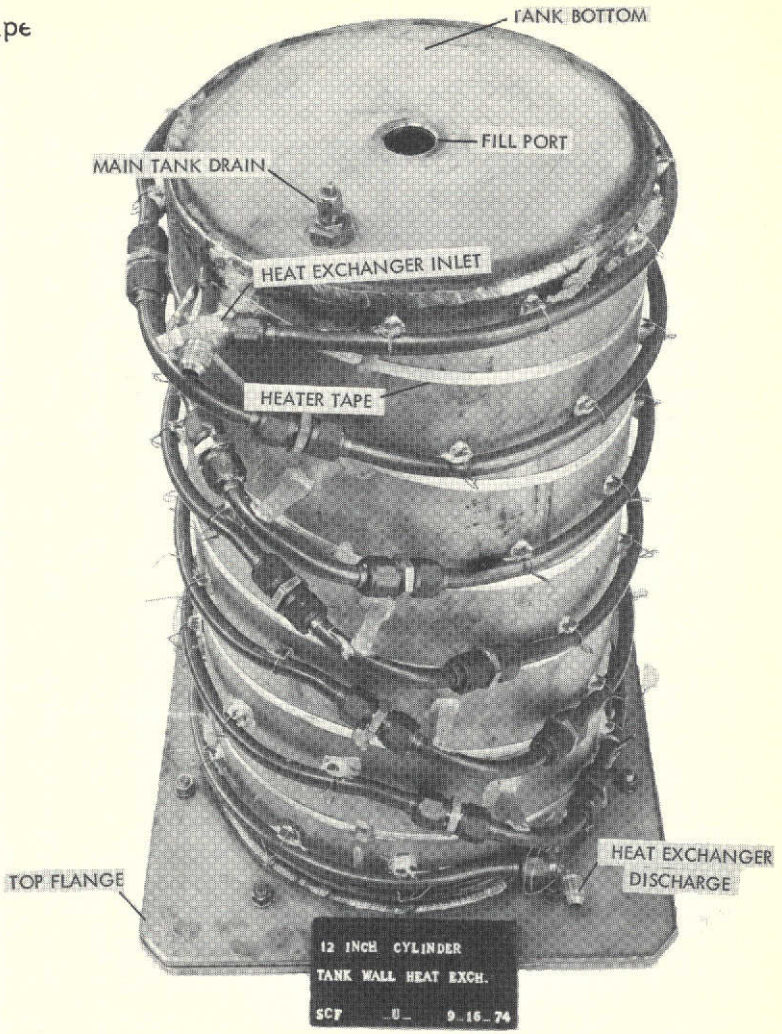

(b) Hardware

Figure 4-1 Non-Cryogenic Cylindrical Test Apparatus

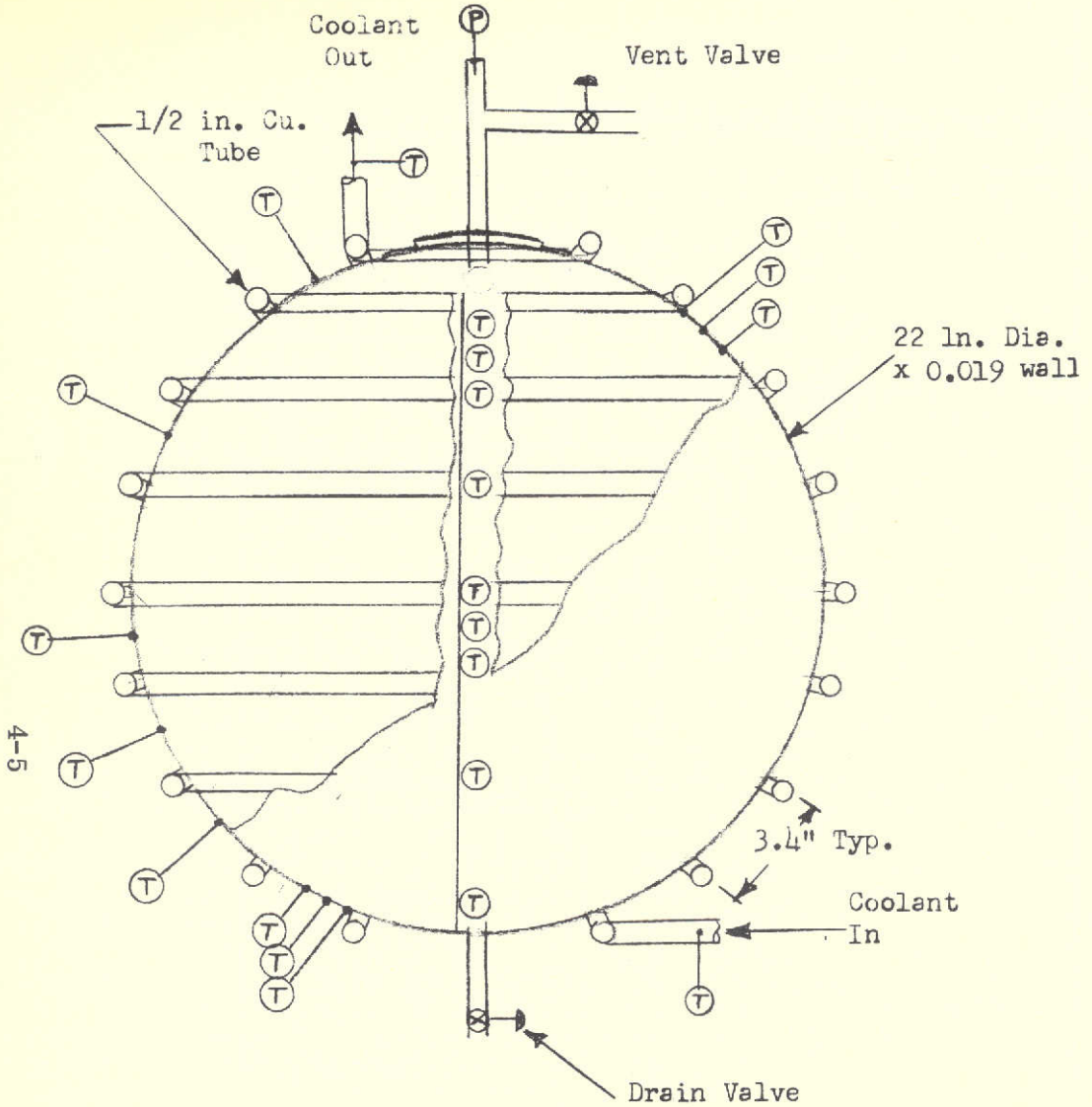

(T) Temperature measurement
(P) Pressure measurement

(a) Schematic

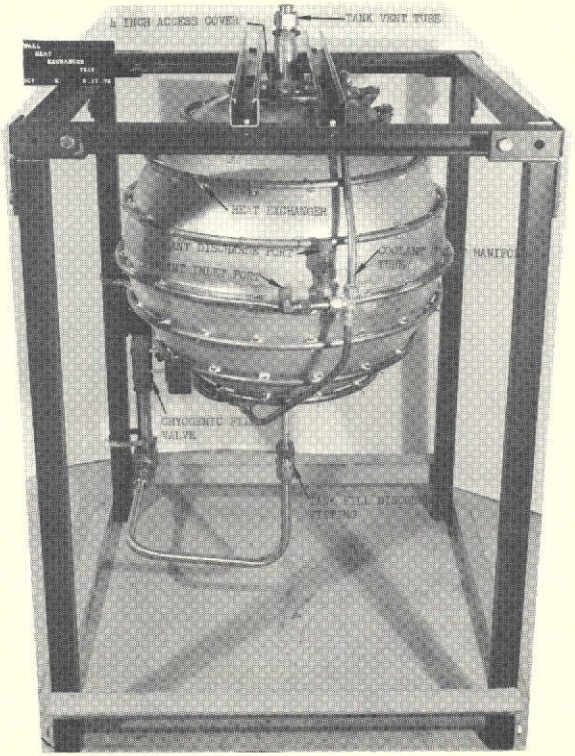

(b) Hardware

Figure 4-2 Spherical Test Apparatus

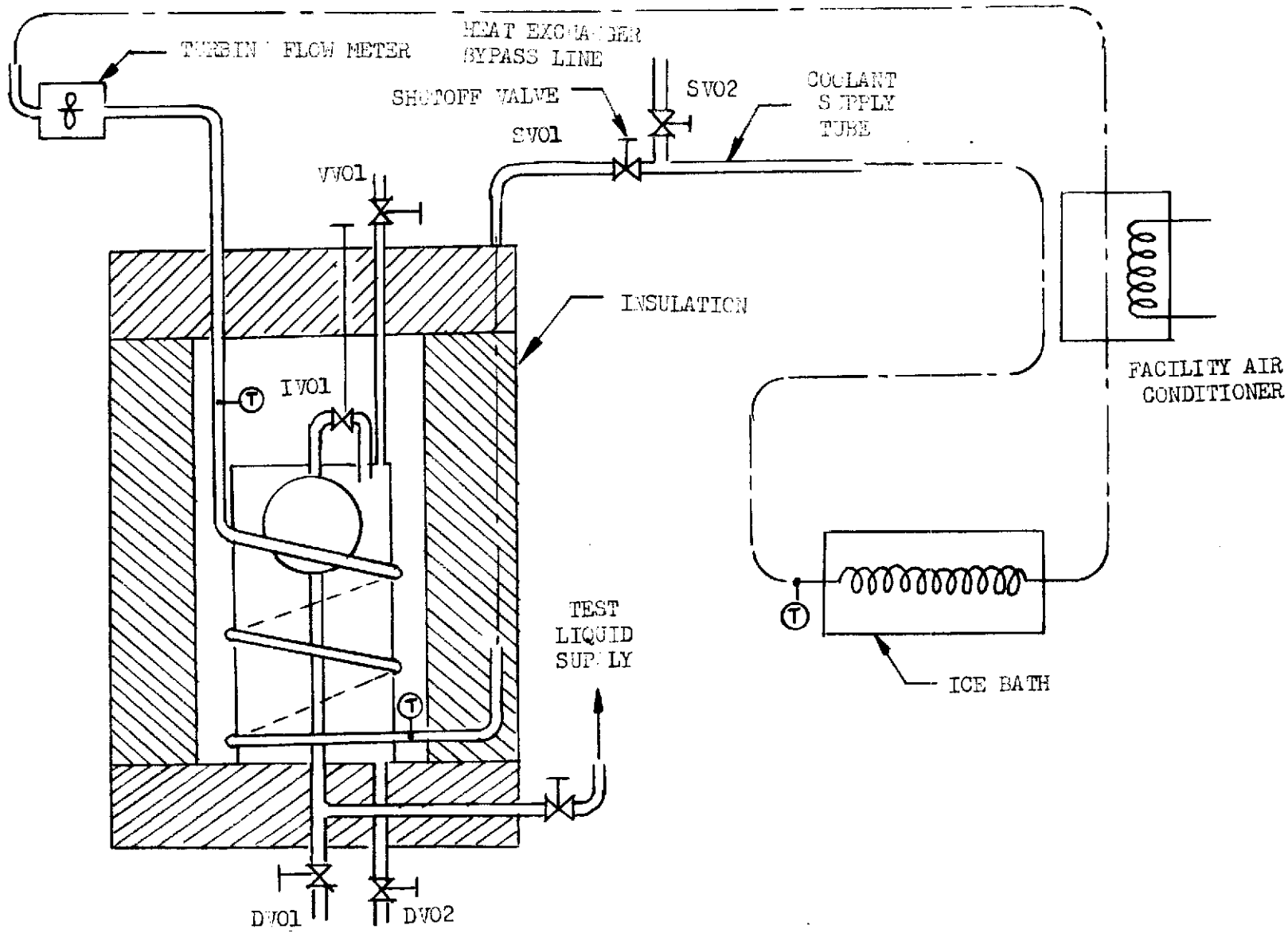

Fig. 4-3 Non-Cryogenic Test Diagram

external environment. The insulation also supported the test tanks. As illustrated, the heat sink (simulating vent fluid in the heat exchanger) was provided by water flowing in a recirculation loop through an air conditioning unit. The controller on this air conditioner permitted coolant temperature cycling between 40 and 48 degrees. This temperature was lowered and the variation was reduced by routing the coolant water through approximately 35 feet of copper tubing that was immersed in an ice bath.

The location of the temperature and pressure measurements are shown to scale on Figs. 4-1 and 4-2. The tank wall was instrumented to give a temperature profile between tube attachment points at two locations. A single temperature was also obtained between the other tube coils to give a measure of the variation from bottom to top of the tank. Liquid temperatures were measured at several points to give a good definition of the profile and for establishment of the average temperature differential history during the cooldown. Table 4-3 is a listing of the instrumentation for these non-cryogenic tests. Figure 4-4 is a photograph of the internal instrument probe.

Table 4-3

NON-CRYOGENIC INSTRUMENTATION

Item	Type	Range	No. of Measures	Elevation (inches)	No. of Measures	Elevation
			Cylinder		Sphere	
Ullage Pressure	C.E.C.	0-25 psia	1	23	1	22
Internal Fluid Temp.	PRT Ch-Cn Differential Thermocouple	30-540°F 0-30°F	1 7	1 5,10,11 12,16,19, 20	1 7	1 5,10,9,11 18,19,20
Wall Temp	Cu-Cu Thermocouples	0-30°F	10	1,2,3, 6.5,10, 13.5,17, 20,21,22	8	.5,1,1.3, 3.2,6,9,16 19,20,21
Coolant Temp In	PRT	30-540°F	1	–	1	–
Coolant Temp Out	PRT	30-540°F	1	–	1	–
Coolant Flow	Turbine Flow Meter	0-4 gpm	1	–	1	–

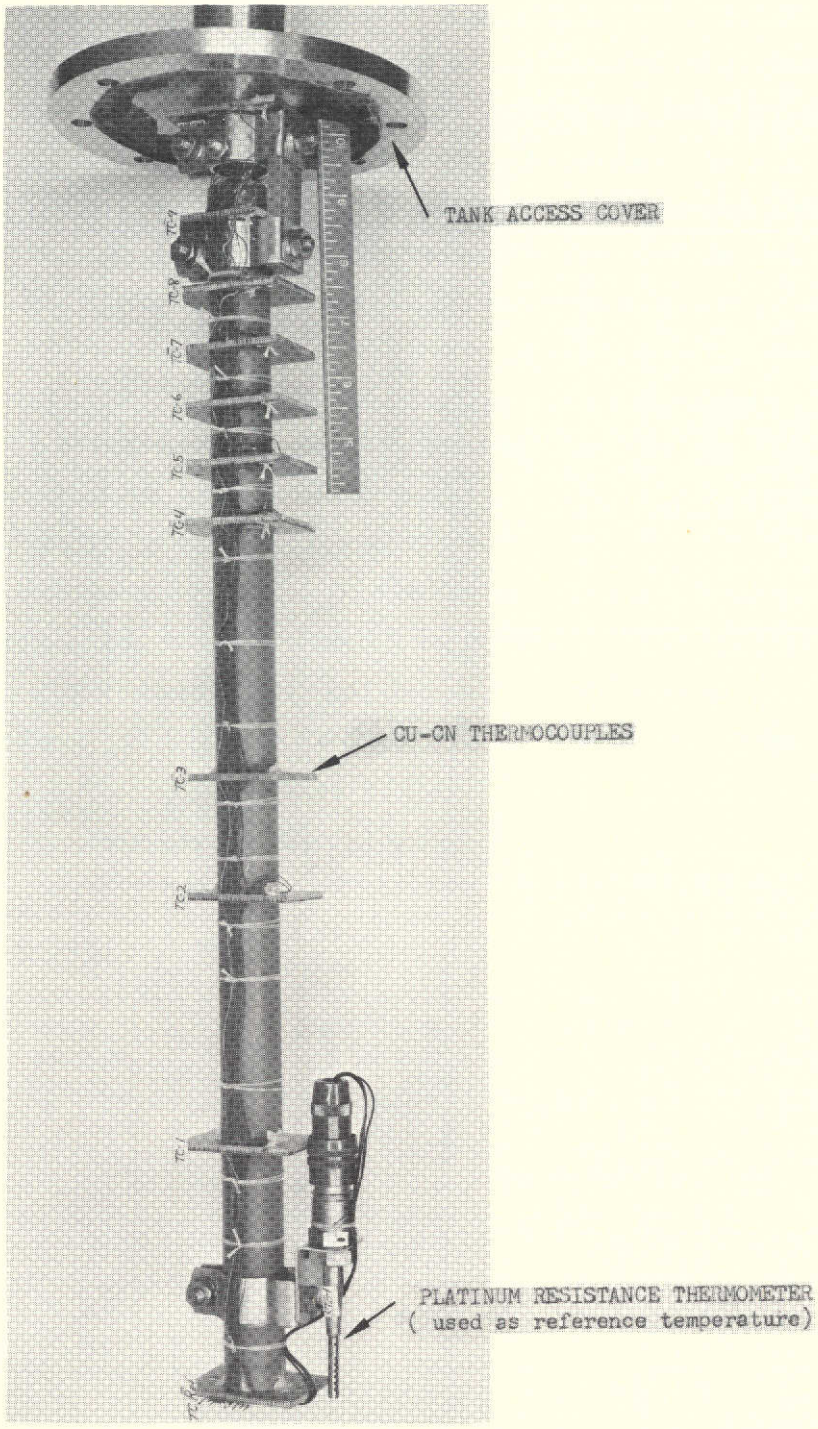

Fig. 4-4 Internal Instrumentation Probe for the 0.56 m (22 inch) Diameter Test Applications

4.1.2 Non-Cryogenic Test/Procedures

Prior to conducting any tests, functional checks were made on all instrumentation, heaters, etc. The test article was slowly filled with liquid. A prescribed quantity of liquid was then drained from the tank to set up the desired ullage configuration. A typical sequence of operations is as follows:

(1) Apply a uniform heat rate until the temperature in the top of the tank increases $10^{o}F$.

(2) Record temperatures and heat rates until the desired temperature rise is achieved.

(3) Initiate coolant flow at approximately 1/2 gpm and record all temperatures as function of time until surface temperature returns to original value.

(4) Drain the tank to the next level and repeat steps (1) through (3).

4.2 CRYOGENIC TESTS

The cryogenic tests were conducted in the 22 inch diameter sphere, using both liquid nitrogen and hydrogen. These fluids extend the Rayleigh No. range another order of magnitude. However, because of their very high vapor pressure they allow a measurable pressure response which provides the best indication of mass and energy transger at the interface, as well as providing a check on the validity of the pressure control model.

For the non-cryogenic tests, the coolant in the heat exchanger was supplied from an external, controlled temperature water supply. The cryogenic tests, were intended to demonstrate the automatic control characteristics of a tank wall heat exchanger system. Tank fluid was extracted, and expanded across a Joule-Thompson device to give a temperature drop. This subcooled fluid was then vented through the heat exchanger to cool the tank contents. The approximate Rayleigh Numbers that were anticipated for the cryogenic tests are shown in Table 4-4. It was intended to include the 1-1/2 inch polyethelene sphere media. However, the non-cryogenic tests proved conclusively that this media did not significantly reduce the strength of the convention boundary layer. Thus, the porous media tests were not conducted with cryogens.

Table 4-4

ANTICIPATED COOLING RAYLEIGH NUMBERS – CRYOGENIC

CRYOGEN	LN_2		LH_2	
Ullage – %	15	50	15	50
Rayleigh No.	10^{12}	3×10^{11}	2×10^{12}	7×10^{11}

4.2.1 Cryogenic Test Apparatus

The cryogenic test apparatus is the same as the spherical article described above, with one minor change. Whereas for the non-cryogenic tests the coolant was supplied by the external loop, for these tests it was extracted directly from the tank. Therefore, the coolant inlet was connected to the Joule Thompson valve as illustrated in Fig. 4-5.

The apparatus was installed in the vacuum chamber as shown in Fig. 4-6. In as much as the cryogen had to be expanded to less than 1/2 an atmosphere to get sufficient temperature differential, a vacuum pump was used downstream of the heat exchanger to suck the vent fluid through. Vent fluid flow was measured with a Hastings cryogenic thermal mass meter. The quality of the vent fluid was determined indirectly by use of a calibrated heater in the vent line downstream of the heat exchanger. This heater was used to bring the vent fluid to a superheated condition. The exit quality was then calculated from measured power, flow rate, and temperature rise across the heater.

The instrumentation for the cryogenic tests will be the same as previously described for the sphere in the Task II tests, except for the flow measurement device. The Hastings thermal mass meter, which has a range of 0 to 2 pounds per hour of hydrogen, was used to measure the flow rate through the tank wall heat exchanger. A Rosemount thermal mass meter located in the tank vent line was used for boiloff determination.

4.2.2 Cryogenic Test Procedures

The cryogenic tests were conducted using the pressure switch that was used with the active LIQUID PROPELLANT THERMAL CONDITIONING SYSTEM (Contract NAS 3-12033). A typical sequence of operations is as follows:

(1) Install test article as per Fig. 4-5.

(2) Evacuate chamber and test apparatus.

(3) Open facility shutoff valve and initiate fill until liquid level is at 5% ullage.

(4) Allow tank pressure to stabilize and determine equilibrium heat rate.

(5) Place system on automatic operation with the heat exchanger system.

(6) Record all temperatures and pressures and vent flow rate at prescribed intervals during the cooldown portion of a pressure cycle.

(7) Record temperatures and pressure at prescribed intervals during the pressure rise portion on the cycle.

(8) Drain the liquid level to the next ullage point and repeat steps (4) through (7).

(9) When all three ullage volumes have been completed with LN_2, drain and evacuate the test article. Then repeat steps (3) through (8) with LH_2.

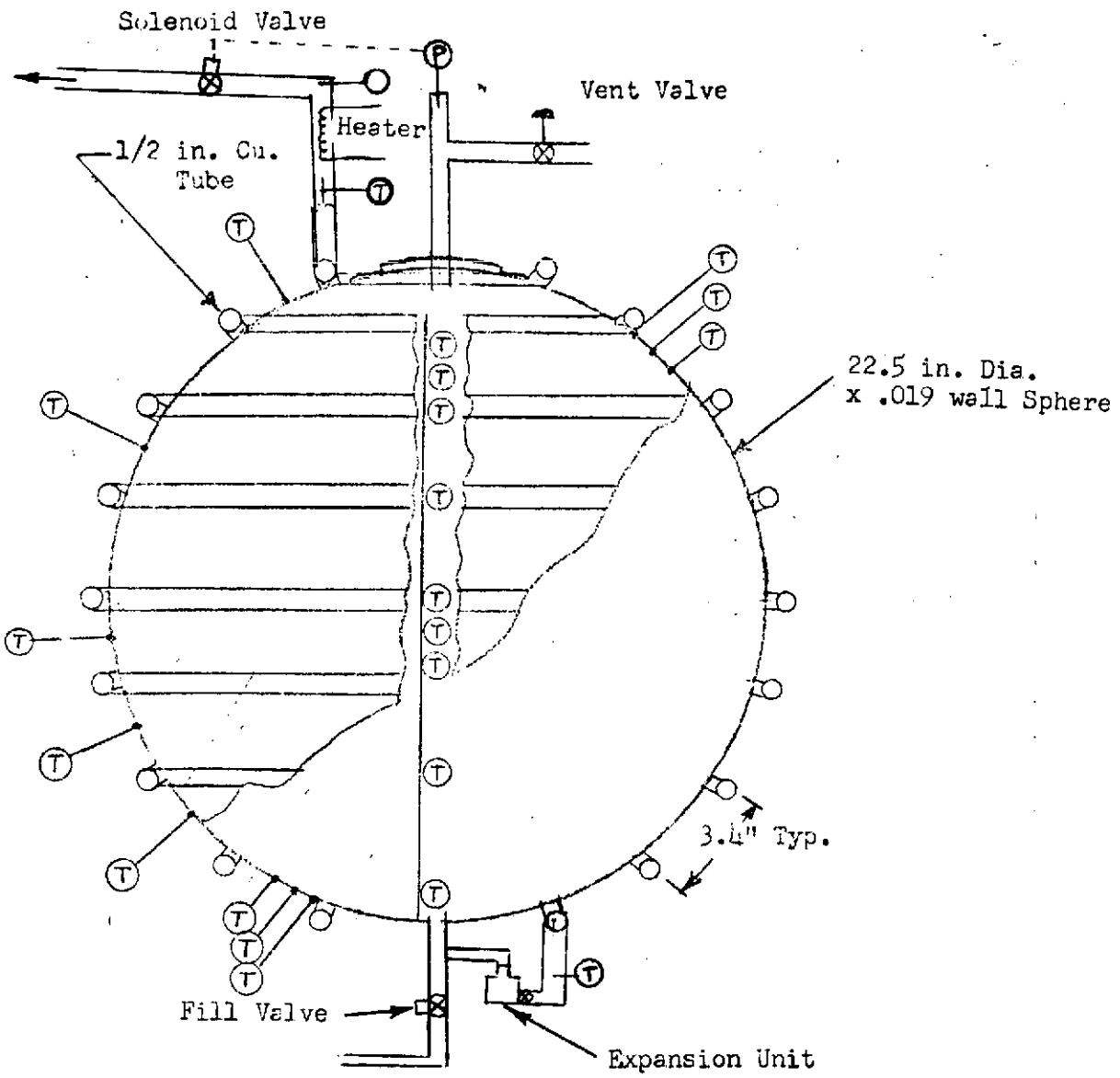

Fig. 4-5 Cryogenic Test Article

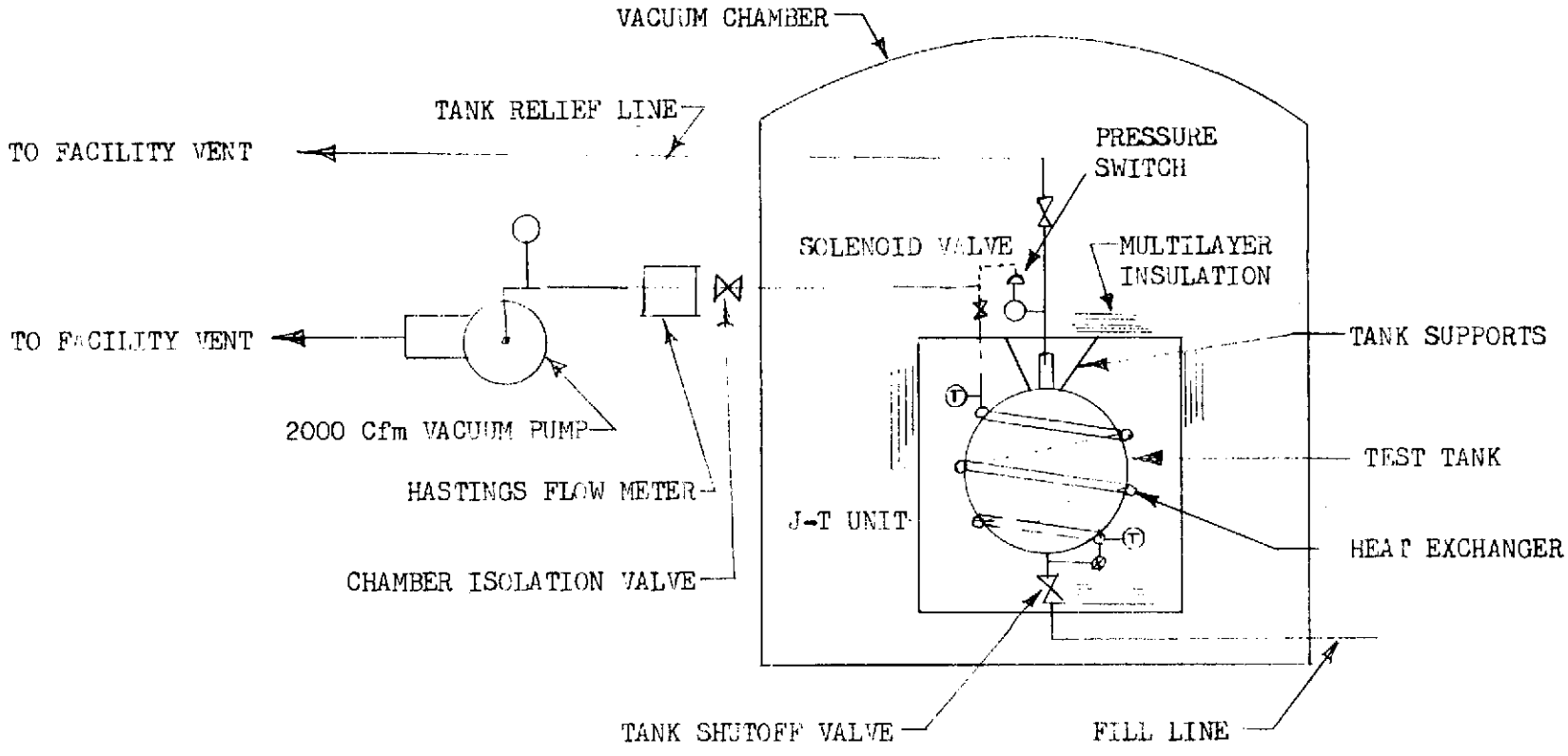

Fig. 4-6 Facility Test Schematic – Cryogenic Tests

4.3 TEST RESULTS AND ANALYSIS

4.3.1 Discussion of Results

A summary of all the test conditions is presented in Table 4-5. The initial liquid temperature shown is the average of the measurements in the liquid at the start of cooling. The coolant temperature is the average between the heat exchanger inlet and outlet values. The heat flux was determined from the heater power measurements for the cylindrical tank and from boiloff measurements for the cryogenic tests.

The temperature histories presented in Figs. 4-7 through 4-23 illustrate the typical performance of the tank wall heat exchanger, as affected by the various geometrical and fluid property factors. Figure 4-7 is for spherical tank with the liquid (Freon-11) level at 48.3 cm (19 in.). The tank was locked up and allowed to stratify before the coolant was turned on at 46,800 sec. Both the fluid and tank wall temperatures responded very quickly, although those nearest the bottom and the top of the tank have the fastest response. At the end of the lockup period, there was approximately 1.7°K (3 °R) stratification in the liquid, and an additional 1.7°K (3°R) in the ullage. At the end of the cooldown period the spread had increased to 3.6 and 5.6°K (6.5 and 10°R) respectively. The mean cooling coefficient between liquid and wall was approximately 15% below the theoretical value for the mean Rayleigh Number of 3.15×10^{10} which would result in a slower pressure response than that predicted by the model. This was computed on the basis of experimental mean temperature differences, with boundary layer run length as the characteristic dimension.

Figure 4-8 is for the sphere with a 50% ullage. The same general response is noted; i.e., the temperatures near the top and bottom drop off faster initially than those in the center of the tank. The experimental cooling coefficient is approximately 65% lower than the theoretical value based on boundary layer run length. However, if liquid height is used in the Rayleigh number, the discrepancy is reduced to 35%.

A comparison between Figs. 4-9 and 4-7 show the influence of the polyethelene spheres which were put into the tank to retard convection. However, the reverse

Table 4-5
TEST SUMMARY

Test No.	Apparatus	Fluid	% Ullage	Porous Matrix	Initial Temperature °K	Initial Temperature (°R)	Coolant Temperature °K	Coolant Temperature (°R)	Heat Flux W/m^2	Heat Flux (Btu/Hr)
A-ICF	Sphere	F-11	5	None	288	(519)	278	(500)	5.4	(1.7)
A-1	Sphere	F-11	5	None	288	(519)	276	(497)	5.4	(1.7)
A-2	Sphere	F-11	15	None	292	(526)	278	(499)	5.4	(1.7)
A-3	Sphere	F-11	50	None	293	(528)	277	(498)	5.4	(1.7)
A-4	Sphere	F-11	5	3.8 cm (1.5)	293	(528)	277	(498)	3.2	(1.0)
A-5	Sphere	F-11	15	3.8 cm (1.5)	283	(510)	282	(507)	6.4	(2.0)
A-6	Sphere	F-11	50	3.8 cm (1.5)	284	(511)	279	(503)	5.4	(1.7)
B-1	Cylinder	H_2O	10 (Sphere)	None	277	(498)	275	(495)	178	(56)
B-2	Cylinder	H_2O	15	None	277	(499)	276	(497)		
B-3	Cylinder	H_2O	5	None	278	(501)	275	(495)	178	(56)
B-4	Cylinder	H_2O	50	None						
B-5	Cylinder	F-11	10 (Sphere)	None	279	(503)	276	(497)	165	(54)
B-6	Cylinder	F-11	5	None	–	–	–	–	–	–
B-7	Cylinder	F-11	15	None	278	(501)	274	(494)	165	(54)
B-8	Cylinder	F-11	50	None	277	(499)	274	(493)	86	(27)
B-9	Cylinder	F-11	10 (Sphere)	1.9 cm (0.75)	279	(503)	276	(498)	174	(55)
B-10	Cylinder	F-11	5	1.9 cm (0.75)	277	(499)	274	(494)	(156)	(49)
B-11	Cylinder	F-11	15	1.9 cm (0.75)	280	(504)	275	(495)	344	(109)
B-12	Cylinder	F-11	50	1.9 cm (0.75)	277	(499)	275	(494)	344	(109)
B-13	Cylinder	H_2O	10 (Sphere)	3.8 cm (1.5)	279	(502)	275	(494)	344	(109)
B-14	Cylinder	H_2O	5	3.8 cm (1.5)	277	(499)	276	(497)	344	(109)
B-15	Cylinder	H_2O	15	3.8 cm (1.5)	275	(494)	275	(494)	330	(105)
B-16	Cylinder	F-11	10 (Sphere)	3.8 cm (1.5)	275	(496)	275	(496)	330	(105)
B-17	Cylinder	F-11	5	3.8 cm (1.5)	280	(504)	278	(501)	340	(108)
B-18	Cylinder	F-11	15	3.8 cm (1.5)	280	(504)	277	(499)	340	(108)
B-19	Cylinder	F-11	50	3.8 cm (1.5)	284	(511)	277	(499)	340	(108)
B-20	Cylinder	F-11	15	1.9 cm (0.75)	–	–	–	–	–	–
B-21	Cylinder	F-11	10 (Sphere)	1.9 cm (0.75)	285	(513)	278	(501)	338	(107)
B-22	Cylinder	F-11	15	1.9 cm (0.75)	284	(511)	278	(501)	338	(107)
B-23	Cylinder	Oil	10 (Sphere)	1.9 cm (0.75)	279	(502)	278	(500)	338	(107)
B-24	Cylinder	Oil	5	1.9 cm (0.75)	281	(506)	278	(500)	340	(108)
B-25	Cylinder	Oil	15	1.9 cm (0.75)	283	(510)	278	(501)	338	(107)
B-26	Cylinder	Oil	10 (Sphere)	None	283	(510)	278	(501)	338	(107)
B-27	Cylinder	Oil	5	None	283	(509)	278	(500)	338	(107)
B-28	Cylinder	Oil	15	None	282	(508)	277	(499)	338	(107)
B-29	Cylinder	F-11	10 (Sphere)	None	284	(511)	277	(498)	338	(107)
B-30	Cylinder	F-11	5	None	284	(510)	276	(496)	338	(107)
B-31	Cylinder	F-11	10	None	284	(511)	277	(498)	338	(107)
C-1	Sphere	LN_2	15	None	79.9	(143)	65.5	(118)	30.6	(9.7)
C-2	Sphere	LN_2	50	None	78.8	(142)	65.0	(117)	30.6	(9.7)
C-1a	Sphere	LN_2	15	None	76.2	(141)	65.5	(118)	30.6	(9.7)
C-3	Sphere	LH_2	15	None	19.8	(35.6)	17.7	(31.9)	21.4	(6.8)
C-3a	Sphere	LH_2	15	None	20.6	(37.0)	18.8	(33.9)	21.4	(6.8)
C-4	Sphere	LH_2	50	None	20.2	(36.4)	18.0	(32.4)	21.4	(6.8)

appears to be the case. The cooling rates and film coefficients were actually higher with the porous media. The theoretical porosity of this media is 0.476 and the pore size is the same order as the boundary layer thickness. Consequently, the media may have increased the turbulence rather than inhibit growth of the boundary layer. The average film coefficient for this run was 15% higher than the thoretical value, computed without regard to the media.

Figure 4-10 is for water in the cylindrical test apparatus. In Test B-3, the mean coolant temperature was approximately 274°K (493°R) until 42,000 sec reaching 282°K (507°F) at 52,000 sec when the test was discontinued. Figure 4-11 shows the wall temperatures reversing their trend at approximately 42,000, and leading the reverse in the liquid temperatures, as the mode goes from cooling to heating. The cooling rate decreased from 17.3 to 10.3 W (59 to 35 Btu/hr) before the coolant temperature excursion started a heating trend. The average Rayleigh Number for this test was computed to be 2.5×10^8 which is in the laminar regime. The average cooling coefficient was 28% higher than the theoretical laminar value.

Figure 4-12 is for essentially the same conditions as for Fig. 4-10 except that the test fluid is oil. The Rayleigh Number for this run was approximately two orders of magnitude lower than for Test B-3. However, it is obvious that the heat exchanger is still effective.

A comparison between Tests B-5 and B-9 (Figs. 4-13 and 4-14) indicate that the 3/4-in. media apparently did not reduce the convection as planned. Indeed, the cooling rate for Test B-9 was between 46 and 34 W (160 and 116 Btu/hr) with a coolant temperature of approximately 273°K (507°R). Pressure was decreasing at approximately 0.35 psi per hour. For Test B-5 the cooling rate was between 28 and 11 W (96 and 37 Btu/hr) and the rate of pressure change was 0.18 psi per hour. The average coolant temperature was 276°K (496°R) for this test. Test B-16 (Fig. 4-15) used the 1-1/2-in. media and it confirms the fact that low gravity convection was not simulated. The cooling rate varied from 25 to 6.1 W (86 Btu/hr to 21 Btu/hr) with the same coolant temperature as for Test B-9. The lower rates are due to the fact that the tank contents are approximately 6°K (10°R) lower than for Test B-9.

Further confirmation of the ineffectiveness of the media is reflected in Figs. 4-16 and 4-17. The difference between them is in the ullage configuration which has an insignificant effect on the energy distribution. Moreover, when compared to Fig. 4-12, one notes similar temperature response with and without the media.

Figures 4-18 and 4-19 primarily illustrate the influence of ullage volume on the performance of the tank wall heat exchanger. The heat flux for Test B-7 is twice that for B-8, but the rate of temperature rise is three times as high and the rates of pressure rise are nearly identical. This indicates that the vaporization rates at the interface are higher for the large ullage during self-pressurization. However, once the heat exchanger was turned on, both the temperature and pressure responses were nearly the same. Figure 4-20 is directly comparable to 4-19 with the addition of the 3/4-in. media. Once again it reveals no marked effect on performance.

Figures 4-21 and 4-22 show temperature histories for liquid hydrogen with 15 and 50% ullage, respectively. It is apparent that the heat exchanger was not keeping up with the incoming heat. The heat rate into the hydrogen tank was determined to be 2.2 W/m^2 (6.8 $Btu/hr\text{-}ft^2$), which was too high for this heat exchanger design. The maximum heat rate that a tank wall heat exchanger can handle is given by:

$$q_{max} = \frac{1}{R_{cw}} (T_B - T_C)$$

where $(T_B - T_C)$ is the mean difference between the bulk fluid and the coolant.

For the hydrogen runs, this is the temperature drop across the expansion valve which was 4.4°K (8°R) for these tests. The mean value of the tank wall resistance was determined to be 0.57 $°K\text{-}m^2/W$ (0.4 $°R\text{-}ft^2\text{-}hr/Btu$). Taking into account the reduction in thermal conductivity of the 2021 aluminum, the corresponding resistance at liquid hydrogen temperatures is 4.85 $°K - M^2/W$ (3.4 $°R\text{-}ft^2\text{-}hr/Btu$).

Consequently, the absolute maximum heat flux to the hydrogen that could be accommodated is:

$$q_{max} = 4.44/4.85 = 0.9\ W/m^2\ (0.28\ Btu/hr\text{-}ft^2)$$

which is less than half the experimental value. The pressure histories for these hydrogen tests are shown in Fig. 4-23.

4.3.2 Comparison With Analytical Convection Model

In the development of the analytical model, it was assumed that the film coefficients between the liquid and the tank wall were given by the conventional correlations for vertical flat plate. Example:

$$\frac{hL}{k} = C(R_a)^n$$

where:

$$\left.\begin{array}{l} C = 0.1 \\ n = 1/3 \end{array}\right\} \text{for } R_a > 10^8$$

$$\left.\begin{array}{l} C = 0.54 \\ n = 1/4 \end{array}\right\} \text{for } R_a < 10^8$$

In addition, it was assumed that the fluid stratifies when heated, such that the surface temperature rise (which establishes the pressure) is given by:

$$\frac{T_s - To}{q_w(Xc/_R)} = \frac{2(Xc/_R)\,\phi H}{F\ Pr\ (\Delta/Xc)}$$

The temperature at any location X is given by:

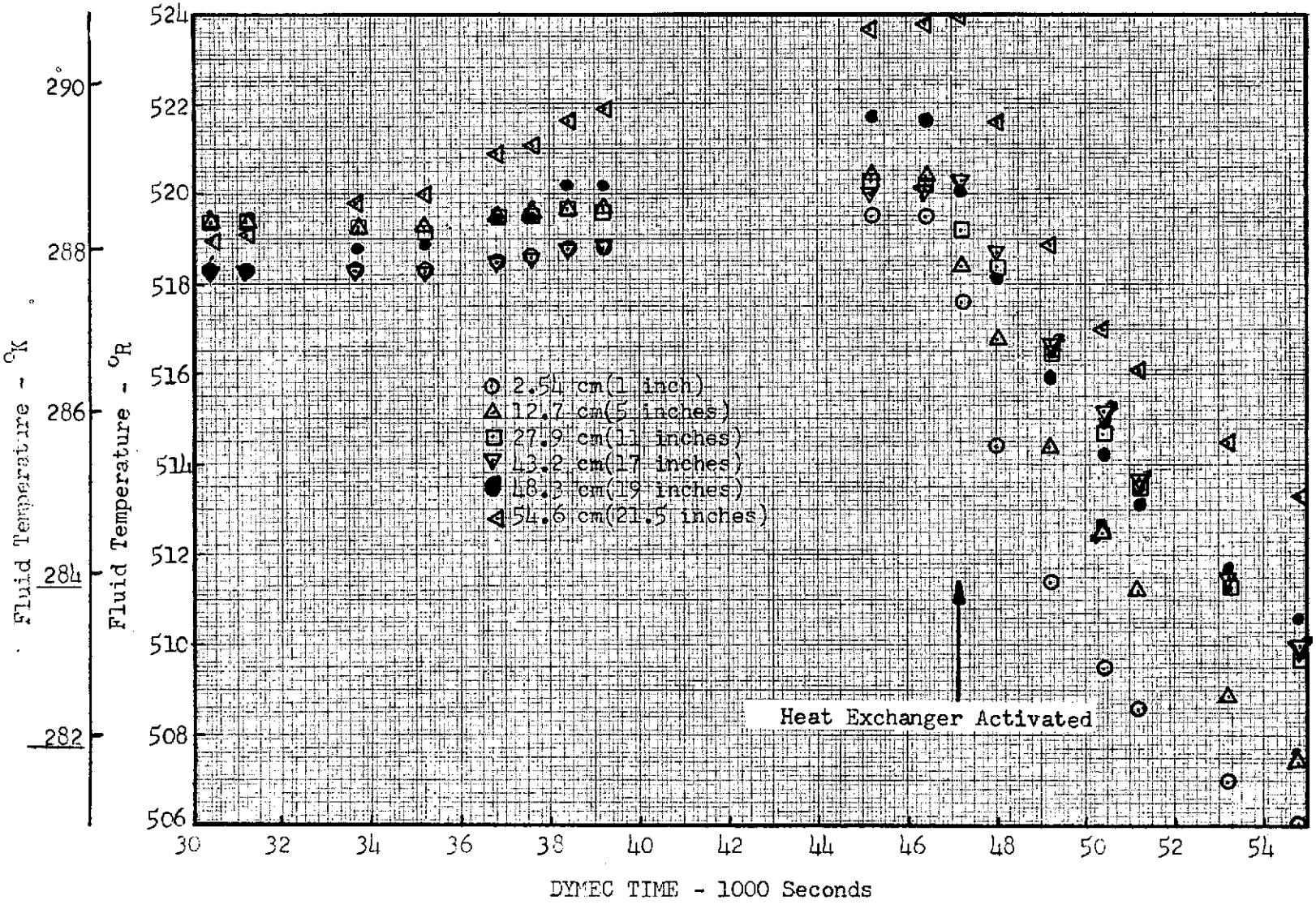

Fig. 4-7 Fluid Temperature Histories for Test A-1, Test Tank-Sphere, Test Fluid-F-11, Ullage Volume 5%

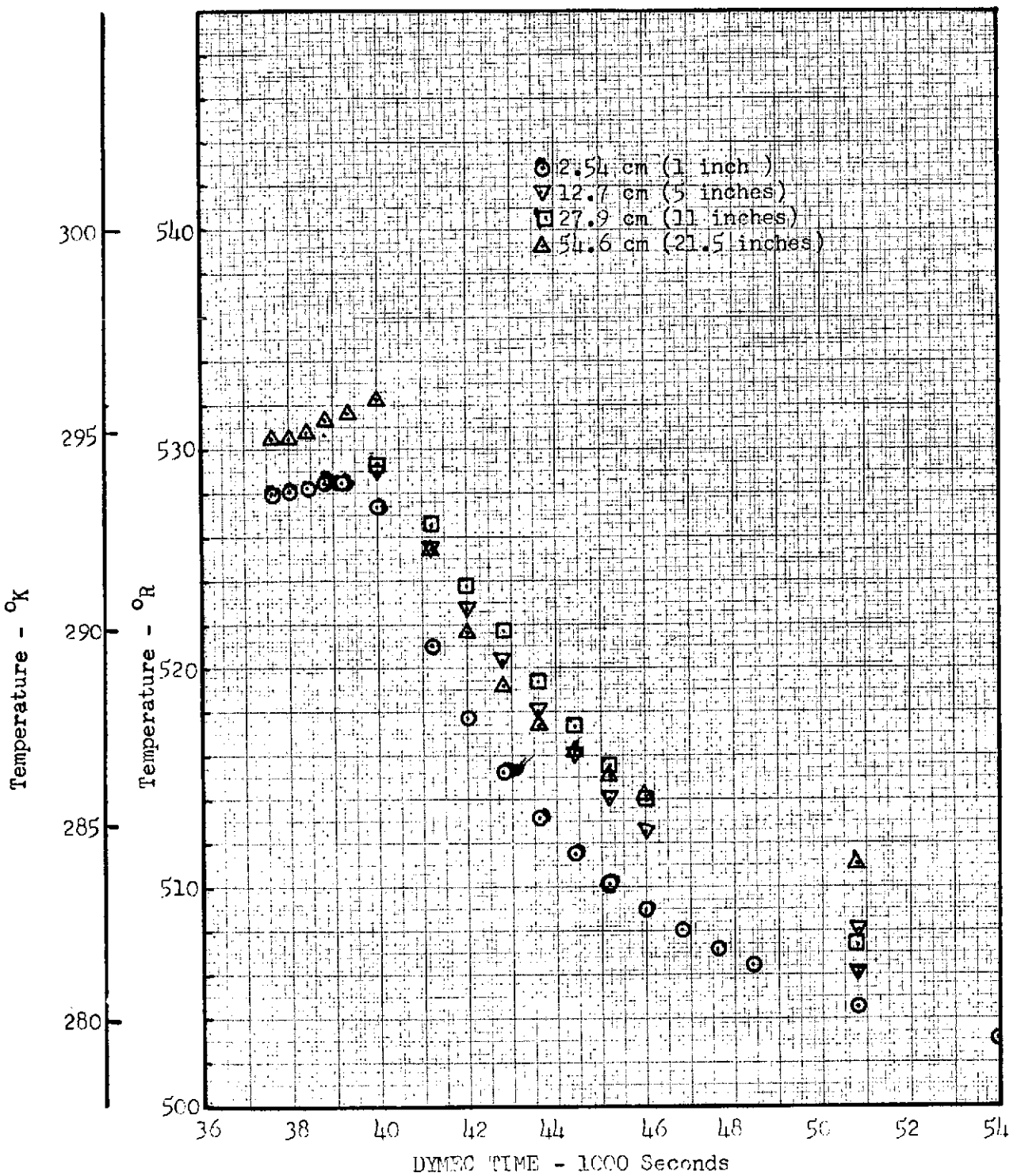

Fig. 4-8 Fluid Temperature Histories for Test A-3, Test Tank-Sphere, Test Fluid-F-11, Ullage Volume 50%

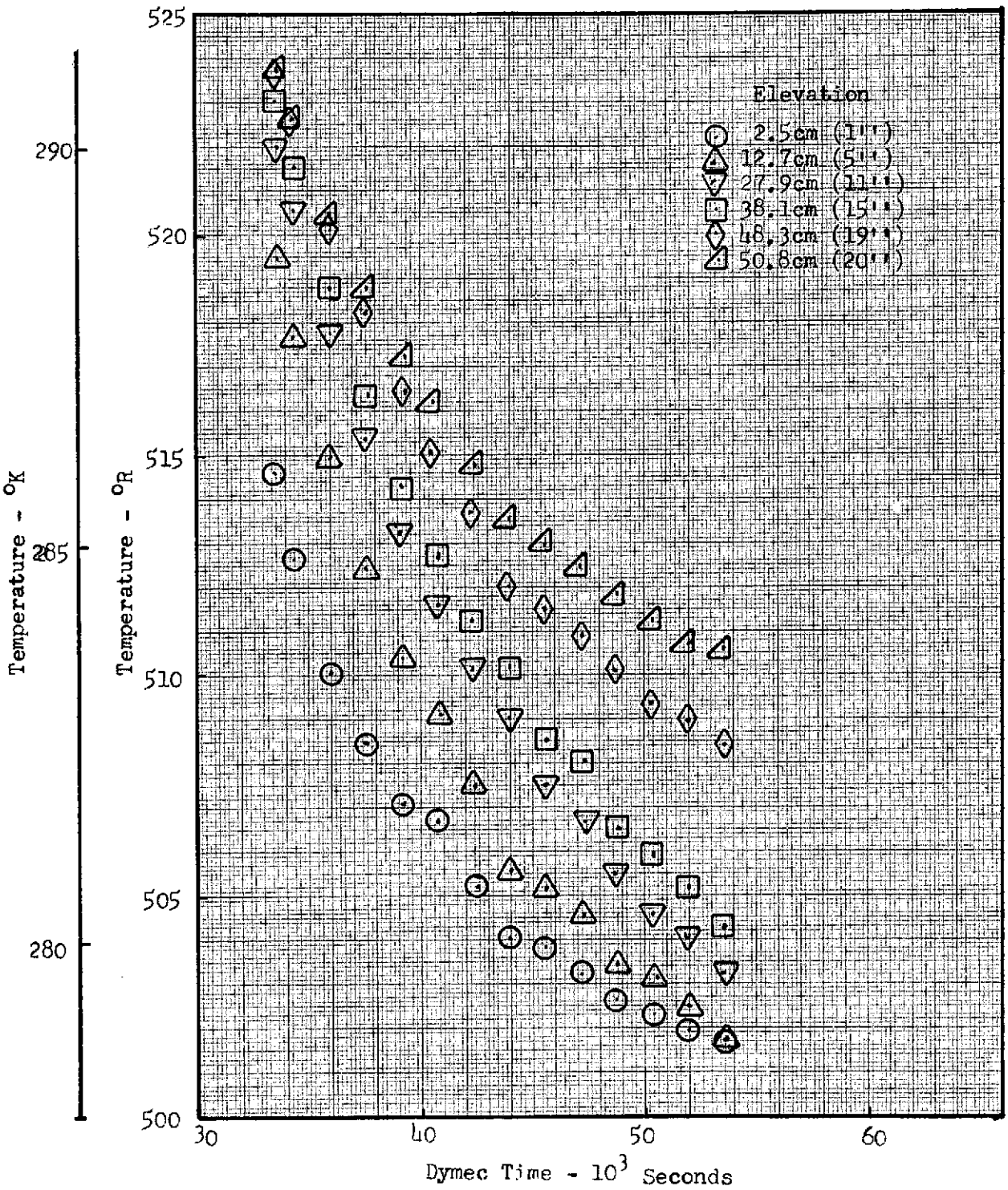

Fig. 4-9 Fluid Temperature Histories for Test A-4

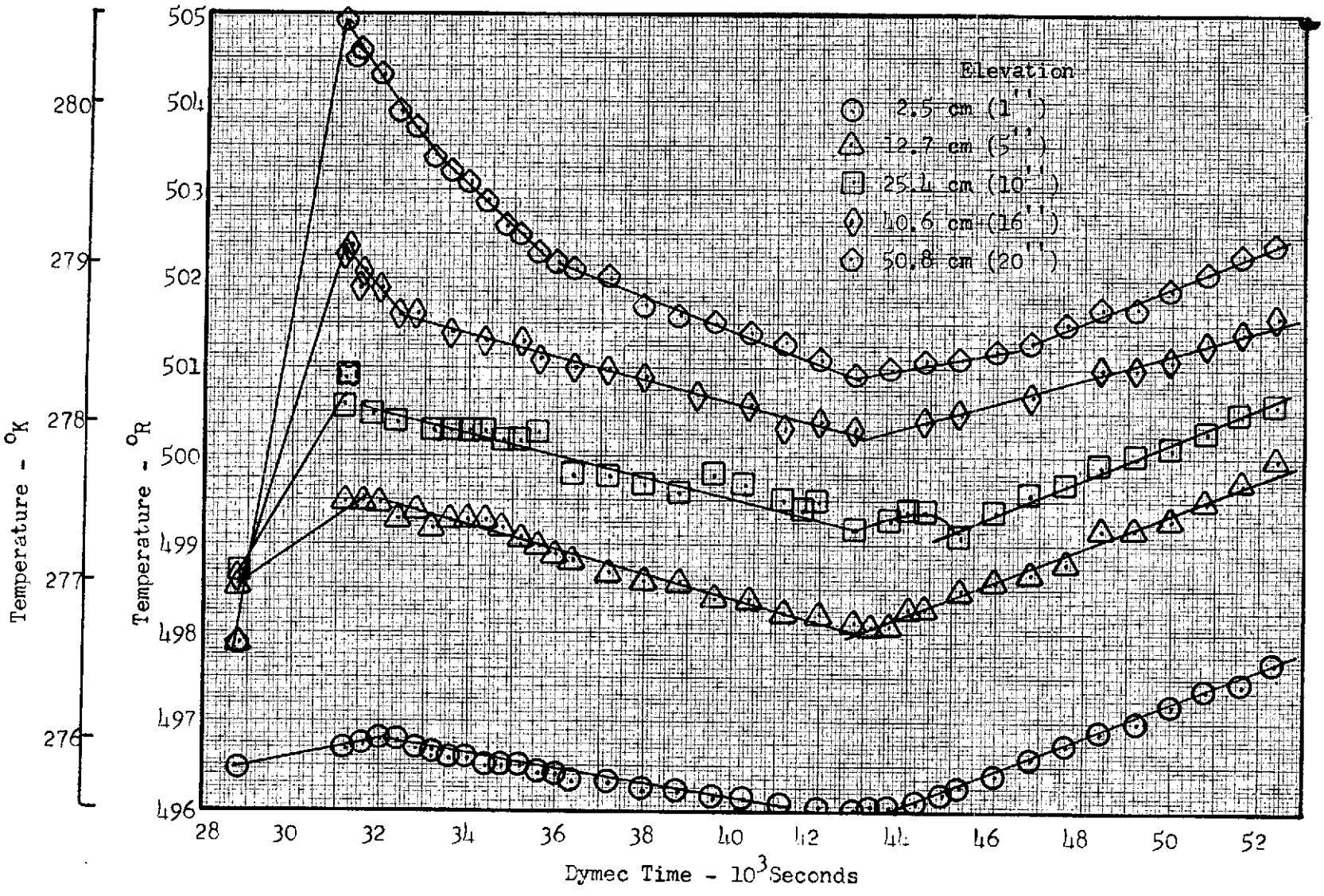

Fig. 4-10 Liquid Temperature Histories, Test B-3

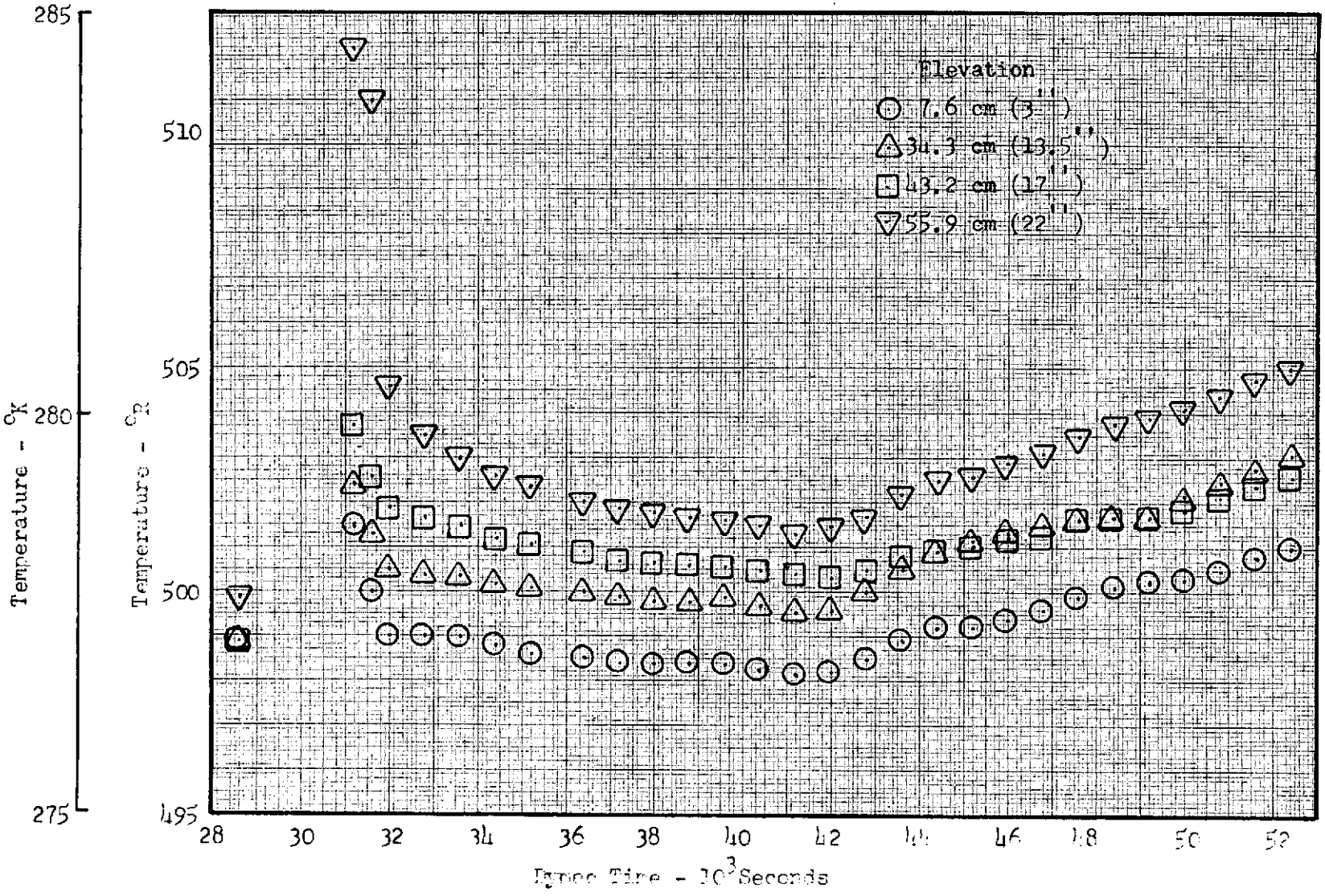

Fig. 4-11 Wall Temperature Histories, Test B-3

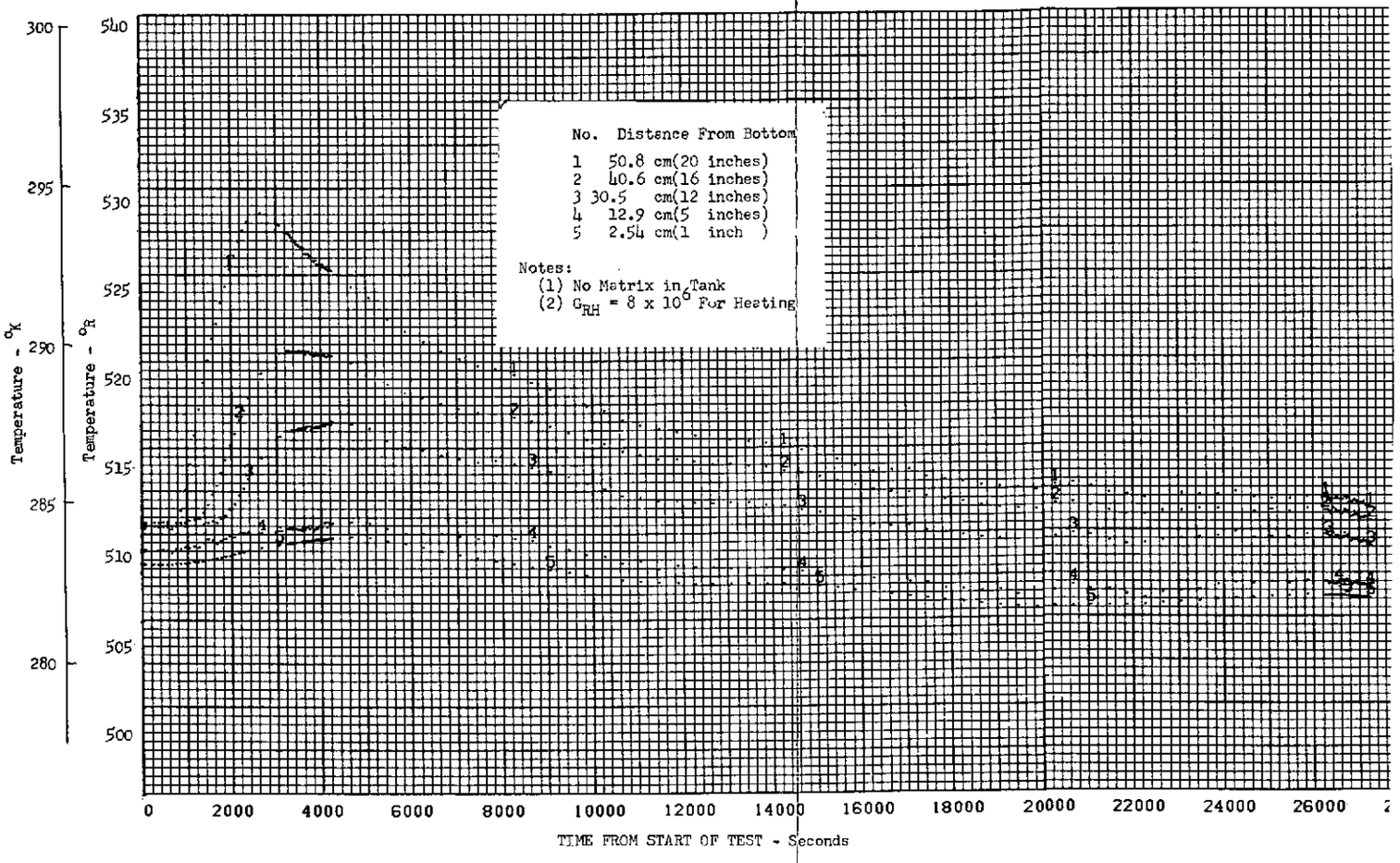

Fig. 4-12 Fluid Temperature Histories for Test B-27, Test Fluid-Oil, Test Tank - Cylinder, Ullage Volume-5%

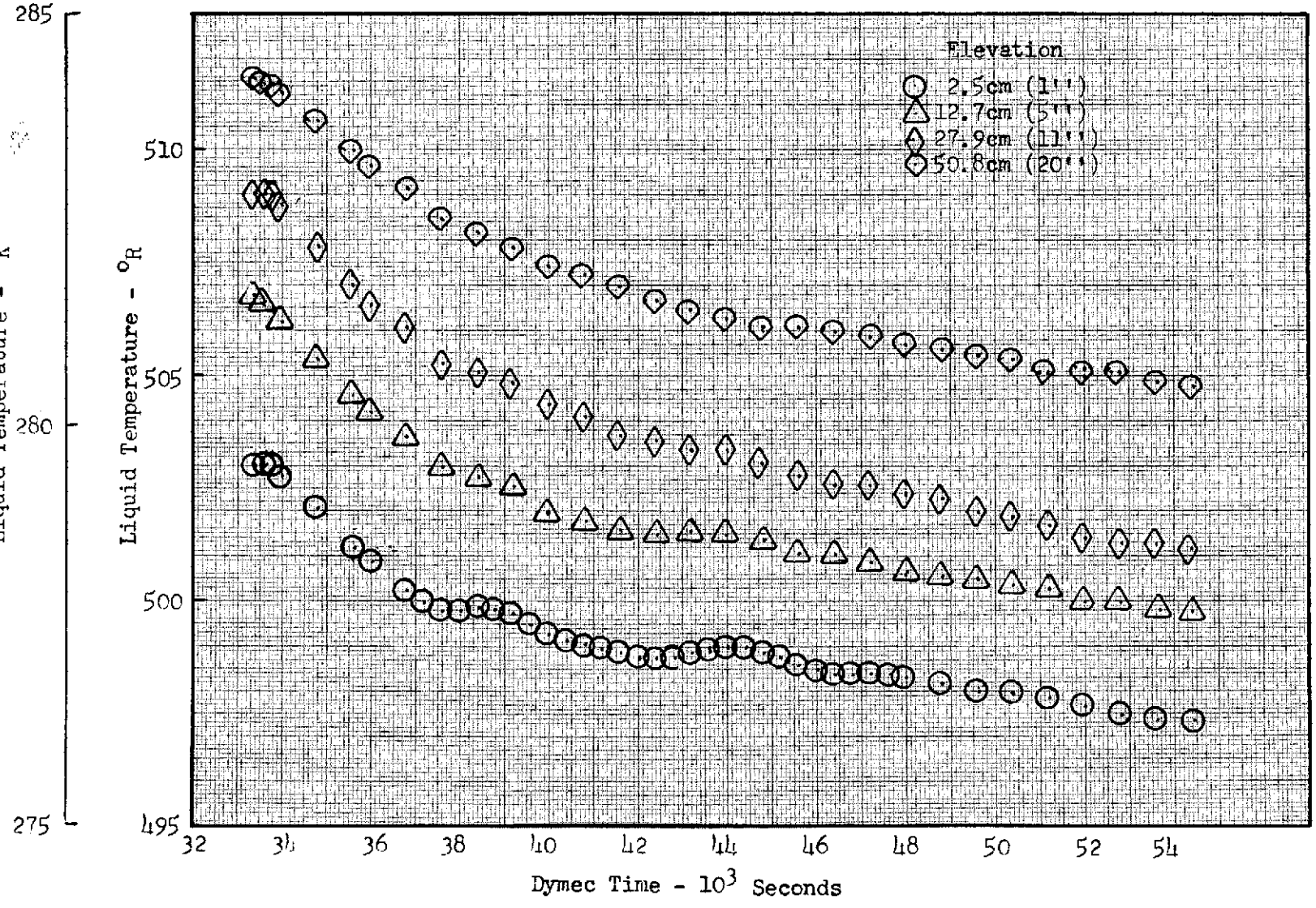

Fig. 4-13 Liquid Temperature Histories, Test B-5; Fluid-F-11; 10% Spherical Ullage; No porous Media

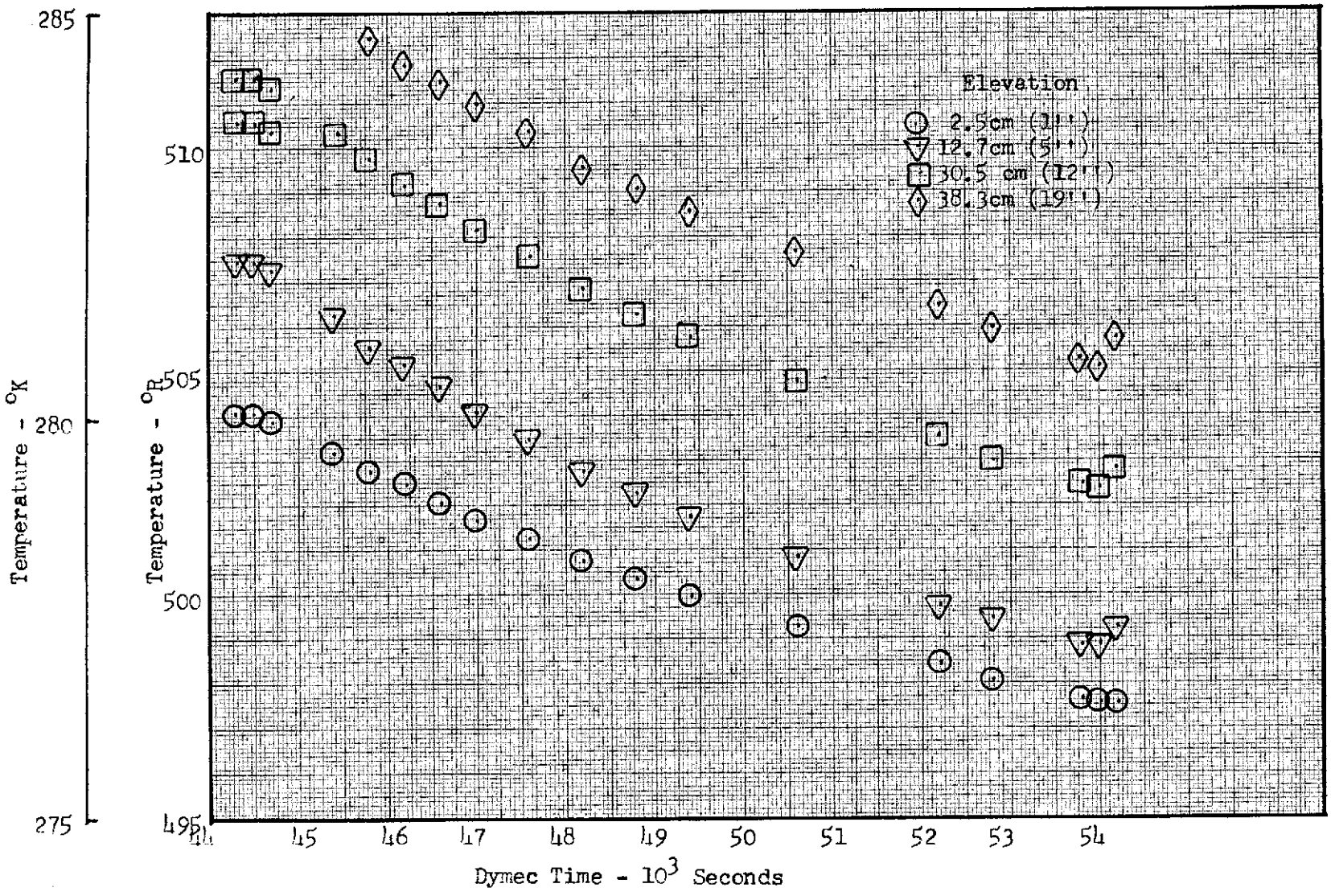

Fig. 4-14 Liquid Temperature Histories, Test B-9; Fluid-F-11; 10% Spherical Ullage; 3/4-In. Media

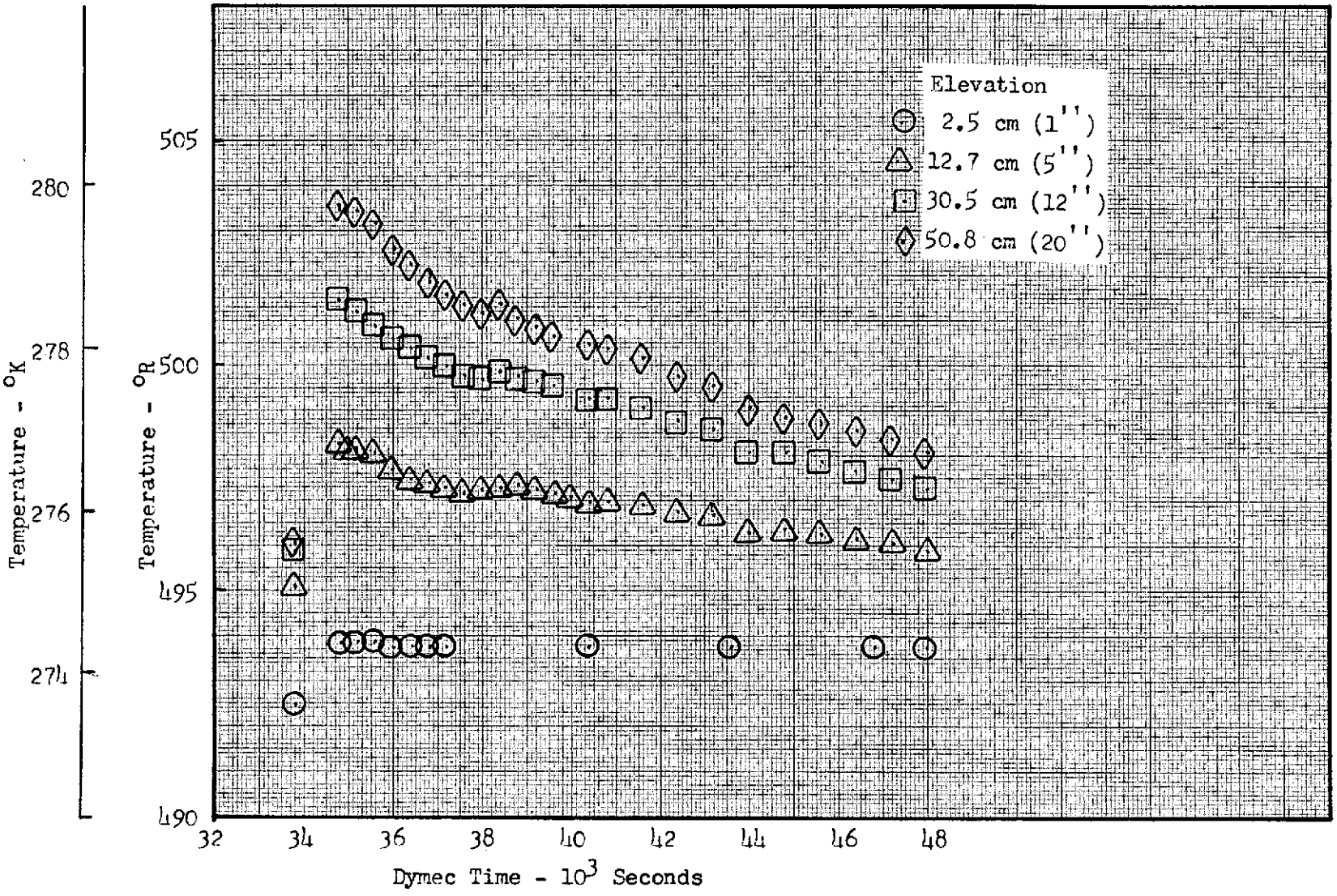

Fig. 4-15 Liquid Temperature Histories, Test B-16; Fluid F-11; 10% Spherical Ullage; 1-1/2-In. Porous Media

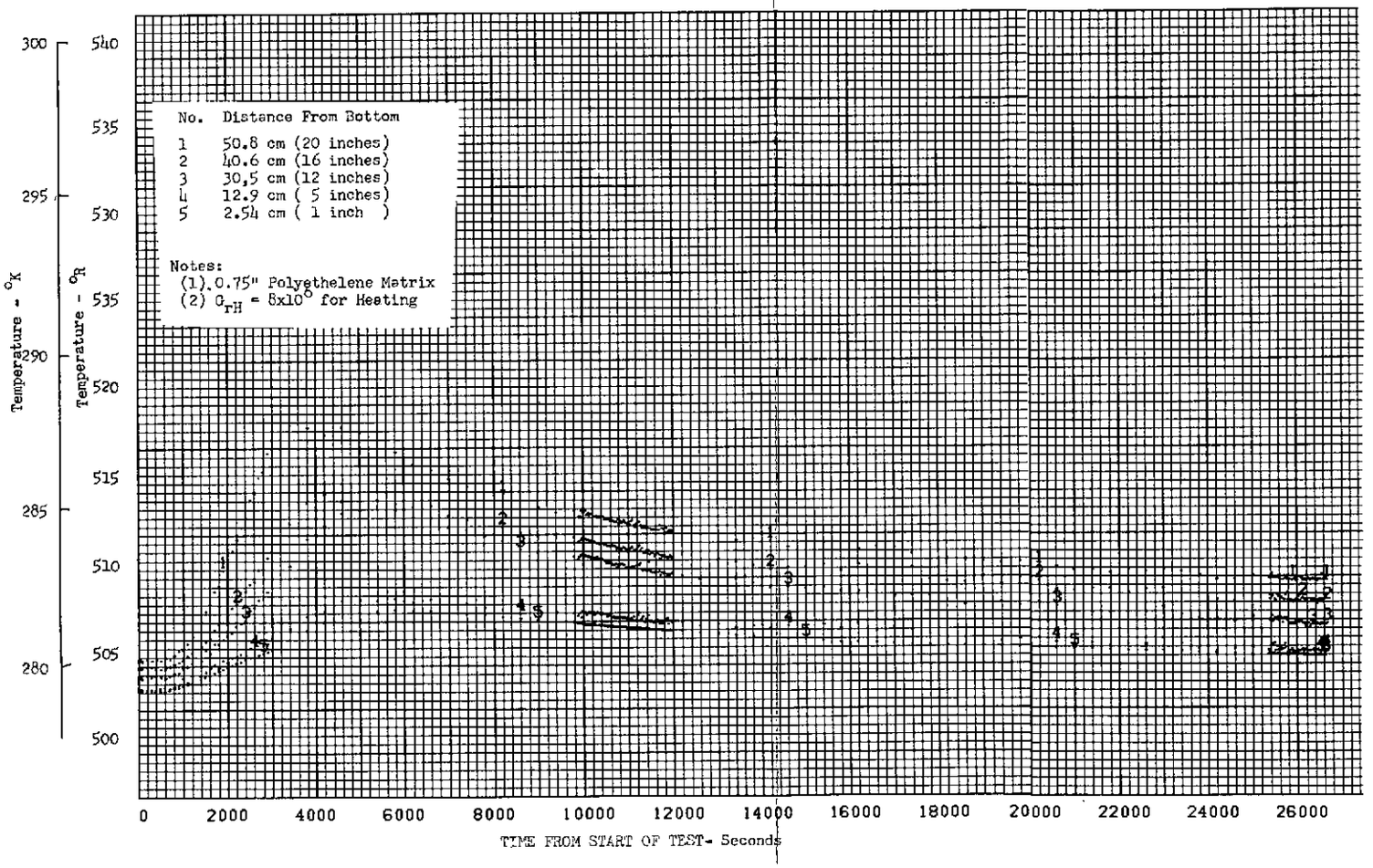

Fig. 4-16 Liquid Temperature Histories for Test B-23, Test Fluid-oil, Test Tank-Cylinder, Ullage Volume 10% Spherical

PRECEDING PAGE BLANK NOT FILMED

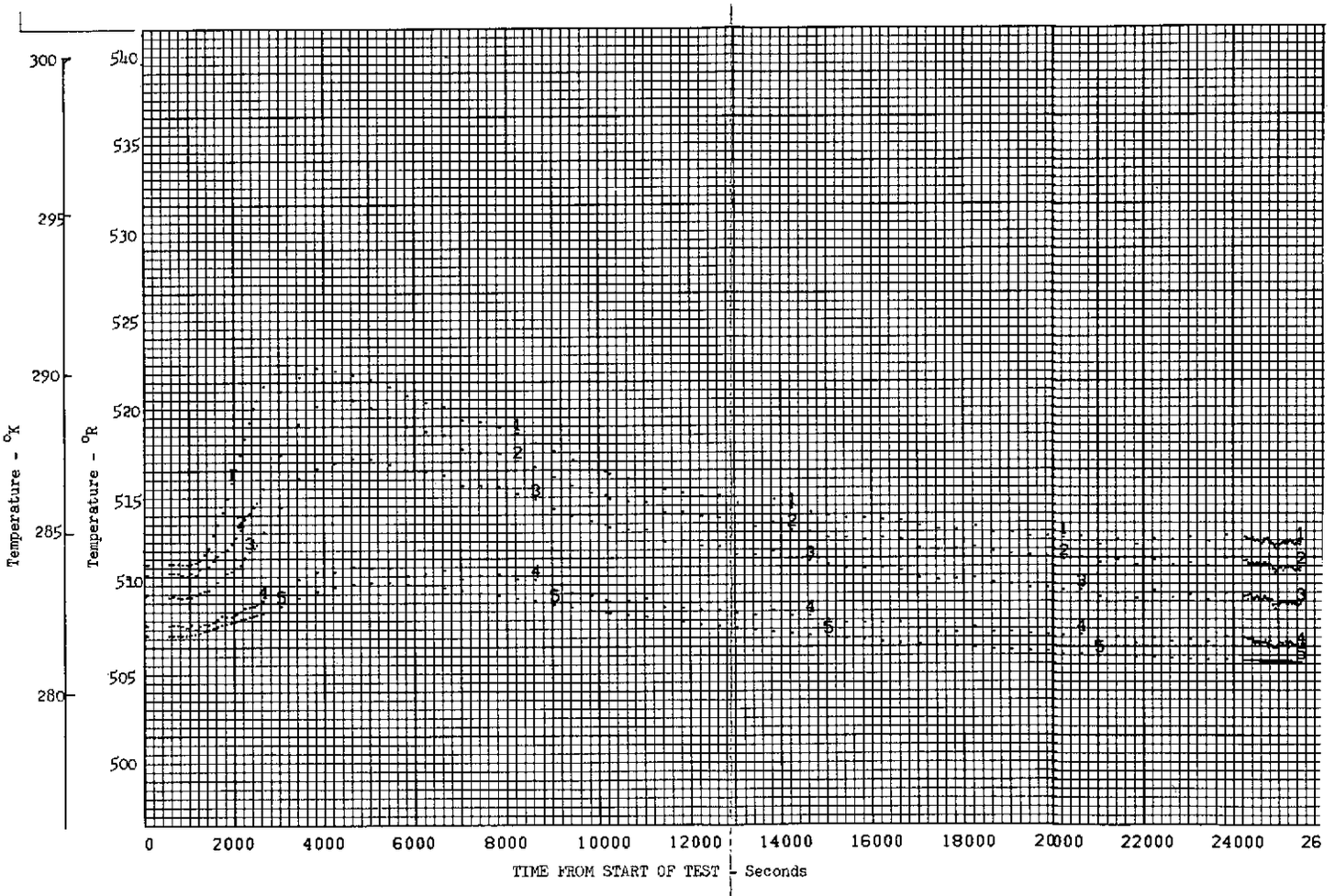

Fig. 4-17 Fluid Temperature Histories for Test B-24, Test Fluid-Oil, Test Tank-Cylinder, Ullage Volume 5% Flat

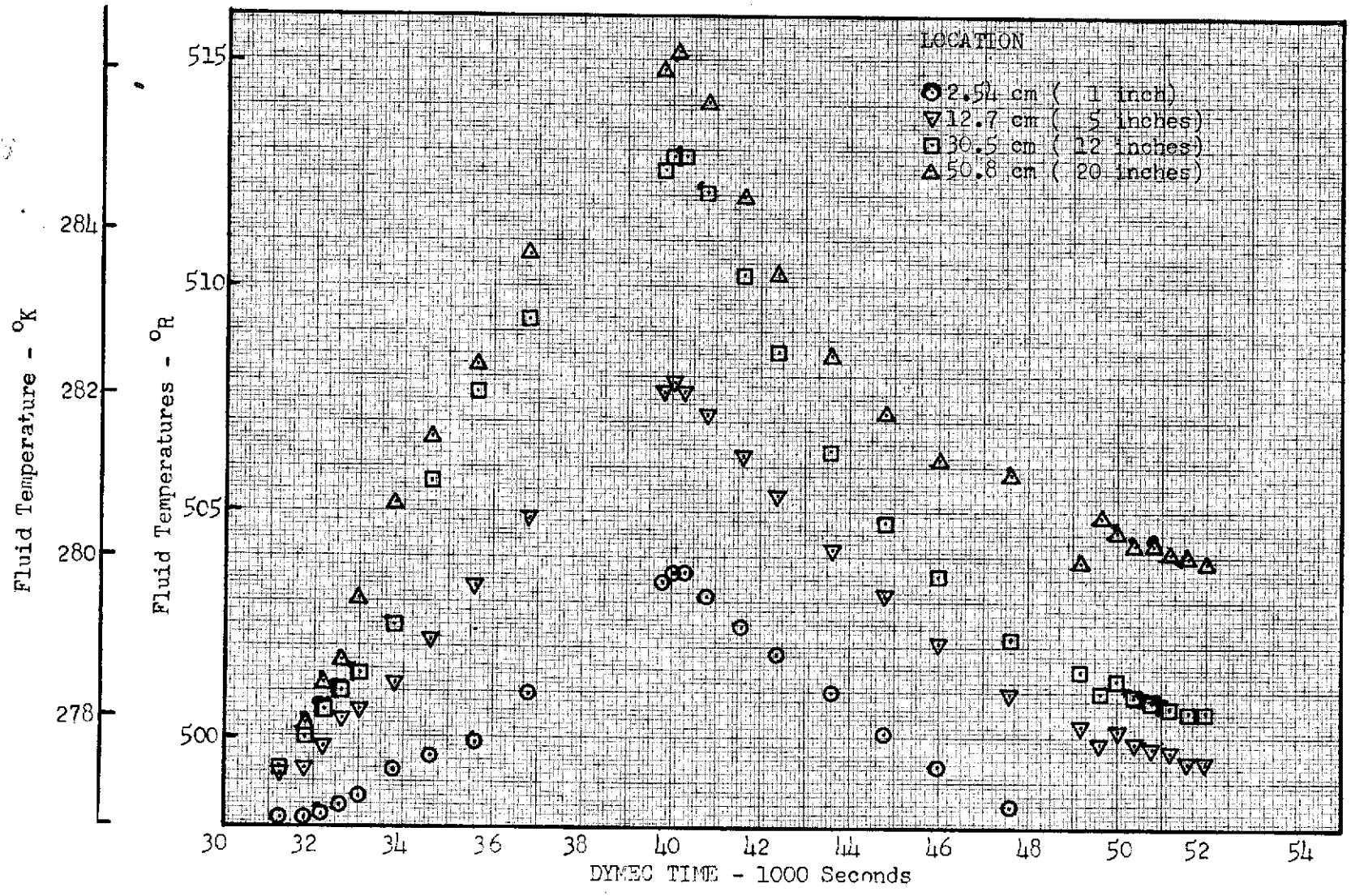

Fig. 4-18 Fluid Temperature Histories for Test B-8, Test Fluid - F-11, Test Tank - Cylinder, Ullage Volume 50%, No Internal Porous Media

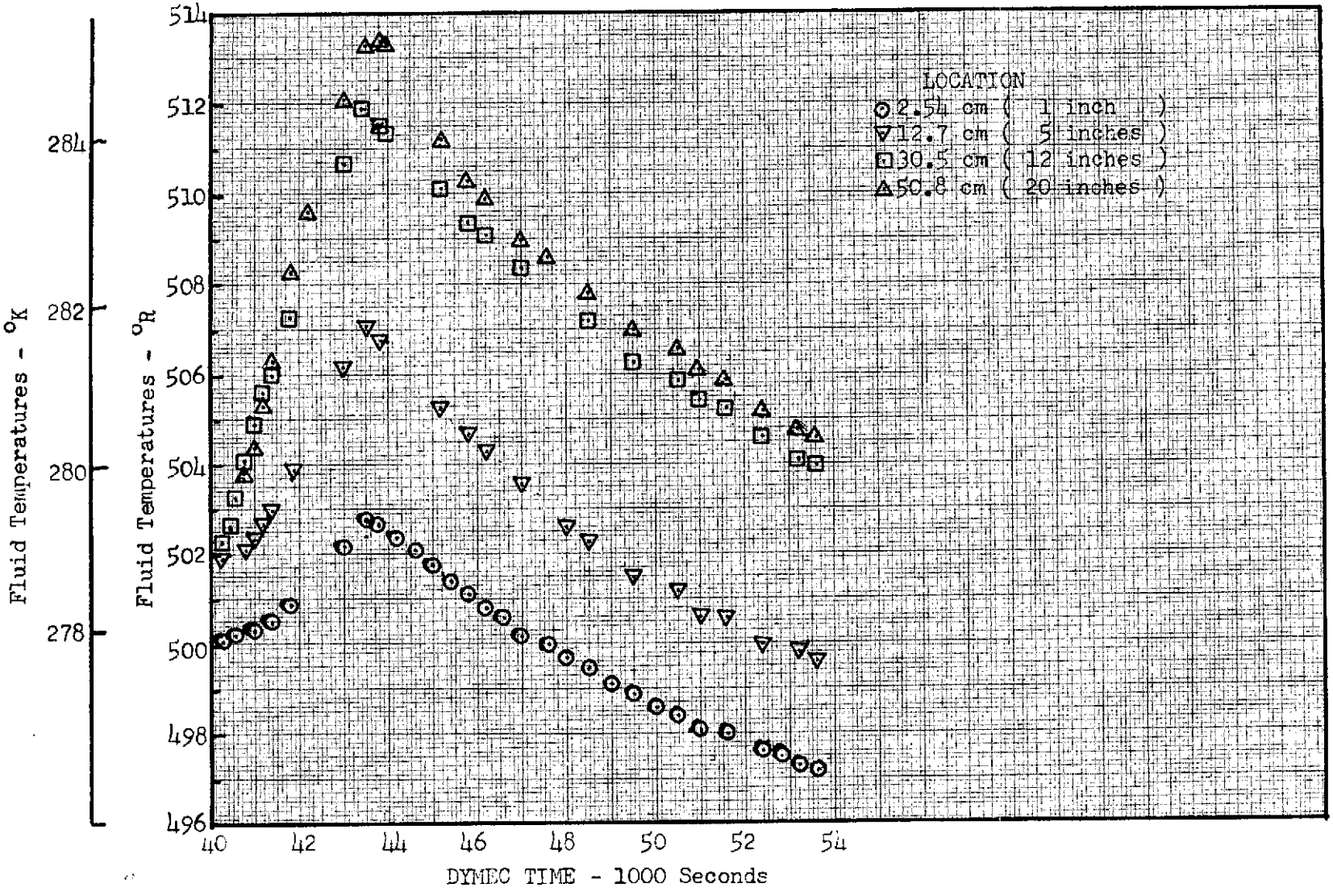

Fig. 4-19 Liquid Temperature Histories for Test B-7, Test Fluid-F-11, Test Tank - Cylinder, Ullage Volume 15%, No Internal Porous Media

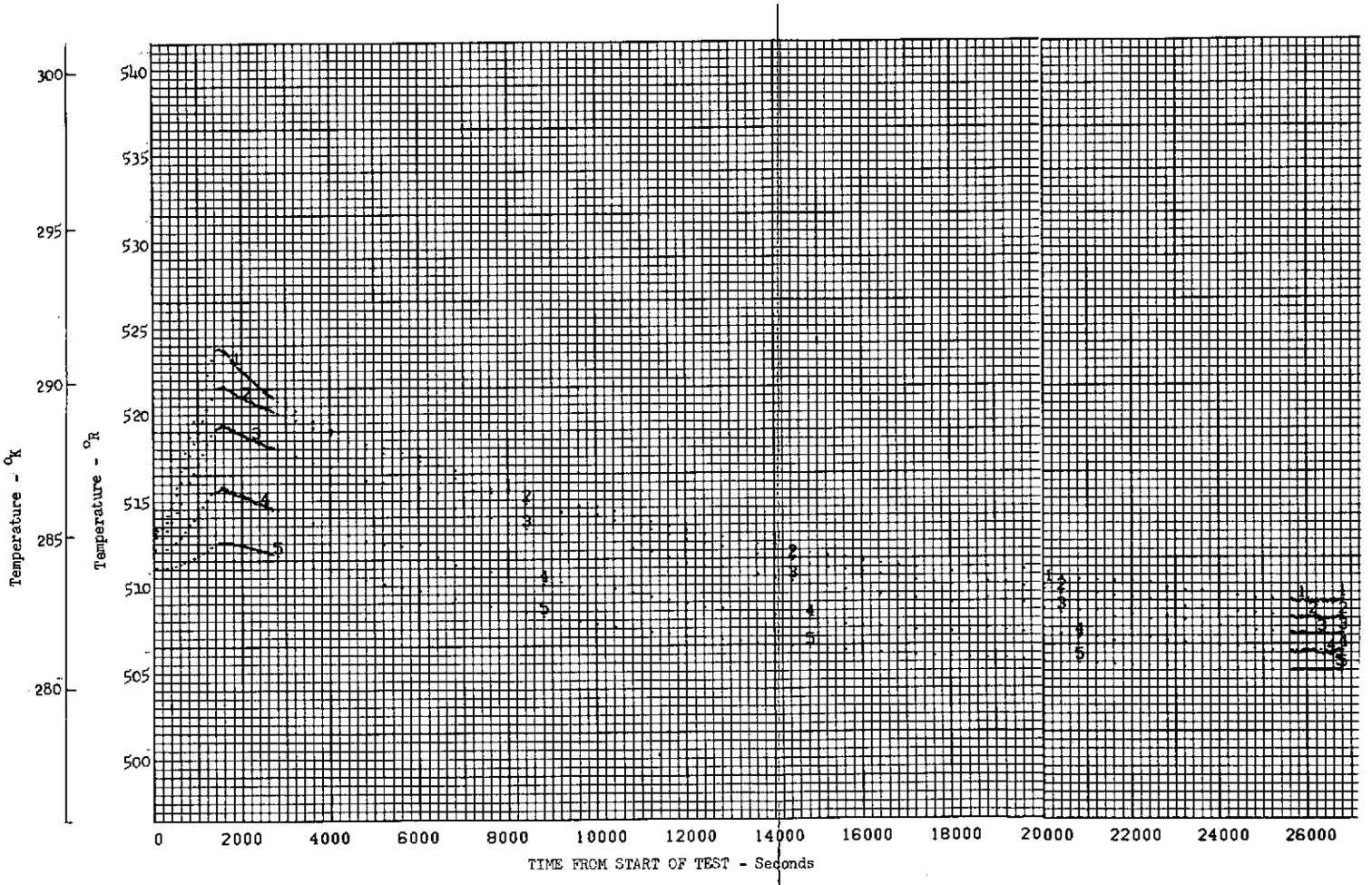

Fig. 4-20 Liquid Temperature Histories for Test B-22, Test Fluid - F-11, Test Tank - Cylinder, Ullage Volume 10% Spherical

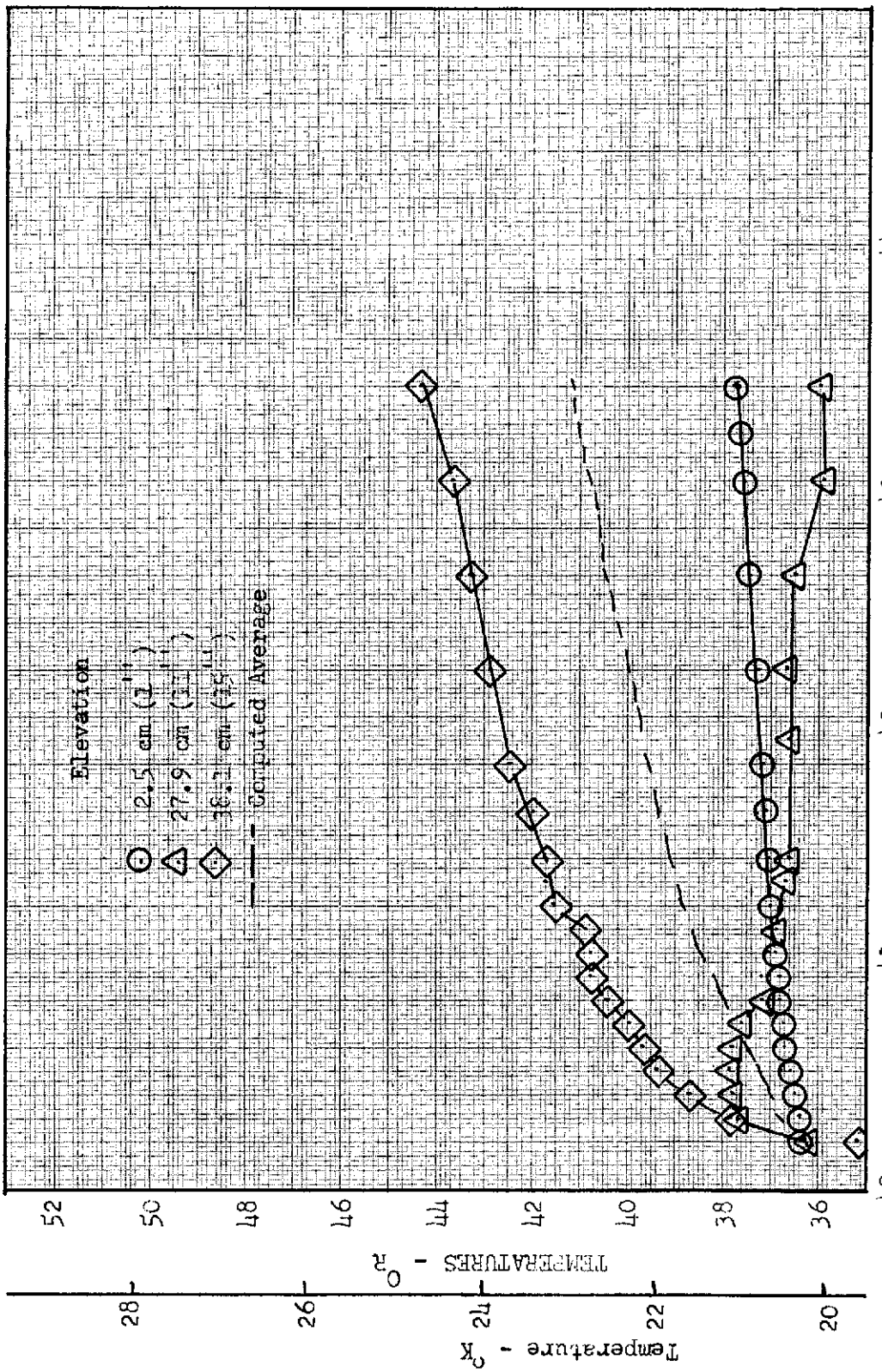

Fig. 4-21 Temperature Histories for Liquid Hydrogen Test C-3; Ullage Volume 15%

PRECEDING PAGE BLANK NOT FILMED

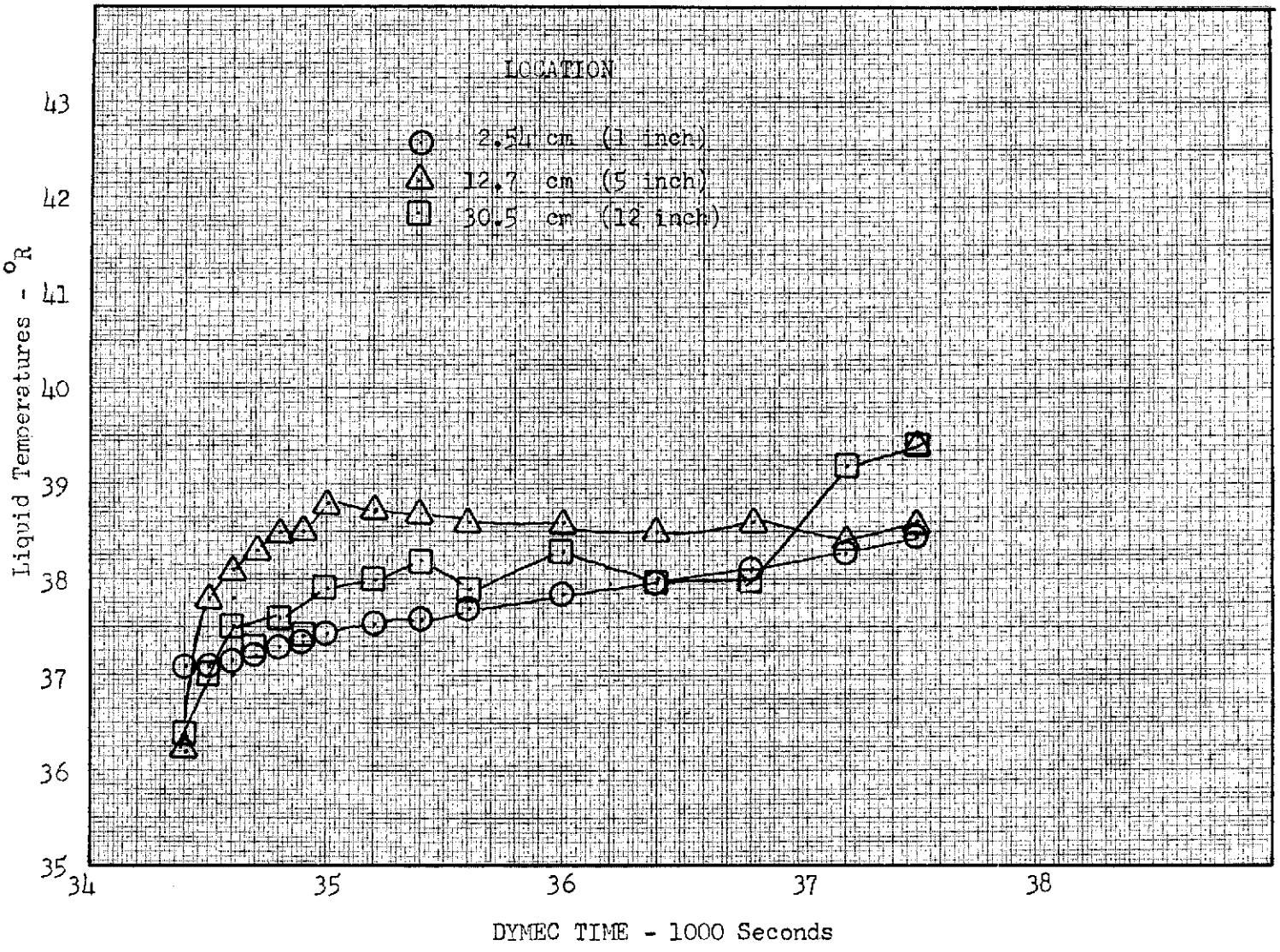

Fig. 4-22 Temperature Histories for Liquid Hydrogen Test C-4; Ullage Volume 50%

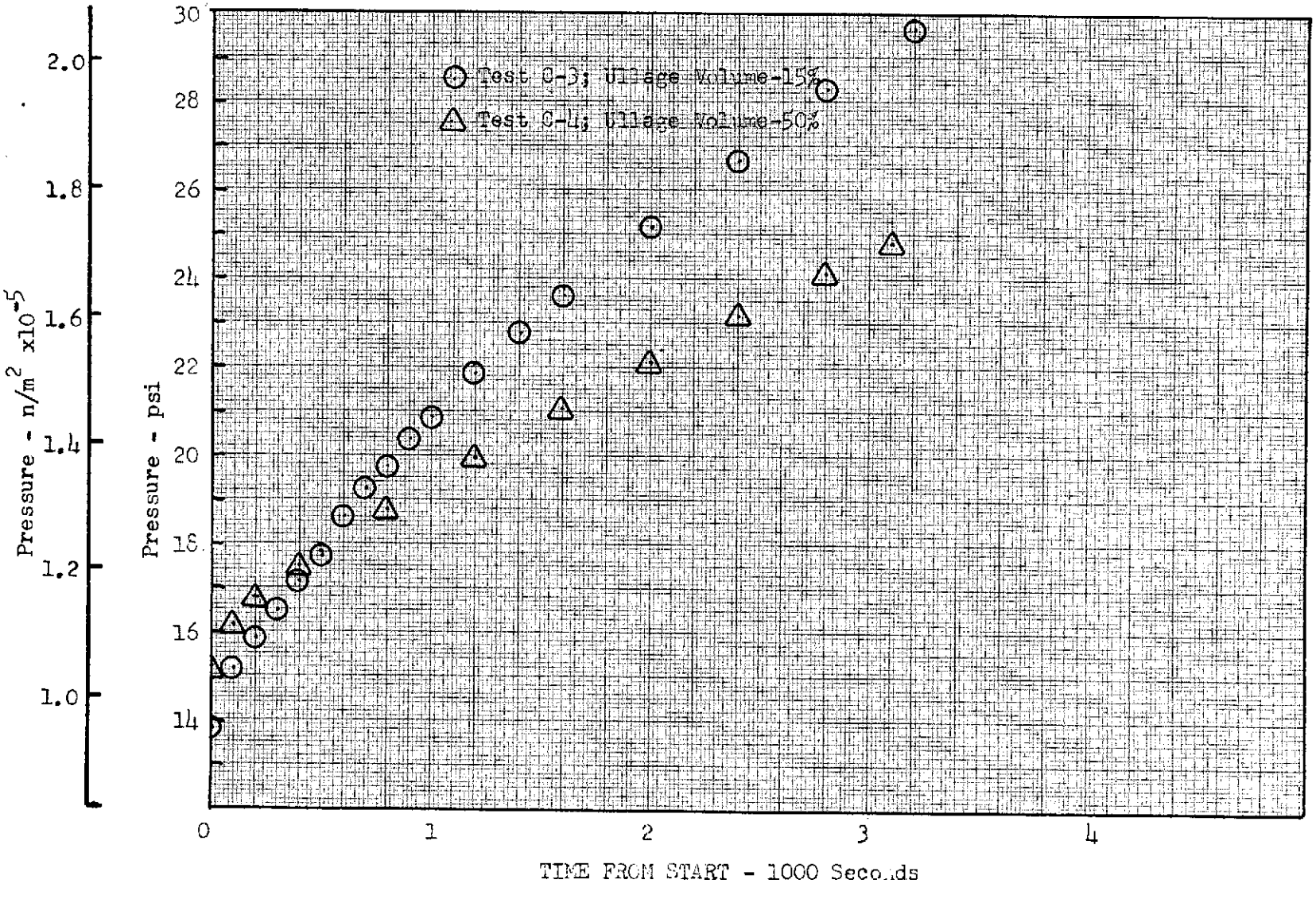

Fig. 4-23 Pressure Histories for Liquid Hydrogen Tests C-3 and C-4

$$\frac{T - T_B}{Ts - T_B} = (1 - Z/\Delta)^{\left(\frac{1-F}{F}\right)}$$

Assuming the characteristics shape of the stratified temperature profile to be time invariant, F is given by:

$$F = \int_0 \frac{T - T_i}{T_s - T_i} d\,(Z/\Delta)$$

where Z is the distance below the interface and Δ is the total depth of the temperature stratification. Figures 4-24 and 4-25 show typical temperature profiles at various times from the start of heating for Tests B-7 and B-11. In each run the interface is at 51.8 cm (20.4 in.). Test B-7 has only freon in the tank, while B-11 has Freon with the 3/4-in. polethelene media. The respective heat fluxes are 136 and 334W/m^2, (43 and 106 Btu/hr-ft^2). The stratified layer depth was obtained and the nondimensional profiles were plotted as shown in Figs. 4-26 and 4-27. These confirm the time invariancy of the profile shape and result in energy integrals of 0.42 and 0.37 for Tests B-7 and B-11, respectively. The dashed lines shown in Fig. 4-26 are obtained with the above equation for $(T - T_B)$ using the experimental value $F = 0.42$.

Figure 4-28 shows the temperatures for Test B-26. The test fluid is oil. Also, the tank is filled all the way to the top; the ullage is spherical; and the 3/4-in. porous media is used. Even discounting the porous media, the effective Rayleigh Number is 6 orders of magnitude below that for Run B-7. Neverthless, the value of F is 0.4 as shown on Fig. 4-29. Figure 4-30 shows the nondimensional profile for Test B-1 (water) for which F is approximately 0.4 also.

Figure 4-31 shows some temperature profiles for Test A-2 during warm-up period. These are nondimensionalized on Fig. 4-32. Again, the time invariancy is confirmed.

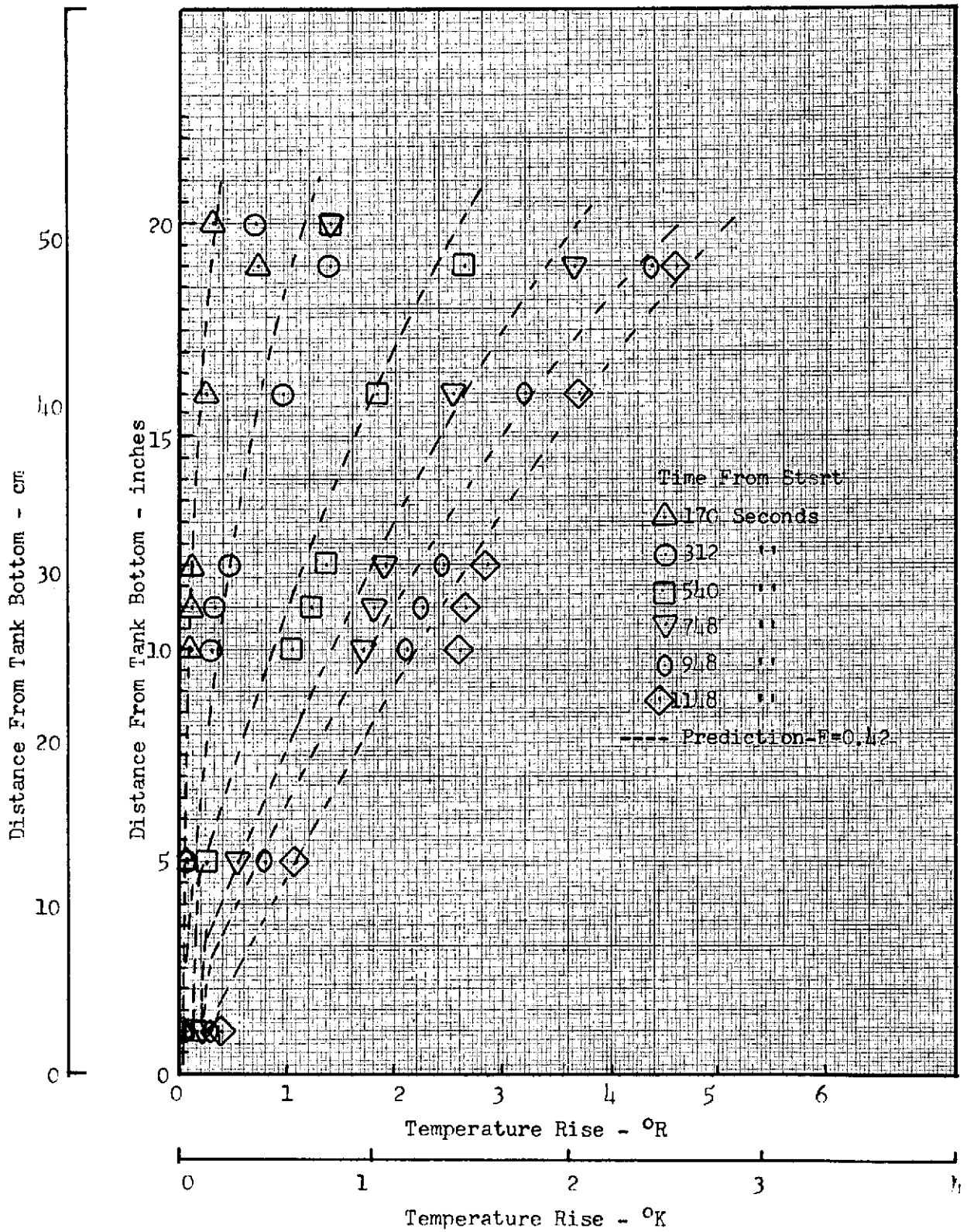

Fig. 4-24 Temperature Stratification Profiles, Test B-7

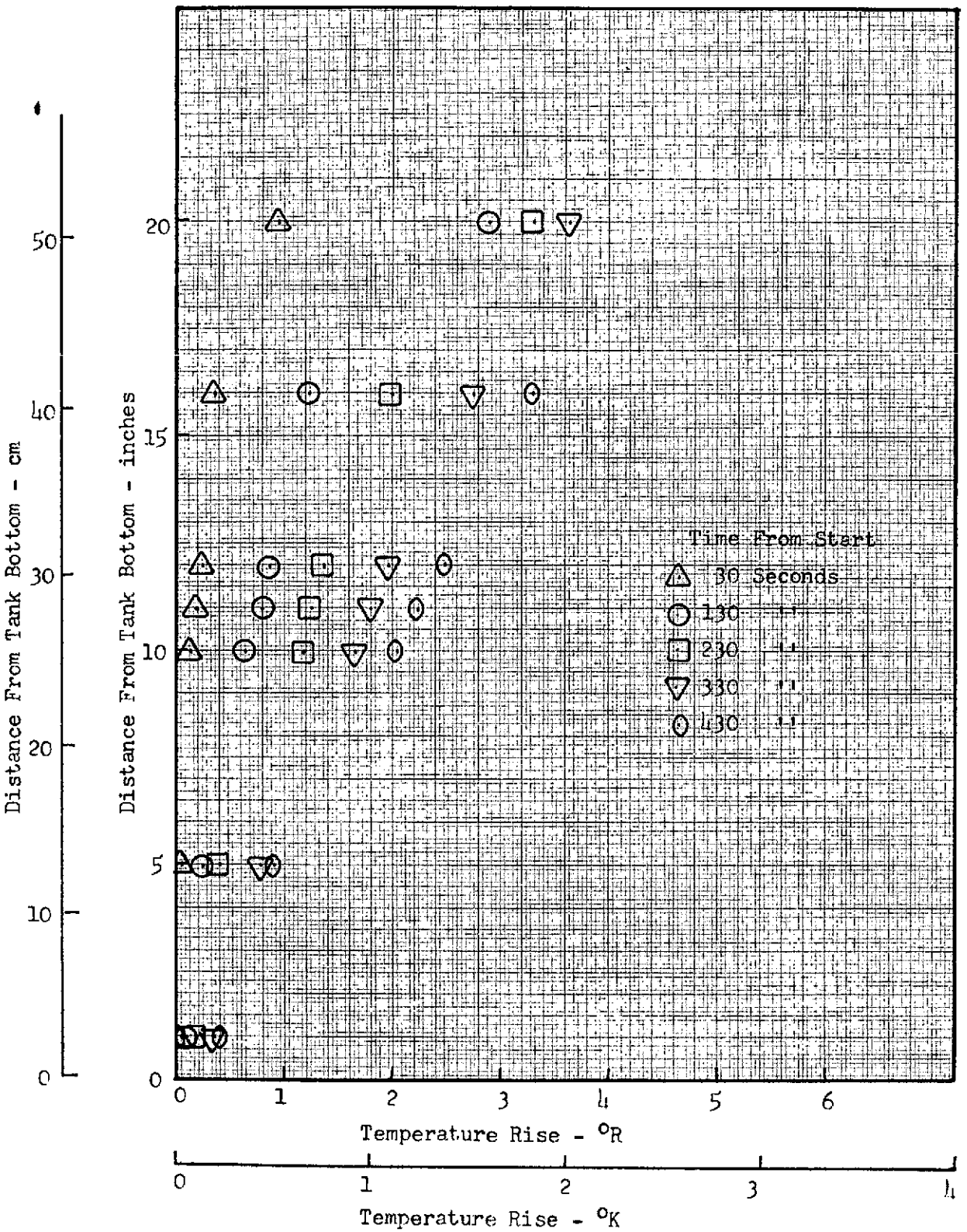

Fig. 4-25 Temperature Stratification Profiles, Test B-11

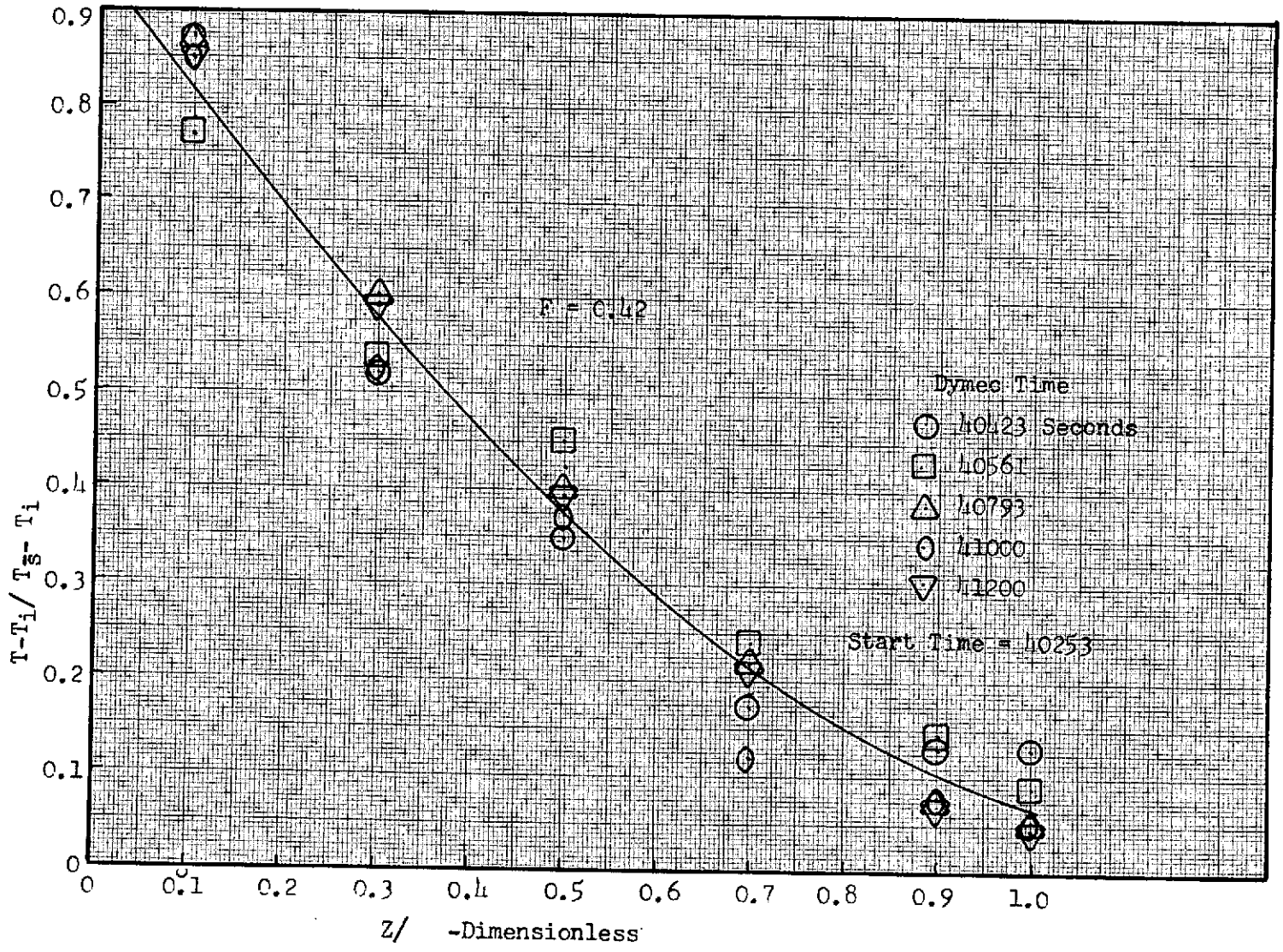

Fig. 4-26 Nondimensional Temperature Profiles, Test B-7

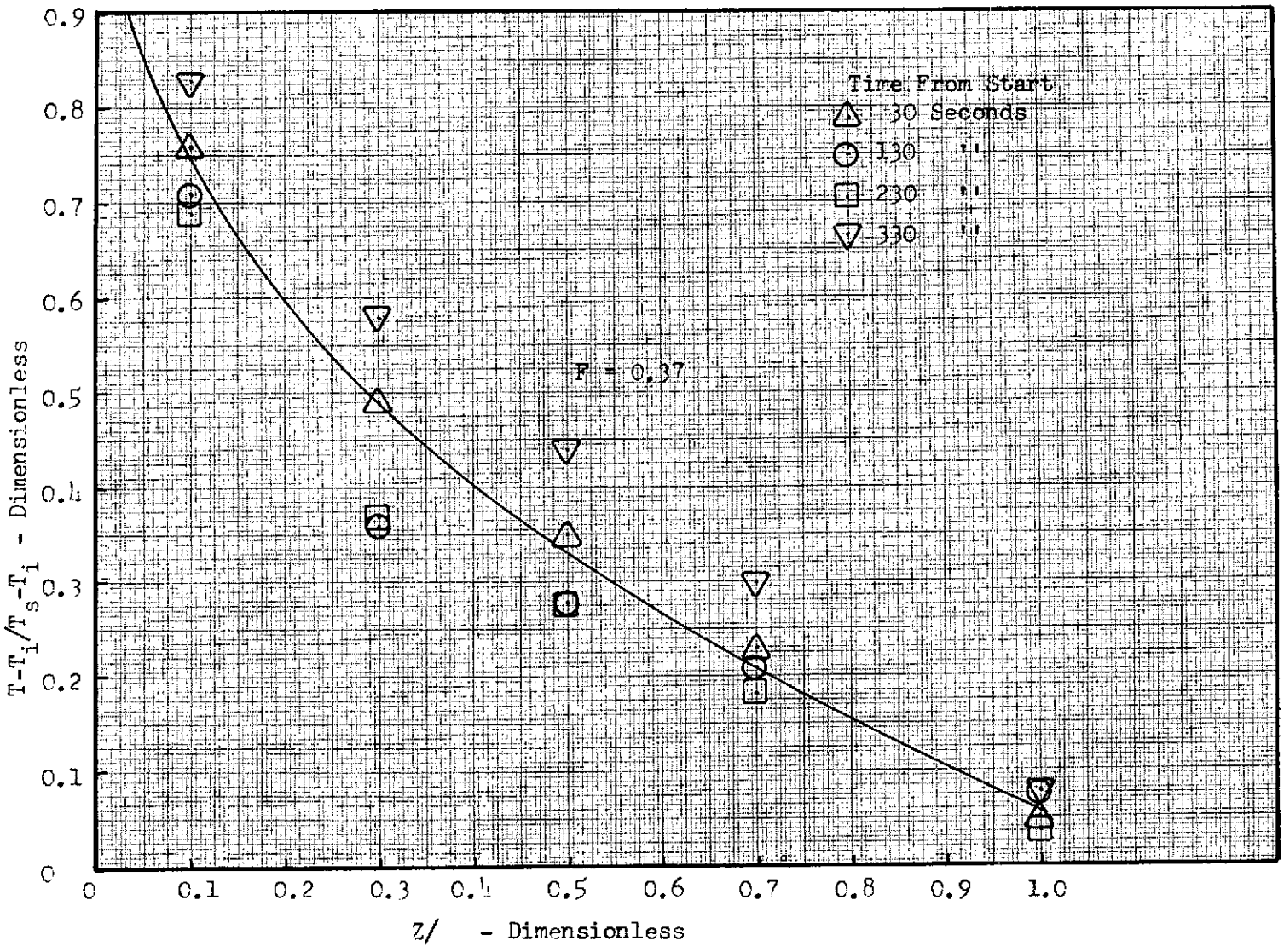

Fig. 4-27 Nondimensional Temperature Profiles, Test B-11

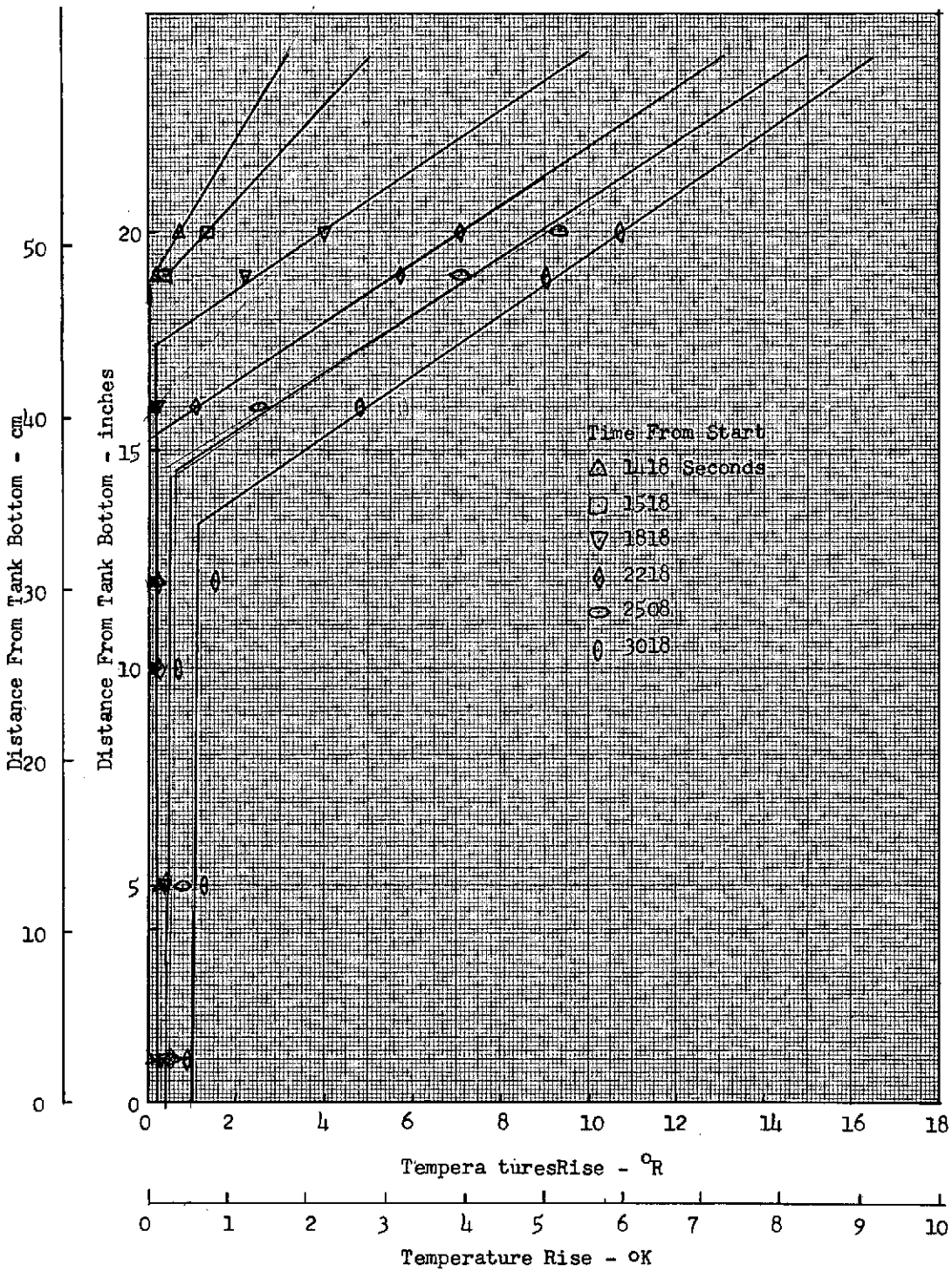

Fig. 4-28 Temperature Profiles for Test B-26, Test Fluid-Oil, Ullage Volume 5%, 3/4-in. Porous Media

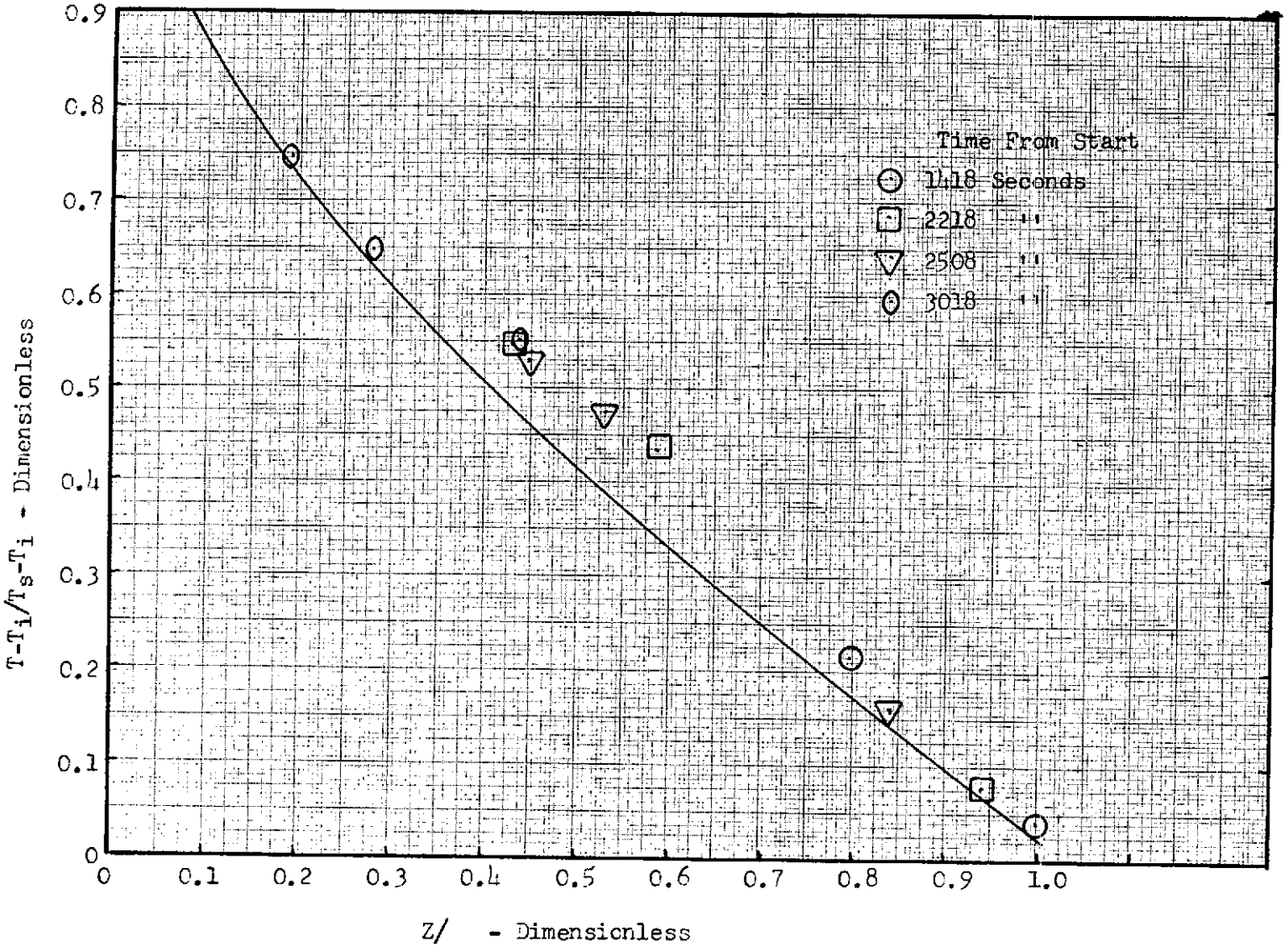

Fig. 4-29 Nondimensional Temperature Stratification Profile, Test B-26

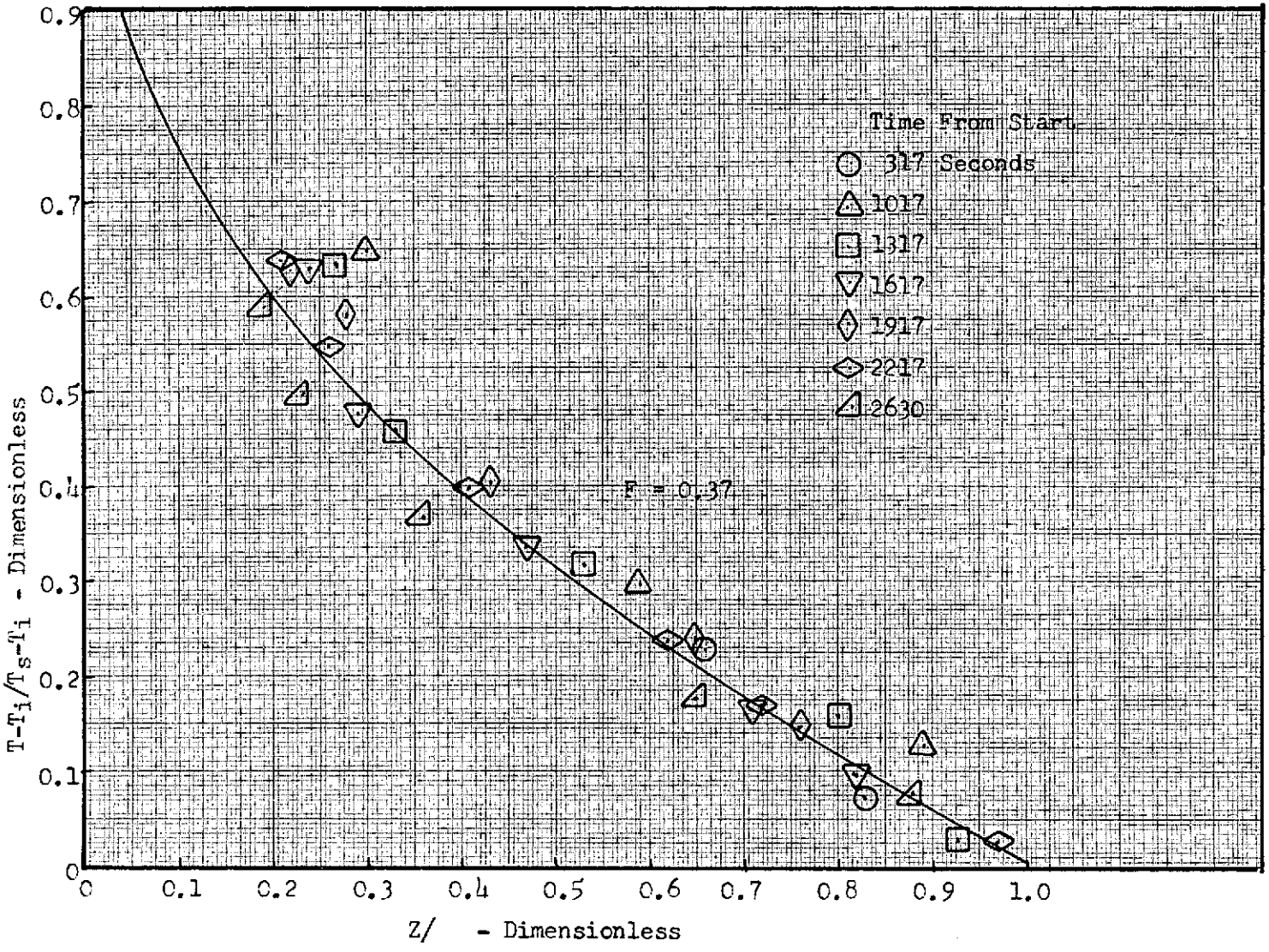

Fig. 4-30 Nondimensional Temperature Stratification Profile, Test B-1

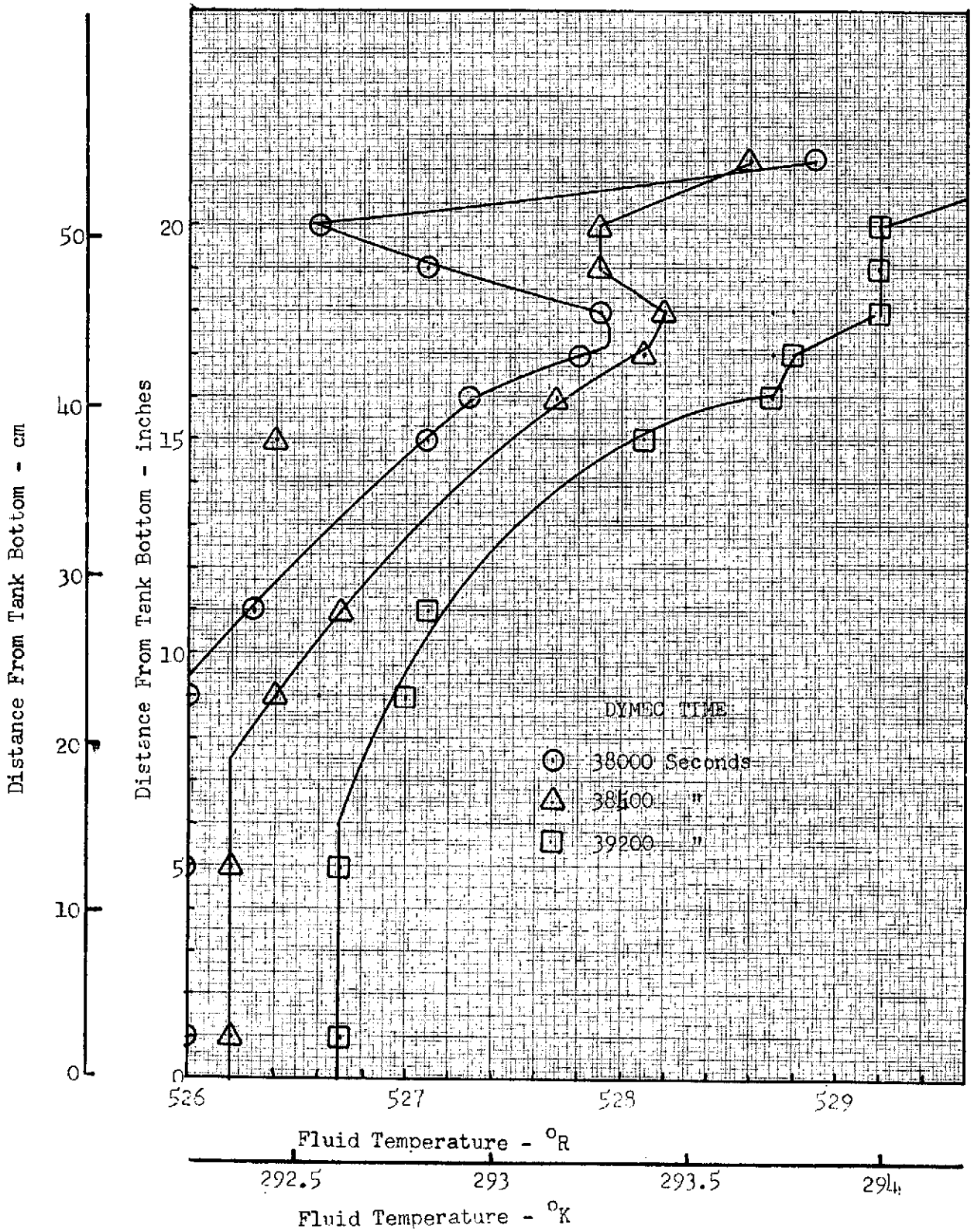

Fig. 4-31 Temperature Profiles for Test A-2, Test Fluid-F-11, Ullage Volume 15%

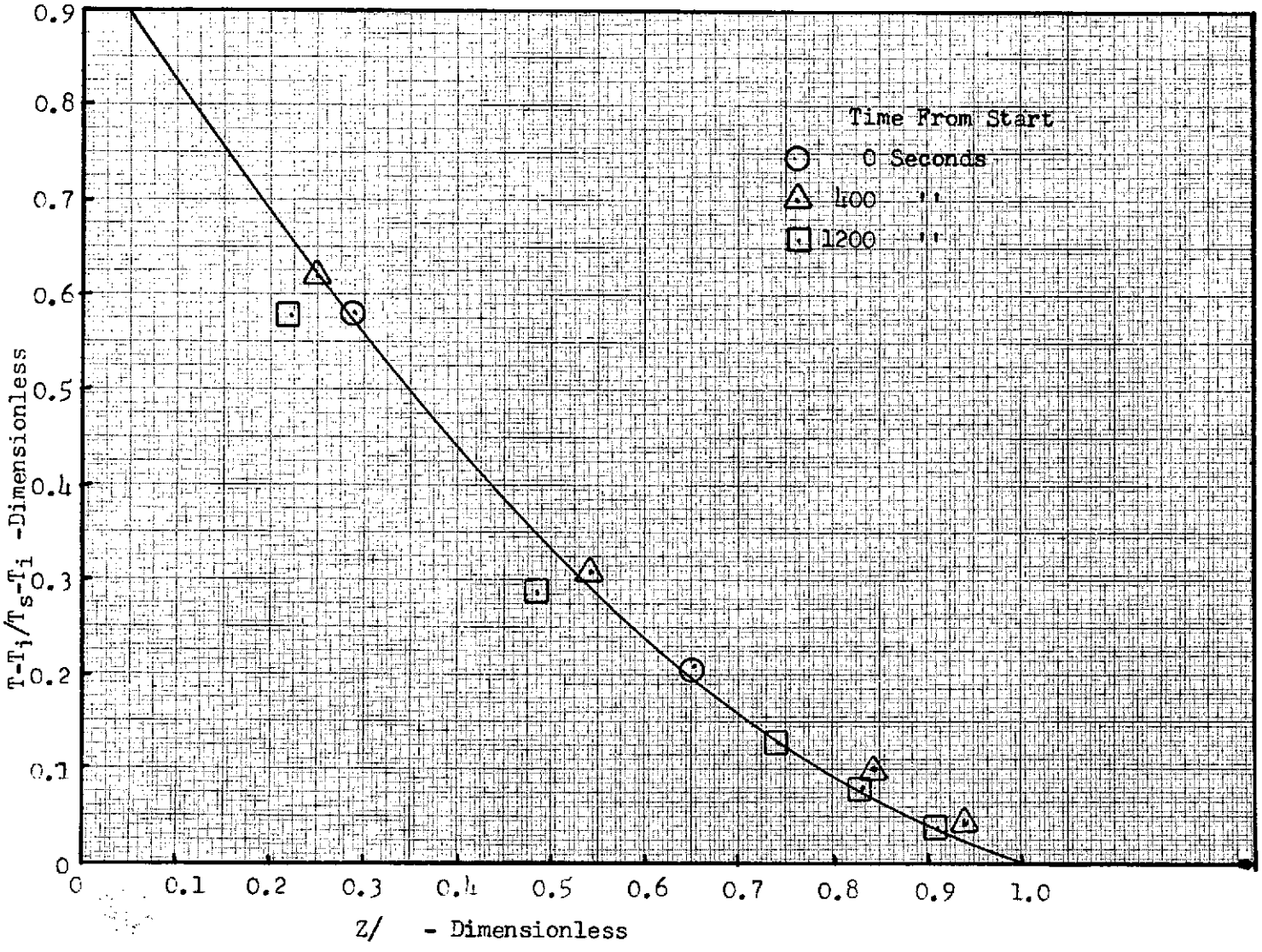

Fig. 4-32 Nondimensional Temperature Stratification Profile, Test A-2

The value of F, determined by graphical integration of Fig. 4-32, is 0.37. The liquid level for this run was at approximately 17 in. which corresponds to the maximum liquid temperature. The tank was vented just before the beginning of the test which caused some instability in the vapor temperatures above the interface. Thus, the temperature at 50.9 cm (20 in.) started off slightly subcooled relative to the surface liquid. However, within 1200 sec, the vapor exceeded the liquid temperature and a stable condition existed before the heat exchanger was activated.

Figure 4-33 compares the results from these tests with the correlation for $\bar{F}$ which had been developed and reported in Ref. 8. The data from this program are in good agreement with the correlation.

The other major assumption employed in the model is the relationship between the Nusselt and Rayleigh Numbers. The average heat transfer coefficients between the liquid and wall were computed from the measured cooling rates and temperatures at several times during a test. Nusselt Number was then calculated, using boundary layer run length as the characteristic dimension, for comparison with a theoretical value determined from the experimental Rayleight Number. The temperature difference used to determine both the experimental film coefficient and the Rayleigh Number was the difference between the mean liquid and mean wall temperatures, i.e.,

$$\Delta T_{WL} = \frac{1}{N_L} \sum_{i=1}^{N_L} T_{L_i} - \frac{1}{N_W} \sum_{i=1}^{N_W} T_{W_i}$$

For a few cases, this was compared with the mean of the differences, i.e.,

$$\Delta T_{WL} = \frac{1}{N_L} \sum \left(T_L - T_W \right)_L$$

which was evaluated graphically. This method was considerably more time-consuming and did not improve the data correlation. Therefore, it was discarded in favor of the

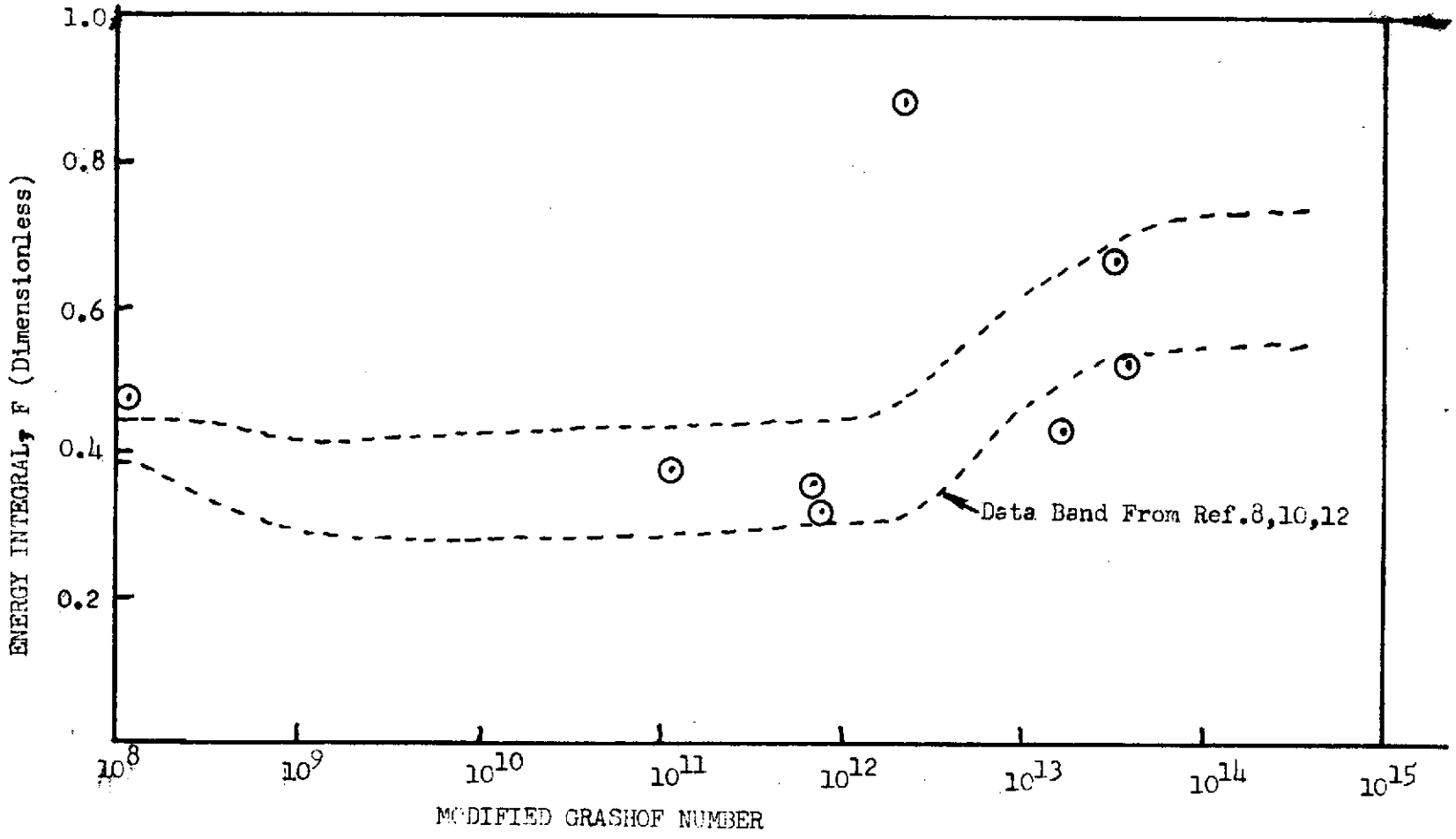

Figure 4-33 Comparison Between Energy Integral Data Form Current Program and That of Previous Investigators

Fig. 4-33 Comparison Between Energy Integral Data From Current Program and That of Previous Investigators

difference in the mean temperatures which could be determined rapidly with the aid of an electronic calculator.

The results from this portion of the comparison between model and experiment are shown on Fig. 4-34. The data generally support the model, although there is considerable scatter, particularly at the high Nusselt Numbers. However, the Nusselt temperature differences were rather small (0.2°K−5°K). The precision of the thermocouples was estimated to be approximately 0.3°K (0.5°R). It is believed that much of this scatter is due to these small temperature differences.

Figure 4-34 also shows the ineffectiveness of the polyethelene spheres. If the matrix had been effective in simulating low-g connection, the Nusselt Numbers for those tests (solid symbols) should be nearly two orders of magnitude lower than for the other tests, which is clearly not the case. Additional work in this area should be considered wherein smaller apparatus and much smaller pore sizes are used.

The confirmation of the heating profile and the cooling coefficients lend a certain amount of validity to the analytical model. However, the real proof comes not from the individual parts, but rather from the integrated model and the extent to which it correlates the test data. Figure 4-35 shows a direct comparison between the model prediction and the experimental pressure response for Test B-7 which was conducted in the cylindrical tank with Freon -11. Figures 4-36 and 4-37 show the temperature histories for the same test. The correlation is very good. On Figure 4-37, the dashed line represents the test data corresponding to the upper liquid node (node 6) and the bottom liquid node (node 14). At intermediate locations, the temperatures are nearly parallel. It can be seen that the major difference between model prediction and test data is that the computed temperatures merge into the surface temperature during the cooling process, which is not the case with the experimental data. The temperature merging occurs in the model when tank pressure drops to local saturation pressure, because no allowance is made for the static head on the subsurface liquid.

In the development of the analytical model, it was assumed that a spherical tank could be represented as a psuedo-cylindrical tank for which the geometry, psuedo heating rates, etc., are computed in the GEOM subroutine based on spherical tank inputs. The validity of this can be assessed from Figs. 4-38 and 4-39. These present a direct comparison between experimental and pressure responses with liquid hydrogen at 15 and 50% ullage. The curves indicated as "model" are based upon the computation with a uniform heat flux established from the boiloff tests. However, when the tank wall heat exchanger was activated, and the tank was locked up, the vent line became a trapped vapor pocket which extended from the top of the tank out to the chamber wall. The effect on ullage volume was insignificant. However, this results in a heat leak that is not determined during a boiloff test when the line is being cooled by the vented vapor, but which goes into direct ullage heating during the tank wall heat exchanger operation. An upper and lower limit was estimated to be 0.85 W (2.9 Btu/hr) and 0.22 W (0.75 Btu/hr), respectively, for this direct heat source. The curves labeled as "modified model" on Figs. 4-38 and 4-39 are for the added effect of the direct addition of 0.85 W to the ullage. The basic model falls below the experimental pressure resp nses and the upper limit overpredicts the test results. Therefore, the deficiency is in the experiment and one can conclude that the analytical model developed in this program, for the tank wall heat exchanger, is a valid performance evaluation instrument.

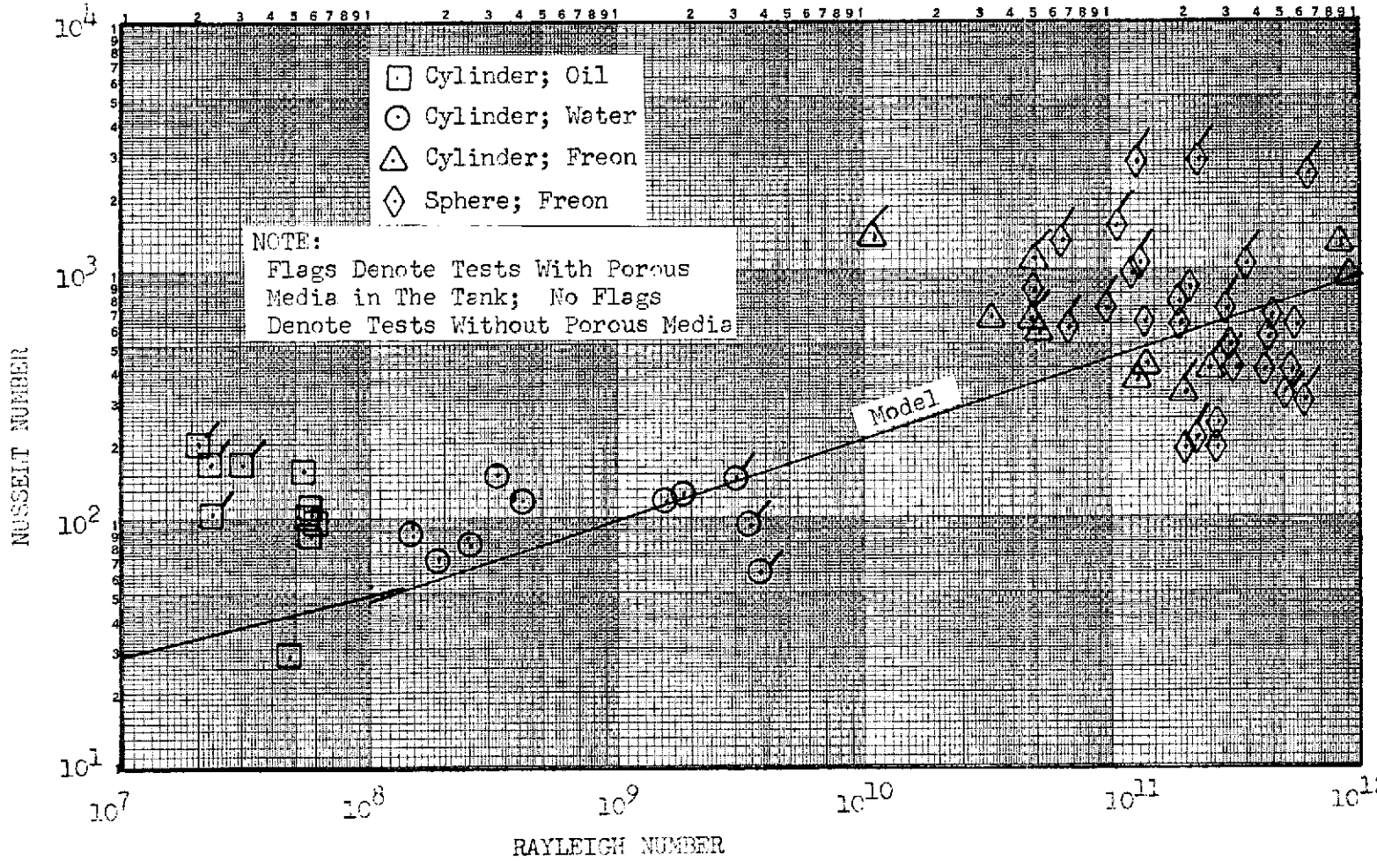

Fig. 4-34 Comparison Between Experimental Nusselt Numbers and Analytical Model

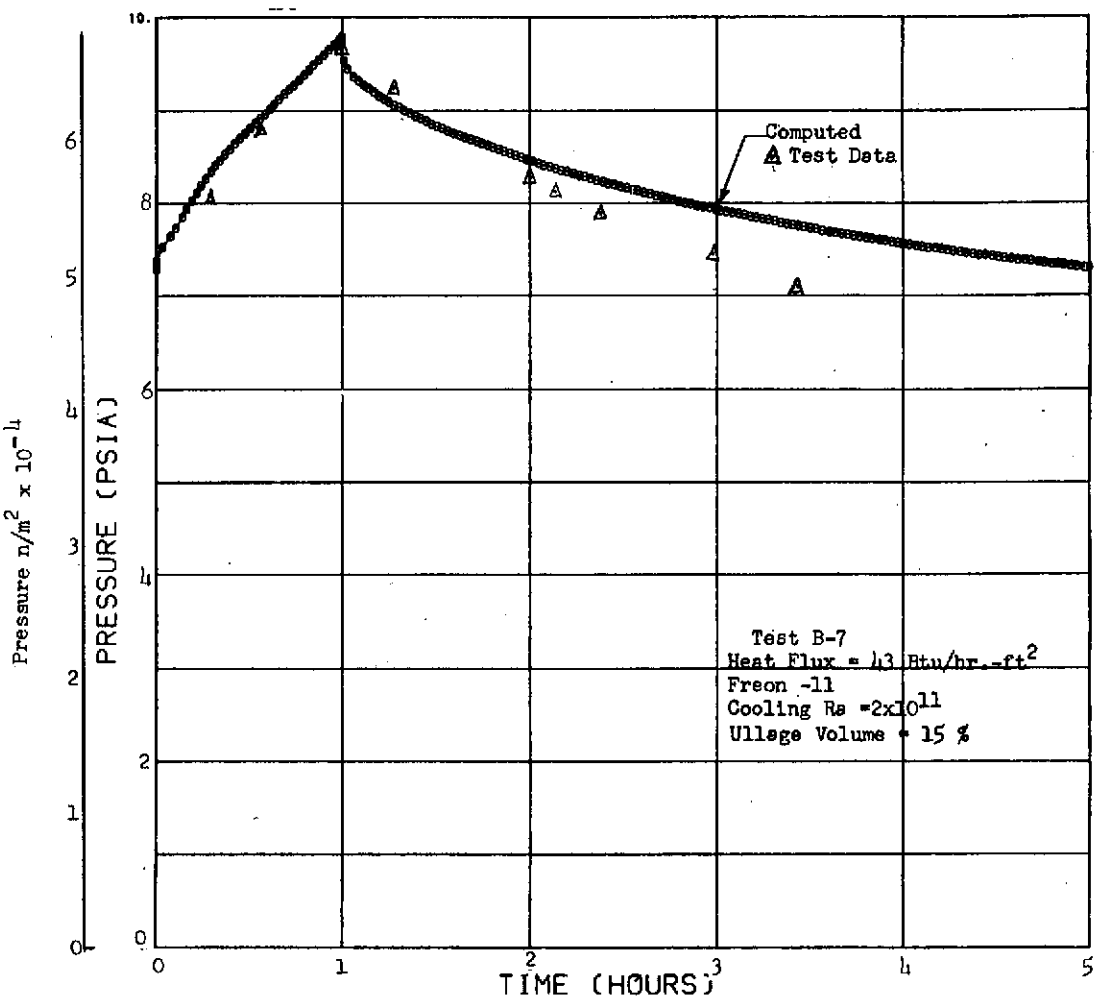

Fig. 4-35 Comparison Between Experimental Pressure History and Analytical Model Prediction, Test B-7

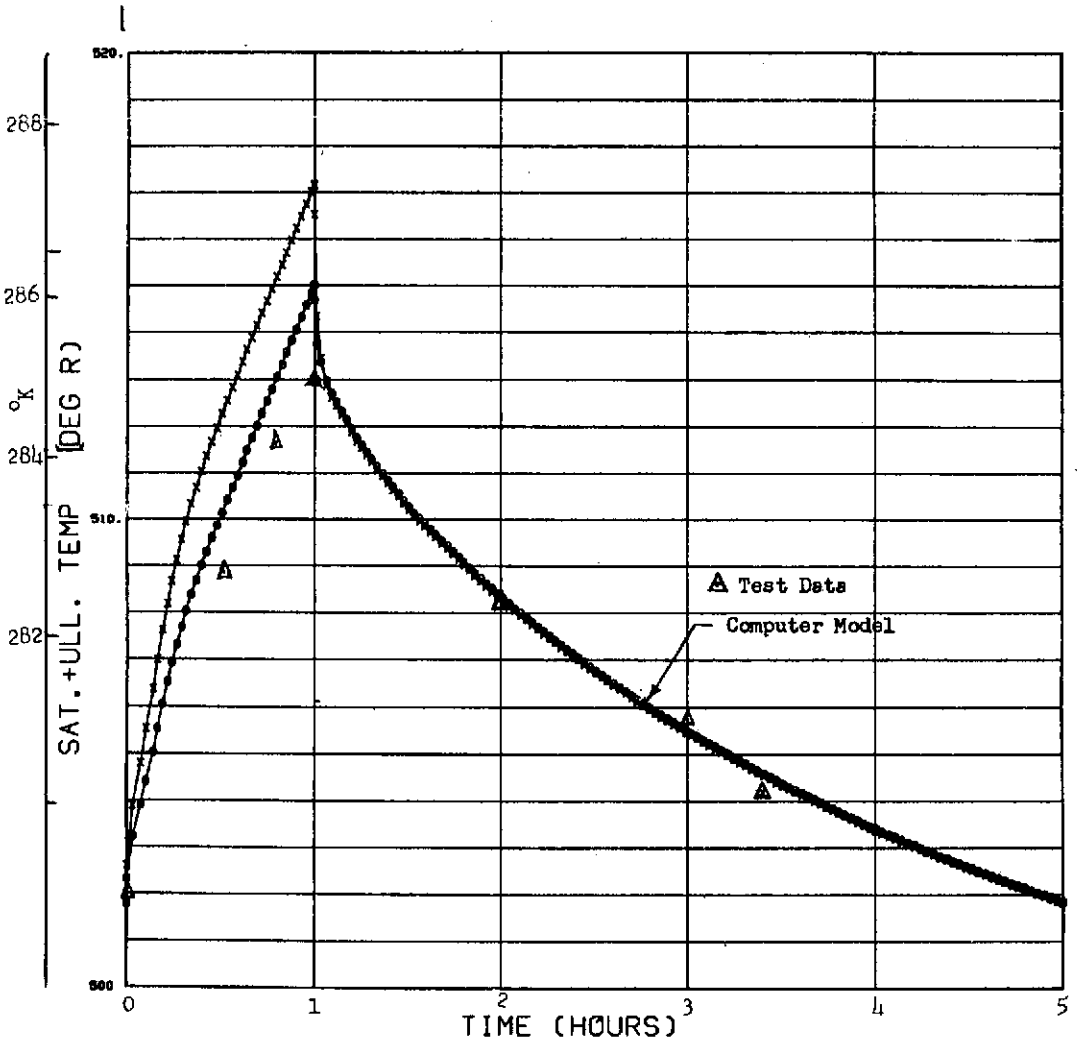

Fig. 4-36 Comparison Between Experimental and Analytical Saturation Temperatures, Test B-7

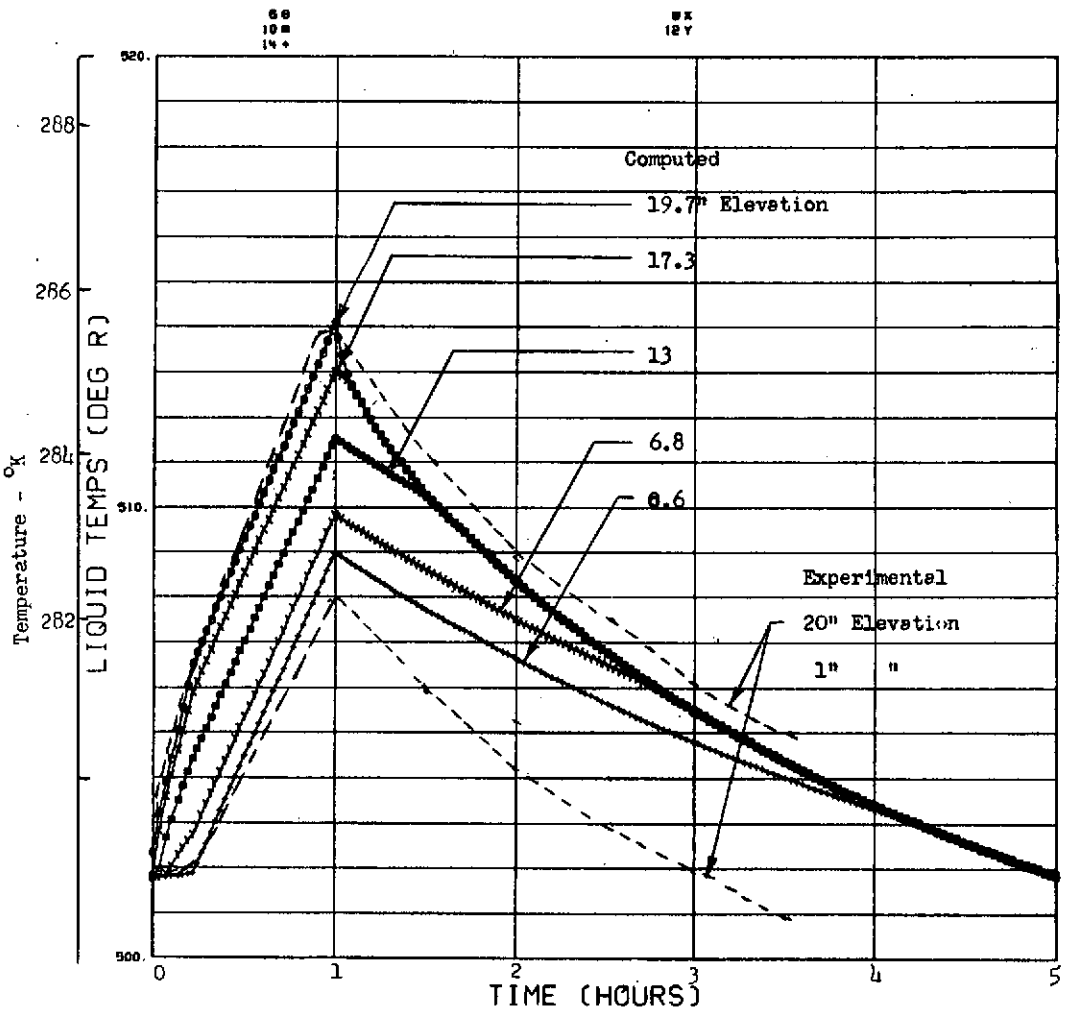

Fig. 4-37 Comparison Between Experimental and Analytical Liquid Temperatures, Test B-7

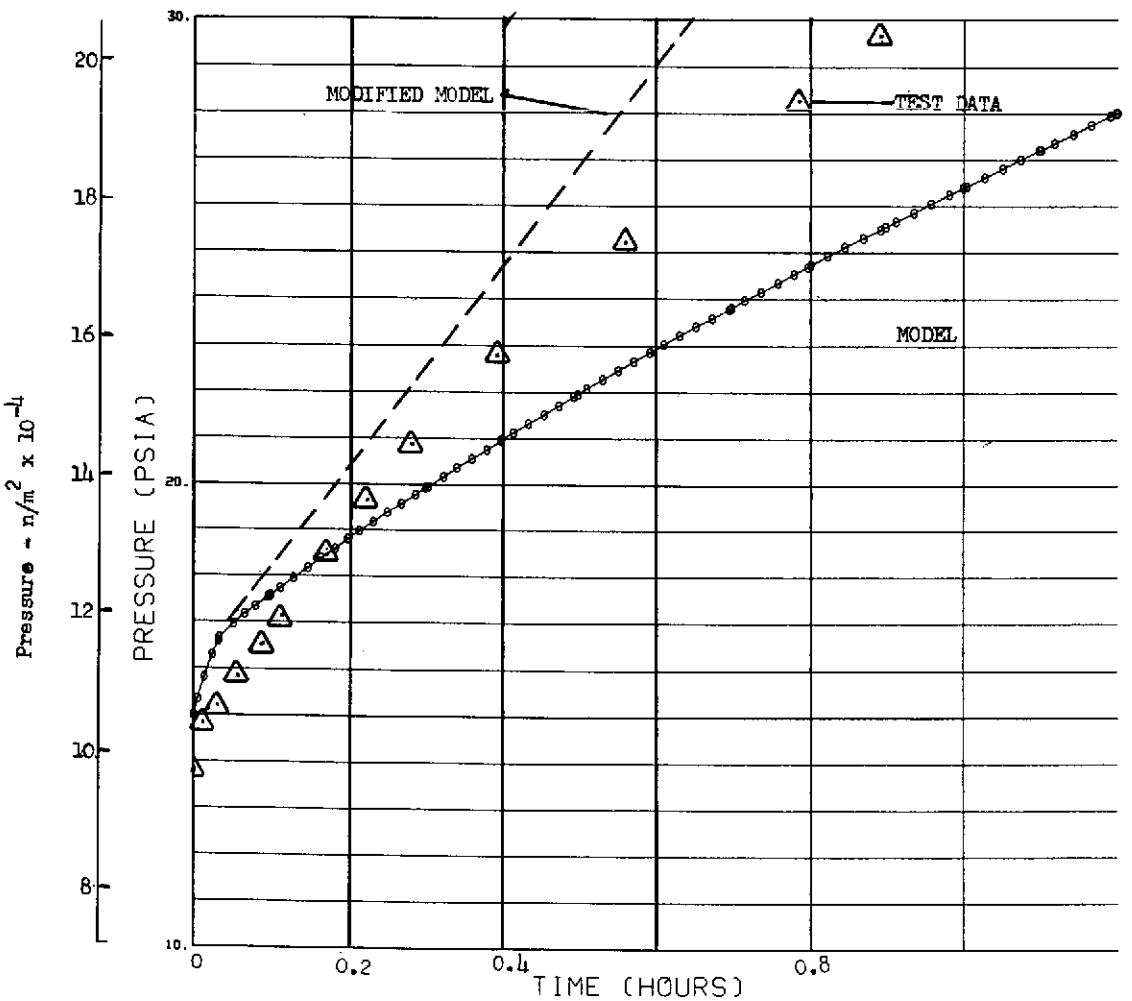

Fig. 4-38 Comparison Between Experimental Pressure and Analytical Prediction For LH_2 Test – C-3; Ullage Volume 15%

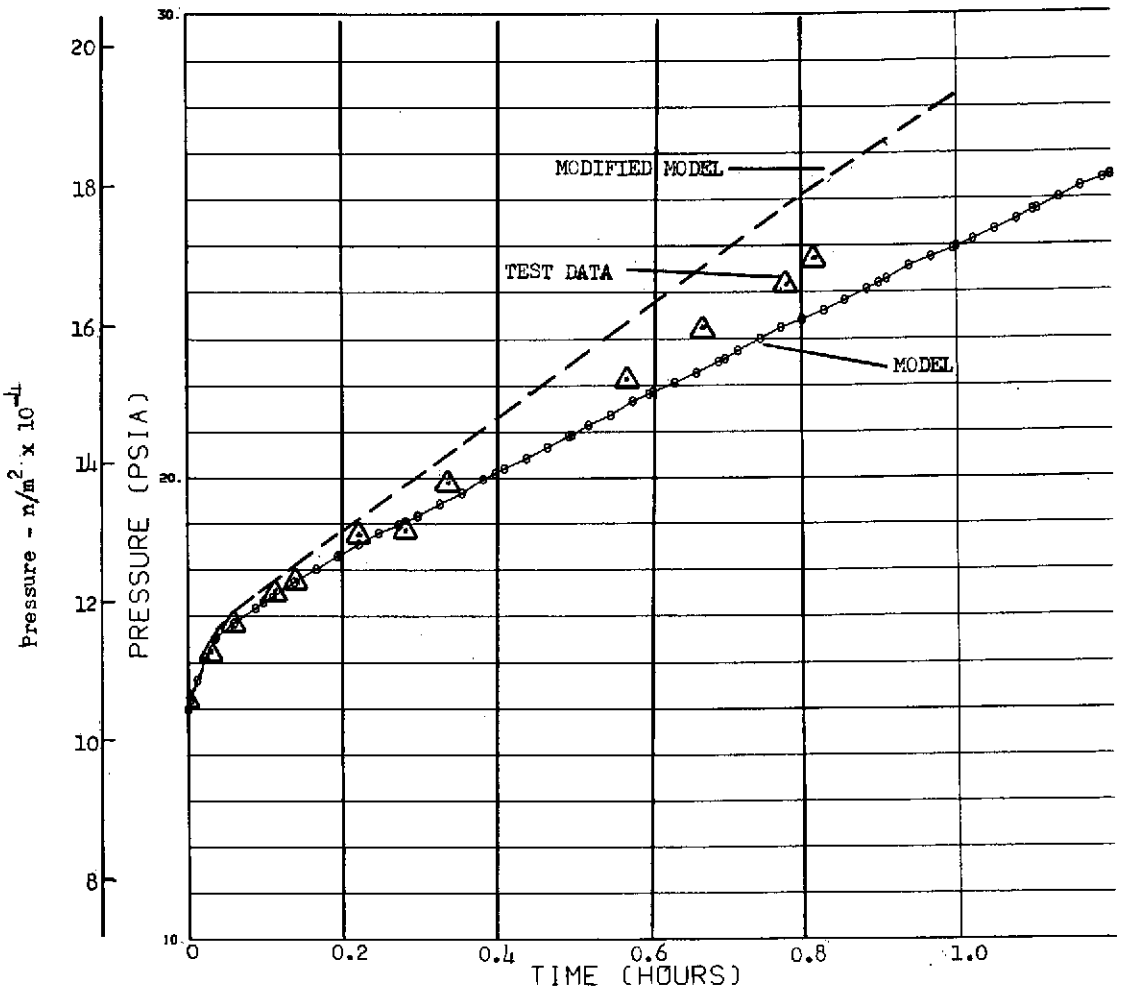

Fig. 4-39 Comparison Between Experimental Pressure and Analytical Prediction For Test C-4; Test Fluid-LH_2; Ullage Volume 50%

C - 3

Section 5

CONCLUDING REMARKS

This program was conducted to develop an analysis technique for evaluating the performance of a tank wall heat exchanger as a means of controlling pressure in a cryogenic tank during space flight. As a result of this work, the following conclusions can be drawn:

(1) A tank wall heat exchanger can be used to control tank pressure.

(2) Some propellant subcooling does occur, resulting in excess loss of propellant. However, the net effect of this inefficiency is insignificant after 5 or 6 vent cycles.

(3) The effectiveness of the tank wall heat exchanger is not diminished in the absence of gravity because subsurface boiling tends to mix the propellants.

(4) A heat exchanger mounted on the external wall is heavier than one mounted internally, but is probably preferred from a reliability standpoint.

(5) Tests conducted in this program have confirmed the validity of the analytical model. Therefore, the parametric data that have been developed with the model can be used to estimate the pressure control characteristics for the range of geometries and environments covered herein.

(6) A packed sphere porous media does not appear to retard free convection for the size of test articles used in this program. Additional investigations for different porous media, and with smaller test articles, should be conducted to extend the results from this program down to lower Rayleigh Numbers (lower gravity simulation).

Appendix A

TANK FILL MODEL

- During the first phase of the fill process liquid which enters the tank is saturated and vaporized instantaneously, mixing with, and being raised to the temperature of, the bulk of the ullage vapor.
- The first phase of fill continues until the ullage vapor temperature has dropped to the point at which a liquid pool forms at the one end of the tank. This point in time is determined by testing the evaporation time of an "average" droplet.
- During the second phase of fill, the liquid forms a pool at one end of the tank with incoming liquid going directly into this pool and the ullage consisting only of vapor (no liquid droplets).

Phase I Fill ($T_u^* > T_s^*$)

With the above assumptions, the general receiver tank equations for phase I are:

$$p^* = \frac{P_i V_\ell}{R T_i} \exp\left[\frac{C_\ell \Lambda}{R}\left(\frac{1}{T_{s_i}^*} - \frac{1}{T_s^*}\right)\right] \frac{dM_u^*}{dt^*} = m_f^* - m_v^* \tag{A-1}$$

$$\frac{dM_u^*}{dt^*} = m_f^* - m_v^* \tag{A-2}$$

$$M_u^*\left[\frac{dT_u^*}{dt^*} - \frac{R}{C_{p_v}} \frac{T_u^*}{p^*} \frac{dp^*}{d_t^*}\right] + m_f^* T_u^* - T_s^* = -\left(\frac{C_\ell}{C_{p_v}}\right)\left[m_f^* \Lambda - h_{wu}^* A_{wu}^* \left(T_{wu}^* - T_u^*\right)\right] \tag{A-3}$$

$$\frac{M_u^* T_u^*}{P^*} = 1 \tag{A-4}$$

Equations (2) and (4) give

$$\frac{dT_u^*}{dt^*} = \frac{1}{M_u^*}\frac{dp^*}{dt^*} - \frac{p^*}{M_u^{*2}}\frac{dM_u^*}{dt^*}$$

$$= \frac{1}{M_u^*}\left[\frac{dp^*}{dt^*} - T_u^*\,(m_f^* - m_v^*)\right] \tag{A-5}$$

Substituting (5) into (3) and using (4) yields

$$dp^* = \frac{m_f^*\left(T_s^* - \frac{C_\Lambda}{Cp_v}\right) - m_v^*\,T_u^* + \frac{C}{CP_v}\,h_{wu}^*\,A_{wu}^*\left(T_{wu}^* - T_u^*\right)}{\left(1 - \frac{R}{C_v}\right)} \tag{A-6}$$

Solving Eq. (1) for T_s^*,

$$T_s^* = \frac{1}{\frac{1}{T_{s_i}^*} - \frac{R}{C_\ell \Lambda}\,\ell n\left(\frac{RTi}{P_i v}\,p^*\right)} \tag{A-7}$$

The ullage vapor temperature is obtained from Eq. (4) as

$$T_u^* = \frac{p^*}{M_u^*} \tag{A-8}$$

The ullage mass is obtained from

$$M_u^* = M_{u_i}^* + \int_o^{t^*}\left(m_f^* - m_v^*\right)\,dt^*$$

or

$$M_u^* = \frac{P_i v}{RT_i} + \int_o^{t^*} (m_f^* - m_v^*)\, dt^* \qquad \text{(A-9)}$$

Substituting (9) into (8) yields

$$T_u^* = \frac{P^*}{\frac{P_i v}{RT_i} + \int_o^{t^*} (m_f^* - m_v^*)\, dt^*} \quad T_u^* \geq T_s^* \qquad \text{(A-10)}$$

The ullage wall temperature is obtained from a heat balance on the ullage wall

$$\frac{dT_{uw}^*}{dt^*} = \frac{1}{M_{uw}^*} \frac{C_\ell}{C_{uw}} \left[q_{quw}^* - h_{uw}^* A_{uw}^* (T_{uw}^* - T_u^*) \right] \qquad \text{(A-11)}$$

Equations (6) and (11) must be solved simultaneously, with the aid of Equations (7) and (10).

Phase II Fill ($T_u^* \approx T_s^*$)

The simplified model assumed is not valid when the gas temperature nears the saturation temperature, since there is not sufficient heat transfer to vaporize all the liquid as it enters the tank. For this reason, Eq. (6) is integrated only until the ullage vapor temperature is approximately equal to the saturation temperature. It is at this point at which the Phase II analysis is applied.

For this analysis it is assumed that:

- o Gas phase only exists in the ullage ($M_D^*=0$)
- o Liquid entering the tank is subcooled having a dimensionless temperature T_L^* and X=0.
- o No boiling at tank-wall bottomed-liquid interface ($\dot{m}_{lsw}=0$)

The general receiver tank equations then reduce to

$$p^* = \frac{p_i v_\ell}{R T_i} \exp\left[\frac{C_\ell}{R}\left(1 - \frac{1}{T_s^*}\right)\right] \tag{A-12}$$

$$\frac{dM_B^*}{dt^*} = \dot{m}_f^* - \dot{m}_{LS}^* = \dot{m}_f^* - \frac{A_s^*}{\Lambda}\left[h_{us}^*\left(T_u^* - T_s^*\right) - h_{SL}^*\left(T_s^* - T_B^*\right)\right] \tag{A-13}$$

$$\frac{dM_u^*}{dt^*} = \dot{m}_{LS}^* - \dot{m}_v^* = \frac{A_s^*}{\Lambda}\left[h_{us}^*\left(T_u^* - T_s^*\right) - h_{SL}^*\left(T_s^* - T_B^*\right)\right] - \dot{m}_v^* \tag{A-14}$$

$$M_B^* \frac{dT_B^*}{dt^*} = \dot{m}_f^*\left(T_L^* - T_B^*\right) - \frac{T_S^* - T_B^*}{\Lambda}\left\{A_s^*\left[h_{us}^*\left(T_u^* - T_s^*\right) - h_{SL}^*\left(T_S^* - T_B^*\right)\right\} + A_S^* h^*_{SL}\left(T_S^* - T_B^*\right) + A_{WL}^* q_{BL}^* \tag{A-15}$$

where q_{BL}^* is the wall heat added to the liquid.

$$M_u^*\left[\frac{dT_u^*}{dt^*} - \frac{R}{C_{pu}}\frac{T_u^*}{p^*}\frac{dp^*}{dt^*}\right] + \frac{(T_u^* - T_s^*)}{\Lambda} A_s^*\left[h_{us}^*\left(T_u^* - T_s^*\right) - h_{SL}^*\left(T_s^* - T_B^*\right)\right]$$
$$= -\left(\frac{C_\ell}{C_{pv}}\right)\left[h_{us}^* A_s^*\left(T_u^* - T_s^*\right) - h_{wu}^* A_{wu}^*\left(T_{wu}^* - T_u^*\right)\right] \tag{A-16}$$

$$M_B^* + \frac{M_u^* T_u^*}{p^*} = 1 \tag{A-17}$$

Equations (14) and (17) yield

$$\frac{dT_u^*}{dt^*} = \frac{-p^*}{M_u^*} \frac{dM_B^*}{dt^*} + \frac{\left(1-M_B^*\right)}{M_u^*} \frac{dp^*}{dt^*} - p^* \frac{\left(1-M_B^*\right)}{M_u^{*2}} \frac{dM_u^*}{dt^*} \tag{A-18}$$

Substituting (18) into (16) and using (17) yields

$$\frac{dp^*}{dt^*} = \frac{1}{(1-M_B^*)} \left\{ \frac{T_u^* M_u^*}{(1-M_B^*)} \frac{dM_B^*}{dt^*} + T_u^* \frac{dM_u^*}{dt^*} - \frac{\left(T_u^* - T_s^*\right)}{\Lambda} A_s^* \left[h_{us}^* \left(T_u^* - T_s^*\right) - h_{SL}^* \left(T_s^* - T_B^*\right) \right] \right.$$

$$\left. - \frac{C_\ell}{C_{pv}} \left[h_{us}^* A_s^* \left(T_u^* - T_s^*\right) - h_{wu}^* A_{wu}^* \left(T_{wu}^* - T_u^*\right) \right] \right\} \tag{A-19}$$

The interface temperature is obtained from (12):

$$T_s^* = \frac{1}{1 - \frac{R}{C_\ell \Lambda} \ln\left(\frac{RT_i}{p_i V_\ell} p^*\right)} \tag{A-20}$$

The masses M_B^* and M_u^* are obtained from integration of equations (13) and (14):

$$M_B^* = \int_{t_i^*}^{t^*} \left(\frac{dM_B^*}{dt^*}\right) dt^* \tag{A-21}$$

and

$$M_u^* = M_{u_i}^* + \int_{t_i^*}^{t^*} \left(\frac{dM_u^*}{dt^*}\right) dt^* \tag{A-22}$$

Where t_i^* is the dimensionless time at the beginning of Phase II fill, Mu_i^* is the ullage mass at t_i^*, and $M_B^* = 0$ at the t_i^*.

The ullage vapor temperature is obtained from (17):

$$T_u^* = \frac{p^*}{M_u^*}\left(1 - M_B^*\right) \tag{A-23}$$

The bottomed liquid temperature is derived from integration of Eq. (15):

$$T_B^* = T_{B_i}^* + \int_{t_i^*}^{t^*} \left(\frac{dT_B^*}{dt^*}\right) dt^* \tag{A-24}$$

where we assume that $T_{B_i}^* = T_{s_i}^*$. (A-25)

The ullage wall temperature is obtained from a heat balance on that portion of the wall exposed to the ullage vapor:

$$\frac{dT_{uw}^*}{dt^*} = \frac{1}{M_{uw}^*}\frac{C_\ell}{C_{uw}}\left[q_{uw}^* - h_{uw}^* A_{uw}^*\left(T_{uw}^* - T_u^*\right)\right] \tag{A-26}$$

where

$$q_{uw}^* = \frac{q_{uw}}{h_o^1 L_o^2 T_o} \; ; \; q_{uw} = q_{o_w}\frac{A_{uw}}{A_w}$$

$$q_{BL}^* = \frac{q_{BL}}{h_o^1 L_o^2 T_o} \; ; \; q_{BL} = q_{o_w}\frac{A_{BL}}{A_w} = q_{o_w}\frac{\left(A_w - A_{uw}\right)}{A_w}$$

Criterion for Transition From Phase I to Phase II

Assume mean drop diameter $\bar{D}_D = \sqrt{3}\ D_D^* = 1.73 \times 10^{-3}$ ft.

From LMSC-A847685, P.A-27, droplet will evaporate before traversing ullage if

$$\phi = \frac{K_u(T_u - T_s)R_I}{\lambda\ \dot{m}_f}\left(\frac{R_I}{D_D^*}\right)^2\left(\frac{\epsilon}{x}\right)\left(\frac{\rho_u}{\rho_\ell}\right) > 10^{-3}$$

where R_I is radius of inlet.

$$\frac{\epsilon}{x} = \left[\frac{\rho_u}{\rho_\ell}\left(1 - X\right) + X\right]^{-1} = \frac{\rho_\ell}{\rho_u} \quad \text{for } X = 0, \text{ so}$$

$$\phi = \frac{K_u(T_u - T_s)\,R_I^3}{\lambda\ \dot{m}_f\ D_D^{*2}}$$

Therefore, transition from Phase I to Phase II occurs when

$$\left(T_u - T_s\right) < \frac{\lambda \dot{m}_f D_D^{*2} x 10^{-3}}{K_u R_I^3}$$

or

$$\left(T_u - T_s\right) < \frac{\lambda \dot{m}_f}{K_u R_I^3} \times 10^{-9} \qquad \text{(A-27)}$$

For R_I in feet.

Results

The model was used to calculate pressure histories for a tank that has been depleted and is being refilled in orbit. It was assumed that the tank was not evacuated prior to the fill and that both the tank and its contents were at 244°K (440°R). Starting pressure was assumed to be 1 atmosphere. Figure A-1 is a typical result. It was found that there is a very small drop in pressure ($\approx$ 0.1 psi) when the cold fluid first enters the tank. Thereafter, the pressure starts to climb rapidly until the ullage and saturation pressure approach equilibrium, near the end of Phase 1. Apparently, the combination of mass addition and heating from the tank walls more than offsets the cooling of the original gas. After the walls have been cooled to near saturation the pressure begins to decline slowly. Flow rates were varied from 0.65 percent to 65 percent of tank capacity per hour with only a small effect on the peak pressure. However, the time at which peak pressure occurs is nearly inverse to the fill rate. On the basis of this analysis, it appears that if a tank is to be refilled in space, it should first be evacuated and cooled with the vent open.

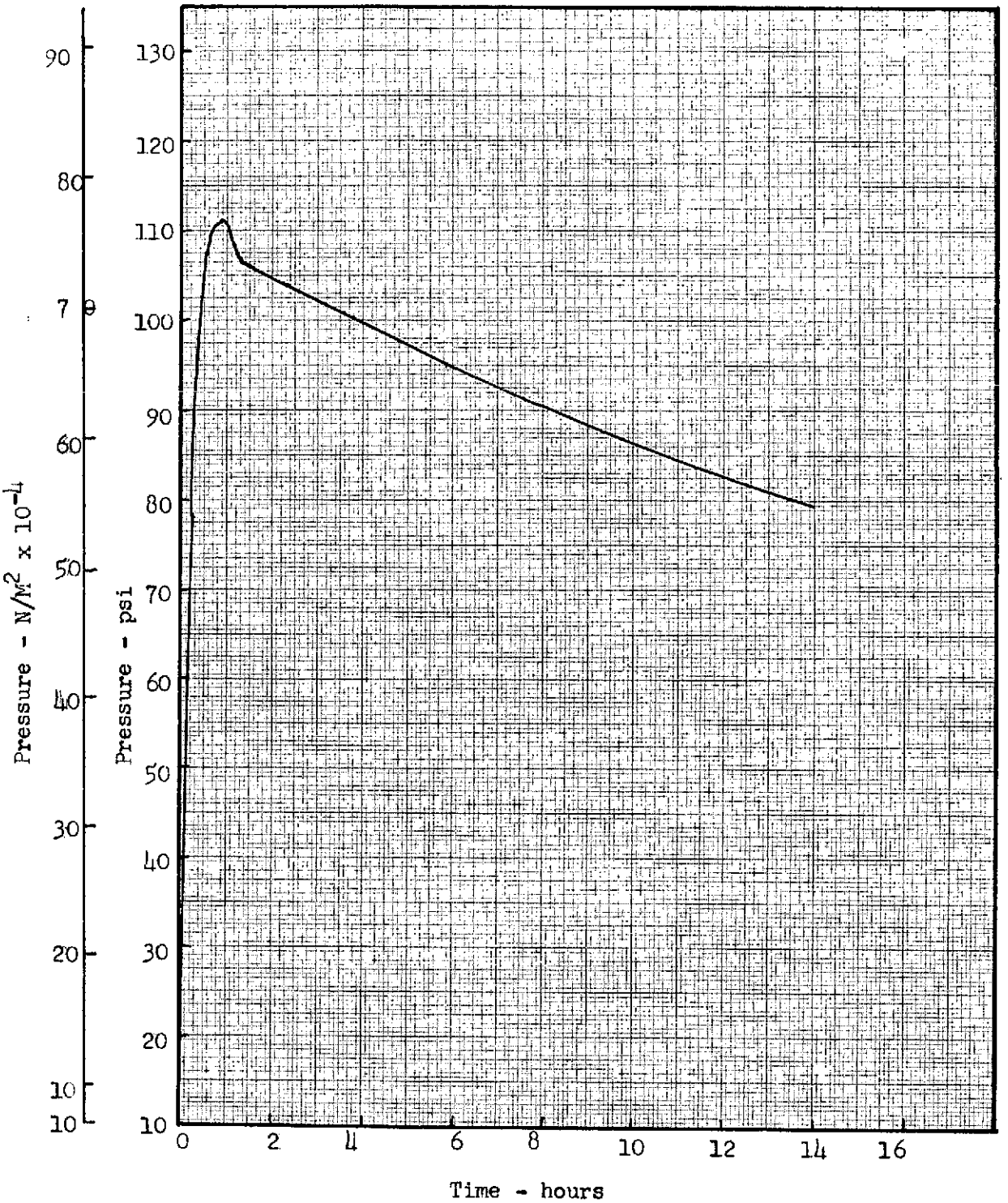

Fig. A-1 Typical Pressure History During an In Space Refilling Operation With LH_2; Tank Diameter = 1.2m (4 Ft), Fill Rate = 6.5 Percent Tank Capacity per Hour

DEFINITION OF SYMBOLS

A	Cross-sectional area for flow, ft^2 (m^2)
A_s	Interfacial surface area between bottomed liquid and tank ullage, ft^2 (m^2)
A_D	Interfacial surface area between dispersed-liquid system and ullage-vapor system, ft^2 (m^2)
C_p	Specific heat at constant pressure, Btu/lbm-°F (J/kg-°K)
C_v	Specific heat at constant volume, Btu/lbm-°F (J/kg-°K)
D_D	Droplet diameter, ft (m)
g_c	Conversion ratio, 32.2 lbm-ft/lbf-s^2
g	Acceleration of gravity, ft/s^2 (m/s^2)
h	Heat-transfer coefficient based on surface area, Btu/hr-ft^2-°F (W/m^2 °K)
J	Mechanical equivalent of heat, J = 778 ft lbf/Btu
k	Thermal conductivity, Btu/hr-ft-°F (W/m °K)
M	Mass, lbm (kg)
m	Mass flowrate, lbm/hr (kg/hr)
m_f	Mass flowrate of fluid entering tank through fill line, lbm/hr (kg/hr)
m_{LS}	Mass rate of vapor addition to tank ullage due to vaporization at the free surface minus the mass rate of condensation of incoming vapor which condenses directly into the bottomed liquid, lbm/hr (kg/hr)
m_v	Mass flow rate of vapor through tank vent, lbm/hr (kg/hr)
p	Pressure, lb/ft^2 or psi (N/cm^2)
Q	Volumertric flow rate, ft^3/hr (m 3/5)
q_{ow}	Heat flux density, Btu/hr-ft^2 (W/m^2)
q_{BL}	Heat flux density into bottomed liquid from tank wall, Btu/hr-ft^2 (W/m^2)
q_{UW}	Heat flux density into ullage vapor from tank wall. Btu/hr-ft^2 (W/m^2)
R	Gas constant, ft-lbf/lbm-°R (J/°K mol)
S	Surface area, ft^2 (m^2)
T	Temperature, °F (°K)

t	Time, hr
V	Volume, ft^3 (m^3)
v	Specific volume, ft^3/lbm (m^3/kg)
v_{fg}	Specific volume change during evaporation, ft^3/lbm (m^3/kg)
Z	Vapor compressibility factor

Greek Letters

γ	Constant, ratio of specific heats
ϵ	Void fraction or porosity
k	Constant
Λ	Dimensionless heat of vaporization
λ	Latent heat of vaporization, Btu/lbm (J/kg)
ρ	Density, lbm/ft^3 (kg/m^3)

$$\sigma = 0.1714 \times 10^{-8} \text{ Btu/hr-ft}^2\text{-}^\circ\text{R}^4$$

$$= 5.6697 \times 10^{-8} \text{ W/m}^2\ ^\circ\text{K}^4$$

ϕ	A function

Superscripts

*	Refers to nondimensional quantity
-	Refers to time average or mean value
+	Refers to critical value

Subscripts

B	Bottomed-liquid condition
b	Bubble property or bulk-flow condition
c	Core condition
D	Droplet or dispersed-liquid condition
DI	Drop condition at tank inlet
e	Exit condition

DEFINITION OF SYMBOLS (Cont.)

f	Fill condition
g	Gas or gaseous-phase condition
i	Inner diameter or surface
ℓ	Saturated liquid or liquid phase
LI	Inlet-liquid condition
o	Initial condition or outer surface
s	Saturation condition
T	Tank Condition
u	Ullage vapor condition
V	Vapor condition
v	Vent condition
w	Wall condition

Dimensionless Groups

$$T^* = \frac{T}{T_i}$$

$$\gamma^* = \frac{\gamma}{\left(\frac{RT_i}{V_\ell}\right)}$$

$$M^* = \frac{M}{\left(\frac{V_t}{V_\ell}\right)}$$

$$A^* = \frac{A}{L_o^2}$$

$$h^* = \frac{h^1}{\left(\frac{k\ell}{L_o}\right)}$$

$$\Lambda = \frac{\lambda}{C_\ell T_i}$$

$$t^* = \frac{t}{\left(\frac{V_t C_\ell}{V_\ell K_\ell L_o}\right)}$$

$$\dot{m}^* = \frac{\dot{m}}{\left(\frac{K_\ell L_o}{C_\ell}\right)}$$

L_o = Characteristic tank dimension (diameter for spherical tank).

Appendix B

HEAT EXCHANGER PRESSURE DROP

The liquid extracted from the tank is expanded to a low pressure and temperature and passed through the heat exchanger to absorb enough energy to vaporize the two-phase mixture. This vented vapor is then vented into the vacuum of space.

From a momentum balance, as the fluid flows through the heat exchanger, the pressure gradient at any point in the tube is given by:

$$-\left(\frac{dP}{d\ell}\right)_T = -\left(\frac{dP}{d\ell}\right)_f - \left(\frac{dP}{d\ell}\right)_a - \left(\frac{dP}{d\ell}\right)_g$$

where the subscripts, T , f , a , g refer to the total, frictional, acceleration, and gravitational gradients, respectively.

Dr. Owens* has shown that the frictional gradient with two-phase flow is related to that with liquid only flowing in the tube, by the following expression:

$$-\left(\frac{dP}{d\ell}\right)_f = -\left(\frac{dP}{d\ell}\right)_f \left[1 + X\left(\frac{v_g}{v_\ell} - 1\right)\right]$$

where x is the mass fraction of vapor, and subscripts g , ℓ pertain respectively to vapor and liquid properties. The frictional drop with liquid is given by:

$$-\left(\frac{dP}{d\ell}\right)_{f\ell} = \frac{f_\ell G^2 v_\ell}{2 D g_c}$$

---

*W. L. Owens, "Two-Phase Pressure Gradients" International Developments in Heat Transfer, Part II, pp. 363-368, January 1962

The acceleration pressure gradient is given by:

$$-\left(\frac{dP}{d\ell}\right)_a = \frac{G^2}{g_c}\ \frac{dv}{d\ell}$$

where:

$$v = v_\ell\ (1 - x) + x\ v_g$$

$$\frac{dv}{d\ell} = \frac{\partial v}{\partial v_\ell}\ \frac{\partial\ v_\ell}{d\ell} + \frac{\partial v}{\partial x}\ \frac{dx}{d\ell} + \frac{\partial v}{\partial v_g}\ \frac{d\ v_g}{d\ell}$$

$$= (1 - x)\frac{d\ v_\ell}{dP}\left(\frac{dP}{d\ell}\right)_T + (v_g - v_\ell)\ \frac{dx}{d\ell} + x\ \frac{d\ v_g}{dP}\left(\frac{dP}{d\ell}\right)_T$$

The gradient due to the gravity vector is given by:

$$-\left(\frac{dP}{d\ell}\right)_g = g/g_c\ \ \frac{\sin\theta}{v} = g/g_c\ \ \frac{\sin\theta}{v_\ell\ (1 - x) + x\ v_g}$$

Substituting these various expressions into the first equation, we get for the total pressure gradient at any point

$$-\left(\frac{dP}{d\ell}\right)_T = \frac{\dfrac{f_\ell\ G^2\ v_\ell}{2\ D\ g_c}\left\{1 + x\left(\dfrac{v_g}{v_\ell} - 1\right)\right\} + \left(\dfrac{v_g}{v_\ell} - 1\right) v_\ell\ \dfrac{dx}{d\ell} + \dfrac{g/g_c\ \sin\theta}{v_\ell\ (1 - x) + x\ v_g}}{1 + \dfrac{G^2}{g_c}\left\{(1 - x)\ \dfrac{d\ v_\ell}{dP} + \dfrac{d\ v_g}{dP}\right\}}$$

For cryogens, the term $(1 - x)\dfrac{d\ v_\ell}{dP}$ is insignificant compared to the vapor term $x\dfrac{d\ v_g}{dP}$. Therefore, the preceding expression can be somewhat simplified to give:

$$-\left(\frac{dP}{d\ell}\right)_T = \frac{\text{Numerator}}{1 + x\ \dfrac{G^2}{g_c}\ \dfrac{d\ v_g}{dP}}$$

The total pressure drop in the heat exchanger tube must be obtained by integration, i.e.,

$$(P_1 - P_2) = \frac{\int_o^L \left\{ \frac{f_\ell \, G^2 \, v_\ell}{2 \, D \, g_c} \left[1 + x \left(\frac{v_g}{v_\ell} - 1 \right) \right] + \left(\frac{v_g}{v_\ell} - 1 \right) x \, \frac{dx}{d\ell} + \frac{g/g_c \sin \theta}{v_\ell \, (1 - x) + x \, v_g} \right\} d\ell}{\left\{ 1 + x \left[\frac{G^2}{g_c} \, \frac{d \, v_g}{dP} \right] \right\}}$$

This equation is not amenable to direct solution except by the tedium of trial and error with step wise integration. However, we note that in the denominator, the quantity, $\frac{G^2}{g_c} \, \frac{d \, v_g}{dP}$ is the $(\text{ratio})^2$ of actual to sonic velocity if the vent fluid is all vaporized. It must be less than 1 in the heat exchanger tube. Since $\frac{d \, v_g}{dP}$ is a function of pressure and the mass flux is determined by the vent rate and tube size, we can use the limit condition to estimate the minimum tube size that can be used. Fig. B-1 shows the maximum mass flux as a function of pressure in the tube.

The mass flux in the heat exchanger is related to the cooling rate and the tube diameter, i.e.,

$$G = \frac{\dot{w}_v}{A_{tube}} = \frac{4 \, q_c \, A_s}{\lambda \pi \, d_t^{\,2}}$$

where:

$\dot{w}_v$ = vent flow rate
A_s = tank surface area
d_t = tube diameter
q_c = average cooling flux at the tank wall

Also, the cooling flux is related to the average wall resistance, R_{cw}, by:

$$q_c = \frac{(1 - \eta)\ (T_L - T_c)}{R_{cw}}$$

Combining the two preceding equations and replacing tube diameter d_t by tab diameter 2a , we get:

$$G = \frac{A_s\ (1 - \eta)\ (T_L - T_c)}{\pi \lambda R_{cw}\ (a)^2}$$

This equation can be rearranged to describe the minimum tube size in terms of tank size, R_{cw} and the maximum mass flux.

$$\frac{a_{min}}{(A_s)^{1/2}} = \left[\frac{(1 - \eta)}{R_{cw}} \frac{(T_B - T_c)}{\pi \lambda G_{max}}\right]^{1/2}$$

The effectiveness has been shown to be related to the value of R_{cw} . The expansion temperature drop, $(T_B - T_c)$ is related to the heat exchanger pressure, for a given tank operating pressure, as is the maximum mass flux. Therefore, for a given pressure at the tube inlet, the last equation can be used to estimate the minimum tube size for any tank and design value for R_{cw} .

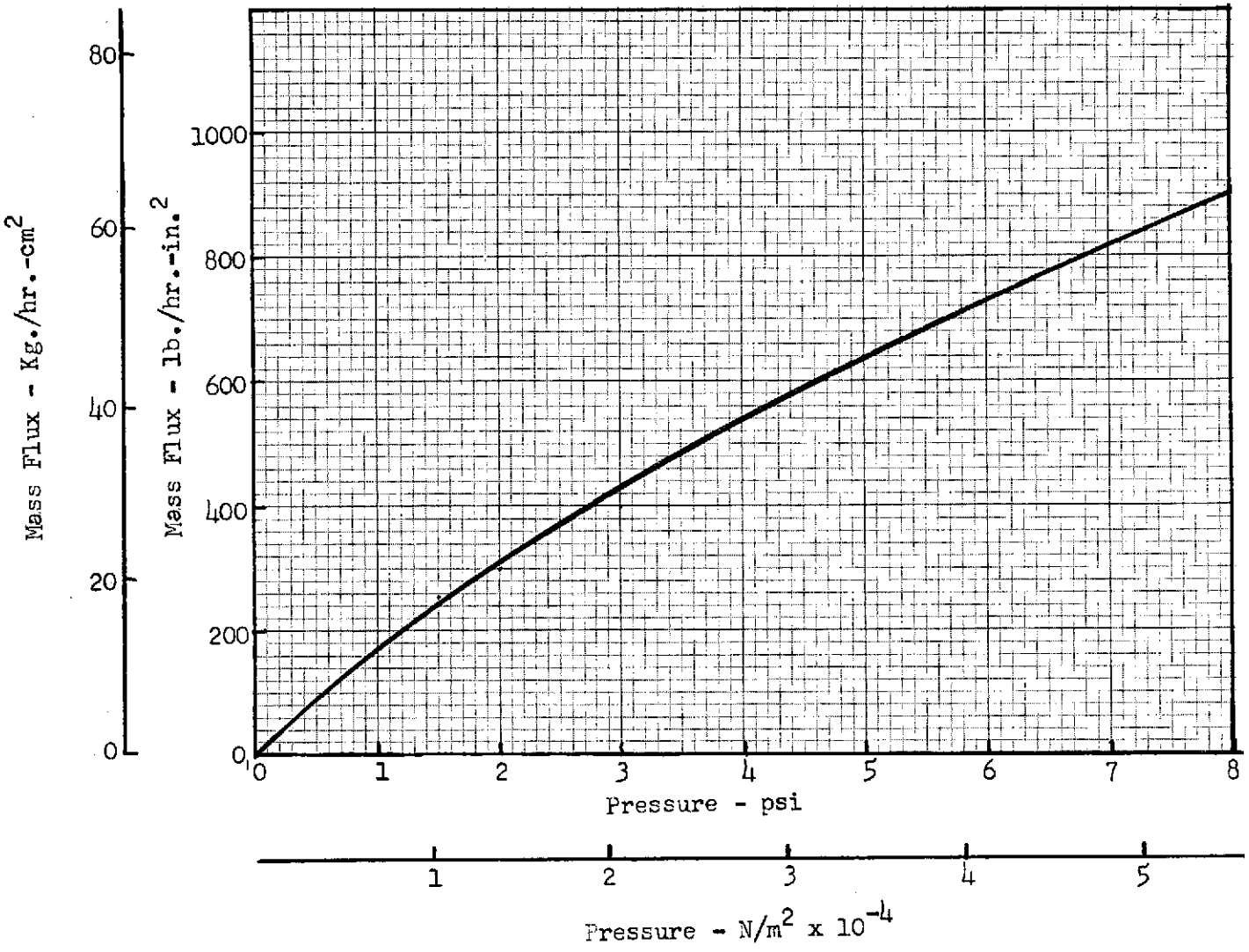

Figure B-1 Limiting Mass Flux to Prevent Choking in the Heat Exchanger

APPENDIX C

List of Symbols

	-	Heat exchanger attachment radius	- M (Ft)
A	-	Area	- M^2 (Ft^2)
A_F	-	Flat interface area	- M^2 (Ft^2)
B			
B_o	-	Bond Number	- dimensionless
C	-	Sensible heat capacity	- cal/gr ($^{Btu}/_{lb}$)
Cp	-	Specific heat at constant pressure	- cal/gr-ok ($^{Btu}/_{lb\text{-}^oR}$)
C_V	-	Specific heat at constant volume	- cal/gr-ok ($^{Btu}/_{lb\text{-}^oR}$)
D	-	Tank diameter	- M (Ft)
f_l	-	Friction factor inside heat exchanger tube	
F	-	Energy integral defined by temperature profits	- dimensionless
G	-	Coolant mass flux through heat exchanger	- $Kg/sec\text{-}M^2$ ($lb/sec\text{-}Ft^2$)
g	-	Gravitational acceleration	- M/sec^2 (Ft/sec^2)
g_o	-	Standard gravitational acceleration	- M/sec^2 (Ft/sec^2)
g_c	-	Universal gravitational constant	
G_R	-	Grashof Number	- dimensionless
G_R^*	-	Modified grashof number based on heat flux	- dimensionless
h	-	Heat transfer film coefficient	- $W/M^2\text{-}^oK\left(\frac{Btu}{hr\text{-}Ft^2\text{-}^oR}\right)$
k	-	Thermal conductivity	- $W/M\text{-}^oK\left(\frac{Btu}{hr\text{-}Ft^{o}F}\right)$
K_s	-	Slope of P-T saturation line	- $N/M^2\text{-}^oK$ ($PSi/^oR$)
L	-	Boundary layer length	- M (Ft)
M	-	Fluid quantity	- Kg (lbm)
$\dot{M}_o$	-	Mass flow rate from boundary layer	- Kg/hr. (lbm/hr.)

$\dot{M}_e$	-	Mass flow rate into boundary layer	- Kg/hr. (lbm/hr.)
N	-	Number of heat exchanger attachment points	
Nu	-	Nusselt number	- dimensionless
P	-	Pressure	- N/M^2 (lb/Ft^2)
P_r	-	Prandtl Number	- dimensionless
q_w	-	Heat flux at the tank wall	- $W/M^2 \left(\frac{Btu}{hr\text{-}Ft^2}\right)$
Q	-	Heat rate	- watts (Btu/Hr)
Q_p	-	Heat rate into each heat exchanger attachment	- watts (Btu/Hr)
R_a	-	Rayleigh Number	- dimensionless
R_a^*	-	Modified Rayleigh Number	- dimensionless
R	-	Tank radius	- M (Ft)
R_{ew}	-	Thermal resistance between the tank wall and coolant stream	- $\frac{M^2\text{-}^oK}{Btu} \left(\frac{hr\text{-}Ft^2\text{-}^oR}{Btu}\right)$
R_F	-	Radius at flat interface	- M (Ft)
S	-	Spacing between heat exchanger attachment points	- M (Ft)
T	-	Temperature	- $^oK(^oR)$
t	-	Tank wall thickness	- M (Ft)
t	-	Time	- sec
U_1	-	Characteristic fully developed, turbulent boundary layer velocity	- M/sec (Ft/sec)
$\bar{U}_s$	-	Average, steady state boundary layer velocity	- M/sec (Ft/sec)
V	-	Volume	- M^3 (Ft^3)
v	-	Specific volume	- M^3/Kg (Ft^3/lb)
Wt	-	Heat exchanger tube weight	- Kg (lbs)
Ws	-	Tank wall membrane weight	- Kg (lbs)
X	-	Axial distance measured from bottom of tank	- M (Ft)
y	-	Radial distance measured from tank wall	- M (Ft)
Z	-	Compressibility factor	- dimensionless
Z	-	Elevation of flat liquid interface	- M (Ft)
α	-	Number of standard gravities	- dimensionless
β	-	Liquid coefficient of thermal expansion	- $^oK^{-1}$ ($^oR^{-1}$)

δ	-	Boundary layer thickness	- M (Ft)
Δ	-	Stratified layer thickness	- M (Ft)
σ	-	Surface tension	- Kg/m (lb_F/Ft)
	-	Porosity	
η	-	Heat exchanger effectiveness	- dimensionless
γ	-	Kinematic viscosity	
	-	Density	- Kg (lb_m)
	-	Latent heat of vaporization	- cal/Kg ($^{Btu}/_{lb}$)
ψ	-	Geometry factor used in GEOM subroutine	- dimensionless
ϕ	-	Characteristic time for stratification	- dimensionless

Subscripts

B	-	Pertains to area or volume subjected to bottom heating
C	-	Pertains to cylindrical geometry
cω	-	pertains to cooling at tank wall
g	-	gas
L	-	Liquid
S	-	Saturation conditions at liquid surface
s	-	Steady state
s,t	-	Steady state, turbulent
s,L	-	Steady state, evaluated at axial distance L
T	-	Total
TURB	-	Turbulent
U	-	Ullage
W,t	-	Pertains to conditions at the tank wall, turbulent boundary layer

APPENDIX D

REFERENCES

1. Lockheed Missiles & Space Company, Liquid Propellant Thermal Conditioning System, Interim Report, NASA CR-72113, LMSC-A839783, Contract NAS 3-7942, Sunnyvale, Calif., 20 April 1967.

2. Lockheed Missiles & Space Company, Final Report, NASA CR-72365 LMSC-K-07-68-2 Contract NAS 3-7942, Sunnyvale, Calif., August 15, 1968

3. Lockheed Missiles & Space Company, Test Program, Final Report, NASA CR-72971, LMSC-D159262, Contract NAS 3-12033, Sunnyvale, Calif., July 5, 1972.

4. General Dynamics, Convair Division, Cryogenic Zero-Gravity Prototype Vent System, DCN 1-6-52-01144, GDC-DDB67-006, Contract NAS 8-20146, San Diego, Calif., October 1967.

5. Schwartz, S. H. and Adelberg, M. "Some Thermal Aspects of a Contained Fluid In a Reduced Gravity Environment," Symposium Proceedings (LMSC), Palo Alto, Calif. June 24, 25, 1965.

6. Siegel, R. "Transient Tree Convection From a Vertical Flat Plate", Trans. ASME Vol. 80, Feb. 1958, pp. 347-359.

7. Lockheed Missiles & Space Co., Stratified Layer Model - A Numerical Approach To Temperature Stratification in Liquids Contained In Heated Vessels, by G. Vliet, Report 8-30-63-4, Palo Alto, Ca. Nov. 1963.

8. Lockheed Missiles & Space Co., Analytical and Experimental Study of Liquid Orientation and Stratification in Standard and Reduced Gravity Fields, 2-05-64-1 Contract NAS 8-11525, Sunnyvale, Calif., July 1964.

9. Satterlee, H. M., Chin, J. H., "Meniscus Shape Under Reduced-Gravity Conditions," Symposium Proceedings (LMSC) Palo Alto, California, June 24, 25, 1965.

10. Lockheed Missiles & Space Co., Analytical and Experimental Study of Stratification and Liquid-Ullage Coupling, 2-05-65-1, Contract NAS 8-11525, Sunnyvale, Calif., August 1965.

11. Lockheed Missiles & Space Co., Analytical and Experimental Study of Liquid-Ullage Coupling and Low Gravity Interface Stability, 2-05-66-1, Contract NAS 8-11525, Sunnyvale, California, August 1966.

12. Lockheed Missiles & Space Co., Analytical and Experimental Study of Stratification In a Spherical Tank, LMSC 6-65-65-6, Sunnyvale, Calif. January 1965.

13. Aydelott, John C. and Spuckler, Charles M., Effect of Normal-Gravity Self-Pressurization of Spherical Liquid Hydrogen Tankage, NASA TND-5196, May 1969.

14. Katto, Y. and Masuoka, T., "Criterion for the Onset of Convective Flow in a Porous Medium," International Journal of Heat Transfer, Vol. 10, pp 297-309, 1967

Appendix E

DISTRIBUTION LIST

Copies	
	National Aeronautics & Space Administration Lewis Research Center 21000 Brookpark Road Cleveland, Ohio 44135
1	Attn: Contracting Officer, MS 500-313
5	E. A. Bourke, MS 500-205
1	Technical Utilization Office, MS 3-16
1	Technical Report Control Office, MS 5-5
2	AFSC Liaison Office, MS 501-3
2	Library MS 60-3
1	Office of Reliability & Quality Assurance, MS 500-211
1	N. T. Musial, MS 500-113
20	D.E. Sokolowski, Project Manager, MS 500-204
1	Director, Manned Space Technology, RS Office of Aeronautics & Space Technology NASA Headquarters Washington, D.C. 20546
1	Director Space Prop. and Power, RP Office of Aeronautics & Space Technology NASA Headquarters Washington, D.C. 20546
1	Director, Launch Vehicles & Propulsion, SV Office of Space Science NASA Headquarters Washington, D.C. 20546
1	Director, Materials & Structures Div., RW Office of Aeronautics & Space Technology NASA Headquarters Washington, D.C. 20546
1	Director, Advanced Missions, MT Office of Manned Space Flight NASA Headquarters Washington, D.C. 20546
1	Director, Physics and Astronomy Programs, SG Office of Space Science NASA, Headquarters Washington, D.C. 20546

Copies		
1	Director, Planetary Programs, SL Office of Space Science NASA, Headquarters Washington, D.C. 20546	
1	Office of Aeronautics & Space Technology, R NASA, Headquarters Washington, D.C. 20546	
1	National Aeronautics & Space Administration Ames Research Center Moffett Field, California 94035 Attn: Library	
1	National Aeronautics & Space Administration Flight Research Center P. O. Box 273 Edwards, California 93523 Attn: Library	
1	Director, Technology Utilization Division Office of Technology Utilization NASA Headquarters Washington, D.C. 20546	
1	Office of the Director of Defense Research & Engineering Washington, D.C. 20301 Attn: Office of Asst. Dir. (Chem Technology)	
10	NASA Scientific and Technical Information Facility P. O. 33 College Park, Maryland 20740 Attn: NASA Representative	
1	National Aeronautics & Space Administration Goddard Space Flight Center Greenbelt, Maryland 20771 Attn: Library	Merland L. Moseson, Code 620
1	National Aeronautics & Space Administration Langley Research Center Langley Station Hampton, Virginia 23365 Attn: Library	E. Cartwright, Director
1	National Aeronautics & Space Administration John F. Kennedy Space Center Cocoa Beach, Florida 32931 Attn: Library	Dr. Kurt Debus

Copies		
1	National Aeronautics & Space Administration Manned Spacecraft Center Houston, Texas 77001 Attn: Library	J. G. Thiobodaux, Jr. Chief, Propulsion & Power Division
1	National Aeronautics & Space Administration George C. Marshall Space Flight Center Huntsville, Alabama 35912 Attn: Library	
1	Jet Propulsion Laboratory 4800 Oak Grove Drive Pasadena, California 91103 Attn: Library	
1	Defense Documentation Center Cameron Station Building 5 5010 Duke Street Alexandria, Virginia 22314 Attn: TISIA	
1	RTD (RTNP) Bolling Air Force Base Washington, D.C. 20332	
1	Arnold Engineering Development Center Air Force Systems Command Tullahoma, Tennessee 37389 Attn: Library	Dr. H. K. Doetsch
1	Advanced Research Projects Agency Washington, D.C. 20525 Attn: Library	
1	Aeronautical Systems Division Air Force Systems Command Wright-Patterson Air Force Base, Dayton, Ohio Attn: Library	D. L. Schmidt Code ARSNC-2 R. E. Headrick
1	Air Force Missile Test Center Patrick Air Force Base, Florida Attn: Library	L. J. Ullian
1	Air Force Systems Command Andrews Air Force Base Washington, D.C. 20332 Attn: Library	Capt. S. W. Bowen SCLT

Copies		
1	Air Force Rocket Propulsion Laboratory (RPR) Edwards, California 93523 Attn: Library	
1	Air Force Rocket Propulsion Laboratory (RPM) Edwards, California 93523 Attn: Library	
1	Air Force FTC (FTAT-2) Edwards Air Force Base, California 93523 Attn: Library	Donald Ross
1	Air Force Office of Scientific Research Washington, D.C 20333 Attn: Library	SREP, Dr. J. F. Masi
1	Space & Missile Systems Organization Air Force Unit Post Office Los Angeles, California 90045 Attn: Technical Data Center	
1	Office of Research Analyses (OAR) Holloman Air Force Base, New Mexico 88330 Attn: Library RRRD	
1	U. S. Air Force Washington, D.C. Attn: Library	Col. C. K. Stambaugh, Code AFRST
1	Commanding Officer U. S. Army Research Office (Durham) Box CM, Duke Station Durham, North Carolina 27706 Attn: Library	
1	U. S. Army Missile Command Redstone Scientific Information Center Redstone Arsenal, Alabama 35808 Attn: Document Section	Dr. W. Wharton
1	Bureau of Naval Weapons Department of the Navy Washington, D.C. Attn: Library	J. Kay, Code RTMS-41

Copies		
1	Commander U. S. Naval Missile Center Point Mugu, California 93041 Attn: Technical Library	
1	Commander U. S. Naval Weapons Center China Lake, California 93557 Attn: Library	
1	Commanding Officer Naval Research Branch Office 1030 E. Green Street Pasadena, California 91101 Attn: Library	
1	Director (Code 6180) U. S. Naval Research Laboratory Washington, D.C. 20390 Attn: Library	H. W. Carhart J. M. Krafft
1	Picatinny Arsenal Dover, New Jersey 07801 Attn: Library	I. Forsten
1	Air Force Aero Propulsion Laboratory Research & Technology Division Air Force Systems Command United States Air Force Wright-Patterson AFB, Ohio 45433 Attn: APRP (Library)	R. Quigley C. M. Donaldson
1	Electronics Division Aerojet-General Corporation P.O. Box 296 Azusa, California 91703 Attn: Library	W. L. Rogers
1	Space Divison Aerojet-General Corporation 9200 East Flair Drive El Monte, California 91734 Attn: Library	
1	Aerojet Ordance and Manufacturing Aerojet-General Corporation 11711 South Woodruff Avenue Fullerton, California 90241 Attn: Library	

Copies		
1	Aerojet Liquid Rocket Company P. O. Box 15847 Sacramento, California 95813 Attn: Technical Library 2484-2015A	R. Stiff
1	Aeronutronic Division of Philco Ford Corp. Ford Road Newport Beach, California 92663 Attn: Technical Information Department	Dr. L. H. Linder
1	Aerospace Corporation 2400 E. El Segundo Blvd. Los Angeles, California 90045 Attn: Library-Documents	J. G. Wilder
1	Arthur D. Little, Inc. 20 Acorn Park Cambridge, Massachusetts 02140 Attn: Library	A. C. Tobey
1	Astropower Laboratory McDonnell-Douglas Aircraft Company 2121 Paularino Newport Beach, California 92163 Attn: Library	
1	ARO, Incorporated Arnold Engineering Development Center Arnold AF Station, Tennessee 37389 Attn: Library	
1	Susquehanna Corporation Atlantic Research Division Shirley Highway & Edsall Road Alexandria, Virginia 22314 Attn: Library	
1	Battelle Memorial Institute 505 King Avenue Columbus, Ohio 43201 Attn: Report Library, Room 6A	
1	Beech Aircraft Corporation Boulder Facility Box 631 Boulder, Colorado Attn: Library	Douglas Pope

Copies		
1	Bell Aerosystems, Inc. Box 1 Buffalo, New York 14240 Attn: Library	T. Reinhardt W. M. Smith
1	Instruments & Life Support Division Bendix Corporation P.O. Box 4508 Davenport, Iowa 52808 Attention: Library	W. M. Carlson
1	Boeing Company Space Division P.O. Box 868 Seattle, Washington 98124 Attn: Library	J. D. Alexander
1	Boeing Company 1625 K Street, N.W. Washington, D.C 20006	
1	Boeing Company P.O. Box 1680 Huntsville, Alabama 35801	Ted Snow
1	Chemical Propulsion Information Agency Applied Physics Laboratory 8621 Georgia Avenue Silver Spring, Maryland 20910	Tom Reedy
1	Chrysler Corporation Missile Division P.O. Box 2628 Detroit, Michigan Attn: Library	John Gates
1	Chrysler Corporation Space Division P.O. Box 29200 New Orleans, Louisiana 70129 Attn: Librarian	
1	Curtiss-Wright Corporation Wright Aeronautical Division Woodridge, New Jersey Attn: Library	G. Kelley

Copies		
1	University of Denver Denver Research Institute P.O. Box 10127 Denver, Colorado 80210 Attn: Security Office	
1	Fairchild Stratos Corporation Aircraft Missiles Division Hagerstown, Maryland Attn: Library	
1	Research Center Fairchild Hiller Corporation Germantown, Maryland Attn: Library	Ralph Hall
1	Republic Aviation Fairchild Hiller Corporation Farmington, Long Island New York	
1	General Dynamics/Convair P.O. Box 1128 San Diego, California 92112 Attn: Library	Frank Dore
1	Missiles and Space Systems Center General Electric Company Valley Forge Space Technology Center P.O. Box 8555 Philadelphia, Pa. 19101 Attn: Library	A. Cohen F. Schultz
1	General Electric Company Flight Propulsion Lab. Department Cincinnati, Ohio Attn: Library	D. Suichu Leroy Smith
1	Grumman Aircraft Engineering Corporation Bethpage, Long Island, New York Attn: Library	Joseph Gavin
1	Hercules Powder Company Allegheny Ballistics Laboratory P.O. Box 210 Cumberland, Maryland 21501 Attn: Library	

Copies		
1	Honeywell Inc. Aerospace Division 2600 Ridgeway Road Minneapolis, Minnesota Attn: Library	
1	IIT Research Institute Technology Center Chicago, Illinois 60616 Attn: Library	C. K. Hersh
1	Kidde Aerospace Division Walter Kidde & Company, Inc. 567 Main Street Belleville, New Jersey 07109	R. J. Hanville
1	Ling-Temco-Vought Corporation P.O. Box 5907 Dallas, Texas 75222 Attn: Library	
1	Lockheed Missiles and Space Company P.O. Box 504 Sunnyvale, California 94087 Attn: Library	
1	Lockheed Propulsion Company P.O. Box 111 Redlands, California 92374 Attn: Library, Thackwell	
1	Marquardt Corporation 16555 Saticoy Street Box 2013 - South Annex Van Nuys, California 91409	L. R. Bell, Jr.
1	Denver Division Martin-Marietta Corporation P.O. Box 179 Denver, Colorado 80201 Attn: Library	Dr. Morganthaler F. R. Schwartzberg
1	Orlando Division Martin-Marietta Corporation Box 5827 Orlando, Florida Attn: Library	J. Fern

Copies		
1	Western Division McDonnell Douglas Astronautics 5301 Bolsa Ave Huntington Beach, California 92647 Attn: Library	R. W. Hallet G. W. Burge P. Klevatt
1	McDonnell Douglas Aircraft Corporation P.O. Box 516 Lambert Field, Missouri 63166 Attn: Library	R. A. Herzmark
1	Rocketdyne Division North American Rockwell, Inc. 6633 Canoga Avenue Canoga Park, California 91304 Attn: Library, Department 596-306	Dr. R. J. Thompson S. F. Iacobellis
1	Space & Information Systems Division North American Rockwell 12214 Lakewood Blvd Downey, California Attn: Library	
1	Northrop Space Laboratories 3401 West Broadway Hawthorne, California Attn: Library	Dr. William Howard
1	Purdue University Lafayette, Indiana 47907 Attn: Library (Technical)	Dr. Bruce Reese
1	Radio Corporation of America Astro-Electronics Products Princeton, New Jersey Attn: Library	
1	Rocket Research Corporation Willow Road at 116th Street Redmond, Washington 98052 Attn: Library	F. McCullough, Jr.
1	Stanford Research Institute 333 Ravenswood Avenue Menlo Park, California 94025 Attn: Library	Dr. Gerald Marksman

Copies		
1	Thiokol Chemical Corporation Redstone Division Huntsville, Alabama Attn: Library	John Goodloe
1	TRW Systems Inc. 1 Space Park Redondo Beach, California 90278 Attn: Tech. Lib. Doc. Acquisitions	D. H. Lee
1	TRW TAPCO Division 23555 Euclid Avenue Cleveland, Ohio 44117	P. T. Angell
1	United Aircraft Corporation Corporation Library 400 Main Street East Hartford, Connecticut 06108 Attn: Library	Dr. David Rix Erle Martin Frank Owen Wm. E. Taylor
1	United Aircraft Corporation Pratt & Whitney Division Florida Research & Development Center P.O. Box 2691 West Palm Beach, Florida 33402 Attn: Library	R. J. Coar Dr. Schmitke
1	United Aircraft Corporation United Technology Center P.O. Box 358 Sunnyvale, California 94038 Attn: Library	Dr. David Altman
1	Vickers Incorporated Box 302 Troy, Michigan	
1	Vought Astronautics Box 5907 Dallas, Texas Attn: Library	

Copies

1	Rockwell International Space Division 12214 Lakewood Boulevard Downey, California 90241	Dr. Don Gluck Mail Stop SK-06
1	General Dynamics/Convair P. O. Box 80847 5001 Kearny Villa Road San Diego, California 92138	Mr. John Stark Mail Zone 632-00
1	Minnesota Mining & Manufacturing Company 900 Bush Avenue St. Paul, Minnesota 55106 Attn: Library	